NORTHWESTERN UNIVERSITY

Rovibrational Control of a Diatomic Molecule

A DISSERTATION

SUBMITTED TO THE GRADUATE SCHOOL
IN PARTIAL FULFILLMENT OF THE REQUIREMENTS

for the degree

DOCTOR OF PHILOSOPHY

Field of Physics

By

Patrick R. Stollenwerk

EVANSTON, ILLINOIS

March 2020

ABSTRACT

Rovibrational Control of a Diatomic Molecule

Patrick R. Stollenwerk

Techniques for achieving complete quantum control over atoms have been developed and perfected over the past four decades with great success. This work has lead to multiple Nobel prizes and has been the catalyst for rapid advances in a broad array of research fields. A natural progression forward is to develop control over molecules. Compared to atoms, molecules have an increased complexity in their internal structure due to their additional degrees of freedom of rotations and vibrations. Control over these additional degrees of freedom would allow for the study of chemistry with unprecedented detail, the study of new many-body effects, and more precise tests of fundamental physics. The work in this thesis represents a step forward in the goal of having complete quantum control over a molecule.

We demonstrate rotational cooling on the silicon monoxide cation (SiO^+) via optical pumping with a spectrally pulse-shaped broadband laser. Cooling is achieved on a 100 ms time scale and attains a ground state population of 94(3)% ($T = 0.53(6)$ K). I also describe a novel approach to pulse shaping for populating arbitrary rovibrational states of

molecules with diagonal Franck-Condon Factors (FCFs). This technique is demonstrated on SiO^+ and is used to achieve steady state preparation of so-called molecular super-rotors. We demonstrate a narrow rotational population distribution ($\Delta N = 3$) around arbitrary targeted rotational states between $N = 0$ and $N = 65$. Control is accomplished through asymmetric pumping of transitions that add and remove angular momentum such that population is stochastically driven into a target rotational state. Furthermore, preliminary results demonstrating selective population of the first excited vibrational state are also presented.

The full preparation process for the control experiments of SiO^+ is also described. We characterize the photoionization spectrum of neutral SiO for the purpose of loading an ion trap, we measure the SiO^+ optical branching ratios and lifetimes of states relevant to laser control, and we characterize the dissociating $X^2\Sigma^+ \rightarrow C^2\Pi$ transition for state readout. Finally, we characterize the reaction rate of trapped SiO^+ with the background UHV environment. These steps described for SiO^+ are crucial for demonstrating control, and such a process could be generalized to other molecules of interest. In the remaining portions of the thesis I detail a proposal for optically pumping another molecule with diagonal FCFs, TeH^+, for the purpose of detecting a variation in the proton-to-electron mass ratio.

Acknowledgements

The completion of a Ph.D. is a serious endeavor. It requires one to dedicate a significant fraction of ones life towards problems that have never before been encountered. Failure is a norm and the challenges are often as much psychological as they are intellectual. For this reason it is incredibly important to work with people who uplift your morale as much as they help you overcome your technical challenges. In this respect, I have been very fortunate to be around people that have filled both roles. I must first thank my adviser, Brian Odom, who has consistently amazed me with both his patience and optimism. No matter how badly things may seem to be going, Brian always manages to remain calm and thoughtful. Though he has certainly had an incredible impact on my scientific development through his sharp questioning and his uncanny ability to pull something useful out of my ill-formed thoughts, it is his positive outlook and treatment of his students for which I will be forever grateful.

Early in my Ph.D. I had the fortune of being taken under the wing of Yen-Wei Lin. He made me feel welcome from the beginning and even entertained my ideas for the project before I really understood what was going on. In the two plus years that I worked closely with Yen-Wei on the SiO^+ project, I learned more about experimental design and approach from him than I knew there was to learn. Though the project has evolved and adapted considerably since he graduated, the foundation he laid made for an incredibly

flexible setup ideal for the challenges ahead. There isn't a part of the experiment that doesn't have his fingerprints on it, and for that I am immensely grateful.

A very big thank you goes out to Ivan Antonov who joined the SiO^+ project with me and provided a boost to help me accomplish many important goals. Ivan entered the project with a fresh dose of enthusiasm after I had faced a series of setbacks. He came equipped with the right set of skills, expertise, and a high level of energy at a critical time. His creativity and willingness to try new things and take risks was precisely what was needed to break the project open and make it the success it has become. He also provided useful comments on a first draft of my SiO^+ experiment chapter for which I am grateful.

Sruthi V also joined the SiO^+ project shortly after Ivan and though she has been busy with class requirements for much of her time on the project she has managed to make a significant impact. Learning everything necessary to run the experiment, even when things are working as intended, is no small task on such a complex and dynamic project. Despite this, she has already proven herself as capable of running the experiment even when novel issues appear. I am happy to be handing the project to someone as talented as Sruthi and look forward to seeing what she will accomplish with it.

Another very big thank you goes out to Prof. Tim Steimle and Damian Kokkin. They graciously re-purposed their experimental setup to measure the off-diagonal branching ratio of SiO^+ and made me feel welcome in my visit to Arizona. The experimental setup they built is a true work-horse and was a source of inspiration for many of my own experimental designs. In the short time I spent at their lab, we were able to collect data that literally determined the fate of the project.

A special thank you goes to James Dragan for designing and constructing the RF resonator for the large LIF trap. His contribution had a big impact during a time when I was starting to feel overwhelmed as the only one responsible for the design and construction of the experiment. A similar thank you goes to the Machine Shop at Northwestern who machined many of the parts I needed for the LIF trap. I would also like to thank Antonio G. S. de Oliveira-Filho and Ana P. de Lima Batista for their calculations on SiO^+ which were important for interpreting our dissociation data.

I'd also like to thank Mark Kokish for providing comments on my thesis at a stage when much of it was at the level of stream of consciousness. His comments helped guide me into writing something with much better structure. Mark and I joined the Odom group in the same year and I was fortunate to have a peer in whom I could confide, especially early on before I had confidence in what I was doing. I also want to thank all the previous and current Odom group members that I overlapped with. They all had small impacts over the years that, when integrated over time, add up to a large, positive presence in my life. Cumulatively, I have learned so much from them all.

I would like to thank my partner, Melanie Butler, who has been critical to me in so many ways. She has been both my emotional and intellectual support. Even while facing her own difficult transitions she has been supportive of me throughout my entire Ph.D. and has been more understanding of my commitments to my work than I could ever have hoped. She also provided clarity and a method for organizing my writing during the months spent working on my thesis that made a difficult task so much more bearable. Finally, I would also like to thank my family, especially my parents, Ann and Mark, and my brothers Andy and Chris. They have all been very supportive and created a family

culture where curiosity and a sincere effort to learn about the world are highly valued. I doubt I would ever have made it to this point without their unending encouragement and push to bring me opportunities to pursue my interests.

Note: I used, and highly recommend, the optics components library 'ComponentLibrary' by Alexander Franzen to generate some of my optical schematics.

Dedication

To my cat Kong who acts like I sometimes feel.

Table of Contents

List of Tables

dissociation data with the $\sim$5 cm^{-1} broad pulsed OPO tuned to the $X^2\Sigma^+(v=1) \rightarrow C^2\Pi_{3/2}(v=0)$ transition at 43077 cm^{-1}. The lifetime estimate is derived in appendix B.5. 277

List of Figures

target rotational states spanning $N = 0$ to $N = 65$. The spectra are distributed along the y-axis according to their expected rotational distribution. The line broadening observed in the spectrum near $N = 65$ is a consequence of using the less narrow OPO to record the dissociation spectrum. The observed rotational lines can be identified according to the underlying Fortrat diagram. The branches O (dark blue), P (blue), Q (black), R (red), and S (dark red) are labeled according to ΔN. All of the spectra plotted were recorded using the chirp method with the exception of the spectra at $N = 10$. **(Right)** The expected distribution for each corresponding spectral pulse shaping mask is plotted. **(Left-Inset)** The spectra for masks used to prepare $N = 0, 3, 10$ are zoomed in to show finer structure. The observed distribution can be compared to the expected distribution by extending horizontal lines from the expected range of N for the given mask. As an example this is done for the $N = 10$ mask spectrum. The O and R branch lines of the most extreme transitions present in this spectrum are partitioned with vertical lines. That all the Fortrat dots are contained within the boxed area indicates good agreement between the expected and observed distributions. 263

7.19 **(Left)** The $X^2\Sigma^+(v = 0) \rightarrow C^2\Pi_{1/2,3/2}(v = 1)$ Fortrat diagram and dissociation spectra of SiO^+ in the steady state during optical pumping via the pulse shaped broadband distributions with various target rotational states spanning $N = 0$ to $N = 65$. The spectra are

distributed along the y-axis according to their expected rotational distribution. The observed rotational lines can be identified according to the underlying Fortrat diagram. The branches O (dark blue), P (blue), Q (black), R (red), and S (dark red) are labeled according to ΔN. Unlike the spectra in Fig. 7.18, all of the spectra in this plot were recorded using the single frequency method. **(Right)** The expected distribution for each corresponding spectral pulse shaping mask is plotted. **(Left-Inset)** The spectra for masks used to prepare $N = 0$ are zoomed in to show finer structure. The observed distribution can be compared to the expected distribution by extending horizontal lines from the expected range of N for the given mask. 264

7.20 **i)** Shown are the two different masks used for preparing $v = 1$ population. Upper and lower red and blue spokes indicate the R and P branch transitions of the $X - B$ $v = 0$ and $v = 1$ diagonal transitions respectively. **ii)** The simulated population distributions for each mask are shown in black and the red and blue curves show the relative pumping rates of the R and P branches at each N. Solid (dashed) lines refer to population and pumping rates for $v = 0$ ($v = 1$) rotational states. **a)** The first mask relied on driving population to $v = 0, N \approx 20$ and rapidly cycling population before decaying into $v = 1$ where it would be driven down into the low N. **b)** The second mask relied on blackbody assistance to pump and cycle population to

the $X^2\Sigma^+(v = 1) \rightarrow C^2\Pi_{1/2}(v = 1)$ hotband (simulated in blue) and a combination of the $X^2\Sigma^+(v = 0) \rightarrow C^2\Pi_{1/2}(v = 0)$ and $X^2\Sigma^+(v = 1) \rightarrow C^2\Pi_{3/2}(v = 1)$ transitions. The red dotted lines simulate the uncontrolled population left in $v = 0$ between $N = 13$ and $N = 18$. The blue dotted lines represent the simulated spectrum for population in $v = 0, 1$ between $N = 0$ and $N = 3$. As indicated by the arrows the origin of $X^2\Sigma^+(v = 1) \rightarrow C^2\Pi_{3/2}(v = 1)$ is nearly 7 cm^{-1} to the red of the $X^2\Sigma^+(v = 0) \rightarrow C^2\Pi_{1/2}(v = 0)$ origin. 274

CHAPTER 1

Introduction

There is a prescription being followed in the research described in this thesis and more broadly within the experimental atomic, molecular, and optical physics community that is useful to make explicit. The prescription generally being followed goes something like this:

(i) Identify sensitive tests of fundamental theories
(ii) Improve control of light-matter interaction
(iii) Use control to study progressively more extreme regimes and make progressively more precise measurements
(iv) Expose deviations from fundamental theories

In many cases the goal of an experimentalist is to break known physics in a comprehensible way. In this sense physicists are paradoxically the unfortunate victims of the success and failure of modern physical theories. If we run the calculations for the Standard Model we are left with embarrassing inconsistencies with observed realities. For example, our own existence in a matter-dominated universe contradicts simple extrapolations of established theory, a conundrum for which currently no satisfactory explanation exists. The catch is that no matter how hard we push limits in the laboratory, the predictions of the Standard Model won't stop being accurate. Something has to give. This tension between observations and theory, we think, must eventually appear in our controlled experiments

too. The hope is that a deviation will offer us a hint to the details of a more fundamental theory from which our currently unexplained parameters are derivable. Ultimately, the goal is that a more fundamental theory will provide us with a deeper understanding of the universe.

A small portion of the work in this thesis concerns part (i) of the general prescription. This work can be found in Chapter 3 with a proposal discussing the use of tellurium monohydride cations in the search for possible proton-to-electron mass ratio (m_p/m_e) variations. In that chapter I also propose a bound on the attainable limit of m_p/m_e variation using a single molecule clock. The majority of the work in this thesis, however, is focused on part (ii) of the prescription. In Chapters 2 and 3 I describe methods for controlling the internal degrees of a diatomic molecule using optical pumping and discuss two molecular ions, silicon monoxide(+) and tellurium monohydride(+), well-suited for optical control. This is followed by a discussion in Chapters 4 through 6 of experiments performed for characterizing, producing, and preparing to optically control SiO^+. Finally, the culmination of this systematic effort is presented in Chapter 7 where multiple experiments demonstrating the range and degree of control over the internal degrees of freedom of SiO^+ are documented. The control demonstrated in this thesis is my attempt to provide a new tool for proceeding with parts (iii) and (iv).

1.1. Why Diatomic Molecules?

Motivation for controlling molecules is largely driven by the potential applications in a broad variety of disciplines. Diatomic molecules in particular are an alluring choice for control. They are simple enough to model with high accuracy, but they are simultaneously

complex enough to provide a rich structure full of non-trivial results and interactions. Furthermore, physicists have as yet only demonstrated complete quantum control over single atoms Thus diatomic molecules provide a natural next step forward in control. A sample of the broad array of potential applications includes quantum information science [**63**], many-body effects [**133, 134**] and Anderson localization [**18, 115**], and quantum controlled ultracold chemistry [**12, 66, 9**]. Precision measurement [**128**] is another exciting area that requires control of molecules, including search for the electron electric dipole moment [**64**], parity violations [**34**], and m_p/m_e variation [**46, 35**].

The motivation for control of molecules in this thesis is both intrinsic and derived from its application in the search for new physics through the detection of variation of fundamental constants. It is my belief that improving our ability to control nature is itself a worthy scientific pursuit, independent of any potential application, scientific or otherwise, that may come from it. When we ask what are the limits of control over nature, we are asking questions that are fundamental to understanding nature itself. In the search for new physics, the motivation is derived from molecules' sensitivity to m_p/m_e. Applying the definition from Uzan that the fundamental constants of a theory are *any parameters that cannot be explained by the theory itself* [**160**], we find that m_p/m_e meets the criteria as a fundamental constant of the Standard Model. That is, it is a fitting parameter that we can place into our models of the universe only after asking nature for the answer. The variation of a fundamental 'constant' such as m_p/m_e would unambiguously be the consequence of physics beyond the Standard Model.

The sensitivity of molecules to m_p/m_e is derived from the kinetic term of the nuclei. The kinetic energy of the nuclei is a consequence of the motion of the nuclei mass. The

nuclei mass, however, is a dimensionful term and therefore must be properly dedimensionalized before one can make sense of a measurement[1]. This detail is often ignored because in most experiments the distinction is irrelevant, but in the search for variation of fundamental constants[2] the distinction cannot be avoided. Otherwise, interpretation of the measurement becomes dependent on the system of units being used[3].

Dedimensionalization of the nuclei mass can be seen in the Born-Oppenheimer approximation of a diatomic molecule. For a given electronic state, the Hamiltonian can be written in the form

$$H = \frac{P^2}{2M} + E(R) \approx \frac{P^2}{2M} + \frac{k}{2}(R - R_0)^2 + E(R_0) \tag{1.1}$$

where $k \propto E(R)/R_0^2$ and M is the reduced mass of the molecule. The electronic part of the Hamiltonian is the energy of an electron orbiting a positively charged particle. The electronic energy for a given electronic state will be the total energy of the inner core electrons plus the energy of the valence electrons. The energy of the valence electrons will generally be proportional to the electron mass. Thus in the process of dedimensionalizing the Hamiltonian, the mass term in the kinetic energy is determined in 'units' of the electron mass.

[1]This is the source of a great amount of confusion in the literature with a prominent example pointed out in [**13**]. See the article by Duff [**39**] for a discussion of dimensional versus dimensionless constants of nature.

[2]Variation of constants here is acting as an oxymoron. Instead, whenever one encounters the phrase in literature one should read it as a search for new couplings to known fields. Indeed the standard interpretation for such a variation would be the existence of a previously unknown degree of freedom.

[3]A seeming exception to this rule is in the comparison of a time averaged dimensionful quantity with itself. See e.g. [**2**] where a search for *unit-independent* quantity $m_e/ < m_e >$ has been proposed.

In general the reduced mass of the molecule will be some composition of neutrons and protons and their binding energies with $m_n \approx m_p \approx 3\Lambda_{QCD}$. The reduced mass of the nuclei is therefore primarily derived from the strong interaction. In the literature it is usually assumed that all nuclear masses will scale with the proton mass and therefore the dependence of energy on M/m_e is often summarized as a dependence on m_p/m_e exclusively. In reality M/m_e will have a complicated dependence on quark and electron masses in 'units' of the strong interaction scale Λ_{QCD} [**48**]. The masses of the fundamental particles are themselves derived via the Higgs mechanism and are proportional to the Higgs field vacuum expectation value [**14**]. Thus attempts to detect an m_p/m_e variation should generally be considered as tests of the ratio of the strong and weak scales of the Standard Model. If a variation is detected, comparison of isotopes and different molecular species can conceivably be used to control for variation with respect to the electron mass and the different quark masses relative to Λ_{QCD}[4]. Thus any effort to detect variation of 'm_p/m_e' will benefit from comparison of an array of atomic and molecular clocks with different nuclear masses and isotopic composition.

1.2. Variation of m_p/m_e

The possibility for variation of fundamental constants has been a topic of inquiry since at least 1937 when Dirac proposed his large number hypothesis [**37**]. From an experimentalist's point of view, the search for variation in m_p/m_e is partly motivated by predictions of so-called Grand Unified Theories (GUTs), i.e. theories that attempt to unify strong, weak, and electromagnetic interactions at ultra-high energies that were

[4]It can be convenient to hold Λ_{QCD} constant and consider any variation to be a variation in the quark or electron masses, however as the masses themselves are dimensionful there is again no meaningful interpretation of their variation in a unit-free way.

possibly present in the very early moments of the universe with a single coupling constant. Under such models, changes in the unified coupling constant over cosmic time scales would appear as variations of the fine structure constant α and variations in strong interaction parameters present in $\mu \equiv m_p/m_e$ with a predicted variation of μ being 20 to 40 times greater than α [**159**]. Thus because the ceiling for precision on μ and α variation are comparable, detection of μ variation is considered to be more likely.

Constraints on a slowly drifting μ have been performed using both astrophysical observations and laboratory measurements. By comparing spectroscopic lines observed from astrophysical observations to terrestrial measurements, limits on the variation of μ in space and time have been constructed. The strongest limits are typically just below the ppm level [**100**] and come from comparison of methanol, ammonia, and hydrogen molecule transitions. Depending on the model, further limits can be introduced. For example, when asking if there is a slow linear drift in μ over time, high-redshift spectra of methanol dating back 7 Gyr can be used to place a drift limit of $\dot{\mu}/\mu = 1.4 \pm 1.4 \times 10^{-17}$ yr^{-1} [**69**].

Astrophysical observations have also been complemented by direct laboratory measurements searching for a variation. The most stringent limits are derived from a comparison of ^{87}Rb and ^{133}Cs atomic clocks over a period of 14 years with a value of $\dot{\mu}/\mu = 0.2 \pm 1.1 \times 10^{-16}$ yr^{-1} [**129**]. As the sensitivity of atomic clocks to μ is derived from hyperfine intervals the limits on variations using strictly atomic clocks is unlikely to significantly improve. Molecular clocks, however, are sensitive to μ in the optical regime through the use of vibrational overtone transitions and thus are potentially able to improve on the atomic clock-based limits by two or more orders of magnitude. Unfortunately the lack of

true optical cycling transitions and control of over molecular states has prevented comparable progress in molecular clocks. This is apparent in the the most stringent limit from a molecular clock set by comparing a rovibrational transition of SF_6 to the hyperfine transition in Cs which gives a value of $\dot{\mu}/\mu = -3.8 \pm 5.6 \times 10^{-14}$ yr^{-1} and more recently improved to a value of $\dot{\mu}/\mu = 0.3 \pm 1.0 \times 10^{-14}$ yr^{-1} [**143**] by comparing a transition of nearly degenerate vibrational levels in different electronic states of KRb to the Cs clock [**77**].

Aside from GUTs and slowly drifting variations, it has recently been proposed that dark matter interactions with matter may reveal themselves through dynamical variations of fundamental constants. Molecular clocks could therefore act as dark matter detectors and constrain the mass and coupling constants of possible dark matter candidates. In a network of clocks, the array of possible dark matter signatures includes coherent oscillations passing through the entire network or even transient oscillations that propagate through the network [**129**]. The frequency of these oscillations will be determined by the dark matter mass. Because virtually nothing is known about dark matter, the search for μ variations calls for highly sensitive clock transitions that can demonstrate high stability over both short and long time scales. Thus the clock that is most suitable in searching for slow drifts is not necessarily the best clock for all time scales. This is an important distinction because it suggests that there may not be a singular 'best molecular clock for probing the potential dark matter parameter space[5].

[5]It is possible that the transitions that are the most stable over long and short periods are also the most sensitive in which case the distinction may be moot. For example, homonuclear overtone transitions may optimize both criteria, however other considerations may still be relevant (see section 3.5.3).

To quantify the sensitivity of an energy level to μ (or generally any parameter), we must answer how a small change of $\Delta\mu$ changes the energy. This is essentially the task of standard error propagation. For any change in μ the change in energy of the i^{th} energy level can be expressed as

$$\Delta E_i = E_i(\mu + \Delta\mu) - E_i(\mu). \tag{1.2}$$

If we keep $\Delta\mu$ small compared to μ we can assume an approximately linear response in the change in energy. Thus for a fractional shift $\Delta\mu/\mu << 1$ the energy shift per fractional change in μ is given by

$$\Delta E_i / \left(\frac{\Delta\mu}{\mu}\right) = \left(\frac{E_i(\mu + \Delta\mu) - E_i(\mu)}{\Delta\mu}\right)\mu. \tag{1.3}$$

In the limit where $\Delta\mu \to 0$, the term on the right hand side of Eqn. (1.3) simply becomes the derivative of E_i with respect to μ multiplied by μ. With this expression we arrive at the usual definition of sensitivity found in the literature [**35, 84**]

$$q_\mu^i \equiv \frac{\partial E_i}{\partial(ln\mu)} = \mu\frac{\partial E_i}{\partial\mu} \tag{1.4}$$

where the logarithm is included as a matter of calculational convenience and q_μ^i is in units of energy.

The sensitivity of a particular energy level will depend on choice of the reference energy level and whether the reference energy level has a dependence on μ or not. Because we always measure transition energies, it is convenient to use the reference energy level as

the lower energy level in the transition and this is often how the absolute sensitivity is presented in the literature.

When discussing the sensitivity of transitions another convenient quantity, albeit one inducing a great deal of confusion[6], is the dimensionless sensitivity *coefficient* K_μ for a transition from $i \to f$ defined by

$$K_\mu \equiv \frac{q_\mu^f - q_\mu^i}{E_f - E_i} \tag{1.5}$$

which provides the enhancement of a fractional shift in the transition frequency relative to a fractional shift in μ via

$$\frac{\Delta\nu}{\nu} = K_\mu \frac{\Delta\mu}{\mu}. \tag{1.6}$$

Somewhat surprisingly, despite K_μ being a dimensionless quantity, its value still depends on what units are used. For example, although perverse, nothing prevents us from applying units of energy as being $\mu\times$ the Hydrogen 1s$\to$2s energy. In this case $K_\mu \to K_\mu + 1$ compared to when using atomic units. What keeps it honest is the realization that any transition energy can only be measured in reference to another measurement. That is all measurements are fundamentally comparisons[7]. In this sense the choice of experimental comparison provides us with the natural 'units' that we ought to use (i.e. in units of whatever our comparison clock is). Thus the most straightforward way to find the unit-independent sensitivity is to determine the sensitivity coefficient for the ratio of the

[6]See reference [**84**] for a recent, lucid discussion of common misconceptions found in treatment of sensitivity coefficients.

[7]It is interesting to note that we can take the lesson learned in our introductory physics courses that 'only differences in energy matter' and replace it with 'only ratios of differences in energies matter'.

two clock transitions at frequency ν_1 and ν_2 that will be experimentally compared. This expression is given by

$$\frac{\Delta(\nu_1/\nu_2)}{\nu_1/\nu_2} = (K_\mu^1 - K_\mu^2)\frac{\Delta\mu}{\mu} = K_\mu\frac{\Delta\mu}{\mu} \tag{1.7}$$

where we can observe that unit-dependent terms will cancel in the difference between the two coefficients. In practice the coefficients listed for particular transitions are determined using atomic units (i.e. no dependence on μ) and are typically compared to electronic transitions in atoms which have a very weak dependence on μ in atomic units. Thus what you see is usually what you will get in an experiment. However, the subtleties become important if, for example, two different molecular overtone transitions are used—a comparison that may be useful for ignoring the effect of common-mode errors. A large difference in absolute energy sensitivities does not imply the comparison will be sensitive to μ variation. This is because only a comparison of transitions with different sensitivity *coefficients* will provide a test on the variation. For overtone transitions this means the sensitivity of a comparison will be limited to anharmonic contributions which scale with μ differently than the harmonic contributions. Calculating the sensitivity of molecular transitions is relatively straight forward if the molecular constants are known. Descriptions of how to estimate the sensitivities using the Dunham coefficients are provided in e.g. [**130**] and [**159**].

CHAPTER 2

Optical Control of Diatomic Molecules

Complete control of a quantum system means the ability to prepare an arbitrary quantum state distribution beginning from an arbitrary distribution. In practice this means the ability to 'cool' the system and prepare a well-defined quantum state. Control over the internal and external degrees of freedom of molecules represents a substantial increase in difficulty compared to atoms. As an introduction to controlling molecules, it is worth first analyzing what has enabled the successful control of atoms. The list of atoms that have been laser-cooled is largely composed of neutral alkalis and singly ionized alkali-Earth species due to their simple electronic structure. The simple structure limits the number of possible states that need addressed to sustain laser control and therefore limits the number of lasers required for control.

Simple structure is useful, however it is not sufficient. In order to achieve cooling and therefore control, an increase in phase space density is necessary. Without dissipation, unitarity implies that an increase in the phase space density is not possible (see e.g. [**76**] for an introduction to this conception of cooling). In laser cooling, the dissipation is a consequence of spontaneous emission. Importantly, the rate of energy dissipation needs to vastly exceed the rate of thermalization with the external environment to achieve efficient cooling. In practice this means that shorter excited state lifetimes and therefore fast spontaneous emission rates are necessary to rapidly dissipate energy from the atoms.

Because the spontaneous emission rate scales like ω^3, optical transitions are the preferred transitions for achieving this.

The phase space of a system increases exponentially with each additional degree of freedom. This is perhaps the source of inspiration for Arthur Schawlow's famous quote that "a diatomic molecule is a molecule with one atom too many" as diatomic molecules exhibit two additional degrees of freedom, i.e. rotations and vibrations. The quote is now often used to warn AMO physicists who dare to venture into research that includes molecules with $N > 1$ atoms. However, despite the substantially increased complexity of molecules, rapid progress has been achieved within the last decade in generating cold and ultracold molecules using a variety of techniques including optical pumping [**148, 136, 11, 91**], buffer gas cooling [**55**], sympathetic cooling of state selected ionized molecules [**155**], supersonic expansion of molecular beams [**142**], and photoassociation [**111**]. Though no cooling of the phase space is used in the technique, remarkable control of the rotations of molecules has also been extended to very high energies with the generation of "super-rotors" using optical centrifuges [**82**].

Unfortunately, the process of populating excited rotational levels through coherent manipulation is non-dissipative and therefore the efficiency of populating a target state is limited by the initial population distribution. Furthermore, non-dissipative manipulation is fundamentally limited by the coherence time and therefore not conducive to sustained control. State preparation by photoassociation or state-selective ionization suffers from the same issue as these methods offer no mechanism by themselves for returning population to a particular prepared state. These methods limit the possible applications

available to molecular ions which are particularly well-suited for interrogating and observing dynamics over time scales exceeding minutes or even hours with the use of ion traps, but typically suffer from low densities due to Coulomb repulsion. Other schemes such as buffer gas cooling or supersonic expansion are dissipative but not driven methods and are therefore unable to populate anything besides ground states with high efficiency. Ideally, one would prefer to have the capability of efficiently populating a selected rotational state starting from an arbitrary initial population on command. Such a capability would open up high resolution studies of collision dynamics, access high energy rotational spectra and obviate their line assignments, allow for tuneability for quantum logic manipulations [**63**], and act as a blackbody radiation (BBR) spectral power monitor [**78**]. There is also opportunity for studying state dependent chemistry [**117, 12, 66, 9**] and many-body effects [**133, 134**].

Optical pumping combined with pulse shaping presents a potentially robust strategy for sustaining control over high energy rotations. Such strategies have been applied for populating select vibrational states in Cs_2 [**147, 146**] and have been used to shift the rotational distribution to larger average rotational quanta with some narrowing of the distribution [**31**]. In [**99**], a CW laser with a frequency sweep was added to populate specified low rovibrational states (up to $N = 4$) of Cs_2. However, these methods were performed on neutral molecules in supersonic beams where control is limited to submillisecond time scales, and had limited versatility over control of target rotational states.

Our approach to control molecular ions relies on optical pumping of electronic transitions with diagonal Franck-Condon Factors (FCFs) using a spectrally filtered broadband laser source. Electronic transitions driven at optical frequencies imply fast dissipation,

and diagonal FCFs restrict changes in vibrational energy and imply a simpler structure amenable to control by a small number of lasers. In this chapter I discuss what it means for a molecule to have diagonal FCFs and describe how this unique structure can be manipulated using a robust technique with relatively modest requirements for implementation. In particular I develop a model for the technique and detail a strategy for controlling the rovibrational degrees of freedom of the diagonal FCF silicon monoxide cation.

2.1. Diagonal Franck-Condon Factors

Noting the common features of laser cooled atoms, it is advantageous to identify molecules with relatively simple low-lying electronic structure so that optical pumping can be used without the concern of having multiple electronic states that require repumping. However, filtering species by this criterion alone does nothing to simplify the complexity associated with rotations and vibrations. Rotations are subject to strict dipole selection rules that limit the number of states to which excited states can decay. Vibrations, however are not subject to any selection rules. Molecules with (nearly) diagonal Franck-Condon factors (FCFs) however can exhibit quasi selection rules and, to a first approximation, participation of vibrations in electronic transitions can be ignored. This fact dramatically simplifies control and, as I discuss later, also has other useful implications associated with the rotational fine structure.

The transition dipole moment between two states is given by

$$\mu_{iv',fv''} \equiv \langle \Psi_{v',J'} | \langle \Psi_{el'} | \hat{\mu}^{el}(r) | \Psi_{el''} \rangle | \Psi_{v'',J''} \rangle. \tag{2.1}$$

Under the Condon approximation, the transition moment operator, $\hat{\mu}^{el}(r)$, is assumed to be constant as a function of internuclear distance over the extent of the vibrational wavefunctions. In practice this means the vibrational wavefunction overlap can be separated from the rest of the expression and thus the relative transition dipole moments between vibrational states of different electronic states is proportional to $\langle \Psi_{v'} | \Psi_{v''} \rangle$[1]. Consequently, the intensity of the transition is modulated by the FCF defined as

$$q(v', v'') = |\langle \Psi_{v'} | \Psi_{v''} \rangle|^2, \tag{2.2}$$

where $\Psi_{v'}$ and $\Psi_{v''}$ are the vibrational wavefunctions for the upper and lower electronic states respectively. For a more detailed discussion of branching ratios and their relationship to FCFs see chapter 4. To better understand the properties of species with diagonal FCFs, a qualitative and semi-quantitative understanding of FCFs is useful. Following the approximation outlined in [**113**], if we approximate the vibrations as harmonic oscillators then one can derive the analytic expression

$$q(0,0) = exp(-\frac{\pi c \mu_A \overline{\omega_e} (\Delta r_e)^2}{\hbar}) = exp(-\frac{\mu_A \overline{\omega_e} (\Delta r_e)^2}{67.44}), \tag{2.3}$$

where the expression has been simplified to evaluate using common spectroscopic units. Here, μ_A is the reduced mass of the molecule in amu, $\overline{\omega_e} \equiv 2\omega''\omega'/(\omega''+\omega')$ is the harmonic mean of the two vibrational constants in cm^{-1}, and $\Delta r_e \equiv r' - r''$ is the difference in the equilibrium internuclear separations of the two electronic states expressed in Ångstroms. From this expression it is clear that the diagonality of the FCFs is most sensitive to

[1]Note that the Condon approximation becomes less valid as vibrational overlap approaches unity.

Δr_e. Consequently, molecules with nearly diagonal FCFs will typically have equilibrium constants that agree to within a few pm or a few parts in a thousand.

Physically, we might expect a molecule to have diagonal FCFs whenever a non-bonding electron heavily localized on only a single atom is excited. This leaves the binding structure intact and the localization of the excited electron on a single atom limits the excitations influence on the bond energy. As discussed in section 4.1.2, this is the likely mechanism for the near diagonality of the SiO^+ $X \rightarrow B$ transition. In the case of different spin-orbit states the vibrational transitions also tend to be highly diagonal as their electronic structure is largely unchanged between levels. Transitions between Rydberg levels can also be expected to be nearly diagonal as the large electron orbit radius limits the influence on the binding structure of the core molecule.

2.1.1. Rotational Structure

In the context of control, diagonal FCFs afford us the luxury of considering rotational and vibrational structure separately. The rotational structure of transitions with diagonal FCFs is also well-behaved in a way that is conducive to simple spectral filtering for control. The close agreement of bond equilibrium distances for diagonal FCFs implies similar agreement between their rotational constants. This can be seen by observing that the rotational constant for a rigid rotor is given by

$$B_v \equiv \frac{h}{8\pi^2 cI} \tag{2.4}$$

where $I = \mu_A r_e^2$ is the moment of inertia.

Given the rotational constant, one can derive the total rotational energy of a rigid rotor which can be expressed as

$$F(N) = B_v N(N+1) \tag{2.5}$$

where N is taken to be the rotational quantum number. Generally, angular momentum selection rules restrict dipole transitions to those that result in $\Delta N = N' - N'' = -1, 0, +1$. However if the electronic angular momentum $\Lambda = 0$ for both electronic states (e.g. the SiO^+ $X \rightarrow B$ transition), then $\Delta N = 0$ transitions are forbidden. Thus, the rotational structure of an electronic transition is categorized into two or three series categorized as P, Q, and R branches for $\Delta N = -1, 0$, and $+1$ respectively. The P and R branches in particular are the important transitions for control as they allow one to change the rotational angular momentum of the molecule and hence control the rotational state. Complete control of the molecule's rotational energy therefore requires the ability to independently address all P and R branch transitions[2]. In practice this means hundreds of transitions and naively hundreds of lasers. As I discuss in section 5.7, a single broadband laser source can instead be spectrally filtered to independently select specified transitions. However, the resolution for spectral filtering is limited and one should consider the impact of the rotational constants on the fine structure as demonstrated below.

[2]Depending on the transition involved, the Q branch may also need to be optically pumped. See, e.g. TeH^+ in chapter 3

Neglecting an offset frequency associated with the electronic energy, the spectrum for each branch is

$$E_P(N) = F'(N-1) - F''(N) = 2B'_v + (3B'_v - B''_v)N + (B'_v - B''_v)N^2 \tag{2.6}$$

$$E_Q(N) = F'(N) - F''(N) = (B'_v - B''_v)N + (B'_v - B''_v)N^2 \tag{2.7}$$

$$E_R(N) = F'(N+1) - F''(N) = -(B'_v + B''_v)N + (B'_v - B''_v)N^2 \tag{2.8}$$

where $N = N''$ is the ground rotational quantum number. Following Herzberg [**56**], the P and R branches can be expressed by a single formula

$$E_{P,R}(m) = (B'_v + B''_v)m + (B'_v - B''_v)m^2 \tag{2.9}$$

where $m = -N$ for the P branch and $m = N + 1$ for the R branch.

From Eqn. (2.9) we can see that, for low N, the P branch is decreasing in frequency with increasing N and conversely, the R branch is increasing in frequency with increasing N. There is also a separation between the origin of the two branches equal to $2B'_v$. This initial separation and branching in opposite directions is evident in the Fortrat diagram of the diagonal SiO^+ $B^2\Sigma^+ \rightarrow X^2\Sigma^+(v, v)$ transitions plotted in Fig. 2.1. This initial oppositional branching is eventually overruled by the quadratic term in the equation, which ensures that one of the two branches will change direction assuming the molecule does not dissociate first. If $B'_v > B''_v$ then the quadratic coefficient will be positive and therefore the P branch must change direction for some N. Conversely, if $B'_v < B''_v$ then the R branch will change direction. In the event that higher order corrections to the

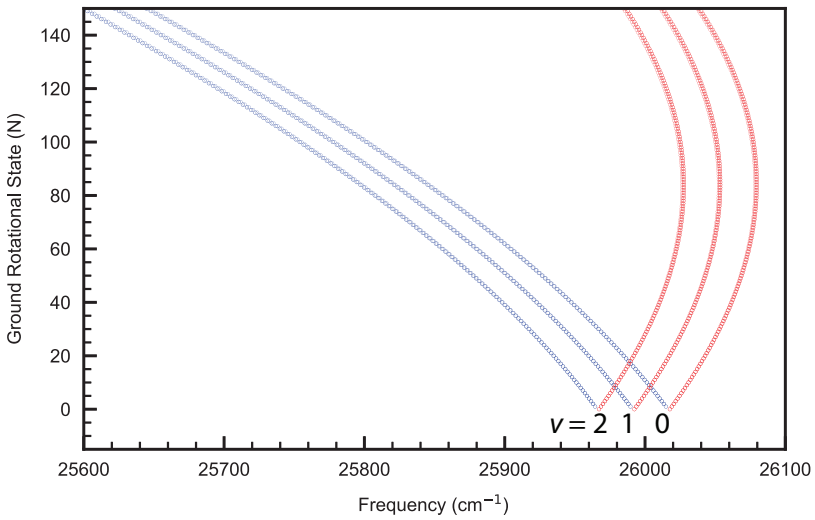

Figure 2.1. Fortrat diagram of the SiO^+ $B^2\Sigma^+(v) \rightarrow X^2\Sigma^+(v)$ transition for $v = 0, 1, 2$. Blue (Red) points refer to P (R) branch transitions. Close by band origins indicate similarity of vibrational constants for X and B states. The band head of each vibrational transition occurs at a relatively large rotational number $N = 85$ indicating very similar rotational constants for each electronic state (see text for details).

rigid rotor description of the molecule are necessary, more direction changes are possible and any detailed analysis of an actual molecule will depend on these parameters. For a qualitative and semi-quantitative analysis, however, the rigid rotor is sufficient.

The value for m where the series changes direction occurs when $dE_{P,R}/dm = 0$ and thus occurs at

$$m_{turn} = -\frac{B'_v + B''_v}{2(B'_v - B''_v)} \tag{2.10}$$

which can be rounded to the nearest integer to find the most extreme N. The transitions in the neighborhood of this turn around point are commonly referred to as the *band head* in molecular spectroscopy literature. The spectrum is said to be *red-degraded* for

$m_{turn} < 0$ and *blue-degraded* for $m_{turn} > 0$. Therefore the Fortrat diagram of the SiO^+ $B^2\Sigma^+ \rightarrow X^2\Sigma^+(v, v)$ transitions in Fig. 2.1 are examples of a nearly diagonal *red-degraded* structure.

From Eqn. (2.10), we can see that for transitions with diagonal FCFs the P and the R branches are monotonically separating for $N < N_{turn} \approx B/\Delta B$. Complete coverage of all these transitions thus requires a bandwidth of $|E_{P,R}(m_{turn}) - E_{P,R}(-m_{turn})| \approx 4B^2/|\Delta B|$. Control of rotational states in this range of rotational states can be accomplished with relatively simple spectral masks and without dynamical control of masks (see section 5.7 for a discussion of spectral pulse shaping of a broadband laser to selectively address molecule transitions).

2.2. The Role of Parity

Parity is a symmetry of the molecular Hamiltonian and therefore the eigenstates of the molecular Hamiltonian are also eigenstates of the parity operator. Because the electric dipole operator is an odd function, every dipole transition will result in a change to the opposite parity. This presents something of a problem for state control via optical pumping. The premise behind controlling the population with optical pumping is that the population is continuously excited electronically until spontaneous electronic decay stochastically brings the population into the desired state. However, excitation followed by decay results in switching the parity of the state twice and therefore the parity is preserved at the end of the process. Thus, population initially in separate parities cannot be transferred or exchanged by optical pumping and the ability to prepare a single molecular state is limited by the parity distribution of the initial population.

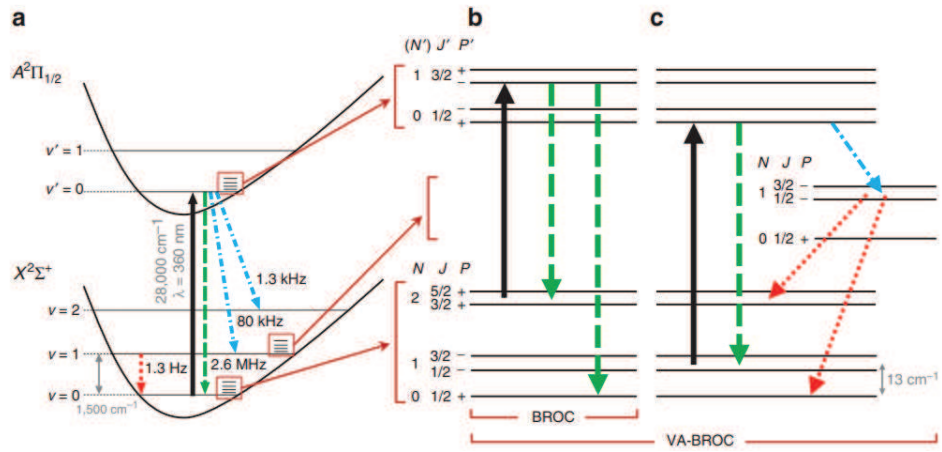

Figure 2.2. Figure is reproduced from [**91**] and shows the parity exchange process for the diagonal FCF transition in AlH^+. **(a)** Optical pumping on $X \rightarrow A$ is used to rotationally cool the population. This is nominally a parity preserving process. **(b)** Final step of population transfer shows $N = 2$ being pumped into $N = 0$, preserving the positive parity in the process. **(c)** Through use of seemingly extraneous optical pumping, an off diagonal decay ultimately results in a second decay into the ground state, changing the parity in the process.

In order to exchange population between each parity a mechanism involving an odd number of photons is necessary[3]. For example, blackbody radiation can cause a purely rotational transition. It is also possible for optical pumping to indirectly exchange parities through a cascading decay into an intermediate state and then the ground state. This can occur through the presence of an intermediate electronic state as in the $A^2\Pi$ state of SiO^+, or an off diagonal decay from the excited state to the ground electronic state. Alternatively, one can avoid reliance on spontaneous decay to an intermediate state by driving an overall odd transfer composed of an even excitation followed by an odd emission, or vice versa. This approach is demonstrated in TeH^+ (see chapter 3), where a strong

[3]More specifically, an odd number of *negative parity transition moments* is needed. This is most straightforwardly achieved through an odd number of electric dipole transitions.

magnetic dipole moment allows for transitions between states of the same parity, which complements the negative parity electric dipole moment. Finally, an external field such as a microwave source can be used to mix rotational states of opposite parity.

Population redistribution via optical pumping will typically dominate the rate of BBR redistribution, and in molecules with diagonal FCFs it will also dominate the parity exchange mechanism via vibrational decay. To a first approximation, this allows control over each subset of parity states to be treated independently. E.g. each parity has its own set of P and R branch transitions and the population dynamics and their relative population distributions due to pumping these transitions can be treated separately. An example of this is in the rotational cooling of AlH^+ shown in Fig. 2.2. Whether this approximation holds with the presence of an intermediate electronic state, as in SiO^+, depends on whether the dominant decay channel is to the ground state or to the intermediate state.

2.3. Rovibrational and Low-Lying Electronic Structure of SiO^+

The relevant low-lying structure of SiO^+ consists of three electronic states: $X^2\Sigma^+$, $A^2\Pi$, and $B^2\Sigma^+$. The potential energy curves of the three states are plotted in Fig. 2.3. One can see from the figure that the potential minima of X and B are well matched unlike that of A. The well-matched potential minima imply that the rotational constants will be similar. This is evident in the Fortrat diagram of the $B \rightarrow X$ transition seen in Fig. 2.1. The location of the bandhead near $N = 85$ is well above the expected distribution of occupied rotational states in a room temperature thermal distribution, reflecting the matched constants. The slightly longer distance for the potential minimum of the B state

Table 2.1. Deperturbed values reported by Rosner et al in [**126**]. A note of warning when applying these parameters to predict transition energies: the basis is unperturbed and so the matrix must be re-diagonalized to find the accurate transition energies and eigenstates. The contribution of the unperturbed terms can be useful for estimating systematic shifts if the reader is so inclined. For convenience I have included fit parameters assuming it is unperturbed. This approach is reasonably suitable for the diagonal $v = 0$ of $B \rightarrow X$ as the differential shifts of X due to A are small in the ground state.

	$X^2\Sigma^+$		$A^2\Pi$		$B^2\Sigma^+$	
	Deperturbed	Fit	Deperturbed	Fit	Deperturbed	Fit
T_e (cm^{-1})	0	0	2242.25(28)	–	26029.0138(16)	26016.56978
ω_e (cm^{-1})	1162.1823(27)	1155.102(3)	94.28(32)	–	1136.5802(12)	1129.677(3)
$\omega_e x_e$ (cm^{-1})	6.9698(15)	–	7.005(72)	–	6.92149(45)	–
B_e	0.7206159(36)	0.71761(1)	0.618588(31)	–	0.7130346(36)	0.71009(1)
r_e (Å)	1.516	1.519	1.636	–	1.524	1.527

compared to the X state is in agreement with the bandhead being observed in the R branch.

The $B \rightarrow X$ transition is also preferred for control because it is in the optical regime ($\sim$ 385 nm) and therefore has a comparatively short 70 ns lifetime. That this transition exhibits diagonal-like properties is also reflected in the spectroscopic constants (see Table 2.1). Diagonal FCFs in the $B \rightarrow X$ transition allow us to ignore vibrations to a first approximation, however this does not preclude radiative decay into the A electronic state. Fortunately, despite $B \rightarrow A$ being a fully allowed optical transition, the rate of decay via this channel is expected to be much slower than off diagonal $B \rightarrow X$. This can be qualitatively explained by $A \rightarrow B$ requiring a two electron promotion as opposed to one. For more detailed discussion see section 4.1.2. Additionally, $X \rightarrow A$ is a fully allowed single electron promotion transition, thus despite a comparatively small ω^3 term in

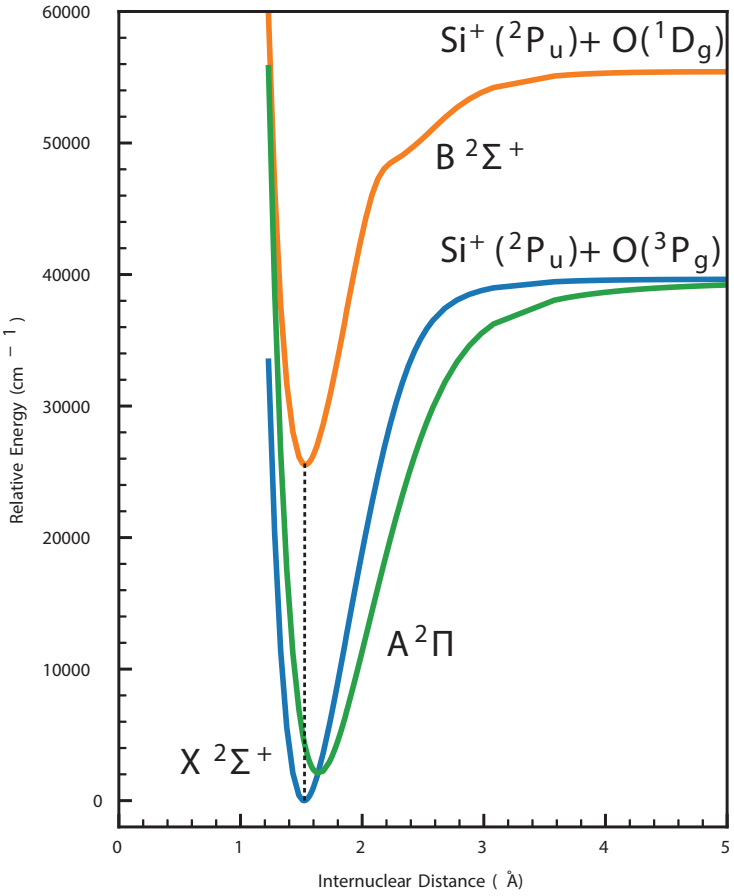

Figure 2.3. Low-lying potential energy curves of SiO^+ as calculated by Antonio G. S. de Oliveira-Filho and A. P. de Lima Batista [**116**]. The B and X states can be seen to have well-matched potential minima (as indicated by the vertical dashed line) implying the presence of nearly diagonal FCFs.

spontaneous emission rates[4], even in the fully saturated case, the time scale for decay from A to X is expected to be comparable or even faster than decay into it [**108**]. Furthermore, due to the ω^3 term of the Einstein $\mathcal{A}$ coefficient, the strongest decay channel from A to X is expected to be into $v = 0$ of X for the lowest v of A.

[4]See [**57**] for an invaluable resource relating common parameters used for describing transition strengths in atoms and molecules.

The role of the A state will be important with respect to parity and rotational state diffusion. As discussed in section 2.2, the A state serves as a parity exchange mechanism by virtue of being an intermediate electronic state. Though branching into A from B is expected be even weaker than off-diagonal B into X, the A state is still expected to be the dominant parity exchange mechanism due to the long vibrational state lifetimes of X and strong overlap of diagonal transitions as seen in Fig. 2.1. The excited vibrational states of X are calculated to be on the order of seconds [**108**] meaning that the average number of excitations before a radiative vibrational decay occurs is much greater than the average number of excitations before decay into A occurs. Parity exchange via BBR redistribution is expected to be slower than both of these time scales.[5]

2.4. Ground State Cooling of SiO^+

The most straightforward application of rotational control is ground rotational state preparation (i.e. rotational cooling). The use of pulse-shaped broadband lasers for rotational cooling of diagonal FCFs [**92**] was first demonstrated on the nearly diagonal $X^2\Sigma^+ \rightarrow A^2\Pi$ transition of AlH^+ [**91**]. As an example of rotational cooling, it is instructive to consider the spectral mask used for rotationally cooling SiO^+ seen in Fig. 2.4. The mechanism of cooling for this type of spectral mask is to simply pump P branch transitions while avoiding the R branch transitions. The net result is a continuous downward 'rotational pressure.' Over time, spontaneous emission will dissipate rotational energy as transitions that preferentially remove rotational energy are continuously driven.

[5]An exception may occur at extremely high N (> 170) where the lifetime approaches the millisecond time scale.

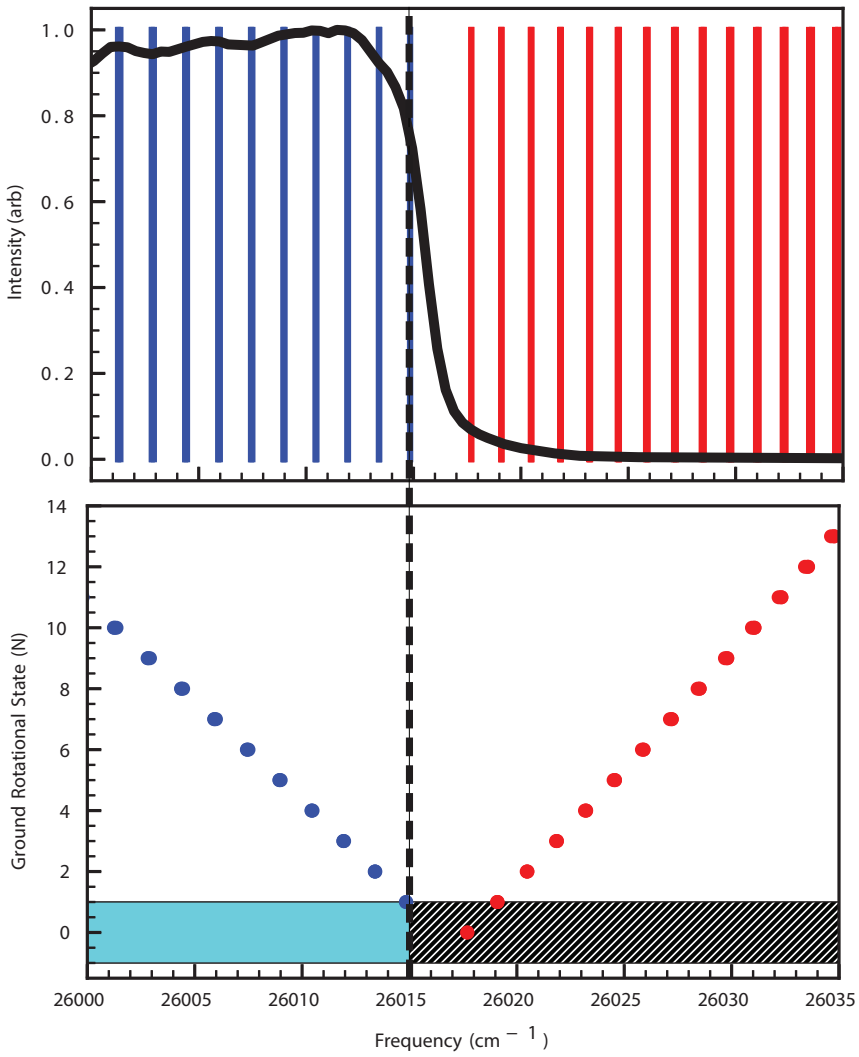

Figure 2.4. **(Upper)** Black trace represents the intensity profile of the pulse-shaped broadband laser source spectrum. Blue lines correspond to P branch transitions and red lines correspond to R branch transitions. **(Lower)** The corresponding mask in the frequency domain to generate this spectral profile is represented by the dark hashes indicating the removal of light from the spectrum and pieces of the spectrum left unfiltered are represented by light blue. The mask is placed on a Fortrat diagram with the vertical position demonstrating the target rotational state. The vertical dashed line indicates the position in the frequency domain of the spectral cutoff for $N = 0$ rotational state preparation.

2.4.1. Simplified Dynamical Model

It is useful to quantify the population transfer rate and identify fundamental limits of the rate of population control using this driven dissipative method. The time scale for pumping the population into the next rung of the rotational parity ladder is proportional to the optical pumping rate below saturation and proportional to the spontaneous emission rate in the saturated case. This can be modeled with the 3 level 'lambda-type' system seen in Fig. 2.5 using Einstein rate equations where $(1-\alpha)$ and α represent the branching ratios of the excited state. The optical pumping rate is given by $P_{i,j} = \rho(\omega_{i,j})B_{i,j}$ where $\rho(\omega_{i,j})$ is the spectral energy density on resonance and $B_{i,j}$ is the Einstein $\mathcal{B}$ coefficient connecting the two states. Note that $P_{i,j} = \frac{g_j}{g_i}P_{j,i}$ where g_i is the degeneracy factor. It is useful to define λ_N^P (λ_N^R) as the rate of population transfer into the next lowest (highest) rotational state of the same parity.

Because we are only concerned with rotational cooling for now, I will only focus on λ_N^P. However, λ_N^R will be important in later discussions involving arbitrary rotational control and descriptions of it can be found in appendix A.1. For quantifying λ_N^P, there are two primary regimes with which we are typically concerned. The first is the regime well below saturation such that $P_{i,j} << \Gamma$ where Γ is the inverse of the total lifetime of the upper state. In this regime we expect that the decay rate into $|N-2>$ will be dominated by the excitation rate. Upon excitation there is a probability of α that the population will decay into $|N-2>$. Therefore the rate for decreasing by two rotational states is simply $\alpha P_{N,N-1}$.

The second regime gives us a fundamental limit for how quickly population can be cooled or transferred to different rotational states. This regime occurs when we are

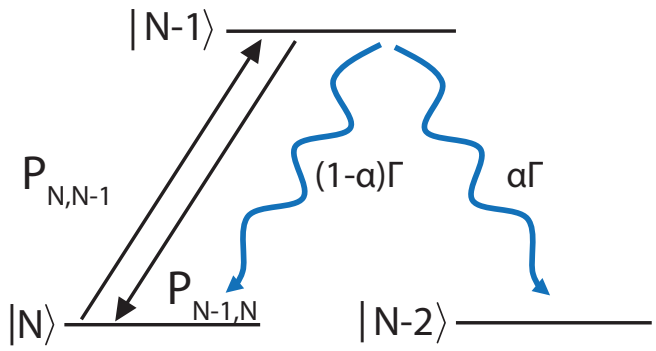

Figure 2.5. Pumping exclusively P or R branch transitions can be modeled with a simple rate equation to determine behavior and relevant time scales. Solid line with arrows represents the driven transition with pumping rates of $P_{N,N-1}$ into $N-1$ and $P_{N-1,N}$ into N. Blue curvy lines represent the partial decay rates according to their branching fractions α and $1-\alpha$ and total decay rate Γ.

pumping well above saturation, i.e. $P_{N,N-1} >> \Gamma$. In this regime, the population forms a quasi-steady state with the population distributed amongst $|N>$ and $|N-1>$ according to their degeneracy factors. Population in the excited state will leak out of the excited state into the next rotational state at a rate of $\alpha\Gamma$. Therefore the total rate of population decaying into $|N-2>$ is given by the fraction of population in $|N-1>$ multiplied by the $\alpha\Gamma$, i.e. the rate is given by $\frac{g_{N-1}}{g_{N-1}+g_N}\alpha\Gamma$.

The branching ratios between the different rotational fine structure is determined by the Hönl-London factors and therefore the details of the model will depend on the particular transition involved. For $\Sigma-\Sigma$ transitions (e.g. SiO^+ $X \rightarrow B$), the line strengths are given by [**56**]

$$S_N^R = N'' + 1 = N', S_N^P = N'' = N' + 1. \tag{2.11}$$

Thus $\frac{\alpha}{1-\alpha} = \frac{N'}{N'+1}$ and so $\alpha = \frac{N'}{2N'+1}$ where the single 'prime' indicates the excited rotational state quantum number and the double 'prime' indicates the ground rotational state quantum number. Thus in the fast $P_{N,N-1} >> \Gamma$ regime, the transfer rate becomes

$$\frac{\lambda_N^P}{\Gamma} = \frac{N-1}{2N-1}\frac{2N-1}{2N-1+2N+1} = \frac{1-1/N}{4} \text{ for } N > 1. \tag{2.12}$$

Thus we can see that $\lambda_N^P \approx \Gamma/4$ for large N and generally $\Gamma/8 \leq \lambda_N^P < \Gamma/4$.

In the slow $P_{N,N-1} << \Gamma$ regime, we are interested describing λ_N^P with respect to the relative spectral intensity of the pumping laser. To do this we note that $P_{N,N-1} = \rho_0 B_{N,N-1} = s_N^P \frac{g_{N-1}}{g_N}(1-\alpha)\Gamma$ for some s_N^P proportional to the spectral intensity on resonance. Thus in the well below saturated regime we have

$$\begin{aligned} \frac{\lambda_N^P}{\Gamma} &= \frac{\alpha P_{N,N-1}}{\Gamma} = s_N^P \frac{N-1}{2N-1}\frac{2N-1}{2N+1}\frac{N}{2N-1} \\ &= s_N^P \frac{1-1/N}{4-1/N^2} \text{ for } N > 1 \end{aligned} \tag{2.13}$$

which quickly converges to $\lambda_N^P \approx s_N^P\Gamma/4$ for large N and generally $s_N^P\Gamma/7.5 \leq \lambda_N^P < s_N^P\Gamma/4$.[6]

Following the discussion of parity in section 2.2 and the SiO^+ A state in section 2.3, we know we can treat dynamics in each parity separately. Considering the idealized version of the spectral mask in Fig. 2.4 with a perfect cutoff at the band origin, this means the transfer from the $2M^{th}$ rotational state (i.e. positive parity states) to the ground state

[6] Note that $N = 0, 1$ do not have the same Λ-type structure and thus the relationship does not hold.

can be modeled with the following rate equations:

$$\begin{aligned}
\sum_{i}^{M} n_{2i}(t) &= 1, n_{2M}(0) = 1 \\
\dot{n}_{2M} &= -\lambda n_{2M} \\
\dot{n}_{2M-2} &= \lambda(n_{2M} - n_{2M-2}) \\
&\cdots \\
\dot{n}_{2} &= \lambda(n_{4} - n_{2}) \\
\dot{n}_{0} &= \lambda n_{2}
\end{aligned} \tag{2.14}$$

where I have chosen $\lambda_N^P = \lambda$, $\lambda_N^R = 0$ for all N. Solving the system for n_0, we find

$$n_0(t) = 1 - e^{-\lambda t} \sum_{i=0}^{M-1} \frac{(\lambda t)^i}{i!}. \tag{2.15}$$

This solution has the interesting behavior in that it is suppressed for short time scales and then it grows exponentially, see e.g. the solid red curve in Fig. 2.6. The summation term can be recognized as a truncated expansion of the exponential $e^{\lambda t}$. The value for t that determines when the approximation becomes invalid can be estimated by noting that the terms in the exponential series only begin decreasing in value once $\lambda t < M$. Therefore the expected time scale for significant population accumulation in the target state will be approximately $t = M/\lambda$. The accumulation will initially be much slower than a standard exponential accumulation rate of λ/M, but will then rapidly outpace it after time $t = M/\lambda$.

In the $N = 0$ preparation case, the population in the negative parity rotational ladder must eventually transfer to the positive parity ladder before all of the population can be pumped into the ground rotational state. As discussed in section 2.3, the dominant parity exchange mechanism is decay into the A state followed by relaxation into X. As decay into the A state from B is rare, essentially all of the odd parity population is expected to be transferred into $N = 1$ and cycle on the $P(1)$ transition before decaying into A. Once in A, it will then decay into the even parity of X. The entire process can be characterized with a single rate λ_A that depends on the decay rate of A and the rate of decay from B into A which is $\propto f_{B,A}\lambda$. Therefore the population accumulation into $N = 0$ can be modeled by modifying Eqn. (2.14) to include an additional term $\lambda_A n_1$ giving us

$$
\begin{aligned}
\sum_i^M n_{2i+1}(t) = 1, n_{2M+1}(0) = 1 \\
\dot{n}_{2M+1} &= -\lambda n_{2M+1} \\
\dot{n}_{2M-1} &= \lambda(n_{2M+1} - n_{2M-1}) \\
&\cdots \\
\dot{n}_3 &= \lambda(n_5 - n_3) \\
\dot{n}_1 &= \lambda n_3 - \lambda_A n_1 \\
\dot{n}_0 &= \lambda_A n_1
\end{aligned}
\tag{2.16}
$$

with solution

$$
n_0(t) = 1 - e^{-\lambda t}\left(\sum_{i=0}^{M}\frac{(\lambda t)^i}{i!} - \frac{1}{(1-\lambda_A/\lambda)^M}\sum_{i=0}^{M-1}\frac{(\lambda-\lambda_A)^i t^i}{i!}\right) - \frac{e^{-\lambda_A t}}{(1-\lambda_A/\lambda)^M} \tag{2.17}
$$

where M is to be interpreted as the population beginning in the $(2M+1)^{th}$ rotational state.

We can translate λ_A into physical parameters when operating in two important limits. In the saturated limit, which will provide us the fastest parity transfer possible using this method[7], the decay rate out of B into A from pumping via the $B-X$ $P(1)$ transition will be $\frac{g_0}{g_0+g_1}\alpha\Gamma = f_{B,A}\Gamma/4$. Depending on which theory calculations you might believe, this rate is expected to be much faster than or comparable to Γ_A [**108, 25, 22**]. If Γ_A is much slower, then we have $\lambda_A = \Gamma_A$. Otherwise, if they are comparable, then the transfer is expected to follow a double exponential. This expression is useful because it means the measured value provides us an upper bound on the lifetime of the A state.

Experimentally we are typically in the low-saturation regime. In this regime we expect decay into A via the $B-X$ $P(1)$ transition to be $\alpha P_{1,0} = f_{B,A}\frac{g_0}{g_1}s_1^P(1-f_{B,A})\Gamma \approx f_{B,A}s_1^P\Gamma/3$. As the decay of A is expected to be comparable to $f_{B,A}\Gamma$, the low saturation regime will be the rate limiting step and the decay is better described as a single exponential process with rate constant $\lambda_A \approx s_1^P f_{B,A}\Gamma/3$. Therefore we can experimentally constrain $f_{B,A}$ by noting that $\frac{3\lambda_A}{7.5\lambda} = 0.4\frac{\lambda_A}{\lambda} < f_{B,A} < 0.75\frac{\lambda_A}{\lambda} = \frac{3\lambda_A}{4\lambda}$.

2.4.2. Einstein Rate Equation Simulation and Comparison to Simplified Model

Laser control over SiO^+ was simulated using an Einstein $\mathcal{A}$ and $\mathcal{B}$ coefficient model similar to prior work [**148, 109, 108, 149**]. The program was written in python using the numpy and scipy packages and represents an updated version of the one used in section 3.3. The simulation includes the $X^2\Sigma^+, A^2\Pi$, and $B^2\Sigma^+$ states with $v = 0, 1, 2$ and $N < 100$

[7]Note, for example, that a microwave source driving a purely rotational transition can be used to more rapidly exchange parity.

included. The model treats Zeeman states as degenerate and their effects are averaged over through their multiplicities in the Einstein coefficients. Details of the spin rotation states, however, are included in the simulation and treated individually. Stimulated rates due to Einstein $\mathcal{B}$ coefficients are calculated assuming a background blackbody temperature of 293 K and adding the contribution of the input spectral density intensity of unpolarized laser sources at every transition wavelength. In this way all possible incoherent coupling between states is included. Each laser source is described assuming a Gaussian line shape with a given spectral width that is modified by a spectral mask if necessary.

Application of the simplified dynamical model can be seen in Fig. 2.6 and Fig. 2.7. In Fig. 2.6, rotational cooling is simulated using the full Einstein rate equation simulation for population initialized in the $N = 12$ even parity state and the $N = 13$ odd parity state. In each case the transitions are driven according to the $N = 0$ rotational cooling mask with an effectively perfect cutoff just after $P(1)$ and using a spectral density well above saturation. The even parity case is fit to Eqn. (2.15) using $2M = 12$ in the summation and an amplitude parameter is included to account for any population not reaching $N = 0$ in the steady state. As seen in the red traces in Fig. 2.6, there is excellent agreement over shorter time scales. The fit returns a value of $\lambda \approx \Gamma/5.7$ which falls between the bounds of $\Gamma/8$ and $\Gamma/4$ as expected. The larger disagreement in the fit at longer time scales is a consequence of population diffusing through excited vibrational levels and to a lesser extent the A state before making it into the dark ground state.

Similarly, for the simulation beginning at $N = 13$, the accumulation into $N = 0$ was fit to Eqn. (2.17) using $2M + 1 = 13$ in the summation and also adding an additional amplitude parameter. The input values into the simulation are such that $f_{B,A}\Gamma >> \Gamma_A$.

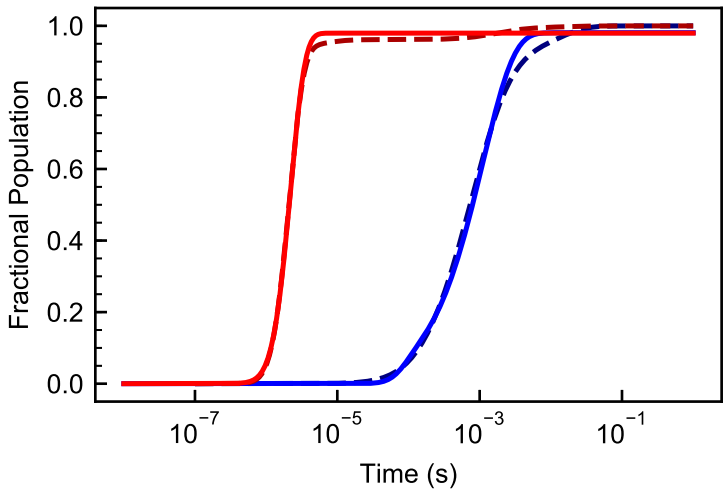

Figure 2.6. Plotted above are the two simulated scenarios (dashed lines) and the simplified model fits to them (solid lines) for the population of $N = 0$ (even parity) as a function of applied laser cooling time in the extreme saturated regime. The red lines are the results for population initialized in the even parity $N = 12$ state and the blue lines are for population initialized in the odd parity $N = 13$ state. The dramatically different time scales for each initial state are a consequence of the slow parity exchange mechanism. See text for details of the fit.

Additionally, the rate of decay into X from A depends strongly on which vibrational state it is decaying from. In the simulation, which includes the first three vibrational levels, the decay rate of the A state varies from 170 s^{-1} to 3000 s^{-1}. Because decay from B will populate multiple vibrational levels, no dominant singular time scale for changing parity exists. Multiple time scales will appear with each weighted roughly according to the branching fractions of $B - A$ vibrational levels. Hence the quality of the fit at longer time scales seen in the blue traces of Fig. 2.6 degrades. As a consequence, the fit for the parameter λ for an exclusively odd parity initial state will differ from the expected range of values to compensate for this larger disagreement and the fit for λ_A is expected to act as a crude weighted average of the multiple time scales. Nevertheless, $\lambda_A \approx 900$ s^{-1} which

is of order the typical decay rate for the different vibrational states of A and $\lambda \approx \Gamma/38$ which is within an order of magnitude of what we expect. The quality of the fit compared to experimental data will indicate if multiple time scales are present and therefore inform us if decay into A or out of A is the rate limiting step.

For testing the simplified dynamical model in the regime well below saturation, I set the input laser spectral density to values that are more typically found in our experimental setup. For the simulation the effectively perfect spectral cutoff after $P(1)$ is again used to cool population into the ground state. The results of the simulation, seen in Fig. 2.7, show rotational cooling for population initialized in $N = 10$ (red), $N = 11$ (blue), and split evenly between $N = 10, 11$ (black). The comparison of expectations to the actual fits are shown in Table 2.2. Unlike in the fully saturated regime, each instance of starting distributions had consistent agreement with shared parameters and was found to be within the expected range of values given the simulation inputs. This is expected because in the low saturation regime, only the time scales set by optical pumping dominate. Thus overall quality of agreement is observed to be improved at at all time scales.

Because the actual experiment will involve a distribution of initially occupied rotational states, I also compared the model to the simulation initialized in a room temperature ($T = 293$ K) thermal distribution. The comparison was repeated twice using a perfect cutoff in one instance and a cutoff with approximately the same sharpness observed experimentally (~ 2.2 cm^{-1} 90-10). In both cases, the estimated power and intensity used in the experiment are assumed. The simulation is later compared to experimental data (see section 7.3). The results of the fit are listed in Table 2.2 and their plots can be seen in Fig. 2.8. For the fit, the choice of N for the summation was chosen according to the

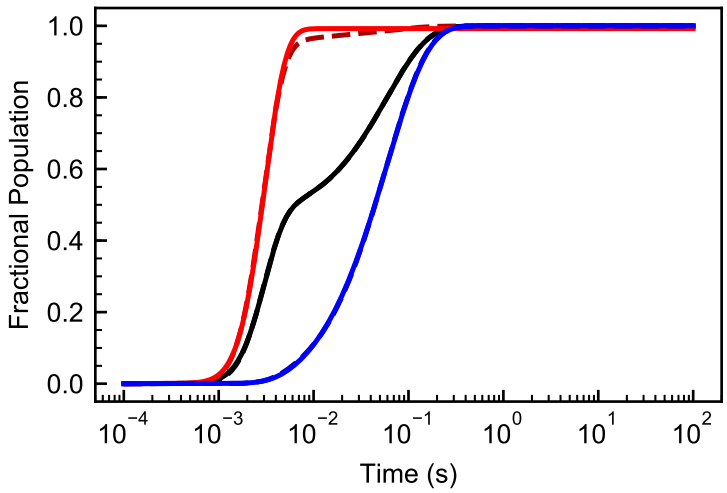

Figure 2.7. Plotted above are the three simulated scenarios in the low-saturation regime (dashed lines) and the simplified model fits to them (solid lines) for the population of $N = 0$ as a function of applied laser cooling time. The red lines are the results for population initialized in even parity $N = 10$ state and the blue lines are for population initialized in the odd parity $N = 11$ state. The black lines represent population initialized evenly between $N = 10, 11$. Analysis of fit parameters can be seen in Table 2.2.

peak of the Boltzmann distribution (i.e. $2M \approx 12$). As expected, agreement in both cases is of lower quality than the non-thermal instances. In the shorter time-scales (of order 1 ms), population initialized in rotational states lower down the rotational ladder than the peak of the thermal distribution will arrive in the ground rotational state earlier. Therefore the model underestimates the population accumulation in the early time scales. Since the parity exchange rate is much slower than any rotational cooling process, the agreement at much later time scales is preserved. When comparing the two initially thermal simulations, we can see that the effect of the cutoff is almost entirely captured by the amplitude parameters. As seen in Table 2.2 the fitted rates are not observed to vary significantly between the two cases. For the more experimentally accurate cutoff, the $N = 0$ population asymptotes at a value of 0.813.

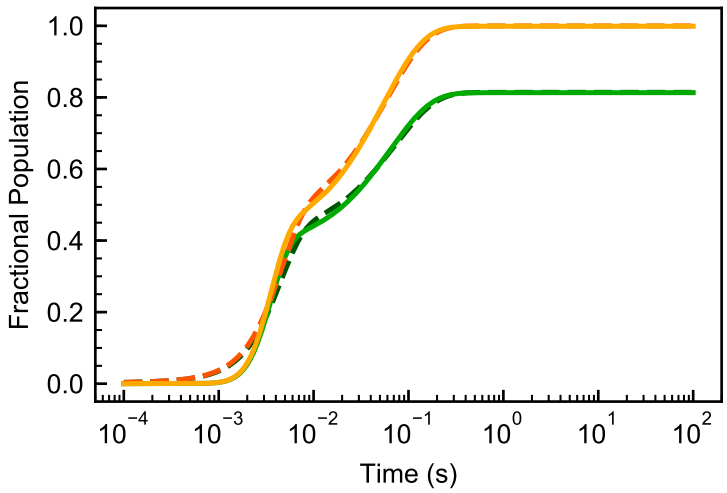

Figure 2.8. Rate equation simulation for the population in $N = 0$ as a function of time with population initialized in a T=293 K thermal distribution. The population is cooled in the low-saturation limit with a perfect spectral cutoff after $P(1)$ (orange dashed line) and with a 90-10 cutoff of 2.2 cm^{-1} (green dashed line). The corresponding fits to the simulation are represented by the solid lines of the same color. Good agreement is observed despite the initial thermal distribution and imperfect spectral cutoff. See Table 2.2 for details of the fitted parameters.

Table 2.2. The results of the fit to the Einstein rate equation simulation $N = 0$ population as a function of cooling time using the simplified dynamical model in Eqn. (2.15) and Eqn. (2.17). The simulations and their fits can be seen in Fig. 2.7 and Fig. 2.8. The simulation assumes a total laser intensity of 170 mW/mm^2 with a bandwidth of 250 cm^{-1}.

Initial Distribution	$N = 10$	$N = 11$	$N = 10, 11$	293 K	293 K, 2.2 cm^{-1} cutoff
λ (s^{-1})	1627	1593	1672	1708	1400
$\frac{s\Gamma}{\lambda}$ †	5.56	5.68	5.41	5.30	6.46
λ_A (s^{-1})	–	16.84	16.94	18.69	15.26
$f_{B,A}/\frac{\lambda}{\lambda_A}$ ‡	–	0.55	0.57	0.53	0.53

† In the simulation $P_{1,0} \equiv s\Gamma = 9049\ \text{s}^{-1}$. The expected range of values is $4 < \frac{s\Gamma}{\lambda} < 8$

‡ In the simulation $1/f_{B,A} = 172.39$. The expected range of values is $0.4 < f_{B,A}/\frac{\lambda}{\lambda_A} < 0.75$

In all the fits to the simulations the ratio of λ and λ_A is observed to vary by less than 10% which suggests its utility for extracting $f_{B,A}$ experimentally.

2.4.3. m_J Mixing

Thus far I have neglected spin-rotation and Zeeman sub-levels. The possibility for dark states is present whenever a transition is being driven by polarized light and the degeneracy of the ground state is equal to or greater than the excited state degeneracy [**15**][8]. In principle this could present a challenge to the model because any $\Delta J = 0, -1$ transition will have some sub-space of magnetic sublevel superpositions that are dark to the polarized light of a laser, rendering the assumptions of the model pumping rates invalid. There are two common methods for avoiding this type of unwanted dark state behavior. The first is to modulate the polarization of the laser and therefore continuously change which states are dark. The second method, which is the simplest to implement in practice, is to mix m_J states with an external magnetic field and use a laser polarization that is not completely parallel or perpendicular to the magnetic field.

Unlike in cases such as Doppler cooling of atoms, rotational control relies on broadband coverage of the spectrum. Thus considerations of Zeeman broadening[9] are not of concern and there is no practical upper limit[10] on the strength of the magnetic field to optimize the pumping rate. Given an optical pumping rate by the laser, the magnetic field need only be strong enough such that mixing is not the rate limiting step. The mixing rate will be on the order of the Bohr magneton ($\sim$ 1.4 MHz/G). For transitions with increasingly larger J, the minimum optimal magnetic field strength progressively decreases. This is

[8]For upper and lower states of equal degeneracy and half integer angular momentum, dark states can be avoided using non circularly polarized light

[9]See [**15**] for a complete discussion.

[10]The only exception is the possibility for Zeeman sublevels to broaden into neighboring rotational states which can effectively degrade the quality of the spectral cutoff.

because the number of states increases but the number of dark states stays constant (i.e. 2).

2.5. Steady State Rotational Control

Here we consider rotational control extended to arbitrary excited rotational states. This can generally be accomplished by ensuring strong optical pumping of the R branch for rotational states below the target state and strong optical pumping of the P branch for rotational states above the target state. This effectively creates an upward and downward 'rotational pressure' around the target state. As an example, the Fortrat diagram and the associated spectral mask for preparing $N = 20$ in SiO^+ can be seen in Fig.2.9. The example masks of $N = 3, 10, 20$ alongside the simple $N = 0$ rotational cooling mask seen in Fig.2.9 demonstrate how extension of control to excited rotational states requires only a slight modification from the technique used for ground state preparation. Indeed, experimentally, the masks require only the addition of a thin wire (with minimal requirements for precision of width) to the razor blade mask used for ground state preparation.

By modifying the rate equations in Eqn. (2.14) to include R branch transitions, we can derive a relationship for the steady state population in a target rotational state t relative to $t \pm 2k$. The result, derived in appendix A.2, is given by

$$
\begin{aligned}
n_t &= n_{t+2k} \prod_{i=0}^{k-1} \frac{\lambda^P_{t+2i+2}}{\lambda^R_{t+2i}}, \\
n_t &= n_{t-2k} \prod_{i=0}^{k-1} \frac{\lambda^R_{t-2i-2}}{\lambda^P_{t-2i}}.
\end{aligned}
\tag{2.18}
$$

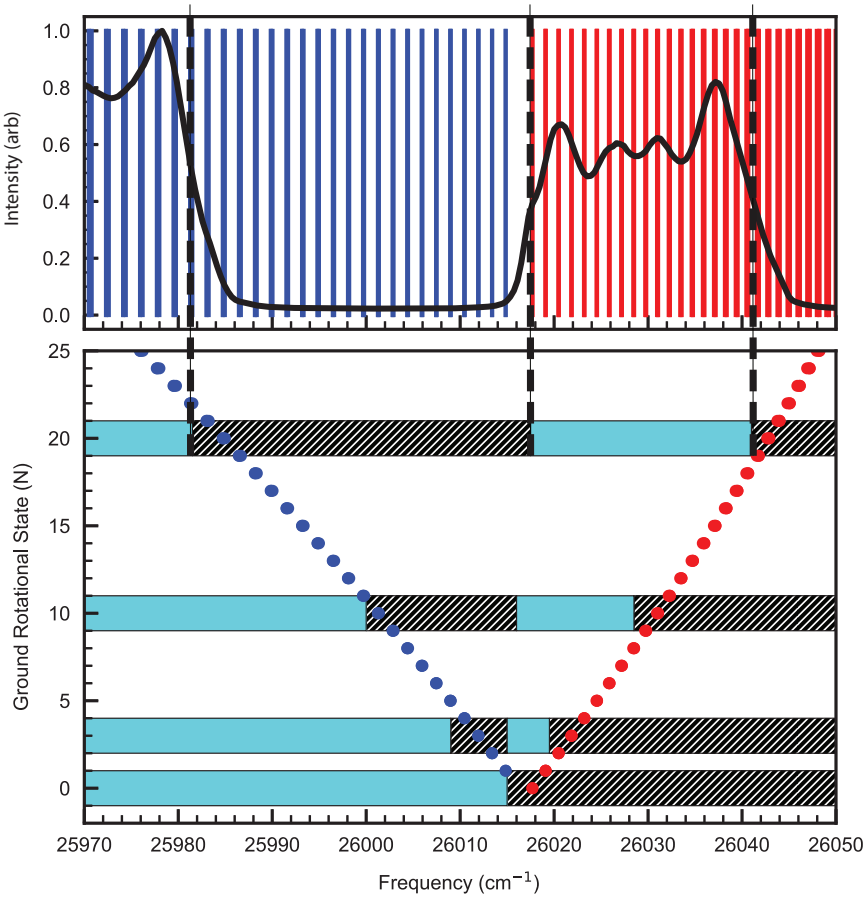

Figure 2.9. **(Upper)** Black trace represents the intensity profile of the pulse-shaped broadband laser source spectrum. Blue lines correspond to P branch transitions and red lines correspond to R branch transitions. **(Lower)** The corresponding mask in the frequency domain to generate these spectral profiles is represented by the dark hashes indicating the removal of light from the spectrum and pieces of the spectrum left unfiltered are represented by light blue. Several example masks are placed on the Fortrat diagram with the vertical position demonstrating the target rotational state. Masks included are for $N = 0, 3, 10, 20$ target preparation states. The vertical dashed line indicates the position in the frequency domain of the spectral cutoff for $N = 20$ rotational state preparation.

Assuming the cutoff has an exponential suppression of spectral intensity, we can derive from the relationship in Eqn. (2.18) that the population distribution around the target

state will be approximately of the form $\sim e^{-\Delta N^2/\sigma^2}$ where σ depends on the sharpness of the spectral cutoff and the spacing between transitions. If the spectral intensity of the cutoff scales like $\sim e^{-\Delta\nu/\gamma}$ where γ is the sharpness of the spectral cutoff, then we expect the rotational population distribution width to scale like $\sigma \sim \sqrt{\frac{\gamma}{2B_0}}$ where $2B_0$ is the approximate spacing between consecutive P and R branch transitions. For the special case of preparing $N = 0$ in SiO^+, the simplified steady state model is worked out in detail in appendix A.2.1.

This analysis suggests that after the population has reached the steady state distribution, most of the spectral coverage of the mask is no longer necessary. All we require to sustain the distribution is a local neighborhood of P and R branch coverage with the laser spectrum equal to four to five R branch transitions below the target state and a similar number of P branch transitions above[11]. The rate for population to leak out of the local neighborhood of states will be of order the population fraction on the boundary multiplied by the pumping rate out of the border states. This rate will therefore also be exponentially suppressed.

The ability to control the population with a small neighborhood of P and R branch transitions has implications for avoiding issues of congested lines during state preparation, such as in the region beyond the bandhead. For example, in SiO^+ the R branch turns around at $N = 85$ and the transition at $R(170)$ is coincident with the band origin (Fig. 2.1) meaning that the R branch transitions for $N = 0$ to $N = 84$ overlap with $N = 85$ to $N = 170$. For thermal populations this coincidence of lines is irrelevant for preparation

[11] A minimum of 3 transitions above and below the target state is necessary no matter the sharpness of the cutoff in order to avoid rotational diffusion outside of the local neighborhood via off diagonal decays or decays to an intermediate electronic state.

of states below $N = 85$ as nearly all of the population begins and remains below $N = 85$. Preparation of states between $N = 85$ and $N = 170$, however, has transitions in the same region that need to be simultaneously pumped and not pumped. If population can be dynamically moved through the rotational ladder, then the contradiction can be ignored.

2.5.1. Population Flow Between Parities

The rate of population flow between different parities is determined by the total population in each state multiplied by its particular leakage rate into the opposite parity. In most cases the BBR redistribution rates will typically be much slower than the rate of cascading decays. Thus the leakage rate from one parity into the other is regulated by the optical pumping rate. In the steady state, the two rates must be equal. This allows us to determine the relative population distribution between each set of parity states. The relationship between the relative populations of opposite parities is derived in appendix A.2.1.

2.5.2. Rovibrational Control

Throughout this analysis, we have relied on the artificial generation of 'dark' states by spectral filtering of a broadband laser. In the ground vibrational states the effective lifetime of these dark states is limited by the amount of 'leakage light' from the spectral filters that optically pump out of the intended target states. The population build up in the target state is then a ratio of the time scale for repopulating the target state and the effective lifetime of the target state due to the leakage light. This relationship is generally true. Any state that can be populated sufficiently fast, i.e. fast compared to

the target state effective lifetime, can also be significantly populated in the steady state. This can be seen in the relationship between population in the A state versus in the X state of SiO^+ when rotationally cooling. The (in)ability to populate the A state is limited by weak radiative branching ratios of the B state and the comparably short lifetime of the A state[12]. The same relationship is not true for excited vibrational states of X or generally in other molecules which tend to have longer lived vibrational lifetimes. Long lifetimes mean that population accumulation can occur in excited states unintentionally if a spectral mask is not carefully considered. In SiO^+, the possibility for significantly populating excited vibrational states of X is aided by significantly longer lifetimes ($\sim$ seconds [**108**]) and stronger off diagonal $B - X$ branching ratios than those observed in decay to A [**151**].

If the diagonal transitions of excited vibrational states are driven, then the distribution for each separate parity rotational ladder of each vibrational level will be determined in the same way that it was for Eqn. (2.18). This relationship is important because molecules with nearly diagonal FCFs will tend to have similar vibrational constants and therefore overlapping diagonal transitions. Thus in the event of an off-diagonal decay, population in the excited vibrational state may be driven to a rotational state far from the 'target' rotational state or may be driven toward a state that is dark to the laser. The consequence of such a scenario would be significant population loss in the target state. One approach to mitigating the effects of off-diagonal decay is to apply a spectral mask

[12]The branching rate and A state lifetime has not been measured and such calculations are not accurate enough to definitively conclude this. However, even if calculations are accurate, this doesn't preclude control being extended to the A state as significant population accumulation could potentially be enabled via excitation to a separate excited electronic level with stronger emission to A. The precise optical pumping requirements for such a scenario are unknown but would undoubtedly involve many more lasers and is therefore not considered.

for the excited vibrational states such that the population is driven towards the same rotational target state *and* insure that the mask avoids population flow towards any dark states. Removing dark states is crucial for limiting the effective lifetime of the excited states and thus limiting the population that accumulates in the excited states.

Constructing spectral masks such that each excited vibrational state has identical target rotational states will sometimes lead to conflicting spectral masks. Such an example can be seen with the $N = 10$, $v = 0$ mask for SiO^+ shown in Fig. 2.10. In this case the target states in the excited vibrational levels are shifted from each other to accommodate the creation of the dark state at $N = 10, v = 0$. As long as the shifted target states are not displaced significantly compared to the average number of scatters before an off diagonal decay, the effect on the total population accumulation in the target state will not be significant.

Our approach for populating an arbitrary target rovibrational state with a minimal number of lasers is shown in Fig. 2.10. Here we slightly modify the spectral masks such that the dark state for a target rotational state is removed by closing the P and R branch coverage gap in the ground vibrational state and opening a gap to create a new dark state in the desired vibrational state. The applicability of this method likely only extends to $v = 2$ for reasons described in appendix A.2.2.

Determining the vibrational population distribution is more involved than determining the rotational distribution within each parity of each vibrational level. The vibrational distribution is also sensitive to the specifics of the FCFs and the lifetimes and branching ratios of excited vibrational levels. Nevertheless, a qualitative and semi-quantitative description of the distribution can be estimated with some reasonable assumptions. The

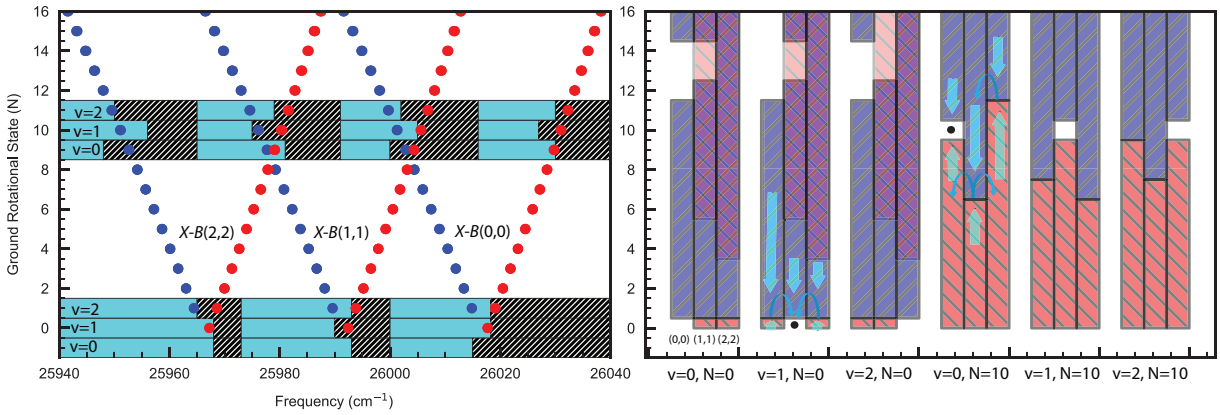

Figure 2.10. **(Left)** Two sets of example masks are shown demonstrating $N = 0$ and $N = 10$ state preparation for $v = 0, 1, 2$. In each case, the mask cutoffs are carefully chosen such that the non-target vibrational states drive population towards the target rotational without leaving the target rotational state such that the effective lifetime of population in the non-target vibrational states are reduced. **(Right)** The corresponding P (blue hashed areas) and R (red hashed areas) branch transitions driven by the broadband laser after the application of each mask are plotted. This way, the steady state flow is more easily determined for a given mask. Blue arrows on the $v = 1, N = 0$, $v = 0, N = 10$ masks indicate population flows. In the $v = 1, N = 0$ case population can be seen to be driven towards the ground rotational state in each vibrational mode, however only $v = 1$ is left dark to the laser spectrum. Following the net flow of population leads one to the $v = 1, N = 0$ state as indicated by the black ellipse where the population preferentially accumulates. In the $v = 0, N = 10$ case, coincidence of conflicting P and R branch transitions of different vibrational transitions is accommodated for by shifting the target state slightly for different vibrational modes. The diagonal nature of the transitions allows for a quasi-steady state distribution to be achieved before a change in vibrational state.

details are omitted from this section and can instead be seen in appendix A.2.2. A simplified steady state model for estimating the absolute population distribution of these masks is derived in appendix A.2.3.

CHAPTER 3

Optical Pumping of Molecular Ions for Probing m_p/m_e Variation

Most of this thesis is focused on efforts to control SiO^+. This chapter focuses instead on the tellurium monohydride cation, that, like SiO^+, is expected to have nearly diagonal FCFs and therefore be amenable to laser control. Here we propose optical pumping of TeH^+ to help extract new, sensitive limits in the search for a variation in m_p/m_e. Polar molecules generally exhibit shorter vibrational lifetimes and greater sensitivity to electric fields than non-polar molecules. However, the systematic uncertainties and statistical properties of TeH^+ are comparable to those found in atomic ions used for optical clocks [**79**]. This has positive implications for other polar molecules amenable to laser control such as SiO^+ and their role in the search for a varying m_p/m_e. The work in this chapter represents a concrete proposal demonstrating how optical control of molecular ions can be leveraged in the search for new physics. The proposal has previously been reported in [**149**] and therefore the remaining text in this chapter closely parallels that work.

Molecular rotational and vibrational energies scale like $E_{\rm h}(M/m_e)^\beta$ where $E_{\rm h}$ is the atomic unit of energy defined by the electronic energy scale, M is the reduced mass of the molecule, $\beta = -1/2$ for vibrations and $\beta = -1$ for rotations [**47**]. Neutrons and protons primarily derive their masses from the strong interaction such that $m_n \approx m_p \approx 3\Lambda_{QCD}$, while electrons derive their mass from the weak scale via the Higgs field vacuum expectation value [**47, 46**]. Consequently, rotational and vibrational transitions

of molecules can act as a probe into the variation of $\mu \equiv m_p/m_e$ and therefore the ratio of the strong to weak energy scales. In many models, for example models assuming Grand Unification, μ varies by a factor of 30–40 more rapidly than the fine structure constant α. Based on these arguments, there is strong motivation for experimental searches for varying μ [**23, 48, 69**][1].

Atomic hyperfine transitions also have dependence on μ, but their sensitivity suffers compared with molecules because of the smaller energy interval [**69**]. However, despite orders of magnitude smaller absolute sensitivities to varying μ, the simpler atomic state preparation requirements have allowed atoms to set the current best laboratory constraints. Comparison of two different hyperfine transitions and an optical atomic clock has yielded a limit of $\sim 1 \times 10^{-16}$/year [**65, 52**]. The best experimental limit from a molecule, set by comparing a rovibrational transition in SF_6 to a Cs hyperfine transition, is 6×10^{-14}/year [**143**].

In TeH^+, a vibrational overtone transition has been identified as a potentially promising candidate for μ variation detection [**79**]. The systematic uncertainties for reasonable experimental conditions are projected at the 1×10^{-18} level or below. Furthermore, TeH^+ is one of a small, but growing class of molecular ions identified as having so-called diagonal Franck-Condon factors (FCFs), offering the possibility of rapid state preparation through broadband rotational cooling [**108, 109, 151, 74, 177, 176**].

We envision the μ variation experiment being performed on a single molecular ion, using quantum logic spectroscopy (QLS) [**132**]. Preparation of the initial spectroscopy state could be accomplished either by optical pumping [**148, 136, 91**] or projectively [**28**].

[1] See also section 1.2.

The speed at which one can initially prepare and reset the spectroscopy state has critical implications for the statistical uncertainty that can be obtained in a measurement. Here, we evaluate realistic optical pumping state preparation timescales for TeH^+ and draw conclusions about statistical uncertainties in the search for varying μ. We also discuss more generally the molecular ion qualities desirable for obtaining low statistical uncertainty and identify some molecular ion species, which can serve as benchmarks for μ variation searches.

3.1. Molecular Structure of TeH^+

The four lowest lying electronic states (Fig. 3.1) of TeH^+ ($X_1 0^+$, $X_2 1$, a_2, $b0^+$) are well described by the Hund's case (c) basis. They are all predicted to have bond equilibrium distances within ∼0.1 pm of each other [**53**], implying nearly identical rotational constants and that each of the transitions will have highly diagonal FCFs. Consequently, each electronic transition will have well separated P, Q, and R branches allowing a spectrally-shaped broadband laser to selectively cover transitions that remove rotational quanta [**92**]. Highly diagonal FCFs lead to suppressed vibrational excitation during the rotational cooling (Fig. 3.2).

Since there does not exist experimental data for TeH^+, we attempt to evaluate the accuracy of the TeH^+ multireference configuration interaction with single and double excitations and Davidson correction for higher excitations (MRCISD+Q/aV5Z) calculations [**53**] by comparing theoretical [**1**] and experimental [**144, 16, 173**] investigations of the isoelectronic species antimony hydride (SbH). Compared with the TeH^+ calculation, the MRCISD+Q calculation for SbH uses a smaller basis set (of quadruple zeta quality)

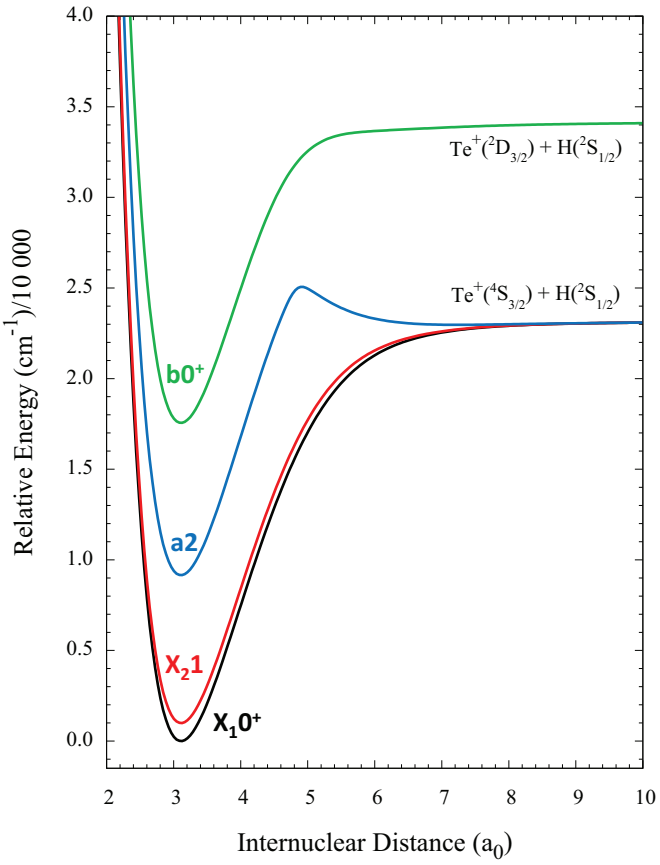

Figure 3.1. Low lying electronic states of TeH^+. Figure generated from [**53**].

and fewer configuration state functions and is expected to be less accurate. FCFs depend most strongly on the difference in equilibrium bond length between electronic states, and the equilibrium bond lengths for SbH were predicted to within 3 pm of the measured values. A comparison between the predictions of the MRCISD+Q/aV5Z level of theory for the CAs molecule [**33**] and experimental measurements [**172**] shows that calculated bond lengths are within 1 pm of experimental values; therefore, the calculations for TeH^+ should be more accurate than the ones for SbH. For optical cooling, we also rely on short lifetimes. The predicted lifetime of the $b0^+$ state of SbH was found to be within a factor

of two. Other properties that have a smaller impact on cooling efficiency such as harmonic frequencies, spin-orbit splittings and electronic energies were also predicted with comparable accuracy.

Typically, multiple low-lying electronic states will complicate cooling. However, in the case of TeH^+, their shared diagonal FCFs open up possibilities for laser control of the internal state population using multiple broadband light sources. Diagonal transitions between the X states have energies accessible by quantum cascade lasers (QCLs), and diagonal transitions between a_2 and X and $b0^+$ and X are predicted to be in the telecom and optical bands, respectively. The lifetimes of the three low lying excited states are calculated using the potential energy curves and dipole moment functions from Gonçalves dos Santos et al. and LEVEL 16 [**88**] and are predicted to be 15 μs for $b0^+$, 2.4 ms for a2 and 460 ms for $X_2 1$. Transition moments between $b0^+$ and a2 and between a2 and $X_1 0^+$ will be insignificant as both are quadrupole transitions.

3.1.1. Magnetic Dipole Moments

The isoelectronic molecule SbH was observed to have significant magnetic dipole transition moments on X $\rightarrow$ b transitions [**144**]. Magnetic dipole transitions will connect states of the same parity, so these transitions are useful for state preparation of a single parity state, which would otherwise require an additional step to the cooling process. The TeH^+ magnetic dipole moments for the $b0^+ - X_2 1$ ($g_s < b0^+|S_x|X_2 1 >$) and $X_2 1 - X_1 0^+$ ($g_s < X_2 1|S_x|X_1 0^+ >$) transitions (Fig. 3.3) were computed using MOLPRO [**163**] and input into LEVEL 16 [**88**] to obtain the Einstein $\mathcal{A}$ coefficients. The magnetic

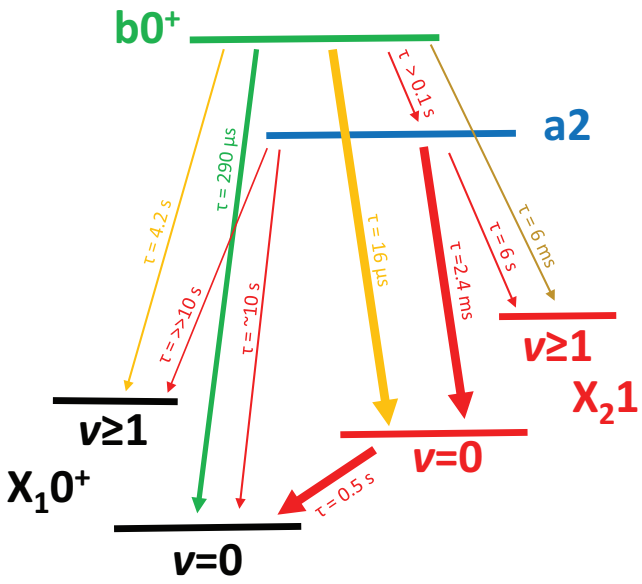

Figure 3.2. Relevant spontaneous emission channels and partial lifetimes of TeH^+. Line thicknesses (not to scale) represents the branching ratios of each excited state.

dipole spontaneous emission rates for the $b0^+ - X_21$ and $X_21 - X_10^+$ transitions are 70-times slower and five-times faster than the corresponding E1 transitions, respectively. We therefore include these M1 transitions in our simulation of the cooling dynamics.

3.2. Internal State Cooling

Generally speaking, broadband sources of light can be spectrally filtered such that frequencies driving transitions increasing vibrational or rotational energy are removed and only frequencies that drive transitions removing vibrational or rotational energy from the molecule are kept. This concept has been used previously in the cooling of rotational degrees of freedom of AlH^+ [**91**] and with cooling the vibrational degrees of freedom of Cs_2 [**161**]. In particular, electronic transitions with diagonal FCFs undergoing spontaneous decay will tend to preserve their vibrational mode. This means that continuous

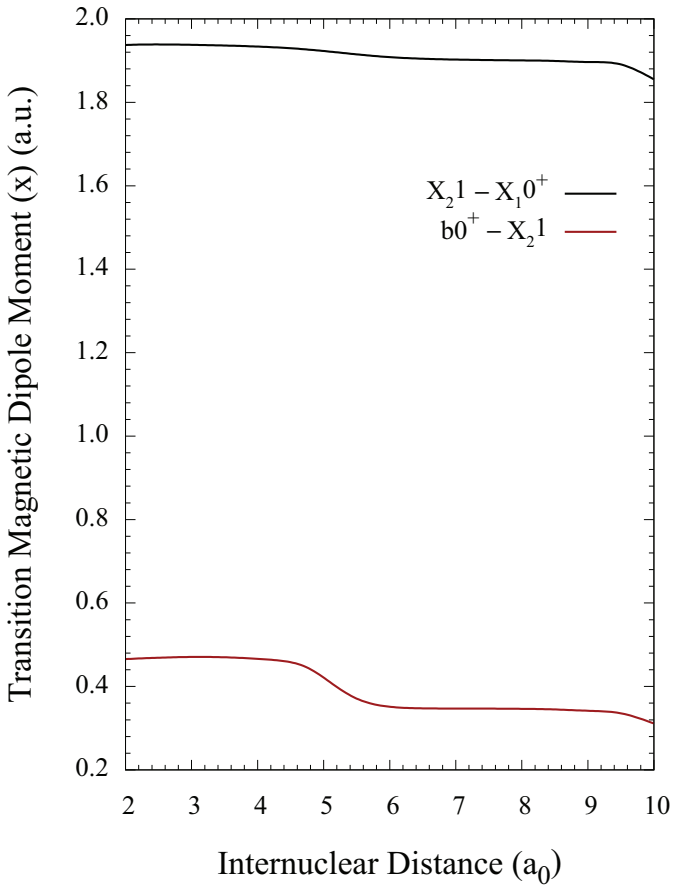

Figure 3.3. Magnetic dipole transition moments of TeH^+.

pumping of rotational or vibrational energy removing transitions will efficiently populate the lowest energy rotational and vibrational states, i.e., efficient internal state cooling. In this chapter, we consider variants of such a scheme on TeH^+. When discussing rotational cooling, we assume a thermal population distribution at room temperature where ∼99% of the population is in $J < 12$ of the ground electronic and vibrational state.

3.2.1. $X_1 0^+ - X_2 1$ Coupling

The lifetime of the $X_2 1$ state is long compared to excited vibrational state lifetimes of $X_1 0^+$, so we do not consider rotational cooling via the $X_1 0^+ \rightarrow X_2 1$ transition. For any cooling scheme, however, $X_2 1$ will be important as it is the strongest decay channel of both $b0^+$ and a2. The addition of this laser significantly reduces the complexity of the four-level system by (1) effectively reducing $v = 0$ of $X_1 0^+$ and $X_2 1$ into a single state and (2) via the relatively strong M1 transition, providing different parity mixing than in E1 transitions (Fig. 3.4).

Because each rotational cooling scheme must involve the population in $X_2 1$, we propose coupling $X_1 0^+$ and $X_2 1$ with a broadband laser on the Q branch. The requirements of the broadband source are simplified by the structure of $X_1 0^+$ and $X_2 1$, which has the first 12 Q branch transitions within one wavenumber of each other. The $X_1 0^+ \rightarrow X_2 1$ transition is 9.6 μm [**53**], which allows for a single QCL to couple rotational states of the two ground vibrational states.

For cooling to proceed at the maximum rate set by upper state spontaneous emission, the $X_2 1 - X_1 0^+$ transition, whose Einstein $\mathcal{A}$ coefficients are <2 s^{-1}, must be driven at well above saturation. For a2 or $b0^+$ as the choice of the upper state, this requires coupling $X_2 1 - X_1 0^+$ at $\sim$3 and five orders of magnitude above saturation, respectively. Given that saturation occurs with a spectral intensity of $\sim$130 μW/(mm^2 cm^{-1}), a 1-cm^{-1} broad QCL with 50 mW of power focused onto the molecule is easily capable of meeting these requirements.

3.2.2. Rotational Cooling on $X - b0^+$ at 600 nm

The most rapid cooling scheme will involve the optical transitions between X and $b0^+$ as $b0^+$ has the shortest lifetime of the diagonal electronic states. We propose cooling by pumping from $X_2 1$ because the transition dipole moment of $X_1 0^+$ and $b0^+$ is expected to be an order of magnitude weaker than $X_2 1$ and $b0^+$.

The P branch of $X_2 1 \rightarrow b0^+$ has been predicted to span 612 nm–618 nm for $J < 12$, and the spectral intensity at saturation is estimated to be $\sim$500 mW mm^{-2}/cm^{-1} (10 W mm^{-2}/nm). Rapid progress on broadband commercial lasers in this spectral region suggests that a light source capable of saturating all the required transitions might soon be available. We note that inclusion of $P(1)$ in the coverage of the P branch with a broadband source will lead to sub-optimal cooling as decay from $|b0^+, J = 0>$ can only increase rotational energy. Exclusion of $P(1)$, however, will limit cooling by leaving $J = 1$ dark to the cooling laser. As seen in Fig. 3.4, this can be avoided with the addition of a CW laser tuned to $|X_2 1, J = 1, +> \rightarrow |b0^+, J = 1, ->$ where $J = 0$ will become the only dark state. Note that the two $|X, J = 1, ->$ states are not dark because the pump also drives M1 transitions.

3.2.2.1. Vibrational Repumping. Though branching from $|b0^+, v = 0>$ into $|X_2 1, v = 1>$ is slow, an additional CW laser and careful choice of the rotational cooling laser spectral cutoff can improve cooling time and fidelity. Because the vibrational constants of $X_2 1$ and $b0^+$ are similar, the rotational cooling laser on $|X_2 1, v = 0> \rightarrow |b0^+, v = 0>$ will also rotationally cool on $|X_2 1, v = 1> \rightarrow |b0^+, v = 1>$. The spectrum is such that the spectral cutoff can be placed between $P(1)$ and $P(2)$ for both vibrational states. Since the rotational cooling laser can connect states of the same parity via M1 transitions, any decays

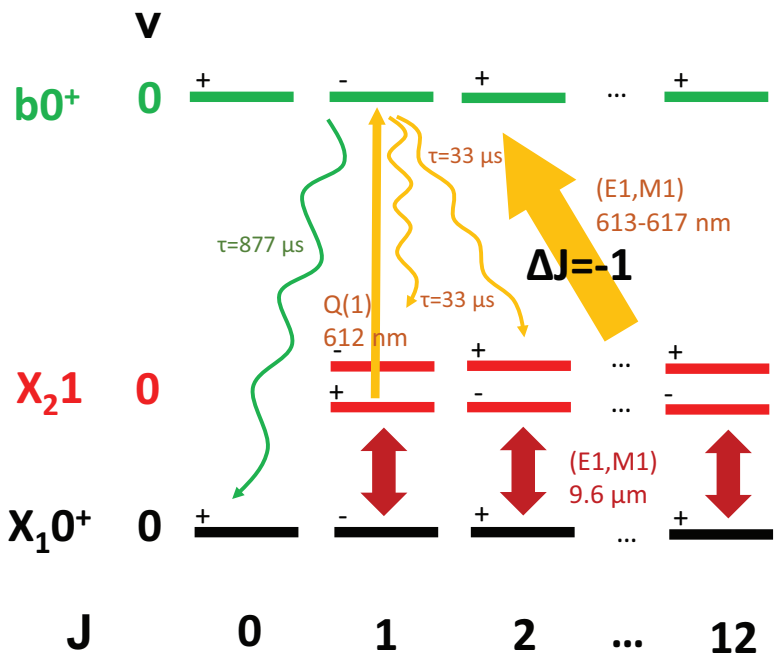

Figure 3.4. Rotational cooling scheme using X $\rightarrow$ b0^+ at 600 nm. Straight arrows show transitions driven by lasers, with arrow width indicating laser linewidth. Both the $X_1 0^+ - X_2 1$ coupling and the $X_2 1 \rightarrow b0^+$ lasers are capable of driving M1 transitions that preserve parity. The wavy arrow indicates the spontaneous emission channel to the dark state.

into $|X_2 1, v = 1>$ will therefore be pumped into $J = 1$ where a CW laser can be used as a vibrational repump into $v = 0$ via the $P(1)$ transition of $|X_2 1, v = 1 > \rightarrow |b0^+, v = 0>$ ($\sim$ 700 nm). Because decays from b0^+ into $X_1 0^+$ are more than an order of magnitude less frequent than into $X_2 1$, an extra laser coupling the $X_1 0^+$ and $X_2 1$ $v = 1$ states is not necessary.

3.2.3. Rotational Cooling on X – a2 at 1300 nm

Rotational cooling with IR frequencies can be done by optical pumping through a2. The relevant $X_2 1 \rightarrow$ a2 P branch transitions at room temperature are predicted to span $\sim$100

cm^{-1} from 1340 nm–1360 nm [**53**], within the telecom O-band. The spectral intensity for saturation of these transitions is <25 mW mm^{-2}/cm^{-1}, meaning a 5 W broadband laser with a 1 mm^2 collimated beam area is sufficient for saturation.

Cooling via this transition will be limited by the 4–7 ms branching decay times of $|a_2, J> \rightarrow |X_2 1, J-1>$. A rough estimate performed by taking the number of occupied rotational states at room temperature and multiplying by the average branching time places the cooling time scale at ∼50 ms. Though cooling on this transition will be slow compared to cooling via the shorter lived $b0^+$ state, depending on the application, it may be advantageous given the availability of telecom technology.

A cartoon of the transitions involved in the X − a2 cooling scheme(s) can be seen in Fig. 3.5. In a more careful analysis of the cooling time scale, we note that the $X_2 1 \rightarrow$ a2 transition has no P branch transitions for $J < 3$. In a cooling scheme relying on a QCL coupling the X states via the Q branch and a broadband laser covering the P branch of $X_2 1 \rightarrow$ a2, the lack of P branch transitions for $J < 3$ implies rotations will cease being cooled once the population has been pumped into $J = 0, 1, 2$. If the broadband laser includes the Q branch of $X_2 1 \rightarrow$ a2, then at the cost of a reduced cooling rate, the broadband laser will pump $J = 2$ such that the population will transfer into $J = 0, 1$. Over much longer time scales (seconds) determined by the $|X_2 1, J = 1> \rightarrow |X_1 0^+, J = 0>$ branching time, the X coupling laser will pump the remaining population into $|X_1 0^+, J = 0>$. The fidelity of this final step will be limited by the much slower rate of blackbody redistribution.

3.2.3.1. CW Assist. With assistance from the $b0^+$ state, it is possible to avoid the rate-limiting steps that were not included in our rough estimate of the cooling time scale.

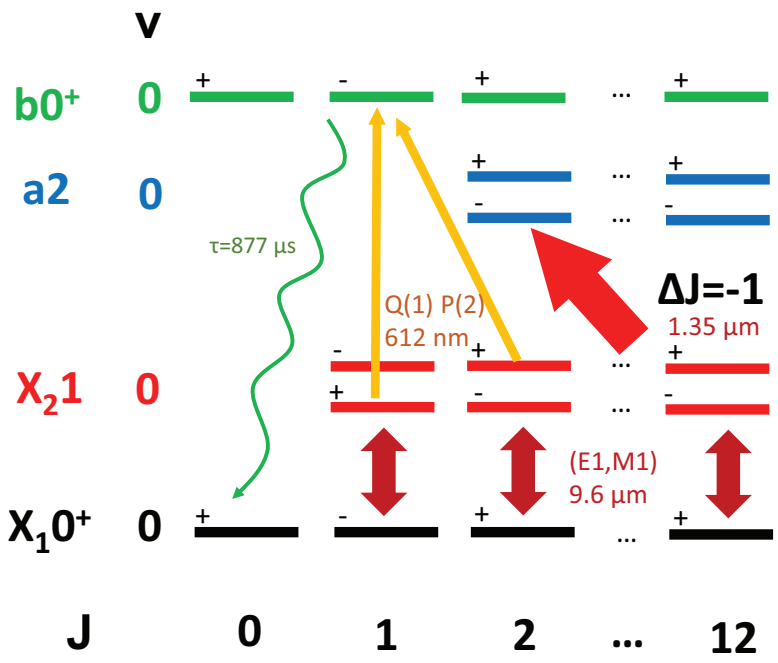

Figure 3.5. Rotational cooling scheme using X → a2 at 1300 nm. Straight arrows show transitions driven by lasers, with arrow width indicating laser linewidth. Yellow arrows indicate CW-assist lasers. The wavy arrow indicates the spontaneous emission channel to the dark state.

In the scheme relying on pumping the P and Q branch of $X_2 1 \rightarrow$ a2, an additional CW laser tuned to $|X_2 1, J = 1, + > \rightarrow |b0^+, J = 1, - >$ will more rapidly pump the population into J=0 than what is allowed for by the $|X_2 1, J = 1 > \rightarrow |X_1 0^+, J = 0 >$ branching time. Similarly, a CW laser tuned to $|X_2 1, J = 2, + > \rightarrow |b0^+, J = 1, - >$ can replace the role of the less efficient cooling from the $X_2 1 \rightarrow$ a2 Q branch pumping. With the simultaneous assistance of both CW lasers, the X − a2 cooling scheme (Fig. 3.5) recovers the ∼50 ms time scale.

3.2.4. Vibrational Cooling

Depending on the choice of excited spectroscopy state in a μ variation measurement, vibrational cooling may be beneficial. Specifically, we envision our spectroscopy states to be of the form $|\mathrm{X}_1 0^+, v'' = 0, J'' = 0>$ and $|\mathrm{X}_1 0^+, v', J' = 1>$. As the excited state spontaneously decays, the rotational state population will slowly diffuse as the molecule vibrationally relaxes. For $v' = 1$, decay can only leave the population in the vibrational ground state, and so, vibrational cooling is not necessary to minimize state re-preparation time. For $v' > 1$ we propose active vibrational cooling by driving $\Delta v = -1$ transitions of the form $|\mathrm{X}_2 1, v> \rightarrow |\mathrm{b}0^+, v-1>$ (see Fig. 3.6). Similar to the rotational cooling schemes, $|\mathrm{X}_1 0^+, v> \rightarrow |\mathrm{X}_2 1, v>$ must also be coupled, and this is accomplished via the Q branch. However, because there is no Q branch transition for $J = 0$, we must include $R(0)$ of each vibrational level. As the $\mathrm{X}_1 0^+ \rightarrow X_2 1$ transitions only span $\sim$100 cm^{-1} for $v = 1$ to $v = 7$ and the rotational spacing is large, a spectral mask blocking unwanted frequencies from a tightly-focused broadband QCL should be sufficient.

The vibrational overtone $v = 0 \rightarrow v' = 8$ of TeH^+ has been proposed for a search for varying μ [**79**]. Cooling vibrational levels $v < 8$ requires a bandwidth of $\sim$400 cm^{-1} in the 685–705 nm range. It is in principle possible to cover exclusively all of the vibrational repump transitions with a supercontinuum laser source. Saturating the weakly-coupled off diagonal transitions, however, will require a spectral intensity of >100 W mm^{-2}/ cm^{-1}, which is currently not commercially available. Another option is to use multiple narrower, but still broad laser sources, since each set of relevant P branch transitions span $\sim$20 cm^{-1} per vibrational level.

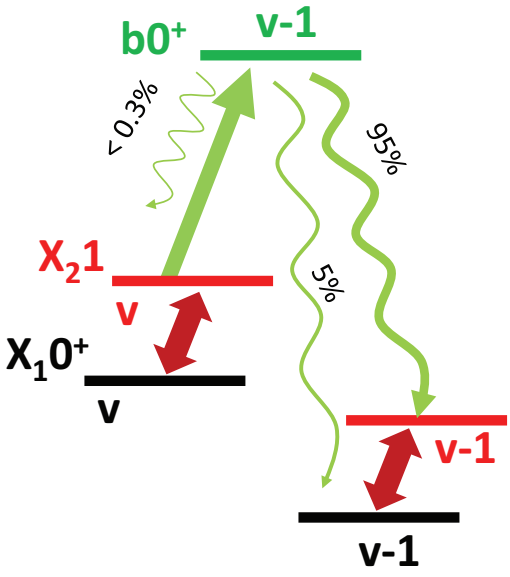

Figure 3.6. Vibrational cooling. Straight arrows indicate transitions covered by lasers, and wavy arrows indicate spontaneous emission channels.

3.3. Rate Equation Simulation

The population distribution as a function of time for different laser cooling schemes was simulated using an Einstein $\mathcal{A}$ and $\mathcal{B}$ coefficient model similar to that used previously [**148, 109, 108**]. The simulation includes up to 864 total states in the set of states including $|\mathrm{X}_1 0^+, v \leq 9, J \leq 15>$, $|\mathrm{X}_2 1, v \leq 7, J \leq 15, \pm>$, $|\mathrm{a}2, v \leq 8, J \leq 15, \pm>$ and $|\mathrm{b}0^+, v \leq 9, J \leq 15>$ to accurately model vibrational cascades and vibrational cooling. The model ignores hyperfine structure, and Zeeman states are treated as degenerate with their multiplicities accounted for in the Einstein coefficients. The full set of spontaneous and stimulated rates is described by an 864×864 matrix that can be represented as the sum of a matrix composed exclusively of $\mathcal{A}$ coefficients and a separate matrix using $\mathcal{B}$ coefficients. The Einstein $\mathcal{A}$ coefficients were calculated using LEVEL 16. The $\mathcal{B}$ coefficients are calculated assuming a background blackbody temperature of 293 K and adding the

contribution of the input spectral intensity of unpolarized laser sources at every transition wavelength. In this way, all possible incoherent coupling between states is included. Each laser source is described assuming a Gaussian line shape with a given spectral width that is modified by a spectral mask if necessary. In Fig. 3.7, we plot the fractional population of $|\mathrm{X}_1 0^+, v = 0, J = 0>$ as a function of time under various rotational cooling schemes beginning from a 293 K Boltzmann distribution at $t = 0$.

The simplest 600 nm cooling scheme uses three lasers: (1) a 100 mW, 1 cm^{-1} broad QCL coupling $\mathrm{X}_1 0^+$ and $\mathrm{X}_2 1$, (2) a 50 mW, 100 cm^{-1} broad laser source with 3 cm^{-1} spectral cutoff before the $|\mathrm{X}_2 1, v = 0 > \rightarrow |\mathrm{b}0^+, v = 0 > P(1)$ transition and (3) a 3 mW CW laser saturating the $|\mathrm{X}_2 1, v = 0, J = 1, + > \rightarrow |\mathrm{b}0^+, v = 0, J = 1, - >$ transition. The results of this combination are given by the solid blue line in Fig. 3.7. As seen in the figure, cooling in this scheme involves two primary time scales. The first time scale is the rapid cooling of rotations for the population that remains in the vibrational ground state during cooling. This results in $\sim$85% of the population in the ground state after 25 ms. The remaining population is primarily the consequence of off-diagonal decay into $v = 1$ and will slowly relax on the time scale of the $v = 1$ lifetime (205 ms) such that >99% is in the ground state after 1 s. The dashed blue line in Fig. 3.7 is the result of our cooling simulation when we add a vibrational repump on $|\mathrm{X}_2 1, v = 1, J = 1, - > \rightarrow |\mathrm{b}0^+, v = 0, J = 0, + >$. As the rotational cooling laser is still effective in the excited vibrational state, driving this lone transition is able to efficiently repump $|\mathrm{b}0^+, v = 0>$ such that the slower time scale is no longer present.

In the 1300 nm cooling schemes, we observe a significant reduction in the cooling rate compared to the 600 nm schemes. The simplest and slowest 1300 nm scheme (solid

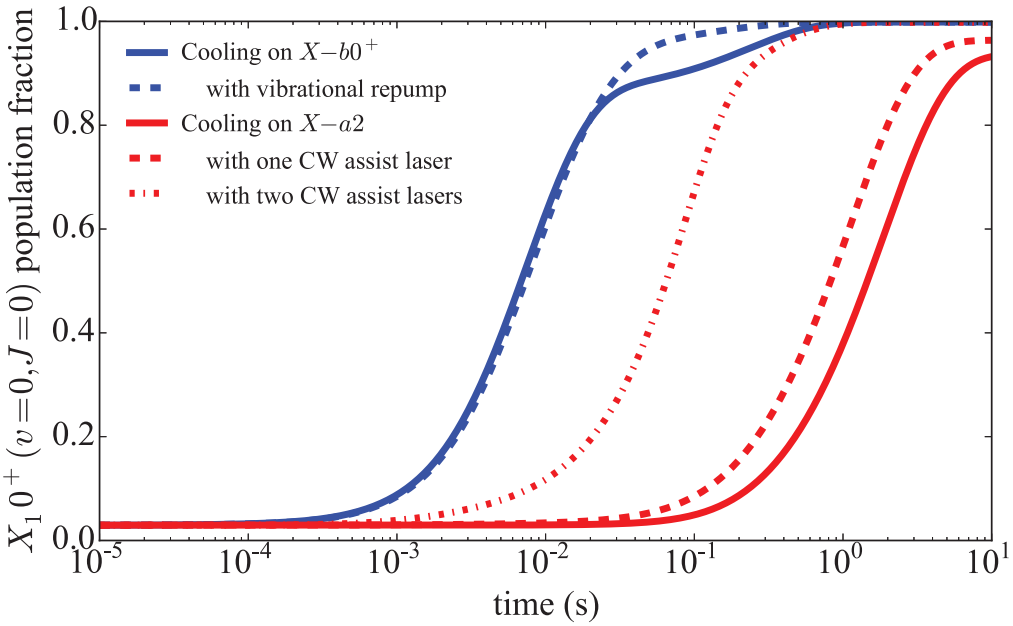

Figure 3.7. Simulation results for the $|\mathrm{X}_1 0^+, v = 0, J = 0>$ population versus cooling time, beginning from a 293 K thermal distribution.

red line Fig. 3.7) uses only two lasers: (1) the same QCL used in the optical scheme and (2) a 5 W (unfocused), 50 cm^{-1} broad O-band telecom laser covering the $\mathrm{X}_2 1 \rightarrow a2$ P and Q branch with a 3 cm^{-1} spectral cutoff before the R branch. As expected, the ground state preparation time is dominated by the slow $|\mathrm{X}_2 1, J = 1>$ branching time into $|\mathrm{X}_1 0^+, J = 0>$. For the two red dashed lines in Fig. 3.7, we add the CW lasers connecting $\mathrm{X}_2 1$ to $\mathrm{b}0^+$ to the IR cooling scheme as described previously. The longer dashed line shows the results with a laser tuned to $|\mathrm{X}_2 1, J = 1, +>\rightarrow |\mathrm{b}0^+, J = 1, ->$. The shorter dashed line shows how we recover cooling rates in line with our naive estimate by adding a laser on $|\mathrm{X}_2 1, J = 2, +>\rightarrow |\mathrm{b}0^+, J = 1, ->$ and removing the inefficient contribution of the $\mathrm{X}_2 1 \rightarrow \mathrm{a}2$ Q branch.

3.4. State Preparation during Spectroscopy Cycle

In a μ variation experiment where we perform repeated measurements on the same molecule, the population distribution will be non-thermal after the spectroscopy transition is driven. We model the scenario where the spectroscopy transition is $|\mathrm{X}_1 0^+, v = 0, J = 0 > \rightarrow |\mathrm{X}_1 0^+, v', J' = 1 >$, and the spectroscopy probe time is similar to the upper state lifetime τ. To optimize the cooling protocol for each choice of v', we conservatively consider that spontaneous emission from the upper state occurred at $t = 0$, and the population subsequently evolved for a time τ. After this simulated evolution, we vibrationally cool and then rotationally cool before the next spectroscopy cycle. It is important to separate the two cooling stages, since simultaneous application of vibrational and rotational cooling lasers will couple separate lower states to the same excited state. This coupling would have the unintended consequence of temporarily pumping the population into higher rovibrational states (we note that the narrowband vibrational repumping scheme for clearing the population from $v = 1$ avoids this issue by exclusively pumping to $|\mathrm{b}0^+, v = 0, J = 0 >$, a state to which the rotational cooling lasers do not couple because of where we place the spectral cutoff).

The cooling time for the vibrational cooling stage is determined by minimizing the following expression:

$$\frac{\tau + T_{\mathrm{VC}}}{\rho_{v=0}(T_{\mathrm{VC}})}, \tag{3.1}$$

where τ is the interrogation time (assumed to be equal to the excited state lifetime), T_{VC} is the amount of time the vibrational cooling lasers are on, and $\rho_{v=0}(t)$ is the fraction of

the population in $v = 0$ at time t. Vibrational cooling was simulated assuming broadband coverage approximately at the saturation intensity of the relevant $|\mathrm{X}_2 1, v > \rightarrow |\mathrm{b}0^+, v - 1 >$ transitions. The cooling times for the first eight excited vibrational states can be seen in Table 3.1. In every case, the vibrational cooling lasers pumped >99% of the population into the ground vibrational state. It is noteworthy that vibrational cooling will not contribute significantly to the overall duty cycle as $T_{\mathrm{VC}} << \tau$ for any choice of vibrational state.

Assuming the rotational cooling stage is applied for time T_{RC}, the average time for a successful experimental cycle is estimated to be:

$$T_{\mathrm{c}} = 2\frac{T_p + \tau + T_{\mathrm{VC}} + T_{\mathrm{RC}}}{\rho_{J=0}(T_{\mathrm{RC}})}, \tag{3.2}$$

where T_p is the total time necessary for state readout and hyperfine state preparation, the term $\rho_{J=0}(t)$ is the fraction of the population in $|\mathrm{X}_1 0^+, v = 0, J = 0 >$ at time t after the start of the rotational cooling stage and the factor of two arises from needing to measure two points to estimate the offset from the line center. The optimal rotational cooling time will thus be the time that minimizes T_c.

3.5. μ Variation Measurement

In a Ramsey measurement on a single ion, the Allan deviation is given by:

$$\sigma_y(T) = \frac{1}{C\Omega\, T_{\mathrm{R}}}\sqrt{\frac{T_{\mathrm{c}}}{2T}}, \tag{3.3}$$

where C is the fringe visibility, T_{R} is the Ramsey time, T_{c} is the cycle time and T is the total measurement time [**125, 60**]. Optimal cycling occurs for $T_{\mathrm{c}} = 2T_{\mathrm{R}}$ and T_{R} set to

Table 3.1. Properties of vibrational transitions $v = 0 \rightarrow v' = n$. T_{VC} is the simulated optimal cooling time for vibrational cooling. $\Omega/(2\pi)$ and $S/(2\pi)$ are in units of THz.

n	τ (ms)	$\Omega/(2\pi)$	$S/(2\pi)$	T_{VC} (ms)
1	210	62	30	0
2	110	120	58	1.0
3	85	180	83	1.2
4	70	230	110	1.4
5	61	290	130	1.6
6	53	340	140	1.7
7	47	380	160	1.9
8	41	430	170	2.0

about the upper state lifetime τ, for which $C \approx 0.6$ [**125**]. Laser cooling of the internal molecular state opens up the possibility for efficient state preparation, which can allow for repeated interrogation of the same molecular sample and low dead time. To evaluate the benefit of laser cooling in TeH^+, we estimate the statistical sensitivity to $\Delta\mu$ when using various laser cooling schemes and different vibrational overtone transitions.

The vibrational interval from $v = 0$ to $v' = n$ at frequency Ω will vary in response to changing μ as described by:

$$\Delta\Omega = S\frac{\Delta\mu}{\mu}. \tag{3.4}$$

Before statistics are considered, the absolute sensitivity coefficient $S = \partial\Omega/\partial(\ln\mu)$ provides the most important figure of merit for the transition, since it expresses the shift in the measured frequency [**35, 174**]. It is also convenient to define a relative sensitivity coefficient K_μ [**69**] given by:

$$\frac{\Delta\Omega}{\Omega} = K_\mu\frac{\Delta\mu}{\mu}. \tag{3.5}$$

We must also account for detrimental statistical effects of the finite upper state lifetime. Fluctuations in the frequency measurements are described by an Allan deviation $\sigma_y(T)$ for some overall measurement time T. The vibrational frequency measurements yield values for μ itself (albeit with a large theoretical uncertainty), and the square root of the two-sample variance in μ is:

$$\sigma_y^{(\mu)}(T) = \frac{\sigma_y(T)}{|K_\mu|}. \tag{3.6}$$

Statistical uncertainty in μ variation can be related to $\sigma_y^{(\mu)}(T)$, with numerical factors depending on the details of the experimental protocol. Further details of statistical considerations for μ variation measurements using polar molecule overtone transitions are discussed in [**79**].

3.5.1. Single-Ion TeH^+ Measurement

In our simulated results for statistical sensitivity of a $\Delta\mu$ measurement using a single TeH^+ ion, the spectroscopy interval is probed using Ramsey's method, and we take $T_R = \tau$ and $C = 0.6$ [**125**]. Results for various state preparation schemes are shown in Fig. 3.8. The results suggest that spectroscopy on a single TeH^+ ion can be used for a significantly improved search for varying μ.

We find that the attainable precision is most sensitive for the larger overtone transitions. The ultimate decision for which vibrational interval to choose for spectroscopy will depend on how much vibrational cooling laser power is available. In the extreme case where no vibrational cooling is used, $v' = 1$ is the optimal choice. At the other extreme, with enough vibrational cooling laser power to saturate all the transitions, the

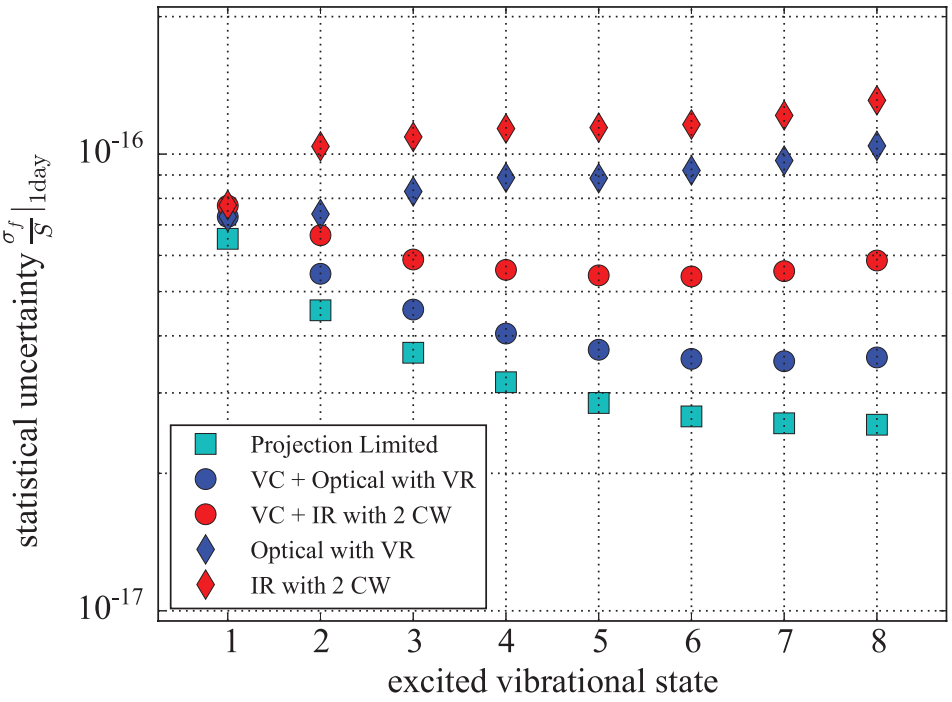

Figure 3.8. Simulation results for statistical uncertainty using various state preparation schemes, a single TeH^+ ion and for one day of averaging. Squares represent the projection noise-limited outcome, corresponding to instantaneous state preparation with 100% fidelity. 'Optical' indicates results for rotational cooling at 600 nm, with vibrational repump (VR) included. 'IR' refers to rotational cooling at 1300 nm, with two CW-assist lasers included. Diamonds indicate results without vibrational cooling, and circles indicate results with each cycle ending with vibrational cooling (VC) followed by rotational cooling.

best simulated statistical sensitivity to $\Delta\mu$ after one day of averaging is described by $\sigma_y^{(\mu)} = 3.6 \times 10^{-17}$. For this transition, the 600 nm cooling scheme significantly outperforms the 1300 nm cooling scheme.

3.5.2. Multi-Ion Spectroscopy

Besides searching for μ variation with a single-ion QLS measurement, an alternative approach using laser coolable polar molecules is to perform multi-ion spectroscopy. In principle, QLS can be extended to N molecular ions with only $log(N)$ overhead in readout time and logic ions [**139**]. A simpler fluorescence readout scheme is normally not possible for molecular ions, since they usually lack cycling transitions. However, for molecules that can be rapidly laser cooled, there exist quasi-cycling transitions capable of scattering enough light for fluorescence detection. Additionally, negative differential (static) polarizabilities are ubiquitous in polar molecules for transitions starting from the ground rotational state [**79**]. A negative differential polarizability allows for choosing of a magic RF trap-drive frequency such that the Stark shift and micro-motion second order Doppler shifts cancel one another [**3, 79**].

In TeH^+, there do exist quasi-cycling transitions amenable to state detection via fluorescence. For example, the population in $|X_1 0+, J = 0>$ can be left dark, while $|X_1 0+, J = 1>$ can be driven in a quasi-cycling scheme by using one laser driving E1 and M1 coupling between $|X_1 0+, J = 1, ->\leftrightarrow |X_2 1, J = 1, \pm>$ and a second laser to couple $|X_2 1, J = 1, +>\leftrightarrow |b0^+, J = 0, +>$. The simulated results, using the same QCL discussed previously for the first laser and a CW laser at saturation for the second are plotted in Fig. 3.9. On average, there will be approximately 400 spontaneously emitted photons at a rate of $\sim$5 photons per ms before an off-diagonal $\Delta v > 0$ decay occurs. In a large ensemble, the result would be a rapid decrease in the scattering rate after $\sim$80 ms.

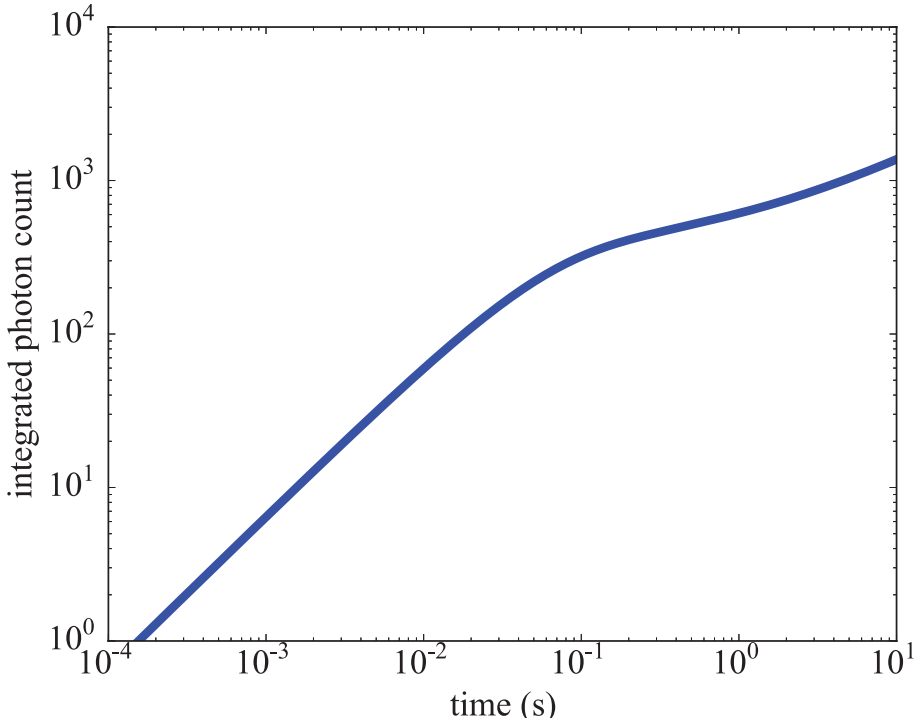

Figure 3.9. The total number of photon scatters from $|b0^+, v = 0, J = 0>$ as a function of time, in the two-laser fluorescence state detection scheme described in the text.

3.5.3. Homonuclear Molecule Benchmarks

It is interesting to note that the logic of choosing the optimal overtone transition in TeH^+ also sets a bound on the statistical sensitivity attainable for any molecule. The strongest known chemical bond is that of CO, with $D = 90{,}000$ cm^{-1} [**98**]. Molecular ion dissociation energies can approach this range; N_2^+ and O_2^+ have $D = 54{,}000$ cm^{-1} and $D = 74{,}000$ cm^{-1}, respectively. For a Morse potential, the upper bound on the sensitivity S is given by $D/4$, where D is the dissociation energy [**35**]. Although calculations are not generally available to describe broadening of overtone linewidths from coupling to other electronic states, the measured linewidths are expected to be limited by laser coherence.

Statistical sensitivity of these species, using probe times set by currently available laser coherence, is shown in Table 3.2. Stark shifts for nonpolar species are favorably small, and other systematic uncertainties can be low, as well [**71, 73, 72**].

Homonuclear molecules can be loaded into the trap in the desired quantum state [**155, 95**], and one can imagine an experimental cycle approaching zero dead time using a quantum logic protocol. Simple projective measurements within the two-level manifold can be used to reset to the lower spectroscopy state at the beginning of each cycle [**28**]. Trapped N_2^+ prepared in its ground rotational state lifetime has been demonstrated to have lifetimes as long as 15 minutes, limited by the collisions with background gas [**154**]. After a collision changes the rotational state, a new molecule could be loaded. Alternatively, one could use a quantum logic state preparation approach that sequentially transfers the population from all possible populated states [**36, 89**]. In the latter approach, the problem of recovery of the pre-collision parity must also be addressed, possibly by two-photon excitation of a short-lifetime electronic transition and then cleanup of resulting vibrational excitation. Since either state recovery approach might be time consuming, it could be preferable to operate at cryogenic temperatures to reduce the rate of collision with background gases.

Comparing the ideal zero dead time performance of TeH^+ and the homonuclear benchmarks in Table 3.2, we find that the best TeH^+ statistical uncertainty is nearly two orders of magnitude larger. However, since simpler optical pumping state preparation is available for TeH^+, its experimental statistical uncertainty should be less sensitive to the vacuum environment. Furthermore, the quasi-cycling transitions of TeH^+ or other polar species offers the possibility of fluorescence readout in multi-ion spectroscopy.

Table 3.2. Benchmark candidates for μ variation measurement. The upper vibrational states n that maximize the absolute sensitivities are calculated from molecular constants [**86**] and achievable precision for zero dead time, $C = 0.6$, an averaging time $T = 1$ day, and a coherence time of 6 s [**17**]. $\Omega/(2\pi)$ and $S/(2\pi)$ are in units of THz.

	n	$\Omega/(2\pi)$	$S/(2\pi)$	$\sigma_y^{(\mu)}(1\text{ day})/10^{-19}$
N_2^+	33	1700	540	6.7
O_2^+	28	1200	390	9.1

3.6. Conclusions

We have identified vibrational overtone transitions in TeH^+ as candidates for a spectroscopic search for varying μ, taking advantage of the optical pumping protocols for state preparation. Rate equation simulations show that TeH^+ can be optically pumped from room temperature to the rotational ground state in ∼100 ms using telecom wavelengths or ∼10 ms using optical wavelengths. In an overtone spectroscopy experiment, we find that realistically achievable experimental cycle times yield a statistical uncertainty as low as 4×10^{-17} for a day of averaging. This demonstrates the possibility for significant improvement on the best laboratory limit of $\sim 1 \times 10^{-16}$/year [**52, 65**] and the current limit set by a molecule at 6×10^{-14}/year [**143**].

We primarily limited our investigation to the performance of single ion spectroscopy using quantum logic, but simulations also support the potential for fluorescence state readout of TeH^+. Large Coulomb crystals of polar molecules, with state detection performed by fluorescence, could have favorably small systematic uncertainties because negative differential polarizabilities can allow for cancellation of Stark and second order Doppler shifts [**3**]. Our analysis suggests that the possibility of searching for μ variation using multi-ion spectroscopy on laser-coolable polar species warrants further investigation.

CHAPTER 4

Branching Ratios Measurement

The work presented in this chapter was motivated by a need to have accurate knowledge of branching ratios and lifetimes of the low-lying electronic states of SiO^+. The fidelity of the molecular control schemes described in chapter 2 and the lasers involved are dependent on the time scales and pathways of relaxation. Similarly, the details and expectations of an optical cycling scheme for SiO^+ such as the one proposed for TeH^+ in section 3.5.2 or the Doppler cooling of SiO^+ proposed in [**108**] depend critically on this information.

After cooling rotational degrees of freedom there needs to be a method of state detection to confirm cooling. The detection schemes we considered were through dissociation [**141, 110**] or through direct fluorescence detection from optical cycling. In his thesis, Dr. David Tabor performed cross section calculations for dissociation [**152**]. The cross section is heavily dependent on wavelength. For large ranges of wavelengths the cross section is estimated to be smaller than can be tolerated in the low statistics experiments of molecular ions. At the time of our first attempts at demonstrating cooling we only had high energy pulsed lasers available at the wavelengths of the Nd:YAG harmonics so scanning for favorable dissociation cross sections was not an option. After initial failed attempts at detection through dissociation, we instead attempted direct fluorescence

detection using rotational cooling and CW excitation on a quasi-cycling transition[1]. Fluorescence detection also failed. Our ability to diagnose the reason for these failed attempts was limited by our knowledge of branching ratios and lifetimes of excited states. We could not be certain if our failure to detect was a consequence of unfavorable relaxation under the prescribed cooling scheme, improper spectral cutoff used in pulse shaping, small dissociation cross section, incorrect wavelength for fluorescent pumping, or unwanted chemical reactions with the trapped SiO^+. More accurate knowledge of branching ratios enables us to narrow and more confidently search through parameter space for detectable signals. Such advantages can be crucial for molecular ion experiments which are typically plagued by low densities and therefore low statistics. Without direct experimental measurement, uncertainties and inaccuracies in theory can have a dramatic impact on the time spent looking for appropriate parameters.

The first part of this chapter involves my work performed with Dr. Damian Kokkin in the lab of Professor Timothy Steimle at Arizona State University (ASU). Sections of text are found in reference [**151**] and are used to describe our results on a preliminary measurement of the radiative branching ratios of SiO^+. The remaining portions of the chapter discuss the limitations of the detection apparatus at ASU for the task of characterizing the lifetimes and dipole moments of molecular ions and my work at Northwestern constructing a new apparatus consisting of a large ion trap optimized to address the limitations of the setup at Arizona State.

[1]The $X \rightarrow B$ $P(1)$ transition effectively forms a two level system until off diagonal decay removes population from the optical cycling.

4.1. SiO^+ Molecular Beam at Arizona State

The experimental setup is nearly that used in the previous experimental detection and characterization performed by my ASU collaborators of the SiHD radical [**80**] and that used for branching ratio determination of ThO [**81**]. Three types of measurements were performed: two-dimensional (2D) spectroscopy, dispersed fluorescence (DLIF) spectroscopy, and radiative decay. In the present study, a cold sample of SiO^+ was produced via a pulsed DC-discharge (40 μs, 1 kV, 1 kΩ) struck through a supersonic expansion reaction mixture of silane (SiH_4) (0.8 %), nitrous oxide (N_2O) (0.05 %) in argon (600 psi). The resulting free-jet expansion containing SiO^+ was subsequently probed 10 cm downstream with the output of an excimer pumped dye laser over the range of 26000-26050 cm^{-1} covering the $B^2\Sigma^+ - X^2\Sigma^+(0,0)$ band system. A commercial wavemeter was used to determine the absolute wavenumber of the pulsed dye laser. Laser induced fluorescence (LIF) was imaged via adaptive optics onto the entrance slit of a 0.67 m fast (f=6.2) monochromator equipped with a 300 lines/mm grating. The monochromator was fitted with a gated, intensified CCD (ICCD) camera cooled to -30°C to reduce dark current.

In order to identify and isolate the SiO^+ LIF signal from the multitude of other molecules generated in the d.c.-discharge source a two-dimensional (2D) spectroscopic technique [**123, 49**] was employed similar to that used previously to study SiHD [**80**] and ThO [**81**]. Briefly, the 2D spectra are created by stepping the probe laser wavelength and capturing a 75 nm wide spectral region of the dispersed laser induced fluorescence (DLIF) for each laser wavelength step. The entrance slit widths were set to 1 mm resulting in an approximately ±2 nm spectral resolution for the DLIF signal. In this way the laser

excitation spectrum of SiO^+ could be identified due to its characteristic, well resolved, DLIF signal.

Following the initial 2D survey scans, higher resolution, more sensitive, DLIF measurements following $B^2\Sigma^+ - X^2\Sigma^+(0,0)$ excitation were taken by tuning the laser wavelength to be on resonance with a branch feature and accumulating a large number (15000) of ICCD exposures for a contiguous set of 75 nm spectral windows across the 380-470 nm range. In this case the entrance slit of the monochromator was narrowed to 0.3 mm resulting in a spectral resolution of ± 0.3 nm. Wavelength calibration of the resulting DLIF spectrum was achieved by measuring the emission from an argon pen lamp. The conjoined spectra were flux calibrated for the detection system. Similarly, a background spectrum was recorded by tuning the probe laser off resonance. Both photon counting and the more traditional current mode processing of the ICCD signal were employed. For photon counting, a photon signal threshold was set such that background dark counts were minimal while still accumulating sufficient signal counts. As the fluorescence signal rate averaged much less than one detected photon per probe pulse, the photon counting mode was found to improve the signal-to-noise ratio (SNR) over conventional operation of the ICCD. The comparatively low signal rate is expected as coulomb repulsion will result in densities of SiO^+ that is several orders of magnitude lower than what can be found in typical neutral beam densities. The $B^2\Sigma^+(v=0)$ excited state lifetime measurements were performed by sitting the pulsed dye laser on an $R(3)$ line of the $B^2\Sigma^+ - X^2\Sigma^+(0,0)$ band monitoring the DLIF spectrum with a relatively wide (1 μs) intensifier detection

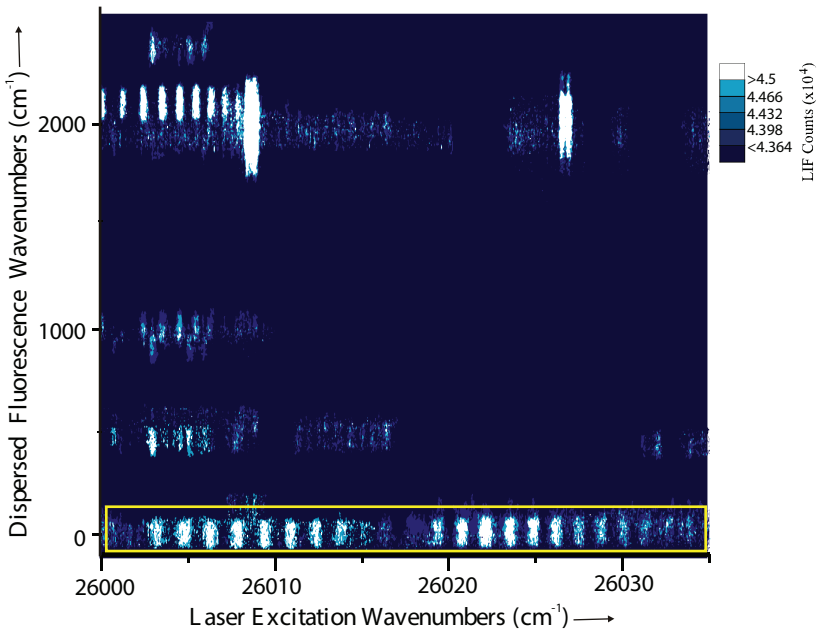

Figure 4.1. The 2D spectrum of the $SiH_4/N_2O/Ar$ discharge covering 26000 cm^{-1} to 26035 cm^{-1} region of the $B^2\Sigma^+ - X^2\Sigma^+(0,0)$ transition. The vertical axis is the relative wavenumber of the dispersed fluorescence to the red of the wavenumber of excitation laser at the beginning of the scan. The viewed spectral region of the monochromator is tracked with laser wavelength. The features in the yellow rectangle are the on-resonance fluorescence of the $B^2\Sigma^+ - X^2\Sigma^+(0,0)$ band of SiO^+, the ${}^SR_{21f}(4.5)(\nu = 26008.3$ $cm^{-1})$, ${}^SR_{21e}(4.5)(\nu = 26008.7$ $cm^{-1})$, ${}^SR_{21f}(5.5)(\nu = 26026.5$ $cm^{-1})$ and ${}^SR_{21e}(5.5)(\nu = 26026.9$ $cm^{-1})$ branch features of the $A^2\Delta - X^2\Pi_r(1,0)$ band of SiH and minor contributions from unknown species. The two intense, partially resolved, doublets 2050 cm^{-1} red shifted from the laser are primarily due to the ${}^RR_{1f}(4.5)(\nu = 23963.1$ $cm^{-1})$, ${}^RR_{1e}(4.5)(\nu = 23963.5$ $cm^{-1})$, ${}^RR_{1f}(5.5)(\nu = 23969.5$ $cm^{-1})$, and ${}^RR_{1e}(5.5)(\nu = 23970.3$ $cm^{-1})$ transitions of the $A^2\Delta - X^2\Pi_r(1,1)$ band.

window. The detection window was progressively stepped further in time from the incident pulsed laser in 2 ns increments. The resulting fluorescence decay curve was then fit with a first order exponential to determine the upper state lifetime.

4.1.1. Results and Analysis

Figure 4.1 shows the 2D spectrum of the $SiH_4/N_2O/Ar$ discharge covering the 26000 cm^{-1} to 26035 cm^{-1} region of the $B^2\Sigma^+ - X^2\Sigma^+(0,0)$ transition of SiO^+. The horizontal axis is the laser excitation frequency and the vertical axis is the dispersed fluorescence wavenumber relative to the wavenumber of the laser. The center of the approximately 75nm spectral window monitored by the monochromator was offset approximately 1700 cm^{-1} to the red with respect to the laser energy and tracked with the laser. The 2D spectrum of Figure 4.1 has been cropped to display only the shortest wavelength 40 nm portion of the 75 nm spectral window. A sum of 50 discharge pulses at each laser excitation frequency was accumulated. The regular pattern of features, indicated by the yellow rectangle, appearing on-resonance are primarily the P- and R-branch structure of the $B^2\Sigma^+ - X^2\Sigma^+(0,0)$ band of SiO^+. The observed spectral resolution of approximately 0.4 cm^{-1}, which is dictated by the bandwidth of the laser, is insufficient to resolve the spectral doubling due to spin-rotation splitting in the $B^2\Sigma^+$ and $X^2\Sigma^+$ states. There is no obvious feature in the 2D spectrum associated with the $B^2\Sigma^+(v=0) \rightarrow X^2\Sigma^+(v=1)$ emission, which would appear at 1162 cm^{-1} ($\Delta E_{0,1}$) on the DLIF axis. This off-resonance emission is observed in the DLIF spectra (see Fig.4.3), which were recorded using a significantly larger number of pulses (50 vs. 15000). The two very intense, partially resolved, doublets that appear in the 2D spectrum near the laser excitation wavelengths of 26008 cm^{-1} and 26027 cm^{-1} are due to laser excitation of the ${}^SR_{21f}(4.5)(\nu = 26008.3\ cm^{-1})$, ${}^SR_{21e}(4.5)(\nu = 26008.7\ cm^{-1})$, ${}^SR_{21f}(5.5)(\nu = 26026.5\ cm^{-1})$ and ${}^SR_{21e(5.5)(\nu=26026.9}\ cm^{-1})$ branch features of the $A^2\Delta - X^2\Pi_r(1,0)$ transitions of SiH [**121**]. The intense, off-resonance, DLIF signal in the 2D spectrum at approximately 2050 cm^{-1} red shifted from the laser are primarily the

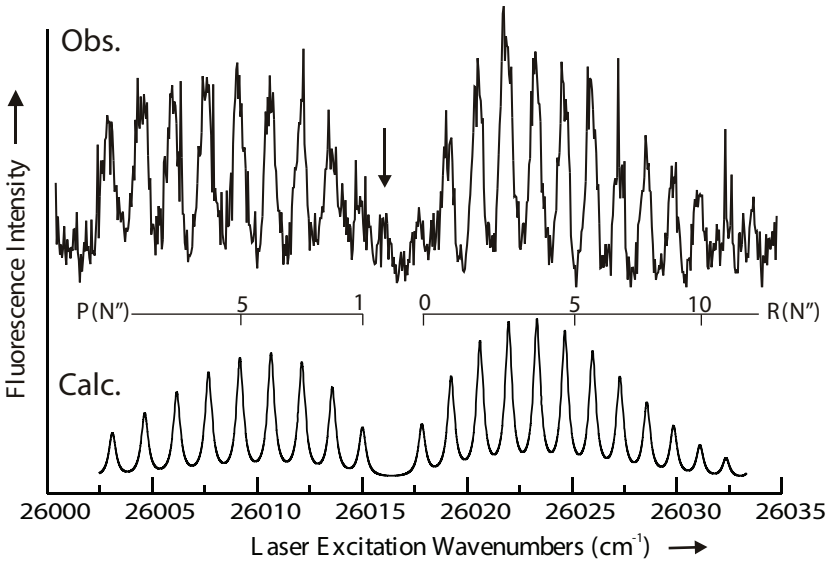

Figure 4.2. Upper trace: The integration of the on-resonance horizontal slice indicated by the yellow rectangle of Figure 4.1. Lower trace: The simulated excitation spectrum of the $B^2\Sigma^+ - X^2\Sigma^+(0,0)$ band of SiO^+ obtained using a rotational temperature of 40 K and a linewidth of 0.4 cm^{-1} FWHM. The line indicated by the arrow is due to an unidentified molecule that emits both on-resonance and 490 cm^{-1} off-resonance (see Figure 4.1). The $P(4)$, and higher branch members, of the $B^2\Sigma^+ - X^2\Sigma^+(0,0)$ band are overlapped with emission from an with an unknown molecule.

emission associated with the intense ${}^RR_{1f}(4.5)(\nu = 23963.1\ cm^{-1})$, ${}^RR_{1e}(4.5)(\nu = 23963.5\ cm^{-1})$, ${}^RR_{1f}(5.5)(\nu = 23969.5\ cm^{-1})$, and ${}^RR_{1e}(5.5)(\nu = 23970.3\ cm^{-1})$ transitions of the $A^2\Delta - X^2\Pi_r(1,1)$ band [**121**]. The carriers of the remaining numerous weak features in the 2D spectrum are unknown.

The one dimensional excitation spectrum obtained by vertical integration of the horizontal slice indicated by the yellow rectangle of Figure4.1 is displayed in Figure4.2 (upper trace). The lower trace in Figure4.2 is the simulated laser excitation spectrum obtained using the previously determined constants for the $B^2\Sigma^+(v=0)$ and $X^2\Sigma^+(v=0)$ states [**126**], an effective rotational temperature of 40 K and a linewidth of 0.4 cm^{-1}

FWHM, which is commensurate with laser bandwidth. The line indicated by the arrow is due to an unidentified molecule that emits both on-resonance and approximately 490 cm^{-1} off-resonance, as evident in the 2D spectrum. The $P(4)$, and higher members of that branch, are partially overlapped and blended with weak emission from an unknown molecule which contributes to the slight disagreement between the observed and predicted relative intensities. With this in mind, it can be concluded that the current production scheme of pulsed d.c.-discharge supersonic expansion is producing a cold ($\approx 40 \pm 5$ K) molecular sample of SiO^+.

DLIF spectra were recorded using both the conventional monitoring mode and a photon counting mode of the ICCD acquisition software. Figure4.3 shows the normalized DLIF spectra recorded using the conventional method for 18 sets of 15000 discharge pulses and the photon counting method for 12 sets of 15000 pulses. In both cases the laser was tuned to be on resonance with the overlapped $R_{11}(3)(\nu = 26022.1691\ cm^{-1})$ [**24**] and $R_{22}(3)(\nu = 26022.1289\ cm^{-1})$ [**24**] branch features, which is the most intense line. Despite the larger acquisition of the spectrum obtained using the convention method, the signal-to-noise (SNR) ratio of the spectrum recorded using the photon counting mode is significantly improved. The large gain of the ICCD allows for the photon count threshold to be well above the dark counts and read noise, removing both sources of noise, without sacrificing signal. Exclusion of dark counts also flattens the baseline as temperature gradients lead to uneven dark count rates across the pixel array. Dark count rates are also subject to drift with changing environmental conditions which can explain the variation of baselines seen in the conventional ICCD acquisition mode plot in Figure4.3(b). DLIF spectra recorded when the laser was tuned off-resonance midway between the $P(1)$ and

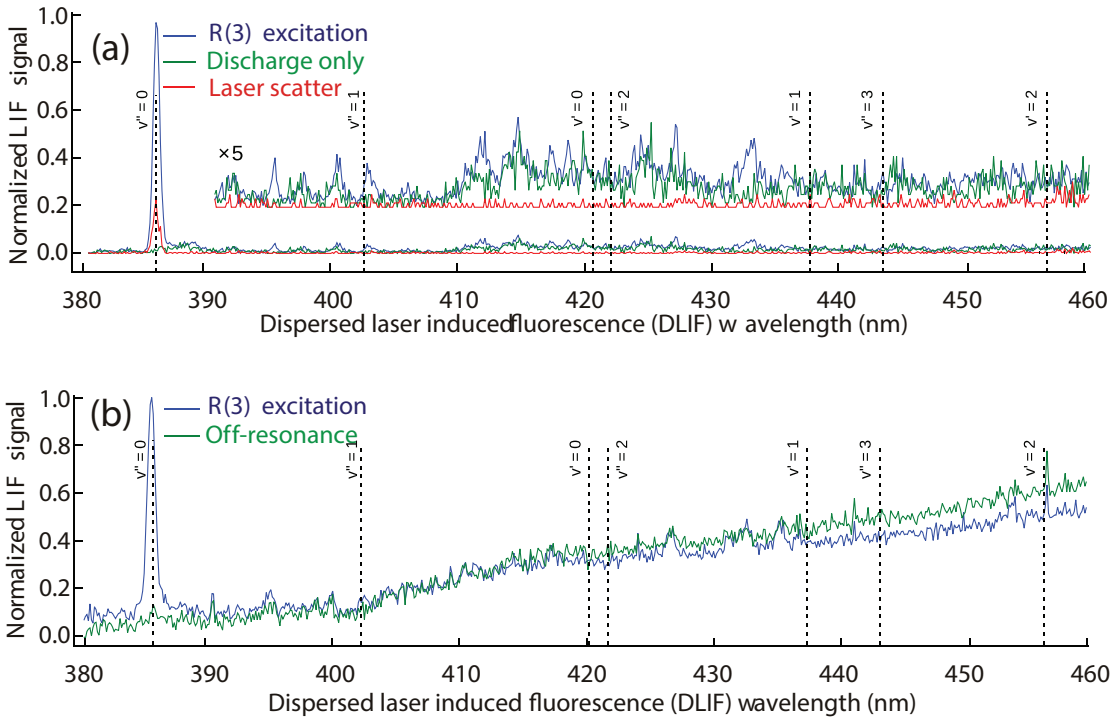

Figure 4.3. Dispersed laser-induced fluorescence (DLIF) spectra measured using (a) photon counting mode and (b) standard acquisition mode of ICCD. DLIF signal is the normalized average of 12 and 18 acquisitions of 15000 laser excitations for (a) and (b) respectively. Expected locations of $B^2\Sigma^+(v = 0) \rightarrow X^2\Sigma^+(v'')$ and $B^2\Sigma^+(v = 0) \rightarrow A^2\Pi(v')$ transitions are marked with dashed lines and show the only observable branching is weak branching to $X^2\Sigma^+(v'' = 1)$. Variation of the baseline seen in the spectra taken with the standard acquisition can be explained by dark count variation from temperature drift in the CCD. The shape of the baseline is primarily a consequence of temperature gradients across the CCD. Intensifier gain allows the photon counting mode to be insensitive to dark count drifts, improving the SNR and eliminating the asymmetric baseline.

$R(0)$ lines and when the excitation laser was blocked were used to measure the background contributions.

The DLIF spectra were used to estimate the branching ratios, $b_{iv',fv''}$, which are reported in Table 4.1. Peaks observed at the expected transition locations were fit to a

Gaussian line shape with a linear offset using the method of least squares. Multiplication of the amplitude and width of the optimized Gaussian line shape was used to assign relative signal strengths and error propagation of the covariance matrix of the fit parameters was used to estimate the statistical uncertainty. Observed background peaks from scattered laser and discharge emission were subtracted away from the signal. After extracting signal sizes, the signals are normalized with respect to the detectors wavelength response before calculating branching ratios. For expected transitions where no peaks were observed (e.g. $B^2\Sigma^+(v=0) \rightarrow A^2\Pi_{1/2}(v=1)(\nu \approx 23780\ \mathrm{cm}^{-1},\ \lambda_{vac} \approx 420$ nm)) the data was fit to a straight line and RMS of the linear fit used as an upper bound on peak heights. Multiplying the peak height limit by the width of observed peaks places a limit on signal size and consequently the branching ratio. In assigning error bars to the branching ratio, the upper-side uncertainty comes from the statistical uncertainty of the fit parameters. The lower-side uncertainty comes from the statistical uncertainty added in quadrature with the one-sigma limit on the unobserved fluorescence from $B^2\Sigma^+ \rightarrow A^2\Pi^+$ spontaneous emission. This uncertainty assumes that branching to higher vibrational levels of the $X^2\Sigma^+$ state are negligible and, as the calculations predict, that the $B^2\Sigma^+(v=0) \rightarrow A^2\Pi^+(v=0,1,2)$ transitions are much more intense than other members of this series. No assumptions about the $B^2\Sigma^+ \rightarrow A^2\Pi$ electronic transition moment are made.

As indicated in Table4.1, and seen in Figure 4.3, excitation of the $B^2\Sigma^+ - X^2\Sigma^+(0,0)$ band resulted in detection of only the strong on-resonance fluorescence and a much weaker $B^2\Sigma^+(v=0) \rightarrow X^2\Sigma^+(v=1)$ emission. Fluorescence branching is observed only to $X^2\Sigma^+$ with all other channels remaining undetected. As the decrease in $b_{iv',fv''}$ from

Table 4.1. The branching ratio, $b_{iv',fv''}$ and magnitude of the transition dipole moments, $|\mu_{iv',fv''}|$, for the $B^2\Sigma^+(N=3,v'=0) \rightarrow X^2\Sigma^+(v'')$ and $B^2\Sigma^+(N=3,v'=0) \rightarrow A^2\Pi(v'')$ transitions.

	$X^2\Sigma^+$				$A^2\Pi$		
	$v''=0$	$v''=1$	$v''=2$	$v''=3$	$v''=0$	$v''=1$	$v''=2$
$b_{iv',fv''}$ (exp.) (%)	$97.0^{+0.7}_{-2.5}$ [a]	$3.0^{+0.7}_{-0.7}$	< 1.2 [b]	< 1.3 [b]	< 1.2 [b]	< 0.7 [b]	< 1 [b]
$\|\mu_{iv',fv''}\|$ (exp.) (D)	$1.631^{+0.025}_{-0.032}$ [c]	$0.31^{+0.04}_{-0.04}$	< 0.21	< 0.23	< 0.21	< 0.17	< 0.22
$\nu_{iv',fv''}$ (cm^{-1})	26,030	24,870	23,711	22,552	23,787	22,847	21,907
$\|\mu_{iv',fv''}\|$ (calc.) (D)	1.822 [d]	0.073	0.006	0.001	0.04	0.06	0.07
FCFs (calc.)	0.988	0.011	0.000	0.000	0.143	0.285	0.280
FCFs [e]	0.988	0.011	0.002	0.011	0.099	0.263	0.306
$b_{iv',fv''}$ (calc.) (%)	99.6 [f]	0.1	< 0.1	< 0.1	< 0.1	< 0.1	< 0.1

[a] Estimated uncertainty comes from statistical uncertainty and limits on possible $B^2\Sigma^+ \rightarrow A^2\Pi$ relaxation (see text).

[b] Upper limit derived from noise floor at expected transition (see text).

[c] Obtained using Eqn. (4.1) and the measured values for using $b_{iv',fv''}$ and τ.

[d] Obtained using RKR potentials and the electronic ab initio transition moment form [**25**] (see text).

[e] Franck-Condon Factors from [**24**].

[f] From Eqn. (4.1).

$v''=0$ to $v''=1$ is so large, the limit placed on $v''=2$ is likely much larger than the true value and the limit should also extend to the sum over all higher vibrational transitions. No branching to the $A^2\Pi$ state was observed, consistent with predictions of a smaller transition dipole moment [**108, 22, 25**] (see below). The fluorescence lifetime of the $B^2\Sigma^+$ state of SiO^+ following excitation was measured. Figure 4.4 displays the integrated fluorescence decay curve for excitation of the overlapped $R_{11}(3)$ and $R_{22}(3)$ branch features. The resulting curve was then fit with a single exponential function giving a determined lifetime of 66 ± 2 ns. This compares well with the previously determined value of 69.5 ± 0.6 ns obtained using an alternative method [**137**], confirming that the carrier of the spectrum is SiO^+.

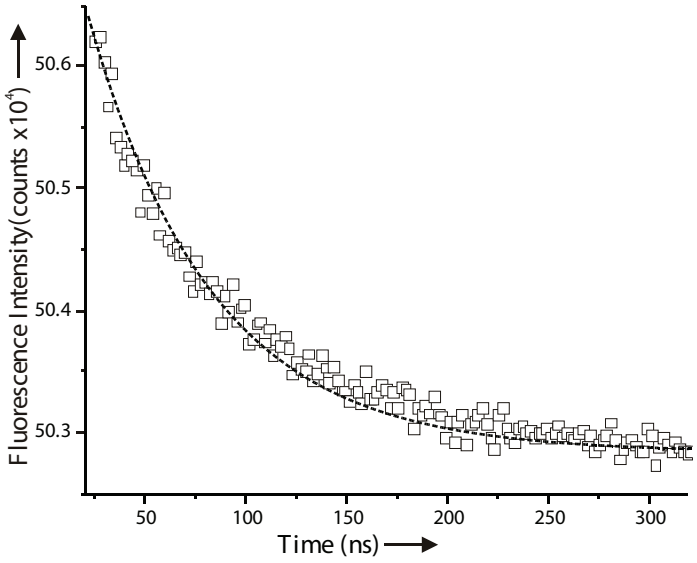

Figure 4.4. Radiative decay curves resulting from laser excitation of the $R(3)$ line of the $B^2\Sigma^+ - X^2\Sigma^+(0,0)$ band and monitoring the on-resonance LIF signal. The dashed curve is the predicted decay obtained using the least-squares optimized lifetime.

4.1.2. Discussion

The observation that the $B^2\Sigma^+(v = 0) \rightarrow X^2\Sigma^+(v)$ emission is near diagonal and much stronger than the $B^2\Sigma^+(v = 0) \rightarrow A^2\Pi(v)$ emission is readily qualitatively explained using a simple molecular orbital correlation diagram or the results of the theoretical prediction [**21, 25**]. The primary configuration for the $X^2\Sigma^+$ and $A^2\Pi_i$ states are $1\sigma^2 2\sigma^2 3\sigma^1 1\pi^4$ and $1\sigma^2 2\sigma^2 3\sigma^2 1\pi^3$ respectively, whereas the $B^2\Sigma^+$ state is an admixture of the $1\sigma^2 2\sigma^2 3\sigma^0 1\pi^4 \sigma 1$ (51%) and $1\sigma^2 2\sigma^2 3\sigma^0 1\pi^3 4\sigma^1 2\pi^1$ (18%) configurations. Here only the $2s$(O), $2p$(O), $3s$(Si) and $3p$(Si) atomic orbitals are considered in labelling the molecular orbitals. To a first order approximation 2σ, 1π, 4σ, and 2π are the $2p$(O)$\pm 3p$(Si) bonding and anti-bonding orbitals with the 2σ and 1π being strongly polarized towards O and the 4σ and 2π towards Si. The 1σ and 3σ are the non-bonding $2s$(O) and $3s$(Si) orbitals

respectively. Simultaneous $3s$(Si) and $3p$(Si) participation in bonding is inhibited because of the large difference in radial extent. The $X^2\Sigma^+ \rightarrow B^2\Sigma^+$ transition is associated with a charge transfer, one electron promotion, whereas the $A^2\Pi_i \rightarrow B^2\Sigma^+$ transition is a much weaker, two electron, promotion. Hence, the $X^2\Sigma^+ \rightarrow B^2\Sigma^+$ electric transition dipole moment is much larger ($\approx$1.83 D at R_e) than that for the $A^2\Pi_i \rightarrow B^2\Sigma^+$ ($\approx$ 0.10 D at R_e) (see below). Furthermore, the $X^2\Sigma^+ \rightarrow B^2\Sigma^+$ transition is near diagonal because the $3\sigma \rightarrow 4\sigma$ electron promotion from a non-bonding Si-centered orbital to a slightly anti-bonding Si-centered orbital results in an insignificant change in Re. On the other hand, the $A^2\Pi_i(v) \rightarrow B^2\Sigma^+(v)$ transition is much less diagonal because the R_e for the $A^2\Pi_i$ state is significantly longer than that for the $B^2\Sigma^+$ state since in the former the strongly bonding 1π orbital has an occupation of 3 whereas in the latter it is fully occupied. The predicted [**25**] permanent electric dipole moment of the $A^2\Pi_i$ state is much less than that for the $X^2\Sigma^+$ supporting the conjecture that the 3 is Si-centered whereas the 1π is an O-polarized bonding orbital. Existing data can also be used to predict $b_{iv',fv''}$. The branching ratio, $b_{iv',fv''}$, is defined as [**4**],

$$b_{iv',fv''} = \frac{A_{iv',fv''}}{\sum_{fv''} A_{iv',fv''}} = \frac{|\mu_{iv',fv''}|^2(\nu_{iv',fv''})^3}{\sum_{fv''} |\mu_{iv',fv''}|^2(\nu_{iv',fv''})^3} = \frac{I_{iv',fv''}}{\sum_{fv''} I_{iv',fv''}}, \tag{4.1}$$

where $A_{iv',fv''}$ is the Einstein $\mathcal{A}$ coefficient, $\mu_{iv',fv''} \equiv \langle \Psi_{v',J'} | \langle \Psi_{el'} | \hat{\mu}^{el}(r) | \Psi_{el''} \rangle | \Psi_{v'',J''} \rangle$ is the transition dipole moment, $\nu_{iv',fv''}$ is the transition frequency, and $I_{iv',fv''}$ is the intensity. The summation in Eqn. (4.1) runs over all the lower vibronic states. If it is assumed that transition moment operator, $\hat{\mu}$, is independent of internuclear separation (i.e. Condon approximation), then $b_{iv',fv''}$ is proportional to the product of the FCF and the ν^3 factor.

The radiative lifetime of an individual excited state vibronic level, $\tau_{iv'}$, is related to $A_{iv',fv''}$ simply by:

$$\tau_{iv'}^{-1} = \sum_{fv''} A_{iv',fv''}. \tag{4.2}$$

Combination of these relationships gives [**81**]

$$\mu_{iv'}^{-1} = \sqrt{\frac{b_{iv',fv''}\tau_{iv'}^{-1}}{3.1362 \times 10^{-7}\nu_{iv',fv''}^{3}}} \tag{4.3}$$

where the conversion factor assumes that $\mu_{iv',fv''}$ is in Debye (D), $\nu_{iv',fv''}$ is in wavenumber (cm^{-1}) and $\tau_{iv'}$ is in seconds. Using the experimentally determined values for $b_{B^2\Sigma^+(v=0),fv''}$ based upon the aforementioned relative intensity measurements given in Table 4.1, and the experimentally determined $\tau_{iv'}$ (66±2 ns), then the $|\mu_{B^2\Sigma^+(v=0),fv''}|$(exp.) values given in Table 4.1 are obtained. The calculated transition dipole moments, $|\mu_{B^2\Sigma^+(v=0),fv''}|$(calc.), and FCFs are also given in Table 4.1. These values were obtained using the spectroscopic parameters [**126**] and predicted transition dipole moments [**25**]. Specifically, the suite of programs developed by Prof. Robert LeRoy (Waterloo University) [**87**] were used to calculate matrix elements of $\hat{\mu}^{el}(r)$. The potential energy curves for the $X^2\Sigma^+$, $A^2\Pi_i$, and $B^2\Sigma^+$ states were predicted using the first-order Rydberg-Klein-Rees (RKR1) procedure with the aid of the previously determined molecular constants [**126**]. The potential energies curves were used as input to a program that numerically solved the radial Schrdinger equation (LEVEL 8.2 program). The same program calculated $\langle\Psi_{v',J'}|\langle\Psi_{el'}|\hat{\mu}^{el}(r)|\Psi_{el''}\rangle|\Psi_{v'',J''}\rangle$. A perusal of the *ab initio* prediction [**25**] reveals that

electronic transition dipole moments, $\langle \Psi_{el'} | \hat{\mu}^{el}(r) | \Psi_{el''} \rangle$ are nearly linear in internuclear separation in the Franck-Condon region. For the purpose of prediction performed here, the slope and intercept for the $\langle B^2\Sigma^+ | \hat{\mu}^{el}(r) | X^2\Sigma^+ \rangle$ linear function were taken as -3.11 D/Åand 6.57 D, respectively, and for $\langle B^2\Sigma^+ | \hat{\mu}^{el}(r) | A^2\Pi_i \rangle$ as -0.46 D/Åand 0.84 D, respectively, which produced the $|\mu_{B^2\Sigma^+(v=0),fv''}|$(calc.) values given in Table 4.1. The calculated branching ratios, $b_{iv',fv''}$(calc.), were then obtained using Eqn. (4.1). The obtained values are consistent with the previously predicted FCF [**122**] ratios which are also listed in Table 4.1.

The observed branching ratios, $b_{iv',fv''}$(exp.), indicate that the $B^2\Sigma^+(v = 0) \rightarrow X^2\Sigma^+(v)$ emission is significantly less diagonal than that predicted (e.g. $\frac{b_{0,1}}{b_{0,0}}$(exp.)= $\frac{3.0}{97.0}$ *vs.* $\frac{b_{0,1}}{b_{0,0}}$(calc.)= $\frac{0.1}{99.6}$). This discrepancy may be due in part to the fact that the prediction does not account for the rotation and spin-orbit mixing of the $X^2\Sigma^+$ and $A^2\Pi_i$ states. Specifically, the spin-orbit mixing term, ξ, and the rotation mixing term, 2η, have been determined [**126**] to be -37.5 cm^{-1} and 0.85 cm^{-1}, respectively. Furthermore, the spectroscopic parameters used for the potential energy predictions were derived from rotational parameters of an effective Hamiltonian operator. Such parameters are contaminated with higher order terms used to account for Born Oppenheimer breakdown.

Finally, it is noteworthy that the *ab initio* predicted radiative lifetime [**25**], $\tau_{iv'}$ (= 59 ns), is near the experimentally determine values indicating that there is no significant non-radiative relaxation of the excited state levels. The $B^2\Sigma^+(v = 0)$ rotational levels are embedded in a dense set of $X^2\Sigma^+$ and $A^2\Pi_i$ excited vibronic levels and could provide an avenue for non-radiative relaxation.

4.1.3. Conclusions From ASU Branching Ratio Study

With our work at ASU we demonstrated a method for producing a cold molecular beam of SiO^+ and performed the first dispersed laser induced fluorescence measurements to determine the radiative branching ratios of decay from the $B^2\Sigma^+(v = 0)$ state. Decay to the $X^2\Sigma^+(v = 0)$ state was observed to occur 97% of the time while the remaining 3% was observed to decay to $X^2\Sigma^+(v = 1)$. All other monitored decay channels were observed to have signals below detectability. Given the results of this study, we would expect an average of 33 spontaneous emissions on $B^2\Sigma^+ - X^2\Sigma^+(0, 0)$ before any off diagonal decay in $X^2\Sigma^+(v = 0)$ and even more before any decays into the $A^2\Pi_i$ manifold. At room temperature the rotational population density peaks near $N = 12$. In regards to the previously mentioned rotational cooling technique, this corresponds to an average of 12 spontaneous emissions before population transfer to the lowest two rotational states. This suggests that efficient rotational cooling should be possible. Indeed, in the time since this study was completed, efficient cooling into the ground rotational state was observed (see section 7.3). Further investigation is still necessary before decay paths and repump schemes can be fully characterized. For example, the Doppler cooling of SiO^+ proposed by Dr. Jason Nguyen et al [**108**] assumes certain theoretical predictions of the $B^2\Sigma^+$ to $A^2\Pi_i$ branching fractions and relaxation rates of $A^2\Pi_i$ to $X^2\Sigma^+$. A related possibility of performing single-molecule fluorescence detection of trapped SiO^+ also would require more scattered photons than does rotational cooling. Given a vibrational re-pump laser, the currently available data does not preclude this possibility, however the limits on the $B^2\Sigma^+$ to $A^2\Pi_i$ state branching fractions need to be improved by approximately two orders of magnitude to meaningfully assess the prospects of Doppler cooling as of order 10,000

photons are needed to Doppler cool. Knowledge of the $A^2\Pi_i$ state lifetimes can also inform cooling schemes. If branching from $B^2\Sigma^+$ to $A^2\Pi_i$ is more common than 1 part in 10,000, the requirement of additional repump lasers for the $A^2\Pi_i$ state will depend on the relaxation rate compared to the heating rate. Similarly, design of a single molecule fluorescence apparatus would depend strongly on these branching fractions. Knowing the $A^2\Pi_i$ state radiative lifetime is also necessary to determine how much population will accumulate in a dark state. The next section of this chapter describes my progress toward constructing an ion trap apparatus with the purpose of measuring the very small branching to the $A^2\Pi_i$ state to help answer such questions.

4.2. Large LIF Ion Trap for Measurement of Small Branching Fractions

In the remaining sections of this chapter, I present my work on constructing and characterizing an ion trap system for the purpose of measuring small ($< 10^{-3}$) branching fractions of SiO^+ via dispersed laser induced fluorescence (LIF). Performing spectroscopy on molecular ions is widely considered challenging due to the relatively low densities afforded by Coulomb repulsion. This issue is compounded by the dozens to hundreds of rotational states occupied under room temperature thermal conditions. These conditions have contributed to the relative dearth of LIF experiments performed on molecular ions compared to their neutral counterparts. Examples of measurements of branching ratios of molecular ions found in the literature are rare and after performing an extensive literature search I was unable to find any branching ratio measurements smaller than the 1% level.

Three different approaches were considered for improving the measurement of the branching ratios. All of them relied on detecting dispersed fluorescence to obtain the

branching ratios. We ultimately decided on the third approach we considered, i.e. using an ion trap. The first approach considered was to use a source of ablated Si in O_2 gas which generates SiO^+ in the ablation plume [**101**]. This approach was abandoned due to the large background signal coming from the plume. Specifically, the expected signal from decay of $B^2\Sigma^+$ to $A^2\Pi_i$ is overwhelmed by the background. Furthermore, the ability to rule out fluorescence from other species that share coincident emission wavelengths would require using the 2D spectrum method as seen in Fig. 4.1. Such a survey may require prohibitively long data collection.

The second approach we considered was another molecular beam source. Because the ASU beam source was not created with the intention of generating SiO^+ (it was rather found by accident on request), the signal size and background species content may be open to considerable improvement. This approach was originally abandoned before any attempts were made due to similar considerations as in the ablation case. The processes for generating SiO^+ are generally performed under extreme conditions that result in significant population of excited states. The consequence is that light from all over the visible spectrum is produced. It can be difficult to suppress this background in a beam to sufficiently low levels due to the constraints on time between source generation and beam probing. This approach has since been revived due to our interest in characterizing new molecules such as TeH^+ (see chapter 3) which does not exist in a convenient neutral form as SiO does. If an efficient method for generating the molecular ion of interest in a beam is found, screening effects from the neutral plasma will result in higher densities in the beam than might be naively expected when considering Coulomb repulsion and may overcome issues with the background. Ultimately, however, the plan is to integrate

the molecular beam with the LIF ion trap as a general method for source production and loading of the LIF trap.

The decision to pursue building an ion trap was primarily motivated by its ability to isolate the molecules. The issue of background due to SiO^+ source production is eliminated because ion traps are capable of storing ions for extended periods of time and therefore probing the ions can be well separated in time from the production. Long trapping lifetimes also have the added benefit of probing the lifetime of longer lived states such as the $A^2\Pi$ state. Impurities and unknown fluorescent sources can also be confidently resolved without a detailed survey of the 2D DLIF method by virtue of mass filtering and selective trap loading processes such as REMPI [**150**].

The goal in the construction of the LIF trap was to attach collection optics and fiber the light into a spectrometer to record the dispersed LIF of SiO^+ as was done in the previous section. Fluorescence of SiO^+ in the trap was never observed and work on the trap was abandoned following successful detection of SiO^+ dissociation in the 'Molecular Ion Trapping and Control Apparatus' described in chapter 5. The failure to observe fluorescence from SiO^+ is likely a consequence of poor loading efficiency of the SiO^+ into the the trap coupled with fast reactions with background hydrogen gas in the vacuum chamber. This hypothesis is formed after similar LIF tests on Ba^+ in the LIF trap perform as expected. If trap loading and reactive gas background partial pressures are kept under control, it is expected that the LIF trap system will be able to function as intended by measuring weak branching ratios in an effectively background free environment and thus avoid potential misattribution of weak signals.

4.2.1. Design

A major concern with using an ion trap to probe the branching ratio of a highly diagonal FCF molecular ion is that the trap rods are reflective. This is an issue because fluorescence wavelength is primarily the same as the probe laser wavelength and therefore filtering of laser scatter must be done with more care. For this reason I largely followed the geometric dimensions of the linear Paul trap designed by Schultz-Johanning et al described in [**140**] which was capable of suppressing laser scatter to sufficient levels and optimizing light collection by using smaller diameter rods. This trap is somewhat unusual as it is significantly larger than the other traps in our lab. Regardless, the trap matched our requirements and was demonstrated on Fe^+ (56 u) and W^+ (184 u). This means the achievable trapping parameters should also be sufficient for our range of masses, i.e. Ba^+ (138 u) and SiO^+ (44 u). A later work done by the same authors was able to detect branching ratios of atomic ions smaller than 10^{-5} using the same apparatus [**135**]. The branching ratios were obtained using a time-resolved nonlinear LIF technique. Though this technique differs from dispersed fluorescence techniques, the detection limits are constrained by the SNR which is shared for both techniques.

4.2.1.1. Trap Parameters, Geometry, and Loading. Following the design described in [**140**], the LIF trap is a linear Paul trap composed of four cylindrical rods (stainless steel) with a diameter of 15.9 mm and arranged to give a trapping radius $r_0 = 19$ mm. An image of the Paul trap can be seen in Fig. 4.5. Each set of diagonal rods is connected to opposite ends of a toroidal resonator circuit described. Unlike in ref. [**140**], the trap has adjustable (along the z-axis) endcap electrodes. They are currently positioned such that $z_0 = 22.5$ mm. Important for corrections in estimating a and q Mathieu stability

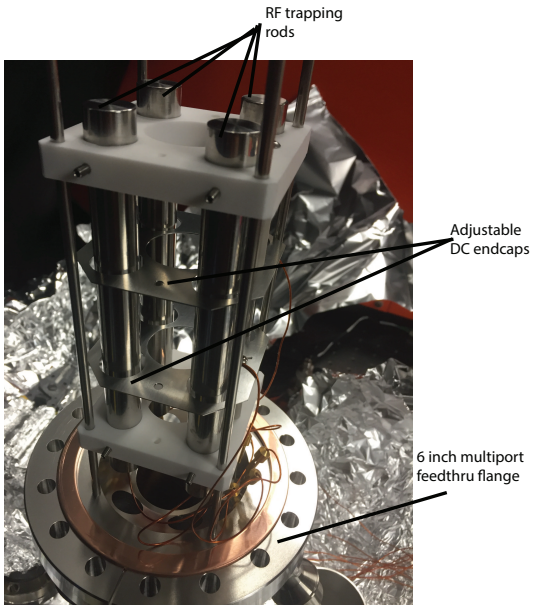

Figure 4.5. The trap and its electrical feedthrus are self-contained on a 6 inch CF multiport feedthru (MultiPortFlng, 6"×6-1.33" AngledPorts MDC Vacuum Products). Four narrow steel rods are screwed into custom tapped holes in the vacuum flange and used to support the trap such that the trap center axis is aligned with the center axis of the flange. The RF rods are held in place by two insulating MACOR mounts. The adjustable endcap plates are attached to the MACOR mounts with bakeable, UHV compatible plastic (PEEK) spacers. The custom parts were all machined by the Northwestern Machine Shop.

parameters is κ. Dr. Yen-Wei Lin performed calculations for both $\kappa_r = 0.39$ and $\kappa_z = 0.36$ using the methods described in chapter 2 of his thesis [**93**].

Each rod is capable of independent control of DC voltage offsets. The RF voltage and frequency is generated by a function generator whose output is fed into a power operational amplifier (APEX microtechnology, PA107) with a gain of 30. The output of the op-amp is fed into a toroidal resonator circuit with a resonance tuned to 650 kHz. The resonance circuit is capable of reaching a circulating RF amplitude of $V_{pp} > 1000$ V

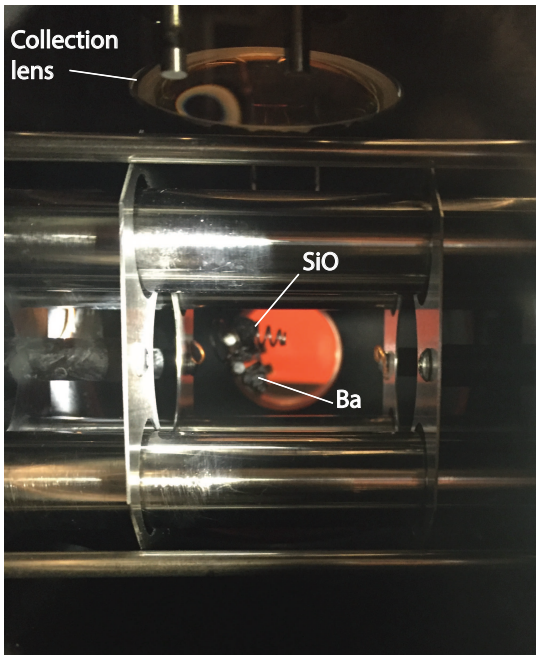

Figure 4.6. image of barium and silicon monoxide sample mounts and the in-vacuum fluorescent light collection lens.

before resistive heating of the toroid changes the impedance of the resonator circuit and reaches a maximum steady state voltage amplitude of $V_{pp} = 850$ V.

Loading of the trap is accomplished in exactly the same way as described in section 5.1. The ablation setup of the main molecular ion trapping apparatus was redirected through the use of flip mirrors to the LIF trap. Somewhat unique to this setup is that the ablation lasers were directed from below through a viewport on the bottom of the 6-way cross. A sample of barium and silicon monoxide were held in a spring close to the trapping volume. The sample holder, trap, and in-vacuum collection lens is shown in Fig. 4.6.

4.2.1.2. Light Collection and Laser Scatter Suppression. Because the goal of this apparatus is to measure branching ratios of molecular ions with (nearly) diagonal FCFs,

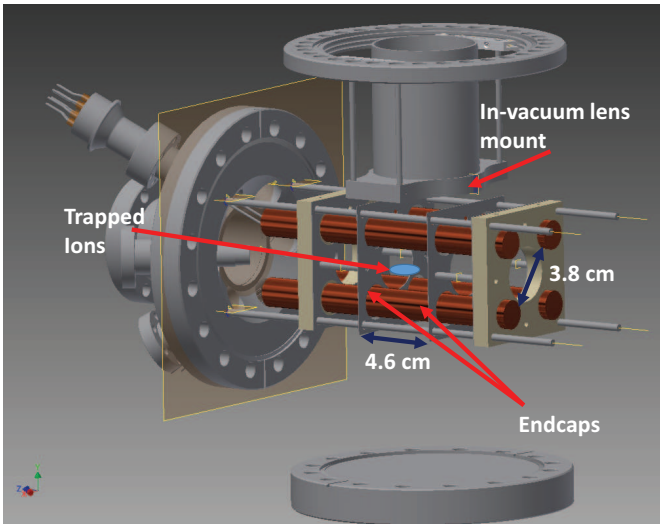

Figure 4.7. CAD drawing of the trap and in-vacuum light collection system.

most of the laser induced fluorescence will be the same wavelength as the probe laser. Therefore suppressing laser scatter is critical for detection and measurement. In the process of reducing laser scatter, multiple approaches were attempted and characterized until the suppression was sufficient.

Several approaches were used for reducing laser scatter. The first approach was through geometry. This means denying scattered light, and preferably secondary scatters, a direct path towards the detector. This is accomplished by adding light baffles and vanes in the beam path to deflect scattered light away from the detector as well as impeding any light reaching the collection optics that doesn't come from the desired imaging volume. The second approach is to increase the absorption on each surface. For this I used UHV compatible black paint (MLS-85-SB, AZ Technology). If a is the absorption, then black paint combined with good geometry should provide exponential suppression that goes like $(1-a)^n$ where n is the number of surfaces scattered light is geometrically required to hit

before reaching the detector[2]. Finally, the last approach is to reduce the scatter from the source. This is done by spatially filtering the laser beam, minimizing the beam size, and using viewports that are AR coated or brewster cut.

The basic light collection system is shown in Fig. 4.7. In order to maximize light collection an in-vacuum lens mount is installed directly above the center of the trapping region. The in-vacuum collimating, collection lens (50.8 mm diameter, f=60 mm) is designed to maximize the numerical aperture without using a custom lens. The lens mount is attached to a groove grabber (6" Kimball Physics) positioned between the top of the 6-way cross and a reentrant viewport. Outside of the vacuum system the remaining optics are modular, similar to the imaging system for the main molecular ion trapping apparatus described in section 5.3. The in-vacuum lens tubing shown in Fig. 4.7 was eventually removed as it was found to not have an effect on the background signal.

For the purposes of quantifying the background laser suppression, an analog PMT was used to estimate the laser scatter signal detected. The results of the laser scatter suppression are summarized in Fig. 4.8. The OPO (Ekspla, see section 5.4.1) was used for studying the background suppression and was tuned to the SiO^+ $B \rightarrow X(0,0)$ transition at 385 nm and aligned along the z-axis of the trap. As a baseline test of the total suppression, tests began without viewports and baffle vanes, and with the vacuum chamber completely unpainted. Addition of the baffle vanes provided some improvement, however, as the viewports were added the background increased. The effect of the viewport was neutralized by replacing the ends of the baffle arms with flexible bellows (see Fig. 4.9).

[2]Important in considering the suppression is whether the surfaces are specular (mirror-like) or diffuse (rough surface). In this case, the paint finish was diffuse. Despite painting light baffles black it is still possible to increase the laser scatter background if the surface changes from specular to diffuse and thus it is important to consider the surface quality in the design.

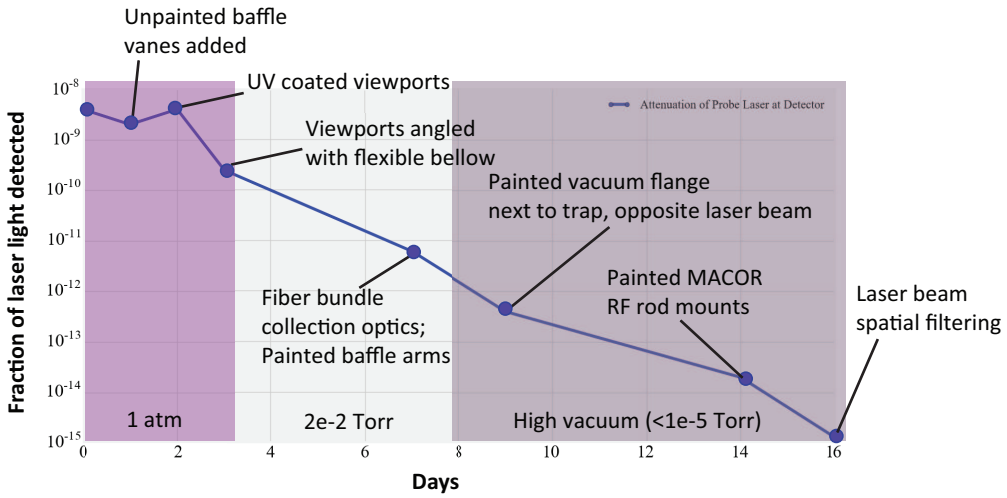

Figure 4.8. Attenuation of probe laser at the detector over two weeks of changes to the system. The first day was taken as a baseline and was recorded outside of vacuum without viewports, black paint, or baffle vanes added. No further improvements were applied after spatial filtering of the beam resulted in a suppression of 1.5×10^{-15} or < 0.2 photon counts per pulse under experimental conditions. See text for details.

This allowed for any light reflected off of the viewport to be sent directly into one of the baffle vanes shown in Fig. 4.10).

Improvements were largely stalled until it was realized that Raleigh scattering was contributing to most of the background scatter. After pumping down the vacuum system, the first major improvement came from the collection optics side. A fiber bundle was attached between the collection optics and the PMT. The fiber bundle effectively filtered light that was not directly imaged from the center of the trapping volume. Suppression was also improved to a less significant degree by painting the baffle arms black. This suggested that most of the remaining scatter was a result of scatter originating inside the 6-way cross. Painting the remaining surfaces in the 6-way cross (excluding trapping electrodes) improved the suppression by more than two orders of magnitude.

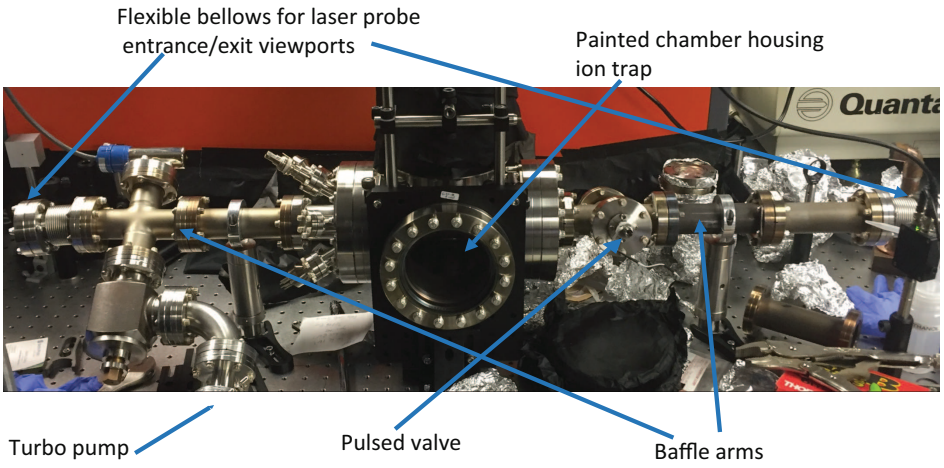

Figure 4.9. Image of 6-way cross and extended baffle arms of the LIF chamber. Each flange connection in the baffle arms uses a painted, solid copper gasket with progressively smaller apertures which act as the baffle vanes. Each arm is between 0.4 m and 0.5 m long and the vane diameters are between 7.5 mm and 20 mm in diameter. An example of the light baffle vanes is shown in Fig. 4.10.

It was determined that the remaining scatter was likely due to the beam quality and the remaining unpainted metallic surfaces inside the chamber after the laser profile was observed to have a weak halo-like profile around the beam. Scattering from the viewport surfaces was ruled out after little change in the background signal was observed when covering the exit viewport with a piece of aluminum foil. This indicated that back-scatter from the viewport and other sources outside of the vacuum chamber were negligible. Though the source of the halo-like profile was never understood, spatial filtering of the beam with a pinhole was able to mitigate some of the effect. No attempt at further improvements was made after the background was sufficiently suppressed to < 0.2 photon counts per pulse.

4.2.1.3. Vacuum System. The vacuum system is shown in Fig. 4.9. The positions of the turbo-molecular pump and the pulsed valve have been changed since the time of

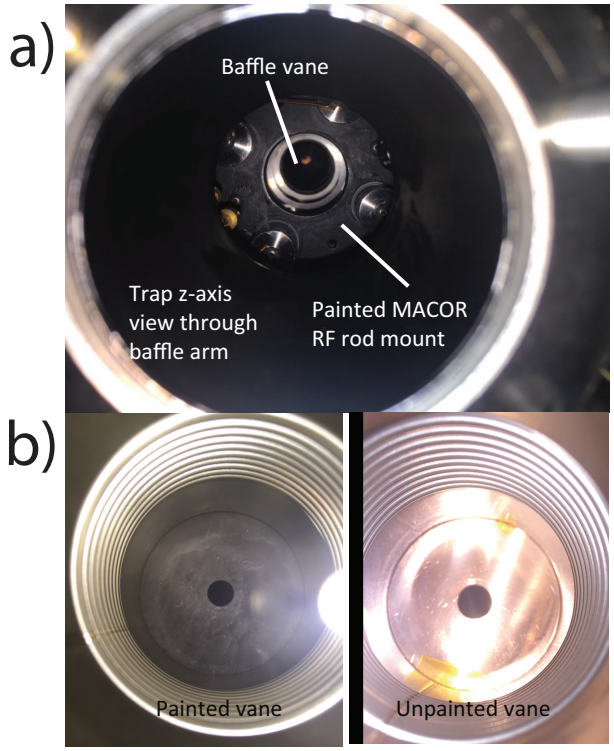

Figure 4.10. **a)** View along the ion trap z-axis through which the probe laser is aligned. **b)** A diffuse light is shined onto the painted and unpainted baffle vanes to demonstrate the suppression from the black paint. Baffle vanes are made out of solid copper CF gaskets. Holes with sharpened edges were machined by the Northwestern Machine Shop to various diameters to be tested for optimal laser scatter suppression.

the picture being taken and before the Ba^+ LIF experiments were conducted. The pump has been moved closer to the 6-way cross through a connection on the back face with an ion gauge (Granville Phillips Stabil-Ion 370) and the pulsed valve has been moved to the multi-port flange on the 6 way cross. Not pictured, is a Channeltron channel electron multiplier (CEM) that is also connected to the multi-port flange. Due to fast reactions of SiO^+ with background H_2, it is necessary to bring the base pressure to UHV levels. For this system a baseline pressure of 1.9×10^{-9} Torr (assuming pure H_2) was observed by the ion gauge. Though the partial H_2 pressure needs to be kept low, the experiment

will benefit from a higher total pressure. The pulsed valve is used to control the flow of helium (or some other inert gas) buffer gas into the chamber and therefore control the total pressure. Higher pressure is known to improve trapping lifetimes and densities and may avoid spectral 'hole burning' or 'bleaching' from the LIF laser. That is, collisions of the SiO^+ with the buffer gas will rapidly rethermalize the rovibrational population. The effect is more pronounced in a LIF probing of the Ba^+ 6S to $6P_{1/2}$ transition at 493 nm. The result is that population is pumped into the $5D_{3/2}$ state which has a natural lifetime of 80 s.

The requirement of a baseline UHV level means baking the chamber is necessary. The quantity of black paint used in the vacuum system presented severe, unexpected complications. Baking the vacuum chamber caused a significant amount of silicone resin to be released from the surface which coated all of the viewport surfaces and permanently damaged an ion gauge. The disaster can be seen in Fig. 4.11. Fortunately, acetone was able to fully dissolve the resin and the viewports were recovered. Since the time of painting the chamber, a relatively simple and easy procedure for creating UHV compatible black cupric oxide surfaces with comparable reflectivities has been published [**114**] that would avoid complications found with the paint.

In order to avoid coating of sensitive equipment and viewports, it was found that all painted items should be first baked between 300 and 420 degrees Celsius for 3 to 4 days under low vacuum using a rough pump only. Between the rough pump and the vacuum system should be attached a "cold trap" (i.e. vacuum nipples that are not heated) with at least two right angle turns before going into the rough pump. This way the resin evaporated from the paint condenses onto the cold trap and can later be removed with

Figure 4.11. Residue from silicone resin evaporated from the paint during baking and left coated onto the front viewport.

acetone after baking. Flaking of the paint following baking was generally found to be a non-issue if two coats of paint were applied to each surface before baking. Following the extended high temperature bake at low vacuum, nearly all of the residual resin should be removed and the remaining sensitive vacuum components can be reattached. As a precaution the IG was kept out of the line of site of any painted surfaces. With all the sensitive components reattached, including the turbo-molecular pump, the vacuum system is again pumped down and baked following standard procedure until UHV is achieved.

4.2.2. Characterizing the trap with Ba^+

The general approach to achieving a branching ratio measurement of SiO^+ using the LIF trap was to first eliminate background laser scatter and then to optimize any detectable signal. As demonstrated in section 4.2.1.2, the background laser scatter was effectively brought to zero. Thus the next step was to optimize the signal. Because SiO^+ is generally more challenging to work with than a laser-coolable atom like Ba^+, I decided to

first optimize the signal for Ba^+ light collection. Optimization is generally much more straightforward once a signal has been detected as each change in a setup provides a clear response in change to the signal. Without a signal it is not clear if a change has improved or degraded the signal collection. Thus the idea here is to use the easier to detect, control, and characterize Ba^+ to optimize the LIF trap for eventual SiO^+ detection. In the process, the well understood Ba^+ can be used to provide quantitative estimates on the equivalent expected Sio^+ signal.

Loading and detection of Ba^+ was first performed using the CW cooling lasers. An image recorded by the ICCD (ANDOR iStar) is shown in Fig. 4.12. From this initial signal I could infer several important, independent confirmations of the LIF trap setup. Observation of the image in Fig. 4.12 confirmed that the trap electronics and geometry were functioning properly, the lasers were aligned through the long baffle arms, and that the Ba^+ loading procedure (ablation followed by photo-ionization) was working as intended.

4.2.2.1. Ba^+ Loading and LIF Pressure Dependence. To characterize the role of the helium buffer gas on Ba^+ loading, the fluorescence signal was recorded as a function of time for various helium buffer gas pressures. The results are shown in Table 4.2. The lifetime and loading rate are measured using the fluorescence signal from the CW lasers. To avoid any effect of Doppler cooling on the Ba^+, both CW lasers were slightly blue detuned. The 493 nm and 650 nm Doppler cooling lasers (see section 5.2) were alternately turned on and off while light collection was time discriminated to only collect during 493 nm excitation. A bandpass filter at 650 nm was used to filter out any 493 nm laser light and collect only fluorescence from the Ba^+ $6P_{1/2} \rightarrow 5D_{3/2}$ transition. To determine

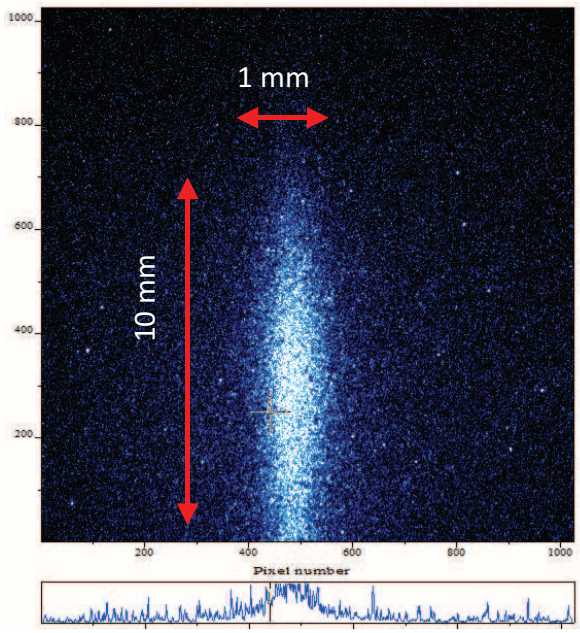

Figure 4.12. Fluroescence (false color) from trapped Ba^+ inside the LIF trap. The bright area does not show the full extent of the Ba^+ cloud, but rather provides a profile of the CW Doppler cooling beams.

Table 4.2. The trapping lifetime and loading time of Ba^+ in the LIF trap. Numbers in parenthesis represent the 1σ statistical uncertainty from a fit to decaying and asymptotic exponential functions.

Pressure (Torr)	Trapping Lifetime (s)	Loading Time (s)
5e-4	17.7(3)	4.9(2)
3e-4	19.5(3)	5.2(2)
1e-4	24.8(3)	7.1(3)
4e-5	41.4(5)	10.0(3)
1.4e-6	48(1)	$< 10^{\dagger}$

† Exact time was not recorded, however saturation was observed to be <10 s.

the loading rate, the ablation laser was fired continuously at 10 Hz as the fluorescence signal was monitored. Conversely, to determine the trapping lifetime, after the signal had saturated, the ablation loading was turned off and the decay of the fluorescence signal was monitored as a function of time.

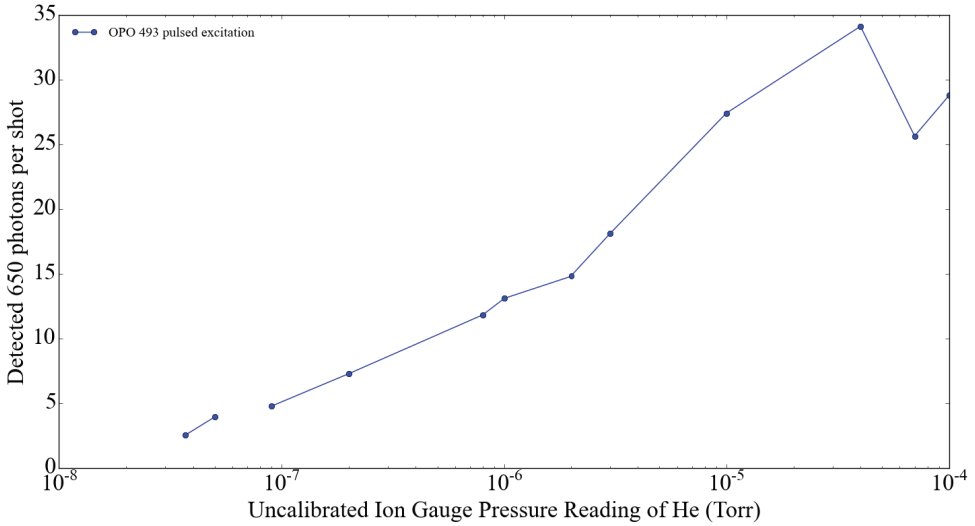

Figure 4.13. The detected signal with continuous ablation loading as a function of He buffer gas pressure. Multiply pressures by 5.6 to obtain the estimated He pressure.

Though the trend indicates that lower pressure leads to longer trapping lifetimes, there is a separate question of what pressure maximizes trapping capacity of the LIF trap and a related question as to what pressure is sufficient for quenching or thermalizing the population. As a proxy for determining the relative trapping capacity, a pulsed LIF experiment using the OPO (Ekspla) tuned to 493 nm was performed over a range of helium buffer gas pressures. For this experiment, the OPO was fired at 10 Hz and the LIF was filtered by a longpass filter removing light shorter than 630 nm such that only light from decay of $6P_{1/2}$ to $5D^{3/2}$ was detected by the ICCD in photon counting mode. The results of this experiment are shown in Fig. 4.13. From the plot it can be observed that the signal appears to asymptote at higher pressure. The behavior beyond this pressure was not probed.

Further tests indicate that the pressure dependence is not acting exactly as a proxy for the relative amount of Ba^+ trapped. The role of quenching was tested by comparing the LIF signal due to 493 nm 10 Hz pulsed excitation with and without the 650 nm CW repump running continuously. Even at the highest pressures, the quenching rate was not overwhelming the excitation rate. For example, at 2×10^{-4} Torr, the signal was enhanced by a factor of 2, and even at a pressure of $1{\times}10^{-3}$ Torr the signal was increased by 10% with the 650 nm CW repump. Thus the actual pressure dependence on the Ba^+ density in the trap is likely much flatter than observed in Fig. 4.13 or even possibly decreasing in density. Compared to rotational quenching, the quenching of the Ba^+ $5D_{3/2}$ state is expected to be much slower given the relatively low energy of collisions compared to the electronic level spacing. So the optimal helium buffer gas pressure for SiO^+ is likely greater than indicated by the plot in Fig. 4.13.

Before I realized that the signal was limited by quenching rates, the maximum signal count was 800 photons per LIF pulse. This is enough information to provide a lower bound on the number of trapped Ba^+. With the transition saturated there is approximately a probability of 0.5 of excitation per atom per pulse. The detection efficiency is also estimated to be nearly 0.01. Thus there are $\sim$160,000 Ba^+ ions in the interaction volume. Based on ICCD images, this represents a volume of 0.3 cm^{-3} and thus a density of more than $5{\times}10^5$ cm^{-3}.

4.2.3. Attempts With SiO^+

From the maximum Ba^+ LIF signal, a signal for SiO^+ LIF can be estimated. Ignoring issues related to loading and reactions of SiO^+ with H_2, we can use the relative detection

efficiency of the the ICCD, the relative estimated density of SiO^+ in the trap, and the relative fractional population that is interacting with the laser. When going from 493 nm to the 385 nm fluorescence of $B \rightarrow X$, the relative detection efficiency is 0.6. At room temperature, the laser is expected to interact with 0.15 of the population. The relative change compared to Ba^+ is unknown because the effect of quenching was not measured for the maximum observed signal however 0.15 provides a lower bound for comparison. The density dependence on mass in the gas phase will go like $\propto m^{-3/2}$ [**27**] and thus is expected to be a factor of 5.6 times larger. The expectation then, is that the signal will be smaller by a factor of 2.

Contrary to expectation, no signal was ever detected with the ICCD camera (background rate of 0.05 counts per pulse using time discrimination) despite averaging for (tens of) thousands of pulses. Independent tests of the OPO wavelength setting were performed in a test vacuum chamber used for initial dispersed LIF measurement attempts. The ablation plume of a silicon sample in a 100 mTorr O_2 environment in the test chamber was probed, confirming of fluorescence from the SiO^+ $X \rightarrow B$ transition. Having ruled out issues with wavelength calibration, the assumption that loading and reaction rates are sufficient was questioned. The helium used as the buffer gas is pure to one part and 10^6. Therefore we expect that the partial pressure in the vacuum system is comparable to the base pressure at 2×10^{-9} Torr and therefore a reaction time of 1 minute or longer (see section 7.2 for a full discussion of reaction rates). This time scale is comparable or longer than the trapping lifetimes observed using Ba^+ shown in Table 4.2 implying that concerns with chemistry are unlikely to explain the lack of signal.

Therefore, we believe poor loading efficiency is the most likely explanation for the lack of detectable signal. At the time of attempting SiO^+ LIF detection, the loading of was performed by ablation of granular SiO followed by 2+1 REMPI (see section 6.1). Compared to Ba^+ loading the process is significantly less efficient. Because it is an unsaturated multiphoton process, optimizing the signal means decreasing the focal spot size in the trap which is counterproductive to increasing the quantity of SiO available to photoionize. Additionally, SiO typically requires nearly an order of magnitude more ablation power than Ba to load in the main, molecular ion trap (chapter 5).

The low efficiency of the 2+1 REMPI loading means that more material needs ablated to provide enough SiO^+ into the trap. However, when tests conducted in the main molecular ion trap were performed on the SiO^+ loading efficiency at higher ablation powers, the purity and composition of the ions changed dramatically. The result of one such test is shown in Fig. 4.14. At low ablation powers, photoionization appears to work as intended with the mass spectrum peaked around where SiO^+ is expected to be. At high ablation powers, ablation loaded without photoionization. From other measurements and other studies we know that very little of this product is actually SiO^+ (see chapter 6). Surprisingly, when the 2+1 REMPI dye laser beam is tuned to the (two-photon) $H^1\Sigma^+ - X^1\Sigma^+$ transition at 287 nm, the signal at the SiO^+ in the mass spectrum is nearly eliminated. This suggests that photoionization not only generates other ions besides SiO^+, it also displaces ions loaded through ablation only.

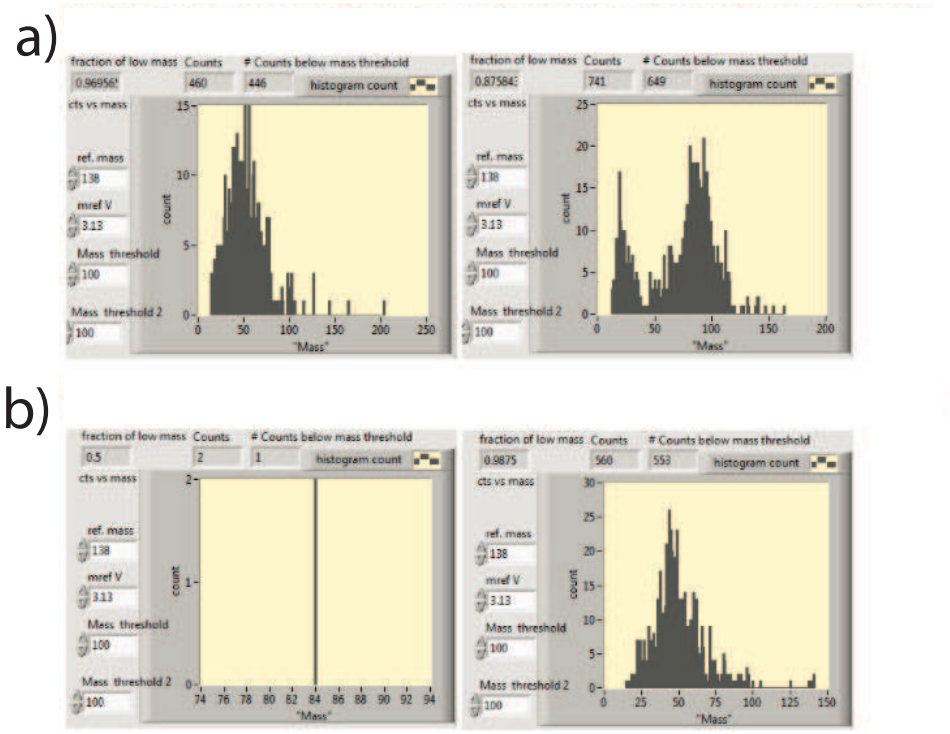

Figure 4.14. Mass spectra recorded using the Q-scan method in the main molecular ion trap in search of SiO^+ production (mass 44 u). **a)** Ablation power set to 550 μJ per pulse. Mass spectrum without (left) and with (right) the 2+1 REMPI dye laser beam at 287 nm. The signal around mass 44 in the ablation only spectrum is likely not significantly SiO^+ (see text). **b)** Ablation power set to 220 μJ per pulse. Mass spectrum without (left) and with (right) the 2+1 REMPI dye laser beam at 287 nm.

4.2.4. Conclusions

Tests on the large LIF ion trap with Ba^+ demonstrate that the trap is functioning as it was designed to. Careful design and testing of the light baffle setup also show that laser scatter can be suppressed to at least sub photon rates per LIF probe pulse under experimental conditions. This background scatter rate can be further suppressed below the dark count rate through the use of time discrimination which provides exponential suppression of the laser scatter relative to the fluorescence signal. Inability to detect LIF from SiO^+

suggests that trap loading using the less efficient 2+1 REMPI or rapid chemical reactions are likely causes of failure. The estimated rate of chemical reactions given the baseline pressure and impurity of the helium buffer gas, however, is not fast enough compared to the loading rate and trapping lifetimes of Ba^+ to explain the lack of LIF detection. On the other hand, the inefficiency of loading as reason for no signal is corroborated by tests performed in the much smaller molecular ion trap where higher ablation intensities combined with 2+1 REMPI resulted in the production of SiO^+ quantities below clear detection thresholds.

The implication of the differing results between Ba^+ and SiO^+ suggest that a more efficient process comparable to direct photoionization of Ba^+ for loading SiO^+ into the trap will allow for a smaller but still comparable LIF signal for SiO^+. Furthermore, the tests of Ba^+ involving pressure dependence and quenching rates suggest that there is still room for significant enhancement of the signal beyond these estimates. Together they suggest that an LIF photon detection rate exceeding 100 counts per pulse is possible. Such a rate leaves open te possibility for detecting branching ratios at the 10^{-5} level in less than a day of averaging. With the integration of a molecular beam source and attachment of a spectrometer for DLIF, the LIF trap is expected to serve its purpose as an apparatus for detecting weak branching ratios of small molecular ions for determining the prospects of Doppler cooling.

CHAPTER 5

Molecular Ion Trapping and Controlling Apparatus

In one sense ions are convenient species to work with. Even the force from relatively weak electric fields on charged particles is capable of dominating their trajectory. Though Earnshaw's theorem tells us that there cannot exist any stable static charge configuration, a simple loophole exists with the introduction of time-dependent fields. These facts have allowed for the development of quadrupole ion traps which are routinely capable of trapping depths reaching multiple eVs. The traps are indifferent to details in the substructure of the charged particles and the only relevant parameter is the charge to mass ratio.

In another sense, the charged properties of ions can make them exceedingly difficult to work with. Coulomb repulsion limits the density of ions making low-statistics an ever-present threat in any study involving ions. Therefore detection and characterization of molecular ions requires sensitive detection techniques. Cycling or quasi-cycling transitions and general state control can have dramatic impacts on detection statistics. Consequently, our experimental methods often make heavy use of Ba^+ which can be controlled using lasers in the visible spectrum.

In this chapter I discuss the apparatus and techniques involved in the SiO^+ control experiments of Chapter 7 and the 1+1 REMPI experiments of section 6.2. All the experiments revolve around what happens in the molecular ion trap pictured in Fig. 5.1. The geometry and the RF electronics of the Paul trap itself are discussed in detail in Chapter 6 of Dr. Yen-Wei Lin's thesis [**93**] and have not been updated.

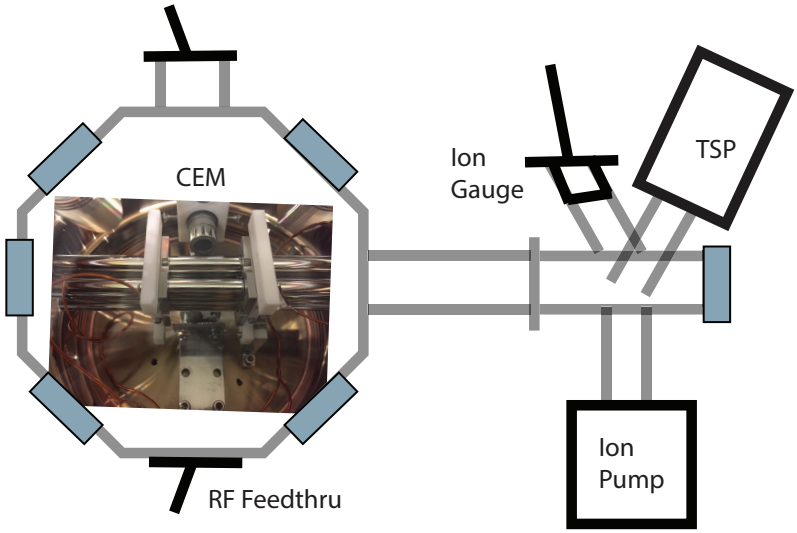

Figure 5.1. Vacuum chamber housing the molecular ion trap. The ion trap is housed in an 8 inch spherical octagon from Kimball Physics along with a channel electron multiplier (Channeltron CEM) for ion detection. Attached to the main chamber along the axis of the ion trap is the ion gauge (Granville Phillips Stabil-Ion 370), ion pump (Varian Starcell 20 l/s), and the titanium sublimation pump (Gamma Vacuum)

5.1. Ablation and Photo-Ionization Loading

Whenever possible, ablation of a material followed by direct photo-ionization is the preferred method for loading ions into the trap for our experiments. If a solid material contains the elements that one is looking to load into the trap, ablation will typically generate the neutral form of the species of interest in some non-zero quantity. This is because ablation is a highly energetic, non-linear process that produces a messy array of products. Unlike with heated vaporization techniques, the background pressure will only increase for acute bursts during the ablation process. With vapor techniques one can expect more issues related to coatings forming on the trapping electrodes and the vacuum viewports. Thin dielectric coatings on the electrodes enable patch potentials that can contribute to RF heating of the ions and changing trapping conditions. On the viewports

a coating will reduce transparency for fluorescence detection and contribute to background scattering of probe light. Furthermore, ablation requires no vacuum feedthrus and can be applied to refractory materials with prohibitively high melting points.

Though it is possible to load exclusively with ablation there are a number of issues that the addition of photo-ionization solves. Fundamentally, the loading of ions by ablation is faced with a contradiction. If the ions have enough energy to enter the trapping volume, then they have enough energy to escape the trapping volume. In practice, if enough ions and neutrals pass through the trapping volume, collisions can cause some ions to randomly lose enough energy to remain in the trapping volume. However this is very inefficient and for non elemental samples, it may potentially load a large distribution of species[1]. Even in the case of elemental samples (e.g. Barium), the ablation power required to produce a sufficient number ions is more likely to produce unwanted effects such as patch potentials. The quantity of ions produced in the plume is also much less stable as the plume production is sensitive to the surface quality which can rapidly change at high powers. If combined with photo-ionization, particularly a species selective photo-ionization, then a pure sample of the desired species can be accumulated into the trap with minimal side effects and relatively stable production. Finally, the efficiency of loading is greatly enhanced because photo-ionized species do not face the energy contradiction described previously. This is because the neutral particles do not respond to the trapping potential until they are photo-ionized. Therefore, if they are photo-ionized in the deepest part of the trapping potential they will remain in the trapping region as long as they started with less kinetic energy than required to escape the trap. Note that even after

[1]E.g. very little SiO^+ is generated in the ablation of SiO [**68**] as confirmed with in house measurements. See chapter 6 for more detailed discussion of associated challenges.

the high intensity laser ablation pulse the neutrals are only averaging speeds between 0.1 to 1 km/s or, equivalently, energies between ones of meV to tens of meV. Compared to typical trapping depths on the order of several eV, the ions are born well below escape energies.

A schematic of the full ablation set up is shown in Fig. 5.2. The ablation laser is a Continuum Mini-Lite low power pulsed Nd:YAG laser that outputs 3-5 ns pulses at a 10 Hz repetition rate. The second harmonic of the YAG (532 nm) output is split into two paths by a polarizing beam splitter. The two beam paths are then aligned through an $f = 150$ mm focusing lens and onto their respective targets, typically barium and silicon monoxide. The total pulse energy allowed through each arm of the beam path is controlled by a $\lambda/2$ waveplate attached to a servo motor (TowerPro SG92R Micro Servo) to control the angle. Another servo motor is used to position a beam block for blocking one or both beams. An external trigger of the YAG Q-switch is used to control the timing and the number of pulses fired. For some experiments, where long term stability of the ablation product was important, an additional piece of glass was added to the beam path. This glass was tilted at approximately a 30° angle for parallel shifting of the beam. During ablation, the glass was rotated by DC motor, walking the beam in a circle and refreshing the surface.

Barium is a much softer material than SiO and typically requires 20 to 80 μJ per ablation pulse for efficient loading compared to 0.1-1.0 mJ per pulse for SiO. Under these conditions, the ion pressure gauge in the vacuum chamber is often not capable of detecting the minimal change of 10^{-12} Torr even under continuous (pulsed) ablation. "Too much" ablation does not occur until a change in pressure beyond a few parts at 10^{-11} Torr occurs.

As barium oxidizes easily, even a short exposure to atmosphere will create a white BaO layer on the outside of a sample. In a scenario where we are ablating for the first time after breaking vacuum we find that we need to ablate a little more intensely (i.e. energies closer to 100 μJ per pulse). Over time, the ablation laser will 'dig' a hole through the oxide layer leaving behind a dark spot of pure Ba.

The photo-ionization source is an Nd:YAG pumped OPO (Ekspla NT342/1/UVE OPO, 10 Hz rep rate, 4.2 ns pulse width, 4 cm^{-1} linewidth). As a photo-ionization source, the broad linewidth of the Ekspla OPO prevents it from being capable of isotope selection as the isotope shifts are sub wavenumber. This is not critical as the natural abundance of our preferred isotope (^{138}Ba) is $\sim$70%. Photo-ionization can be performed in a resonant way via 1+1 REMPI, however non-resonant direct ionization of ground state and metastable Ba was found to be plenty efficient in practice. This is useful as it means in practice that any wavelength under 303 nm (wavelength required to ionize from the first excited state of barium) is capable of efficient photo-ionization loading. Thus a number of different pulsed lasers that are specifically purposed for particular transitions in molecules can be re-purposed with minimal effort for Ba^+ loading. The photo-ionization pulse in our setup is typically fired 90 μs after the ablation pulse and the timing was not found to be sensitive to the loading efficiency over a range of $\sim$50 μs. As the target sample is situated approximately 1 cm below the trap center, these two facts provide us an estimate of the neutral velocities in the plume.

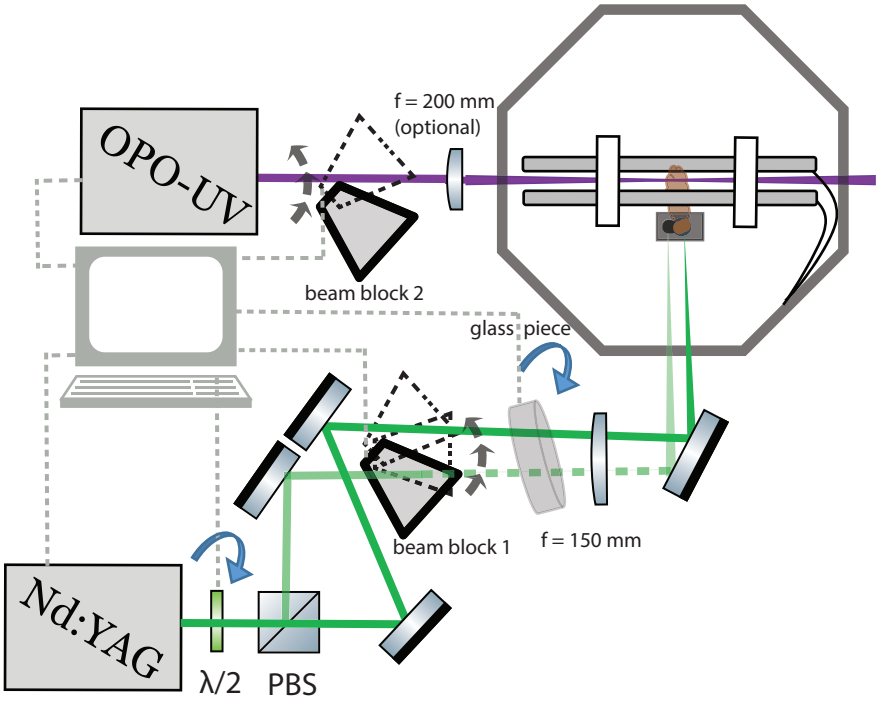

Figure 5.2. A schematic diagram of the ablation loading with photo-ionization setup. Beam block 1 controls which of the two ablation beams is allowed to reach the two ablation targets. A computer controlled $\lambda/2$ waveplate is rotated to control the relative power in each arm of the beam separated by a polarizing beam splitter (PBS). An optional glass piece in the path of the ablation beams is rotated to walk the beams in a small circle and refresh the ablation sample surfaces. A second beam block (2) is used to control the photo-ionization pulse.

5.2. Ba^+ Cooling and Controlling

The barium ion is member of the alkaline earth metal group (group 2 on the periodic table) and as a consequence carries only a single valence electron. This implies it has a relatively simple electronic structure. Importantly this structure limits the number of accessible states to which the atom can spontaneously decay. This simple structure is in stark contrast to molecules, which as I discussed in Chapter 2 can have many, many more states to which the excited state can decay. Like several other members of group 2 ions

(e.g. Ca^+, Sr^+, and Ra^+), Ba^+ contains a long-lived, low-lying D state that can be used in useful and interesting ways as a diagnostic and detection tool. Additionally, the lasers required for controlling Ba^+ are conveniently in the visible portion of the spectrum. A simplified level structure of Ba^+ can be seen in Fig. 5.3.

The ground state of Ba^+ is 6s $^2S_{1/2}$ and with the 6p $^2P_{1/2}$ and the 5d $^2D_{3/2}$ state it forms a closed cycling system. That is, a single pump (493 nm) and repump (650 nm) laser is capable of indefinitely sustaining a continuous cycle of excitation and spontaneous emission resulting in a rapid rate of scattered photons ($> 10^7$ s^{-1}) capable of removing motional energy via Doppler cooling. Coherent population trapping[2] is avoided by applying a magnetic field perpendicular to the z-axis of the trap with a field strength of $\sim$10 gauss. The three states described in the closed cycling system are often referred to as a Λ-type system in the literature. Because decay from D to S is dipole forbidden, this channel can be ignored in the three-level system and thus the inspiration for labeling it a Λ system. Decay into the 5d $^2D_{5/2}$ state from 6p $^2P_{1/2}$ is also dipole forbidden and is thus isolated from the Λ system.

Though it is isolated from the Λ system, the 5d $^2D_{5/2}$ can be intentionally populated with an additional laser. Because the lifetime of the $D_{5/2}$ state is 31.2(0.9) s [**5**], it can be used as a "shelving" state. That is, it can be used to protect the coherence of a process by removing it from the cycling process of the Λ system. This means the Ba^+ in this state is "dark" to the Doppler cooling lasers and will therefore no longer fluoresce. For our purposes, the experiment is not yet making use of coherent control of Ba^+ as would be required in a possible future quantum logic spectroscopy (QLS) experiment. Regardless,

[2]See e.g. Chapter 4 of Yen-Wei Lin's thesis [**93**].

this shelving state is useful for a number of diagnostic and calibration purposes. Any state that is excited outside of the Λ system will have some non-negligible fraction of its population undergo one or more decays that eventually take it to the meta-stable $D_{5/2}$ state. Given the distribution of states, Ba^+ has a number of transitions beginning in the Λ system states that span UV through the visible range of the spectrum. As the level structure of Ba^+ has been well-studied these transitions can be used to calibrate a broad range of wavelengths. Similarly, it can be used to characterize the linewidths of the various pulsed lasers and is useful as a way to ensure proper alignment of the lasers. A guaranteed alignment confirmation can save significant amounts of time potentially wasted searching for previously unobserved transitions in vane. This is particularly true in the case of our experiments where we can have more than seven separate beams that need to be simultaneously aligned.

Alternatively to populating dark states, sufficient intensity in the pulsed laser beam can be used to perform 1+1 REMPI on Ba^+ to generate Ba^{2+}. Because the IP of Ba^+ is 80686.3 cm^{-1}, many of the channels shown in Fig. 5.3 are sufficient. Generating doubly ionized barium is useful for mass calibration in spectrometry techniques such as q-scan or secular frequency excitation. Additionally, when optimizing bicrystals, it can be useful to start with cold ions already in the trap as DC compensation voltages are applied to center the dark core in the coulomb crystal.

Another advantage of the Λ system is deterministic pumping. Namely, by temporarily turning off exactly one of the lasers (either the pump or the repump), the electron can be pumped into either the S or the D state. In this way we could perform an absolute measurement of the quantum detection efficiency of the imaging system (see schematic

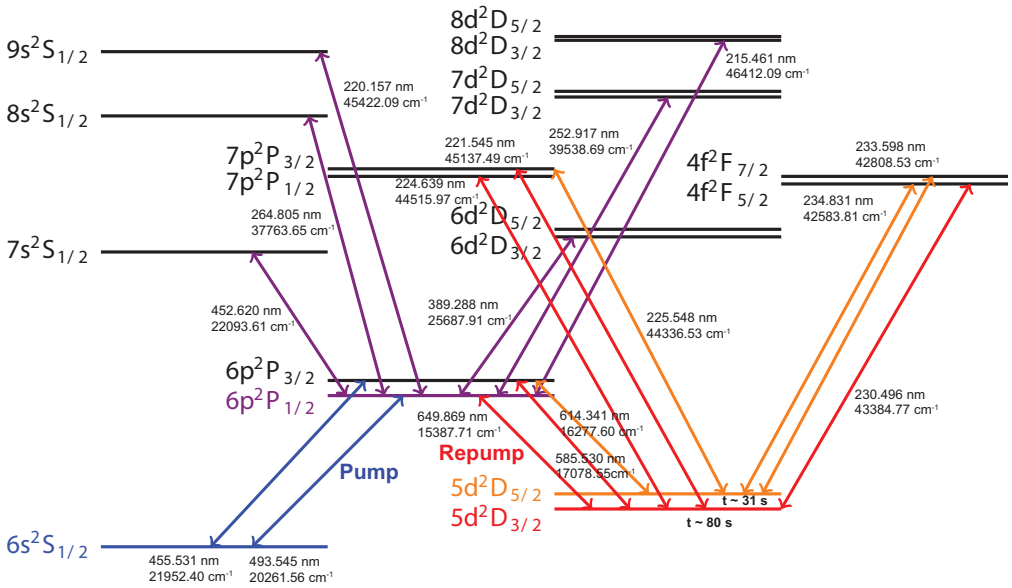

Figure 5.3. Simplified energy level diagram of Ba^+. All of the dipole allowed transitions from the 6S, $6P_{1/2}$, and 5D states with transition wavelengths longer than 210 nm are listed.

in Figure 5.4). This is done by pumping a countable string of bright Ba^+ ions in the $D_{3/2}$ state. This can be guaranteed by applying the 493 nm pumping beam for several microseconds. This allows for cycling between the $S_{1/2}$ and $P_{1/2}$ states until a spontaneous emission results in decay into the $D_{3/2}$ state. This process is virtually guaranteed after tens of spontaneous emission events. A single 493 nm photon per ion can then be deterministically radiated by pumping the $D_{3/2}$ to $P_{1/2}$ transition. With the addition of a bandpass filter blocking everything but light around 493 nm, the signal can be detected effectively background free. Deterministic pumping can also be used to avoid or purposefully populate particular states in the presence of another laser. For example, a pulsed laser scanning the dissociation spectrum of a co-trapped species may encounter a line in Ba^+ that either doubly ionizes Ba^+ or causes the ion crystal to go dark. In this case, the unwanted effect can be avoided by momentarily pumping Ba^+ into a state not involved

in the transition. Conversely, when searching for lines to calibrate laser wavelengths, the state involved in the desired transition can be intentionally populated to enhance the signal. Access to more lines is also possible by populating the meta-stable $D_{5/2}$ state and driving transitions out of the $D_{5/2}$ state that bring the population back into the cycling Λ system after relaxation.

5.3. Modular Imaging and Detection System

The imaging system is largely as described in Chapter 6 of YWL's thesis [**93**] however some parts of the apparatus have been used in a modular way to meet the needs of a given experiment. The most up to date schematic diagram can be seen in Fig. 5.4. A common issue with a such a large imaging system with so many extensions and heavy parts is maintaining stability while keeping micron level control of the image. This issue is solved by separating the first light collecting lens closest to the trap from the remaining portion of the imaging apparatus. This way minor adjustments on the focus and position of the image are accomplished by independently moving the first lens using an X-Y-Z translation stage. After the ions are found to be imaged on the camera, any possible minor negative effects on the image due to optical axis offsets between the lenses can be simply resolved by shifting the imaging system optical axis to match the first lens.

The three main fluorescence detection hardware used are the PMT (Hammamatsu H8259-01), the EMCCD (Andor Luca S), and the ICCD (Andor iStar). The EMCCD is typically used for imaging the Ba^+ crystal. The PMT is used for the laser cooled fluorscence mass spectrometry (LCFMS) measurements described in section 5.6.2. The ICCD is capable of nanosecond gating and is used for low-signal sensitive imaging of

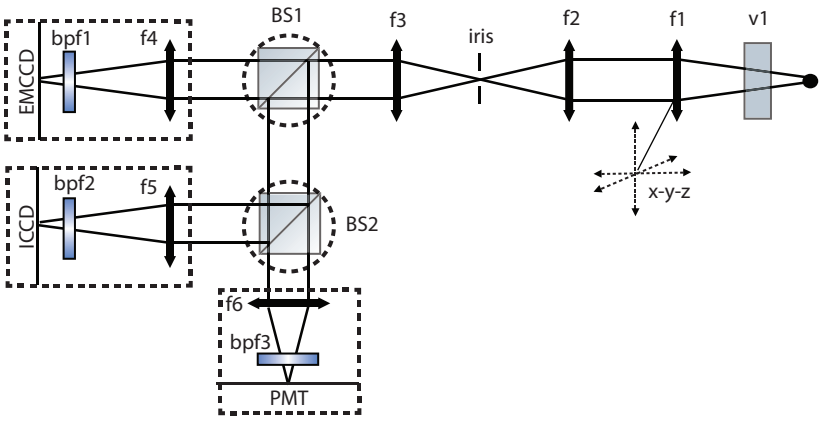

Figure 5.4. Schematic diagram of the imaging system for the molecular ion trap. Modular pieces are indicated with dashed lines. Optical cage system avoids the need for realignment of the entire imaging setup whenever one of the modular pieces is changed. (v1) Vacuum viewport, (f1) f=100 mm achromatic doublet attached to X-Y-Z translation stage, (f2) f=200 mm achromatic doublet, (f3) f=50 mm achromatic doublet, (f4,5,6) f = 125 mm achromatic doublet, (bpf1,2,3) band pass filters used for filtering all light not emitted by the transition of interest (e.g. Ba^+ transition at 493 nm), (BS1,2) option of dichroic, 50-50, or complete removal of beam splitters.

SiO^+. The ICCD was purchased with the intent of completing the CW fluorescence scattering experiments of SiO^+. These experiments have not been completed yet, however the ICCD has been used for experiments in the LIF trap (see section 4.2). The flexibility of the modular design allows for changing of experimental detection methods and shared detection equipment with minimal down time.

5.4. Lasers

The lasers involved in the molecular ion trapping experiments can broadly be placed into 3 major categories: 10 Hz pulsed lasers, broadband femtosecond pulsed lasers, and CW lasers. An example schematic of a typical laser layout is shown in Fig. 5.5.

5.4.1. 10 Hz Pulsed Lasers

Continuum Minilite II This laser is an Nd:YAG that outputs 3-5 ns pulses at the second harmonic (532 nm). I modified it to include an optional exit port out of the side for the fundamental (1064 nm). Currently, only the 532 nm output is used for ablation. This wavelength is not necessary and is chosen out of convenience for visibility concerns.

Ekspla NT342/1/UVE OPO The Ekspla has a 4.2 ns pulse width and a 4 cm^{-1} linewidth. It is moderately powered compared to our other pulsed OPO (see Premiscan below). This laser is used primarily for photo-ionization and dissociation and its range extends the furthest into the UV of any of our lasers (210 nm to 2300 nm tunability). The OPO is pumped by the third harmonic of an internal Nd:YAG laser.

Spectra-Physics Quanta-Ray Pro 290 This is the most powerful laser in our lab and is capable of producing more than 2 J per pulse. It is an Nd:YAG laser. Currently, both the second and third harmonics (532 nm and 355 nm respectively) are used for pumping the Lambda Physik dye laser and the Premiscan OPO (see both below).

PremiScan + UVscan OPO This OPO is pumped by ∼480 mJ of 355 nm from the Pro 290. It is capable of producing wavelengths from 257 nm to 2700 nm. The OPO is used primarily for dissociation as it is capable of generating the most energy per pulse. Though it hasn't been measured, the linewidth is expected to be similar to the Ekspla.

Lambda Physik Scanmate This laser has slowly gone the way of the ship of Theseus. Nearly all of the electronics for controlling the dye grating have been replaced by homebuilt pieces. The grating position is controlled through Labview via a DC motor controller (Phidgets). The doubling stage has also been moved outside the laser body and modified to be controlled by another DC motor. Depending on the desired wavelength range, the

dye laser is either pumped by the second or third harmonic of the YAG. The dye laser is necessary for applications where rotational resolution is required and was observed to have a linewidths of 0.25 cm^{-1}.

5.4.2. Broadband Femtosecond Pulsed Lasers

Spectra-Physics MaiTai HP

This laser is capable of 2.8 W of power at 769 nm. It is a Ti:Sapphire frequency comb with a rep rate of 80 MHz. Its output is passed through an AOM for fast switching and is then doubled before being sent to the spectral pulse-shaping setup. The pulse-shaping setup is described in section 5.7 and is used for controlling SiO^+.

Spectra-Physics Tsunami

This laser is capable of ∼1.8 W output around 800 nm. It is not currently being used but will be available as either a vibrational repump laser or as an extension to the $B - X(0, 0)$ control for pulse shaping. In a duplicate pulse-shaping set up the Tsunami can be used to investigate steady state control of the SiO^+ rotational state near rotational energies approaching dissociation.

5.4.3. CW Lasers

493 nm This laser is a frequency doubled Toptica ECDL amplified by a tapered amplifier (BoosTA, Toptica). This beam is fiber coupled onto the optics table housing the experimental setup and passes through a double pass AOM for frequency control and a single pass AOM for fast switching of the beam. It is used for pumping the Ba^+ 6s $^2S_{1/2} \rightarrow$ 6p $^2P_{1/2}$ transition.

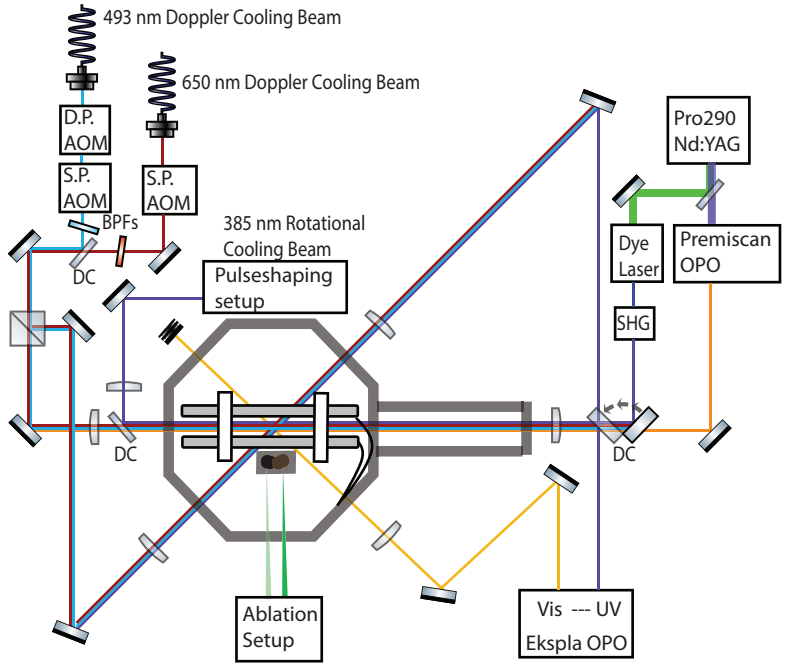

Figure 5.5. Schematic of the lasers in a typical experimental set up. The Doppler cooling lasers, the rotational cooling laser, and the ablation laser are fixed wavelengths, while the remaining pulsed lasers (OPOs and dye laser) frequently change wavelength from UV to VIS wavelengths and serve multiple purposes (e.g. photoionization and dissociation). To accommodate the flexibility required for the dynamic lasers, multiple flip mirrors and dichroic mirrors are installed. The counter-propagating Doppler beams are useful for easy alignment of the multipurpose lasers. Bandpass filters on the fixed wavelengths prevent damage to components downstream of the counter-propagating pulsed lasers along the path of the CW lasers. A single pass AOM is used for fast switching and controlled timing of the Doppler cooling lasers. The 650 nm wavelength is fixed such that it is slightly blue-detuned of the Ba^+ $5D_{3/2}$-$6P_{1/2}$ transition. Fine tuning of the 493 nm Doppler cooling beam frequency is performed using the double pass AOM set up. Not pictured are several motor controlled beam blocks used for selectively blocking each of the pulsed laser outputs.

650 nm This laser is a Toptica ECDL that is amplified using a homebuilt injection locked ECDL. This beam is fiber coupled onto the optics table and passes through a single

pass AOM for fast switching of the beam. It is used for repumping on the 5d $^2D_{3/2} \rightarrow$ 6p $^2P_{1/2}$ transition.

385 nm This frequency is generated by a Toptica DL Pro tuned to 770 nm, amplified by a tapered amplifier (Toptica BoosTA), and doubled in a homebuilt SHG bow-tie cavity. The cavity is locked using the PDH method. This laser is not currently in use however it is being prepared for fluorescence and imaging of SiO^+ by driving select lines of the $B - X(0, 0)$ transition.

5.5. Experimental Timing Controls

Many of the experiments described in this thesis require nanosecond timing of events. The bulk of the timing is done using two 5 V, 8-Channel counter/timer devices (National Instruments PCI-6602) controlled through Labview. As most of the experiments are structured around 10 Hz pulsed lasers, the timing of the experimental sequence is controlled using a 10 Hz 'master clock'. The firing of the flash lamps and Q-switches of the three 10 Hz pulsed lasers, and the single pass AOMs of the Doppler and femtosecond molecular control lasers are all run on a repeated 10 Hz timing sequence with delays in reference to the 10 Hz 'master clock'.

The pulsed lasers need to continuously operate to properly perform, however the number of pulses that are needed to fire into the trap are typically infrequent and for a specified number of pulses. This was accomplished using motorized beam blocks that would open for a specified duration. To ensure precise control of the number of pulses that reach the vacuum chamber, the Q-switch would be turned off for several pulses before and after the opening and closing of the beam blocks. Similar to the selective gating of

the Q-switch, timing of the femtosecond laser sometimes requires specified exposure times that are not repeated at 10 Hz. This was accomplished using external logic gates (AND and OR) and extra timing channels that were programmed to not be retriggerable to the 'master clock'.

5.6. Mass Spectrometry and Detection Techniques

In our trap we perform mass spectrometry via *in situ* methods using Ba^+ fluorescence or via ejection. A common method for high resolution mass spec using ejection is the time of flight method [**138, 75, 141**]. This apparatus does not require such high resolution as the most common use will be for distinguishing Si^+ (28 u) from SiO^+ (44 u). Our primary ejection method is using the 'q-scan' method[3]. This method achieves a mass resolving power of $m/\Delta m = 5 - 10$ with the aid of sympathetic cooling (see below). A downside of any technique relying on ejection is that it requires reloading of the sample after each ejection. This can significantly reduce the duty cycle of an experiment as it typically requires > 30 s to reload a sample. Especially for scenarios involving little to no expected signal (e.g. off resonance in a dissociation spectrum scan), *in situ* methods are preferred. The experimental techniques described in the remaining sections of this chapter are repeatedly used in the trapped SiO^+ experiments described in chapter 7.

5.6.1. Coloading and Sympathetic Cooling

Species coloaded into an ion trap with a Doppler cooled (bright) species will have their external motional degrees of freedom sympathetically cooled via the Coulomb interaction [**20, 118**]. The technique of sympathetic cooling is especially useful for experimental

[3]This is described in detail in Chapter 7 of Yen Wei Lin's thesis [**93**].

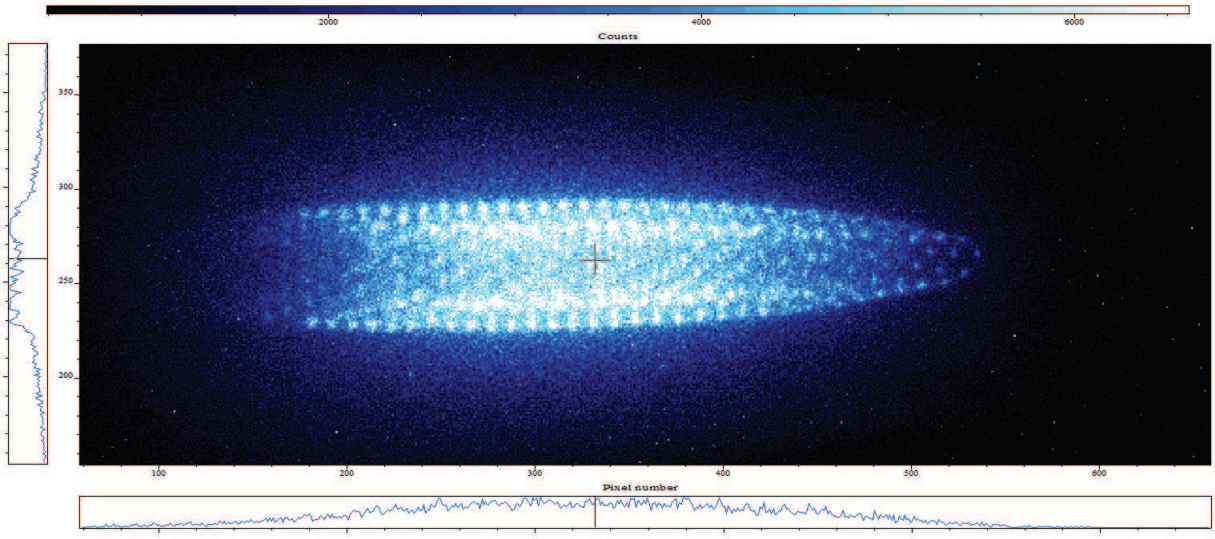

Figure 5.6. CCD image (false color) of a Ba^+, SiO^+ Coulomb bicrystal. Left-right asymmetry is a consequence of dark Ba^+ isotopes being displaced by bright $^{138}Ba^+$ subject to radiation pressure from the doppler cooling beams directed along the trap axis. In the center of the image, the crystal is less bright due to displacement of bright $^{138}Ba^+$ by the more tightly confined, dark SiO^+.

studies of ionic species not amenable to direct Doppler cooling. Colder temperatures imply increased density and reduced second order Doppler shifts. It also generally means improved mass resolution for techniques such as q-scan and time of flight (TOF) techniques. The coupled motion between the bright and dark species also allows for indirect detection techniques that can be done *in situ* such as quantum logic spectroscopy (QLS) [**132**] or, as I discuss in section 5.6.2, used for laser-cooled fluorescence mass spectrometry [**6, 7, 127**].

Depending on the total number of ions in the trap and their bright/dark composition, the stability of a crystalized sample in the trap can be tenuous. The heating rate has a nonlinear relationship with temperature and density. In general, the heating rate will increase with both temperature and density. For a crystal, the density remains constant

with respect to temperature. As temperature increases, the crystal will eventually melt and the density will decrease with temperature such that the heating rate declines [**27**]. However, this implies that the maximum heating rate occurs after melting of the crystal. Therefore it is possible for, and I have frequently observed, conditions such that a stable Coulomb crystal that melts for technical reasons (e.g. cooling lasers momentarily falling out of lock, or shaking the crystal with external fields too hard) cannot be recovered once the technical sources have been corrected.

Coloading can sometimes be difficult to observe when making first attempts. For example, lighter masses will be more tightly confined than heavier masses such as $^{138}Ba^{+}$. Thus patch potentials that are not well compensated can leave the location of the potential well minima for vastly different masses further apart than the radius of a typical coulomb crystal. This can be especially difficult in the vertical direction as the camera angle makes it difficult to determine if the ions are well compensated along the vertical axis. As ablation and photoionization loading represent additional possible failure points to coloading, it can be useful to use doubly ionized barium (see section 5.2) to act as an independent check.

5.6.2. Laser-Cooled Fluorescence Mass Spectrometry

Many of the measurements we performed relied on the fluorescence modulation of Ba^{+} via the coupled motion of dark species excited by a weak AC voltage at their secular frequency. The technique, generally described as sympathetically Laser-Cooled Mass Spectrometry (LCFMS) [**6, 7**], relies on chirping the excitation frequency with simultaneous observation of the fluorescence rate to identify the secular frequencies of the constituent masses in the

trap. This method can be thought of as 'shaking' the ions at their resonant frequencies. The experimental sequence and schematic can be seen in Fig. 5.7.

For a more thorough background on theory behind ion trapping and techniques there are numerous review articles and books available in the literature[4]. The important relation here is that the secular frequency is given by

$$\omega_n = (2n + \beta)\frac{\Omega_{RF}}{2}, \quad 0 \leq \beta \leq 1, \quad n = 0, \pm 1, \pm 2, \ldots \tag{5.1}$$

where β is written in terms of the Mathieu a, q parameters. We typically operate at lower frequencies and thus are only interested in the $n = 0$ modes. Also, for typical trapping conditions the DC components in the radial direction are small compared to the AC components, which results in $\beta \approx q/\sqrt{2}$ where $q \propto \frac{V_{RF}}{(m/z)r_0^2\Omega_{RF}^2}$. Thus we find that the secular frequency scales inversely with the charge to mass ratio. The most straight forward calibration is to use both Ba^+ and Ba^{2+} (see section 5.2). The technique, following the procedure in Fig. 5.7 has a mass resolving power of $\frac{m}{\Delta m} \sim 30$ which sets the scale for the necessary precision and accuracy of the calibration.

5.6.2.1. The Frequency Chirp Method. In a typical measurement we load of order 1000 Ba^+ ions into the trap. For most experiments, we then co-load SiO^+ into the trap using ablation and REMPI (see chapter 6) such that the composition is approximately 10 to 30% dark to bright ions. The amount and ratio suitable for the experiment can change day to day depending on the presence of patch potentials in the chamber or if the Doppler cooling lasers are having difficulty remaining stable in either frequency

[4]See e.g. *Ion Traps* by Ghosh that covers ion traps with an emphasis on AMO physics [**50**] or the review article by Douglas et al on mass spectrometry in linear ion traps [**38**].

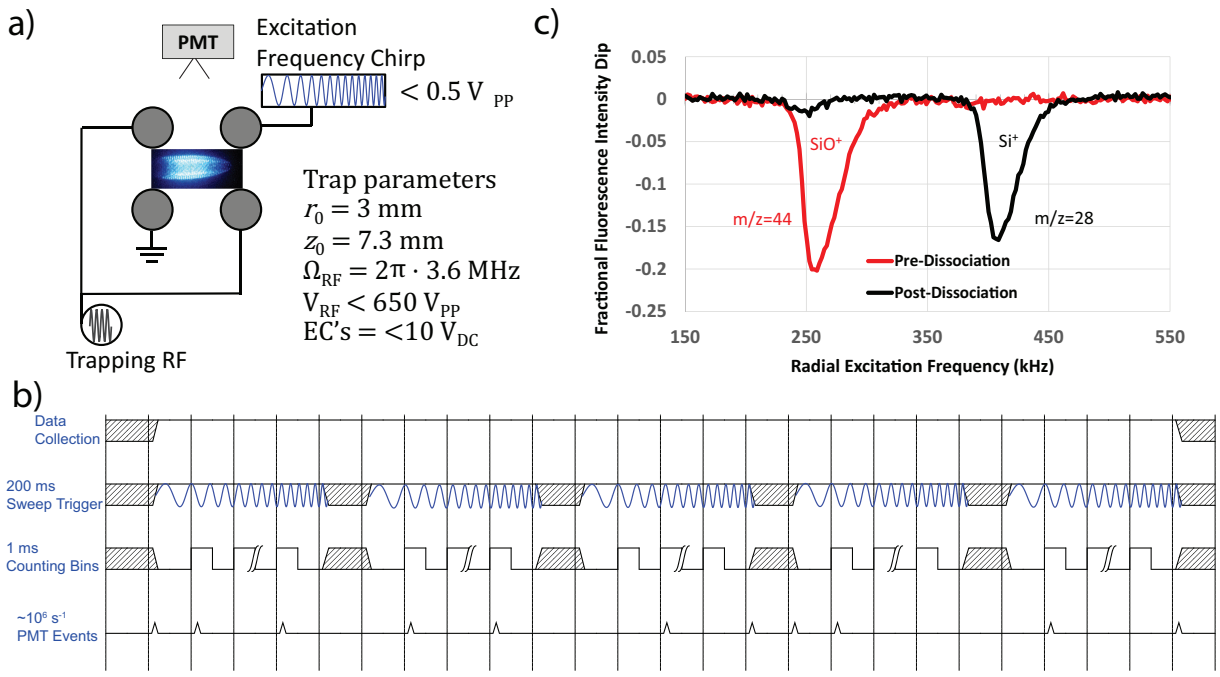

Figure 5.7. **a)** Schematic of the LCFMS frequency chirp method. Two diagonal rods are connected to the RF trapping voltage and with the addition of a third rod are capable of having an independent DC voltage applied to compensate for patch potentials. The remaining rod is attached to the excitation frequency source which periodically undergoes a linear chirp. Typical parameters are listed. **b)** Experimental timing sequence. The excitation frequency chirp is triggered off of the master clock at a repetition rate equal to 5 Hz (200 ms). A counter binned into 1 ms intervals counts PMT events for each frequency sweep such that each time stamp corresponds to a given frequency with resolution determined by the bin size and the frequency range. Typically 5 ms at the end of the cycle are allotted for resetting the frequency sweep of the function generator. **c)** Typical signal observed following the timing sequence described in b). Signals are the average of 10 sets or 50 chirps. SNR is sufficient for observing dynamics on a 100 ms time scale.

or intensity. In practice, the amount of SiO^+ loaded into the trap is determined by monitoring the fluorescence modulation spectrum. The signal is obtained by red-detuning the Doppler cooling laser by 6-10 MHz from resonance. As the secular excitation frequency is chirped across the radial resonance of a dark species (e.g. SiO^+, m/z = 44 u), the

amplitude of motion increases. This motion couples with the Ba^+ motion and increases the Ba^+ temperature. At higher temperatures, the Ba^+ spend less time in resonance with the Doppler cooling lasers and thus the fluorescence rate decreases. The relationship can be reversed if the Doppler cooling laser is red-detuned even further. In this case higher temperatures imply that the Ba^+ will spend *more* time on resonance and thus an increase in fluorescence would be observed when the secular motion is excited. In the weak coupling regime the excitation voltage amplitude and the number of dark ions present are nominally proportional to the maximum contrast in the fluorescence. If either the voltage or the number of dark ions is too large, the ions will be heated into the gas phase and some can potentially be ejected from the trap. In fact even without secular excitation, loading 'too many' dark ions is sufficient to put the trapped ions into the gas phase. The excitation voltage amplitude is typically less than 1 V peak to peak and can be adjusted to optimize contrast without heating the ions into the gas phase or severely limiting the number of dark ions that can be interrogated.

The extent to which non-linear, strong coupling can be avoided is currently more art than science as the number of variables is large and diagnostic tools are not always clarifying. Depending on the application, the DC compensation voltages and the quantity and ratio of bright to dark ions can be adjusted to tune to an acceptable coupling strength. Once a set of parameters has been demonstrated as appropriate, it is relatively straight forward to reproduce them using fluorescence signal size and fluorescence modulation depth (typically 10-25% contrast). Fig. 5.7 c) represents a typical mass spectrum before and after SiO^+ dissociation. The before and after signal of the SiO^+ peak can be used to infer the fraction of SiO^+ dissociated.

Loading and reloading samples in the ion trap can be a time consuming process. This is especially the case if both the laser cooled species and the dark species need to be reloaded. Since this technique is *in-situ* it is useful for quickly scanning and surveying new dissociation spectra. With the frequency chirping technique, the sample can remain in the trap over the gaps between resonances in the dissociation spectrum with the sample only needing refreshed once a significant fraction has been dissociated (or reacted with background hydrogen gas as is the case with SiO^+). It was found that after a sample had been fully dissociated, that the unwanted dark species could be selectively ejected by blue detuning the Doppler cooling laser and continuously chirping the excitation frequency across the resonances of the unwanted masses. In this way the total number of Ba^+ ions could be held constant over an extended period of data taking. Additionally, by coloading a new SiO^+ sample with the fixed Ba^+ sample until the fluorescent modulation depth matches a previous consistent value, a number of possible systematic effects are avoided.

5.6.2.2. The Single Frequency Method. In addition to the timing and data collection methods used in Fig. 5.7 b), another technique referred to as the 'single frequency' method has been employed to monitor dynamics faster than the 1 second averaging time of the 'frequency chirp' method described above as well as maximize data collection for a single experiment from each individual sample. This method relies on using the 'burst' mode of a function generator to alternate between periods of a single secular excitation frequency in resonance with the mass of interest[5] and no secular excitation. This way

[5]In practice, the single frequency is actually multiple frequencies applied simultaneously that cover multiple resonance linewidths around the resonance of interest. This is done to limit systematic effects due to a drifting secular frequency.

the fluorescence contrast between excited and non-excited periods can be compared to monitor the depletion as a function of time. Any changes in the quantity of species at a particular mass will appear as a proportional change in the fluorescence modulation depth. Under these experiments the excitation frequency burst is applied at 10 Hz with a duty cycle between 40-60%. When recording a dissociation spectrum, this method can be useful for characterizing states with small populations and interrogating time scales of population redistribution.

The single frequency method is most useful in two separate regimes: (1) the rate of dissociation is much smaller than the rate at which the distribution reaches steady state and (2) the dissociation rate is much faster than the redistribution rate. In the first regime information about the population can be extracted. This regime occurs when the probability of dissociating a populated state per laser pulse multiplied by the laser rep rate is much smaller than rate for reaching steady state during optical pumping. The slowest redistribution process from optical pumping is typically parity exchange. Because the laser operates at 10 Hz, if the parity exchange occurs near or slower than 10 Hz, then the probability for dissociation needs to be reduced by adjusting the laser power or rate to be firmly in this regime. In the second regime the redistribution is rate limiting and therefore the rate of dissociation will be equal to this rate.

Formally, when operating in the first regime, the measured decay rate of the single-frequency method can be related to the expected signal with the expression

$$S = (1 - Pr_{diss} n_{J''})^N \tag{5.2}$$

where S is the signal, Pr_{diss} is the probability of dissociating per laser pulse, $n_{J''}$ is the fraction of population in the state of interest, and N is the number of dissociating laser pulses fired. Therefore the observed rate (per pulse) of decay, R, in the signal will be

$$R = -\log\left(1 - Pr_{diss} n_{J''}\right). \tag{5.3}$$

The probability for dissociation can be modeled similarly to how the rates of rotational transfer rates in in section 2.4.1 and appendix A.1 were derived. Again, we treat the process as a three level system, only instead of the excited state having a decay path to a separate rotational state, the decay path is to the dissociated state. If the pumping rate $\rho(\omega_{J',J''})B_{J'',J'}$ is significantly slower than the excited state dissociation rate (Γ_{diss}), then the probability can be written as

$$Pr_{diss} \approx 1 - e^{-\rho(\omega_{J',J''})B_{J'',J'}T} \tag{5.4}$$

or, alternatively, in the saturated case with the pumping rate significantly faster

$$Pr_{diss} \approx 1 - e^{-\frac{g_{J'}}{g_{J'}+g_{J''}}\Gamma_{diss}T}. \tag{5.5}$$

where T is the laser pulse duration.

For characterizing populations, we prefer to operate in the regime such that the dissociation probability approaches unity. In this regime we can simply relate the population in the target state to the signal rate R via

$$n_{J''} \approx 1 - e^{-R}. \tag{5.6}$$

If, however, the population is near unity or the redistribution rate is too slow then we need to reduce the dissociation probability and instead we must work in the low saturation, low dissociation probability regime. In this scenario we need to rewrite the pumping rate in terms of intensity multiplied by line strength. This way, the populations can be appropriately compared with each other. Doing so we set $\rho(\omega)B_{J'',J'} = \frac{s_0}{1+4(\Delta/\Gamma)^2}\frac{g_{J'}}{g_{J''}}\Gamma^{C,X}_{J',J''}$ where s_0 is a term proportional to the laser intensity, Δ is the detuning from resonance, Γ is the resultant linewidth of the transition due to all effects[6], g_J is the degeneracy, and $\Gamma^{C,X}_{J',J''}$ is the partial Einstein $\mathcal{A}$ coefficient of the transition.

In this limit we can rewrite the dissociation probability per pulse as

$$Pr_{diss} \approx \frac{s_0}{1+4(\Delta/\Gamma)^2}\frac{g_{J'}}{g_{J''}}\Gamma^{C,X}_{J',J''}T \tag{5.7}$$

and therefore we have the signal rate is approximately given by

$$\begin{aligned} R &\approx -\log\left(1 - \frac{s_0}{1+4(\Delta/\Gamma)^2}\frac{g_{J'}}{g_{J''}}\Gamma^{C,X}_{J',J''}Tn_{J''}\right) \\ &\approx \frac{s_0}{1+4(\Delta/\Gamma)^2}\frac{g_{J'}}{g_{J''}}\Gamma^{C,X}_{J',J''}Tn_{J''}. \end{aligned} \tag{5.8}$$

We note here that in this regime we are therefore able to accurately determine transition linewidths. Additionally, accurate knowledge of populations or line strengths can be used to determine absolute line strengths or absolute populations respectively. As the electronic dipole moment remains approximately constant over a given vibrational manifold, relative populations are also able to be extracted from this regime without knowledge of the absolute line strengths.

[6]The $\frac{1}{1+4(\Delta/\Gamma)^2}$ term could also be generalized to any normalized convolution of the natural linewidth with all other processes. E.g. the laser profile could be Gaussian instead of Lorentzian.

Importantly, the single frequency method provides a much larger dynamic range than the 'frequency chirp' method. Typically, in our set up, we are able to extract rates < 0.01 Hz (i.e. a $1/e$ dissociation rate of 1/1000 pulses^{-1}). This means we can detect fractional populations smaller than 10^{-3} with a single sample despite typical sample sizes of order a few hundred or fewer.

5.7. Spectral Pulse Shaping

Our method for control over the degrees of freedom of diagonal molecules relies on the spectral filtering of a broadband ultrashort pulsed laser to exclude parts of the spectrum that cover transitions we do not want to pump. As discussed in appendix A.2.4, the sharpness of the spectral cutoff is critical for the fidelity of control. The sharpness of the cutoff must be compared to the rovibrational structure of the molecule of interest. For SiO^+ a resolution better than 2 cm^{-1} (60 GHz) is desirable.

Theoretical details and the experimental setup used for pulse shaping largely follows that found in [**94**], though some notable modifications have been introduced as shown in Fig. 5.8. Briefly, a collimated broadband femtosecond laser undergoes angular dispersion by a grating. The angular dispersion is then collimated by a lens that spatially focuses each spectral component such that each frequency component is mapped to a unique spatial location. The tuneable spectral filtering mask seen in Fig. 5.9 is applied at the Fourier plane to remove unwanted frequency components and a back-reflecting mirror reverses the Fourier transform to recreate the beam with only the desired filtered frequency components remaining. The back-reflected beam is directed back at a slight vertical angle

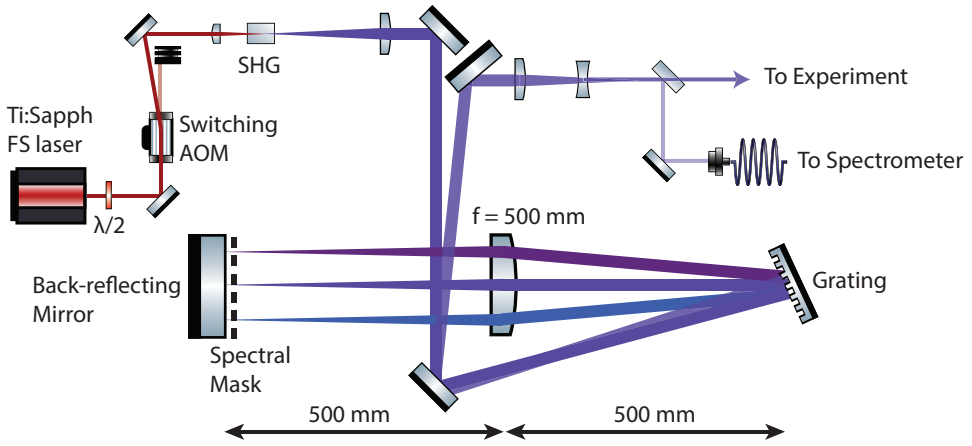

Figure 5.8. Schematic of spectral pulse shaping setup. The design and components largely follow those used in [**94**]. Notable exceptions include the introduction of an AOM for fast on and off switching, replacement of a concave mirror with a lens, and the use of the folded $2f$ configuration. The $2f$ configuration is accomplished using a back-reflecting mirror at the Fourier plane, with the back-reflection at a slight upward angle such that the counter-propagating beam can be separated with a mirror.

such that the counter propagating beam can be separated from the forward propagating beam nearly two meters downstream.

After spectral filtering, the beam is sent to the ion trap for SiO^+ state control. Because of the large bandwidth of the laser, high intensities are needed for fast optical pumping of the SiO^+ transitions. Thus it is preferred that the beam is tightly focused into the trapping volume. This can make alignment difficult as feedback is slow using SiO^+ as an indicator. Fortunately, the Ba^+ 6p $^2P_{1/2} \rightarrow$ 6d $^2D_{3/2}$ transition is at 25687.91 cm^{-1} (389.288 nm) and covered by the tail of the femtosecond laser spectral distribution. The spectral power at the tail of the distribution is sufficient to rapidly pump Ba^+ into a dark state. As discussed in section 5.2, the rate of pumping into the dark state can be used as an alignment tool. Nominal alignment of the beam is achieved by copropagating the beam with the Doppler cooling beams and is typically sufficient to observe Ba^+ going dark

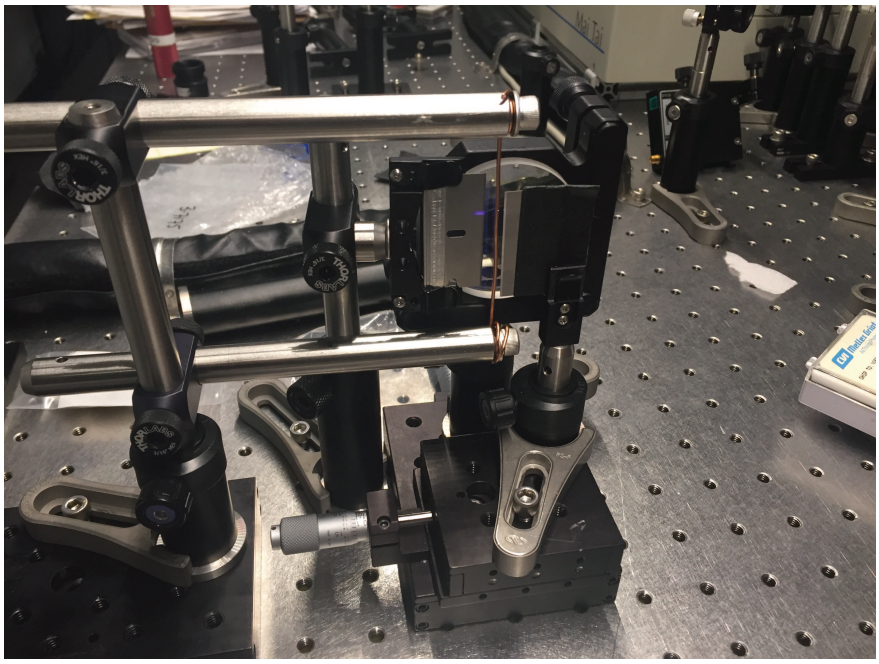

Figure 5.9. Pictured is the tuneable spectral pulse shaping mask at the Fourier plane used for controlling the SiO^+ rovibrational state. The mask consists of two razor blades. The blade on the left is used to suppress light that causes Ba^+ to go dark (see text). The blade on the right is attached to a translation stage and is used for fine positioning of the high frequency cutoff. Positioned between the two blades is a mount with the option for attaching a wire with desired thickness. The wire position is also tuneable using a separate translation stage.

with minimal difficulty. The typical procedure for achieving fine tuning of the alignment consists of adjusting the power in the beam using the AOM RF amplitude so that the dark pumping rate reaches an equilibrium with the decay rate of the 5d $^2D_{5/2}$ where approximately half of the Ba^+ crystal is bright and half is dark in the steady state. The alignment of the beam is then iteratively improved by making small adjustments in walking the beam and observing whether the crystal gets darker or brighter. If the crystal gets darker, the power in the beam is reduced further and the process is repeated until no further improvements are observed. Pumping the Ba^+ into a dark state is of course

not tolerable under experimental conditions and thus a razor blade is use to cut off the low frequency tail of the broadband femtosecond laser spectrum (see Fig. 5.9).

In addition to the AOMs utility as an intensity control knob, it is capable of fast switching of the beam with a rise and fall time of ~ 100 ns. This is used for measurements probing dynamic behavior such as the optical pumping rate or a vibrational lifetime measurement.

5.7.1. Femtosecond Laser Characterization

The femtosecond laser used in the pulse shaping setup does not have a smooth spectral power distribution. Over several pulses the coherence of the laser field increases and a comb-like structure in both the frequency and time domain develops. The structure of the comb teeth is important for details involved in optical pumping of SiO^+ transitions. The laser operates at an 80 MHz rep rate and therefore its spectral comb teeth are separated by 80 MHz. However, the linewidth of SiO^+ $X \rightarrow B$ transitions is only 2.3 MHz. The spacing between comb teeth and transitions will be random and therefore some transitions may be detuned by up to 40 MHz or 17.4 linewidths.

The linewidth of the comb teeth scales as $\frac{1}{N\tau_{rep}}$ where N is the number of pulses. The linewidth will continue narrowing until it is limited by the stability of the carrier or the rep rate. Over experimental time scales, the comb teeth will have a finite linewidth and therefore may need to be taken into consideration. To investigate the lineshape of the comb teeth a passively stable CW laser at 769 nm was used to measure the linewidth of the beat note between the CW laser and the fundamental output of the femtosecond laser (Mai-Tai HP). The spectrum of the beat note can be seen in Fig. 5.10. The

spectrum was recorded by co-propagating the two lasers onto a photo-diode connected to a spectrum analyzer. An optical grating was necessary to spatially filter out comb teeth with frequencies far from the CW laser which otherwise overwhelmed the beat-note signal. To collect the beat note spectrum, the spectrum analyzer swept the frequency over 80 MHz in 50 ms. The observed FWHM is between 1 and 2 MHz suggesting that the comb teeth do not drift significantly over the duration of cooling (<200 ms[7]). The tails of the beat note spectrum appear to be exponentially suppressed and are not well-fit by a Lorentzian profile. The dominant contribution to the oberserved linewidth is likely from the femtosecond laser as the CW laser was observed to have of order 1 MHz drift over a 1 second time scale, however the beat note was observed to drift several MHz per spectrum analyzer scan. Regardless, the comb teeth linewidth is not expected to be relevant to the optical pumping rate. This is because it is small compared to the range of possible detuning and though it is comparable to the natural linewidth of the transition, the tails are exponentially suppressed while the absorption profile is merely quadratically suppressed.

It is worthwhile considering how the teeth structure can influence the pumping rate. If we suppose the worst case scenario such that the transition is a maximal 40 MHz detuned and the SiO^+ is at zero temperature, then the pumping rate is reduced by a factor of $17.4^2 \approx 300$ compared to the on resonance scenario (assuming it is below saturation). There are several nearly equivalent ways to improve the pumping rate. The first is to pass the laser through an EOM or AOM and sweep the frequency over a range of 80 MHz such that on each sweep, all transitions will come into resonance with the laser each

[7]See section 7.3 for cooling results.

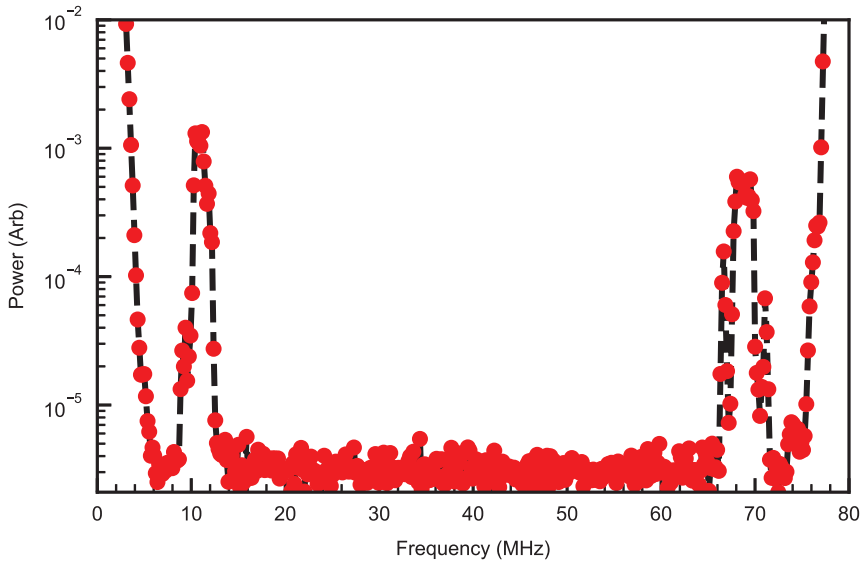

Figure 5.10. Observed spectrum of the beatnotes between a passively stabilized 769 nm laser and the fundamental output of the femtosecond laser (Mai-Tai HP). The beat note is observed for the two nearest comb teeth to the CW laser at $\sim$ 11 MHz and $80 - 11 = 69$ MHz. The tail at 0 and 80 MHz is the collective beatnote between the combteeth. The observed linewidth suggests that the comb teeth linewidth are not relevant to optical pumping rates (see text).

period of the sweep. In this scenario, if the frequency velocity is comparable to or greater than the transition linewidth divided by the average optical pumping time on resonance, the average time spent on resonance will be 1 and 17.4 implying that the pumping rate is only reduced by a factor of 17.4 compared to the on resonance scenario. Equivalently, the ions can be heated (cooled less efficiently) such that their Doppler broadened linewidth is comparable to the comb teeth spacing. For SiO^+ a temperature of 1 K will provide a linewidth of $\sim$ 80 MHz. For comparison, at the Doppler cooling limit of Ba^+ ($T = 1$ mK) the Doppler profile linewidth of SiO^+ is 2.5 MHz. Alternatively, the ions can be shaken in the direction of the laser beam. The net result in each case is equivalent to treating the

comb structure as a smooth distribution. Each method has the added benefit of resulting in a much narrower distribution in the necessary time for cooling the population. In the unaltered scenario where the comb teeth are randomly positioned with respect to the transitions, the optical pumping rate for each transition follows a power distribution law as the pumping rate will depend quadratically on the randomly distributed detuning. The average pumping rate will be comparable to the alternative methods, however the rate will vary significantly from shot to shot between 1 and 300 times the on resonance rate.

At the current standing of the experiment, no particular technique is used to alleviate the issues associated with the comb teeth. In practice it may require some combination of all methods to achieve the most efficient control as the bandwidth of AOMs or EOMs may not be sufficient to reach 80 MHz and the amplitude of motion required for shaking or heating the ions may be too large to avoid putting the crystal in the gas phase. In order to maintain high ion densities, the thermal energy needs to be much lower than the Coulomb energy. This is quantified by the so called Coulomb coupling parameter

$$\Gamma = \frac{\frac{e^2}{4\pi\epsilon_0 a_0}}{kT} \tag{5.9}$$

where a_0 is the average distance between ions and otherwise known as the Wigner-Seitz radius. Simulations typically show that trapped ions will crystallize at $\Gamma \approx 178$ [**70**]. If the thermal energy exceeds the average Coulomb energy between neighbors (i.e. $\Gamma < 1$) the ions will be in the gas phase and the densities will be very low. Between these two regimes ($\Gamma > 2$) is the liquid-like phase where densities will be similar to the crystal phase, but no regular structure is found [**153**]. If we wish to operate with a temperature of 1 K, then to maintain a liquid-like phase, the ions need to be confined such that the average

spacing is smaller than 8 μm. This is comparable to the confinements achieved by typical trapping parameters, but maintaining trapped ions at the edge of the liquid-gas phase is unlikely to be stable. For comparison, with the LCFMS technique (see section 5.6.2) we prefer to operate at the edge of the solid-liquid phase. To maintain this threshold the temperature cannot exceed $\sim$ 12 mK which is equivalent to Doppler broadening of $\sim$ 9 MHz. Thus we can expect that two approaches may need applied together to achieve the desired effect.

5.7.2. Homebuilt Spectrometer

The homebuilt spectrometer has not been updated from the version described in [**94**] and is nearly identical to the pulse shaping setup shown in Fig. 5.8. Unlike the pulse shaping setup, the beam input is through a fiber and at the Fourier plane, a linear CCD array replaces the mask and back reflecting mirror. Though the version is the same, the spectrometer setup has been dismantled and reconstructed and has thus required recalibration. Calibration was performed by manually tuning the ECDL grating of a CW laser frequency doubled to generate 385 nm light over a 50 cm^{-1} range in the region of interest. The CW laser was fiber coupled into the spectrometer setup and the peak pixel was recorded alongside a wavemeter reading (High Finesse WS8-2). The dispersion was found to be 0.39 cm^{-1}/pixel (11.7 GHz/pixel). Taking into account the frequency per pixel, the CW laser focal spot size corresponded to $\sim$ 0.8 cm^{-1} (24 GHz) FWHM which sets the resolution for the spectrometer.

CHAPTER 6

Production and Trapping of SiO^+

Molecules are rarely observed or produced in pure isolation. Consequently, identifying and isolating their spectra can be challenging. Particularly so for radicals as they tend to be very reactive and especially for ions as they tend to be far less densely spaced than neutrals. SiO^+ is both of these things. Amusingly, the history of attempts to identify the SiO^+ spectrum highlights the confusion generated by these challenges. At Imperial College in London in 1940 R.C. Pankhurst first observed part of the SiO^+ $B^2\Sigma^+ \rightarrow X^2\Sigma^+$ spectrum along with multiple other bands from different species in a heavy current hydrogen gas discharge through a constriction in a quartz tube. The complexity of the bands lead to his confusion in thinking they were all from a single, polyatomic source which he tenuously mis-assigned as SiO_2 [**119**]. The experiment was later repeated by Woods at the University of Chicago in 1943 after substituting hydrogen with helium and she was able to correctly identify the bands at 384 nm as belonging to the $B^2\Sigma^+ \rightarrow X^2\Sigma^+$ (0,0) and (1,1) bands of SiO^+ [**169**]. In 1968, Nakaraj and Verma saw the band at 384 nm that Woods had identified as SiO^+ in addition to another $^2\Sigma \rightarrow^2 \Sigma$ band near 412.5 nm that they also attributed to SiO^+ after measuring the spectrum of an RF discharge through a flowing mixture of Argon, $SiCl_4$, and, supposedly, trace oxygen. They mistakenly claimed to have "conclusively" determined that Woods had misattributed the 384 nm band as coming from the ground state and first excited $^2\Sigma$ state of SiO^+ because two low-lying $^2\Sigma$ are not possible according to electron configuration considerations [**104**]. The following

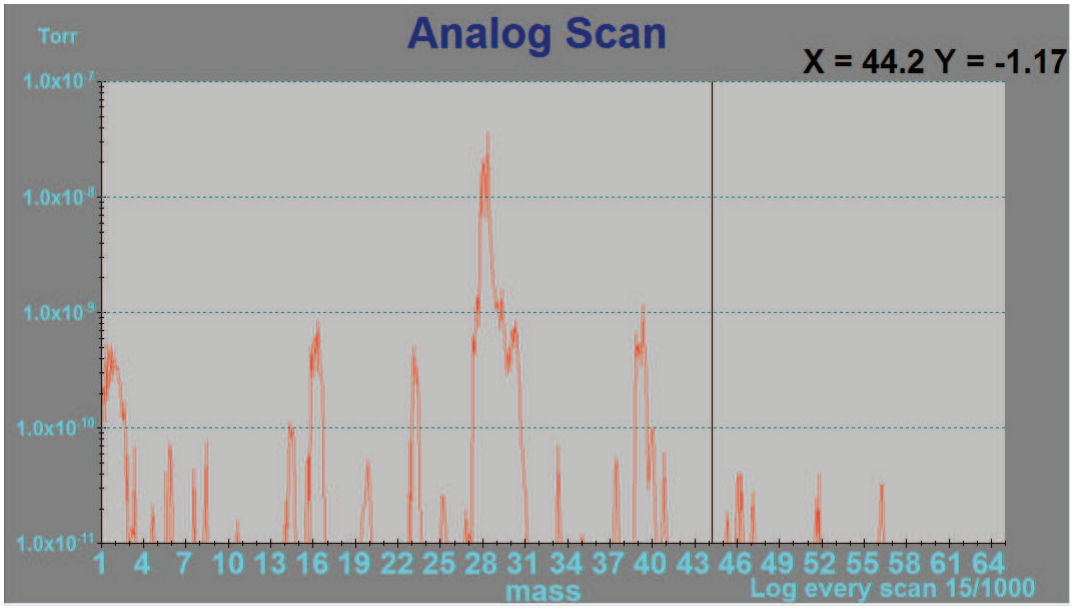

Figure 6.1. The mass spectrum of the ablation products of solid SiO in its original granular form. The filament of the RGA was turned off to ensure that only the charged species of the ablation plume were being mass analyzed. Notably, there is no signal observed at the mass of SiO^+ (44 u) which is highlighted with a black, vertical line.

year, Dunn et al issued a correction noting that Mulliken [**103**] had previously observed the same band at 412.5 nm and had positively confirmed it using silicon isotope analysis as originating from SiN. This, however, lead them to mistakenly conclude that the band at 384 nm must also be assigned to SiN [**40**]. Others later reported that oxygen was necessary to observe Woods' bands and finally, a decade later, in 1979 Ghosh et al confirmed the SiO^+ assignment of Woods after using an oxygen isotope analysis and observing a small shift in the $B^2\Sigma^+ \rightarrow X^2\Sigma^+$ band origin. Thus concluded a nearly 4 decade long confusion on the assignment of the SiO^+ spectrum.

The danger of unwarranted assumptions with SiO^+ without direct confirmation was also experienced by us. Our initial approach for producing and trapping SiO^+ relied

exclusively on ablation of SiO and low resolution mass spectroscopy using the q-scan method described in section 5.6. The logic was as follows: We observe that when we ablate solid purified barium we successfully load Ba^+ into the ion trap. We can resolve silicon's mass from silicon monoxide's mass and when we ablate 99.9% purified solid SiO we observe something consistent with the mass of SiO^+ when analyzing the ion trap's contents. Therefore, we must be loading primarily SiO^+ with perhaps minor quantities of impurities. The false assumption was that the purity of the solid would at least somewhat proportionately reflect the purity of the ablated ions. After some failed attempts at detecting cold SiO^+ in the ion trap we more carefully questioned the assumptions. Indeed, previous studies of the ion products of laser-ablated SiO (both in granular and pressed pellet form) showed that the ion products were heavily influenced by impurity composition [**157, 68**]. The product composition was also influenced by the wavelength of ablation and was broadly split into two categories—thermal for wavelengths longer than 308 nm and non-thermal for wavelengths shorter. Under thermal conditions there tended to be clustering of the form Si_n^+ and $Si_nO_m^+$ which disappeared as the wavelength decreased. Surprisingly, in an earlier study Torres et al found that more NaO^+ (39 u) was produced in the plume than was SiO^+ (44 u) when ablated by 532 nm [**157**] and generally ion products of metallic impurities with low ionization potentials are commonly observed (e.g. Na, Li, K, and Al) [**68**]. The mass difference of these two is on the edge of our ability to resolve the two using the Q-scan method. This result was confirmed by in house measurements as seen in Figure 6.1. Specifically, I laser ablated a granular piece of SiO with 532 nm in a "test" high vacuum chamber and observed the mass spectra of the charged products via a residual gas analyzer (Stanford Research Systems) modified to

operate without a filament. In the main UHV chamber housing molecular ion trap, our sample is a pressed pellet of silicon monoxide. Critically, Jadraque et al also found that a pressed pellet of SiO produced significantly more $(SiO)H^+$ than SiO^+ upon ablation at 266 nm [**68**]. The most likely mechanism was suspected to be direct ejection of SiOH defects that tend to form on the surface of siliceous materials.

6.1. 2+1 REMPI of SiO

As we are unable to resolve $SiOH^+$ (45 u) from SiO^+ (44 u), are on the edge of resolving SiO^+ (44 u) from NaO^+ (39 u), and have evidence that SiO^+ is produced in relatively low abundance, we decided to use a state selective method known as resonance-enhanced multiphoton ionization (REMPI). An investigation of the neutrals in SiO ablation by Torres et al found that the dominant product at lower ablation fluences (0.1 J/cm^2) is SiO [**156**]. The only known REMPI measurements performed on SiO were two-photon resonant transitions of $F^1\Sigma^+ - X^1\Sigma^+$ [**106, 107**] and $H^1\Sigma^+ - X^1\Sigma^+$ states [**105**]. Following excitation of the two photon transition, a third photon was sufficient to photoionize the SiO, hence the process is referred to as 2+1 REMPI. The observed bands were between 282 nm and 293 nm and of these bands, the lowest diagonal $H^1\Sigma^+ - X^1\Sigma^+(v, v)$ transitions were observed to be the strongest transitions [**105**].

6.1.1. Modified RGA

To reproduce the 2+1 REMPI spectrum and confirm production of SiO^+ I modified an RGA (Stanford Research Systems) capable of better than 1 amu of mass resolution such that it could perform mass spec on the ions generated following photoionization. Under

normal operation, a filament acts as a source of thermionically generated electrons. The electrons are then accelerated towards the inner, positively charged anode made out of conductive wire mesh (see Figure 6.2). The electrons have a high probability of passing through and out of the wire mesh until they are repelled by the negatively charged repeller. As the electrons oscillate they will collide with gases in the vacuum. Gases ionized inside the volume contained by the anode are then repelled by the anode mesh and sent through the negatively charged focus plate into the quadrupole mass filter. The electrons will continue oscillating until they are either collected by the anode or recombine with ions present in the volume.

Unlike the experiment observing the ion products produced from ablation (see Fig. 6.1), ions produced by photoionization will be much less energetic ($<<1$ eV) than the anode barrier which is tens of elecrton volts. To get efficient collection of the photoionized species I inserted two holes into the anode grid and two holes into the repeller grid such that a straight line could pass through all four holes. A schematic of the modification can be seen in Fig. 6.2. To preserve the shape of the grids, the holes were created by slowly inserting progressively larger diameter metal rods until an $\sim$5 mm hole was created. The set of holes were produced simultaneously by a single rod to ensure alignment. The RGA, attached to a 2-3/4 inch conflat vacuum 6-way cross, had limited optical access to the ablation target. To compensate, two additional holes in the repeller mesh were needed such that the ablation beam could target the sample without hitting the meshing.

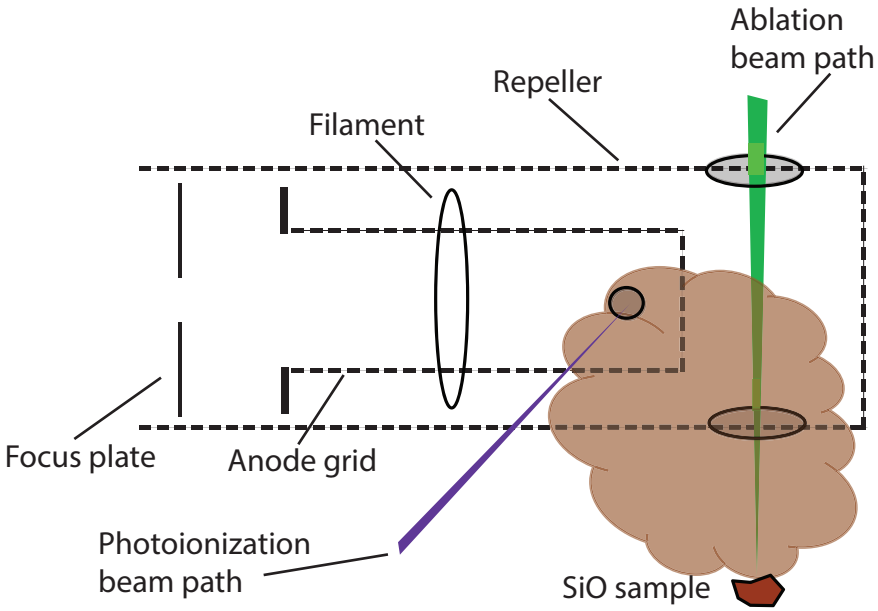

Figure 6.2. A schematic of the modified RGA. Four holes in the wire mesh are created to allow for transmission of the photoionization laser beam to pass through the repeller and anode meshes without clipping the metal mesh. Two extra holes are added to the repeller meshing to allow for the ablation laser to pass through.

6.1.2. Dye Laser Spectrum

The 2+1 REMPI spectrum was first recorded using the modified RGA to monitor the signal produced at mass 44 of ablation (532 nm see Minilite continuum 5.4.1) of granular SiO followed by photoionization using the Lambda Physik Scanmate dye laser (see section 5.4.1). 532 nm pumped Pyromethene 597 dye was used to generate 574 nm and was frequency doubled to 287 nm. The output was attenuated to $\sim$ 0.6 mJ and was focused (f = 300 mm) into the anode volume of RGA (see Fig. 6.2). The SiO target was positioned under the ionizer roughly 1 cm below the dye laser beam. Delay between the dye laser and the ablation laser varied from 15 μs to 125 μs with the largest signal

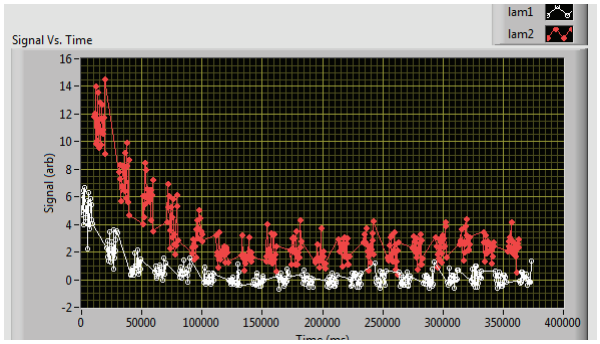

Figure 6.3. Signal seen at mass 44 as a fucntion of time. The dye laser alternated between 286.8 nm (red) and 286.9 nm (white). Though the signal frequently drifted to smaller and smaller values, occasionally I observed it to reverse trends and increase over time.

occurring at $\sim$ 40 μs. The analog output of the RGA was recorded by an oscilloscope which was transferred to a computer and integrated digitally to obtain the signal.

Signal from ablation was rarely able to remain consistent for tens of seconds. This was a serious issue for obtaining the spectrum. The signal strength was strongly dependent on the the details of the surface and consequently changed significantly over time as seen in Fig. 6.3. At the time of the experiment, angle tuning of the SHG crystal of the dye laser was not automated. This meant that comparison of signal strengths between different wavelengths was not reliable. As a quick makeshift compromise, the SHG crystal angle was tuned such that the UV output energy was made to be equal at two separate wavelengths. The spectrum in Fig. 6.4 is constructed by comparing the relative signal of each wavelength to the wavelength before and after it. Due to error propagation the relative peak heights are not expected to be quantitatively reliable. The peak locations, however, will still be reliable and indeed their relative positions match those first observed by Nakamura et al [**105**].

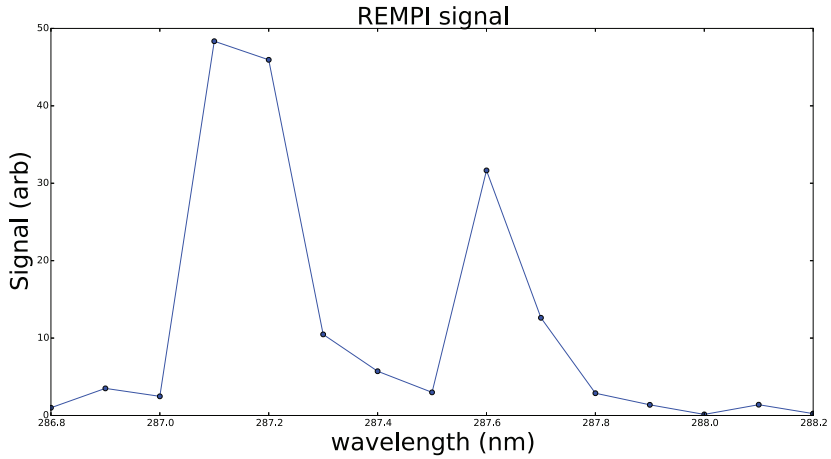

Figure 6.4. The 2+1 REMPI spectrum of SiO. Peaks represent the vibrational progression of the $H^1\Sigma^+ - X^1\Sigma^(v, v)$ transition.

I also used the RGA to monitor other masses besides 44 u. I looked for signals at masses 12, 16-18, 28, 39, 41-46 and 56-59 u. No other signal was detected besides the one at mass 44. The 2+1 REMPI spectrum was reproduced after loading SiO^+ in the molecular ion trap and performing mass-analysis via the Q-scan method (see section 5.6). The mass spectrum generated by Q-scan is consistent with pure production at mass 44.

6.1.3. OPO Spectrum

The first attempt at state detection of SiO^+ was originally planned to involve 1+1' resonance-enhanced multiphoton dissociation (REMPD). Here the 1 refers to the photon energy that is resonant with some transition of the molecule and the 1' refers to a second photon energy that is sufficient to dissociate molecules in the excited state. Rotational state selectivity required the 1 photon be from the dye laser as the OPO linewidth is too broad for rotational resolution. The 1 photon transition was planned for use on the $B-X$ transition at 384 nm and consequently the dye laser could not be simultaneously used for

REMPI and REMPD as it would require a laborious, time-intensive dye change every time the wavelength needed changed. Because loading into the ion trap only required species selectivity and not state selectivity, I tested the Premiscan OPO (see section 5.4.1) for loading SiO^+. Unfortunately, for reasons not completely understood, the OPO was unable to load pure SiO^+ into the trap. The spectrum of different mass ranges is plotted in Fig. 6.5. It was confirmed that both the ablation and photoionization beams needed to be present for a signal to exist, i.e. the signal was entirely due to photoionization.

The spectrum presented for the mass range 0-30 u is likely due to Si^+ and possibly Na^+. The only known relevant difference between the dye laser and the OPO is their linewidths. Conceivably, the narrow linewidth of the dye laser was able to find portions of the spectrum which avoided spectral features that lead to the ionization of unwanted species, however some of the features appear to be broader than the OPO linewidth and so the dye laser should also excite them. It is also possible that the pressed pellet of SiO used in the ion trap chamber has a different ablation plume composition than the solid granular SiO used in the 'test chamber' with the RGA. This is unlikely to explain the discrepancy, however, as loading with the dye laser was observed to be significantly purer than the OPO in the ion trap as well.

Though the discrepancy was never resolved, it is noteworthy that the spectra of the different mass ranges were dependent on the ablation power. With ablation fluences ($\sim$1 J/cm^2) more than twice that used in the recording of spectra seen in Fig. 6.5, I saw evidence for the photoionization of Si_n clustering, consistent with the clustering of neutral species found by Torres et al [**156**]. These complications and generally the relative inefficiency of a two-photon resonant process (i.e. 2+1 REMPI) likely contribute

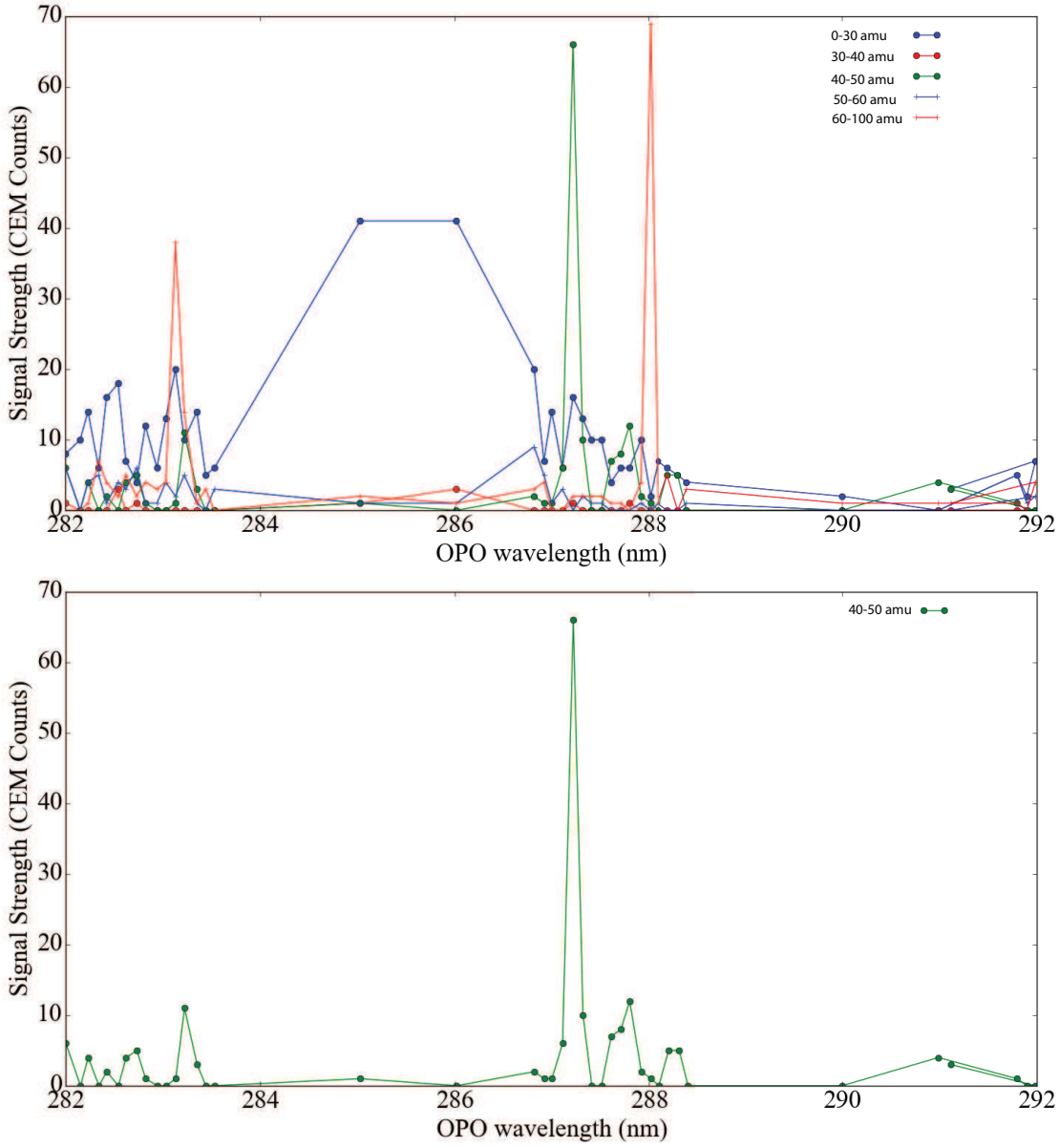

Figure 6.5. The photoionization spectrum as recorded using the broader linewidth OPO. The upper plot shows several mass ranges that were recorded using the sympathetically cooled Q-scan method. The lower plot shows the mass range consistent with SiO^+ and matches the 2+1 REMPI spectrum of SiO recorded in Fig. 6.4.

significantly in the failure to detect SiO^+ LIF in the large LIF trap (see the discussion on loading the LIF trap in section 4.2.3).

The inefficiency of 2+1 REMPI can be understood when considering how to optimize the photoionization signal when below saturation. In a two-photon process excitation efficiency increases quadratically with a linear decrease in focal area. This implies that linearly *decreasing* the number of probed species of uniform density in the interaction volume will linearly *increase* the yield of species that are photoionized until the beam intensity approaches saturation of the transition. As the intensity goes beyond saturation, continuing to decrease the focal area will only decrease the yield. Thus the optimal conditions for photoionization will depend on the transition and the total power in the beam. In contrast, a one-photon process below saturation will be insensitive to the focal area and above saturation the number of photoionized species will be increased with increasing focal area. Thus the optimal focal area will always be the one that maximizes the number of neutral species (assuming uniform density) in the trapping volume.

6.2. 1+1 REMPI of SiO

Motivated by a need for an efficient method for loading pure SiO^+ into an ion trap, we investigated 1+1 REMPI channels in SiO. The 1+1 REMPI technique is the simplest and most efficient method for state selective ionization. The text in this section closely follows [**150**] where much of our work on this topic has been reported. We find that 1+1 REMPI via the $A^1\Pi \rightarrow X^1\Sigma^+$ electronic transition of SiO in the 210-220 nm region is able to efficiently load a pure sample of SiO^+ into an ion trap. Additionally, we discovered a fortuitous band that allows for generation of SiO^+ in the ground vibrational state of

$X^2\Sigma^+$ with a limited distribution of rotational energy. In our investigation we tentatively assign a new transition from $X^1\Sigma^+$ to the $n = 12, 13$ $[X^2\Sigma^+, v^+ = 1]$ Rydberg states and were able to improve on the measurement of the ionization potential of SiO.

Interest in spectroscopy of SiO was initially stimulated by questions in astrochemistry. After detection of vibrational bands of SiO in stellar atmospheres [**59**] a search for electronic transitions followed. Several studies investigated transitions of SiO in the UV region [**45, 85**]. The ionization potential (IP) of SiO was measured by means of electron impact [**58**], spectroscopy of Rydberg states [**8**], photoelectron spectroscopy (PES) [**30**], and direct VUV photoionization [**83**].

The work on this topic was motivated by the need for a reliable, rapid, and pure source of SiO^+ for purposes of laser control in an ion trap. Efficient and reliable loading of SiO^+ into a Paul trap can be achieved by means of photoionization. SiO has a relatively high ionization potential (> 11 eV), therefore a multiphoton process is needed to photoionize it with commonly available laser light sources. The simplest and most convenient multiphoton ionization scheme would be two photon one color photoionization enhanced by resonance absorption of the first photon or 1+1 resonance-enhanced multiphoton ionization (1+1 REMPI). The $A^1\Pi - X^1\Sigma^+$ band system enables 1+1 REMPI for photoionization of SiO. The system has previously been studied via LIF [**171**] and absorption measurements [**44**]. The origin of this band is located at 5.3 eV, slightly below half the ionization energy of SiO; its vibrational overtones with $\Delta v \geq 5$ are energetically allowed for 2-photon 1-color photoionization. Photoionization via this band system has

the additional advantage for trap loading that one can select ionization pathways to produce SiO^+ only slightly above the ionization threshold, i.e. in the ground vibrational and electronic state and with low rotational energy.

No previous 1+1 REMPI photoionization study of this system exists. The ionization energy of SiO has not been measured with precise methods such as PFI ZEKE. The most precise values measured by photoelectron spectroscopy [**30**] and synchrotron-based absorption spectroscopy of Rydberg series [**8**] are only accurate within ∼80-100 cm^{-1} and contradict each other. The photoionization spectrum shape near the ionization threshold can be modified by highly excited states of a neutral molecule, e.g. Rydberg states. Therefore, the spectrum band intensities are not straightforward to predict based on thermal populations in the lower state and vibrational overlap between the neutral and the cation wavefunctions. Instead, direct measurements of photoionization spectra can be used to locate intense and state-selective bands for SiO^+ loading.

6.2.1. Experimental

The apparatus used for all REMPI measurements is described in detail in chapter 5. All measurements occurred under UHV (5×10^{-10} Torr) conditions with the aid of a home built linear Paul trap for ion storage and a channel electron multiplier (CEM) for ion detection. A pressed pellet of SiO, situated below the center of the Paul trap, was ablated by 532 nm light produced by frequency doubling of a pulsed Nd:YAG laser. Photoionization was subsequently performed on the ablation plume inside the trapping volume. After accumulating ions from a predetermined number of photoionization and ablation pulses, the trapped ions were released and detected by the CEM.

The experimental setup is shown in Fig 6.6. The vacuum chamber housed the Paul trap (3.6 MHz trap frequency, $r_0 = 3$ mm, $z_0 = 7.29$ mm, $V_{pp} = 660$ V, $\kappa = 0.22$, $V_{ec} \approx 1$ V), an ablation target of pressed SiO located 1 cm below trap center, and the CEM. The CEM was kept at -3 kV throughout the duration of the experiment. The 532 nm ablation laser light was generated by frequency doubling of an Nd:YAG laser output (Continuum Minilite II, 10 Hz rep rate, 3-5 ns pulse width), attenuated by a $\lambda/2$ waveplate and a polarizing beam splitter to $\sim$0.5 mJ. The 532 nm light passed through a motor-controlled rotating window, and was focused onto the sample with an f=150 mm lens. The rotating window was positioned at a $\sim 30^\circ$ angle with respect to the ablation beam axis to parallel shift it. As the window rotated, the beam was walked in a circle to refresh the ablated surface.

The laser light used for photoionization was generated by an Nd:YAG pumped OPO system (Ekspla NT342/1/UVE OPO, 10 Hz rep rate, 4.2 ns pulse width, 4 cm^{-1} linewidth) and focused into the trapping volume with an f=200 mm lens. The photoionization laser pulse was delayed by 90 μs with respect to the ablation laser. The REMPI signal was found to stay constant over a delay range of $\sim$50 μs. The average pulse energy of the photoionization laser was typically 0.5 mJ. A photodiode located after the vacuum chamber along the beam path was used to monitor the relative output power.

The wavelength of the photoionization laser was scanned from 210-220 nm in steps of 0.025 nm. At each wavelength, the ablation laser and REMPI laser pulsed 5-20 times. After that the RF trapping voltage was linearly ramped down over 0.5 ms and the accumulated ion products were detected by the CEM. Event counting was used to quantify the ion signal. The number of events detected per 0.5 ms voltage ramp did not exceed

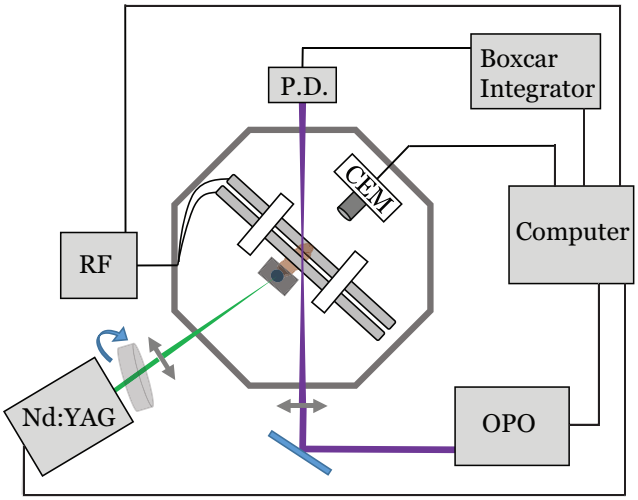

Figure 6.6. Schematic diagram of the experimental setup.

several thousand with typical values around several hundred. Care was taken to avoid saturation effects due to filling the ion trap. A boxcar integrator was used to record the average voltage of the photodiode measuring the REMPI laser output to provide (linear) power normalization of the REMPI signal under the assumption that the $A - X$ transition was saturated and the second, photoionizing one was not. This detection sequence was repeated several times to accumulate statistics before the wavelength was changed. After completion of a wavelength scan over a given range its direction was reversed to discriminate against drifting of the REMPI signal.

6.2.2. Calculations

All electronic structure calculations were performed with the QChem package. The IP of SiO was calculated at CCSD(T)/CBS level. The potential energy curves of the ground electronic states of SiO and SiO^+ were calculated at IP-EOM-CCSD level and fitted to a Morse potential to determine R_e. The values obtained for the neutral SiO (R_e=1.5094 Å)

and for SiO^+ (R_e=1.5166 Å) are in very good agreement with experimentally measured values [**10, 24**]. CBS extrapolation was achieved by fitting CCSD(T)/ aug-cc-pVnZ (n=2-5) ground electronic state energies of SiO and SiO^+ with the mixed exponential/Gaussian formula [**43**]. The adiabatic IP value was obtained by subtracting the CCSD(T)/CBS energy of SiO from that of SiO^+ and correcting for the zero-point energies. The resulting value was IP = 11.6138(1) eV where the number in parenthesis is the 1-σ of the exponential fit parameter.

6.2.3. Notation

The following notation is used throughout the remainder of this section. Rotational and vibrational levels of the ion are followed by the superscript "+" sign, such as N^+ or v^+. Quantum numbers of the ground state of SiO, $X^1\Sigma^+$ are followed by double prime, e.g. $J''$and v''. Energy levels of $A^1\Pi$ state of SiO are followed with a single prime, e.g. J' and v'. We use the total rotational quantum number J for the neutral SiO and the nuclear rotational quantum number N^+ for SiO^+ to avoid dealing with half-integer J^+ values. Rydberg states of SiO are denoted with the Rydberg electron configuration in parenthesis, e.g. $(ns\sigma)$, which is followed by the state term symbol, e.g. $^1\Sigma^+$ and the level of the SiO^+ ion core, e.g. $[X^2\Sigma^+, v^+ = 1]$, in square brackets.

6.2.4. Results

Fig 6.7 presents the 1+1 REMPI spectrum of neutral SiO at 210-220 nm. The upper black trace is experimental data; the colored lines below are simulated transitions. The spectrum consists of two types of features. The first type is the red-degraded bands

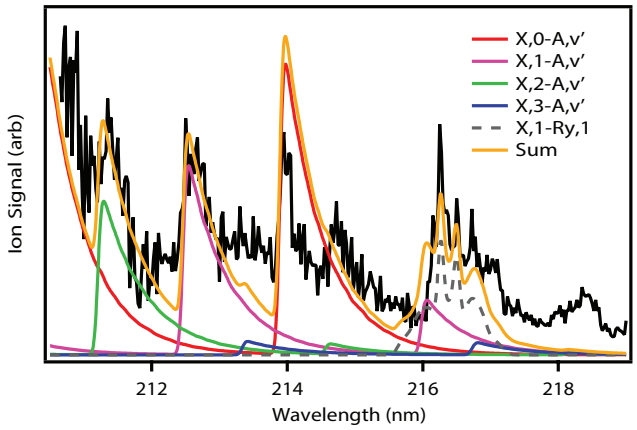

Figure 6.7. SiO 1+1 REMPI spectrum as a function of UV wavelength at 210-220 nm. The black trace is experimental data and colored traces are simulated transitions (see legend).

distributed over the 210-218 nm range. The second type is a complex band at 216 nm with multiple narrow lines. After 218 nm the signal is small and unresolved. The rotational lines of SiO could not be resolved since the bandwidth of the photoionization laser is 4 cm^{-1}, and the rotational constant of SiO is 0.72 cm^{-1}. Therefore the observed bands represent rotational contours of vibronic transitions of SiO.

The bands of the first type were assigned as $(v' = 5-10, v'' = 0-3)$ vibrational bands of the $A-X$ electronic transition (see Table 6.1 and Fig 6.7); they are red-degraded since the rotational constant of the A state is smaller than that of the X state (0.62 cm^{-1} vs 0.72 cm^{-1} for B_0). The intensity of the bands was well reproduced by the Franck-Condon coefficients of SiO $A-X$ transition [**112**] multiplied by a sum of the FCFs of the energetically allowed $X^+ - A$ ionization channels. The best agreement was achieved when both rotational and vibrational temperatures were equal to 1000 K, which is reasonable given the high temperatures of ablation plumes. The 5-0 rotational band contour at 214 nm looks different from other $A-X$ bands and the intensity of this band is not

Table 6.1. Assignment of 1+1 REMPI spectrum of SiO. The energy of SiO above the ionization threshold after 2-photon absorption, ΔE, is calculated assuming IE = 11.586 eV.

λ (nm)	$(v' - v'')$ Assignment	$\Delta E(\text{cm}^{-1})$
210.47†	(6-0), $A - X$	1579
211.29†	(9-2), $A - X$	3671
212.54†	(7-1), $A - X$	1882
213.43†	(10-3), $A - X$	3951
213.98†	(5-0), $A - X$	23
214.66†	(8-2), $A - X$	2185
216.06†	(6-1), $A - X$	349
216.26‡	$(s\sigma)^1\Sigma^+ - X, v'' = 1$	∼240
216.49‡	$(p\sigma)^1\Sigma^+ - X, v'' = 1$	∼140
216.58‡	$(d\sigma)^1\Sigma^+ - X, v'' = 1$	∼100
216.81†	(9-3), $A - X$	2489
218.19†	(7-2), $A - X$	676

† 1+1 REMPI via the $A - X$ system

‡ Tentative assignment of 2-photon excitation of Rydberg states $n = 12, 13$ with an ion core of $[X^2\Sigma^+, v^+ = 1]$

reproduced by Franck-Condon simulations. The reason for this difference is that the 2-photon excitation on the 5-0 transition brings SiO very close to the ionization threshold level where angular momentum conservation restricts ionization for high rotational levels (see section 6.2.5).

The second type of band, observed at 216-217 nm, is qualitatively different from the $A - X$ bands. Instead of a red-degraded contour it has several sharp peaks that resemble Q-branches of electronic transitions between states with similar values of rotational constants. Since there are no electronic states with $B' \approx B''$ in the one-photon energy range, states responsible for the observed band are likely excited in 2-photon excitations. We tentatively assign this band to a two-photon transition from the $v'' = 1$, $X^1\Sigma^+$ state of SiO to the Rydberg states with $n = 12, 13$ converging to the $v^+ = 1$, $X^2\Sigma^+$ ion core.

The assignment is based on energetics and on the "vertical" appearance of the observed bands which results from $B^+ \approx B''$. Since the SiO and SiO^+ ground electronic states have similar bond lengths and vibration frequencies, the $v'' = 1 - v^+ = 1$ excitations have a favorable Franck-Condon overlap. The 2-photon excitation at 216 nm is enhanced by the first photon being in near resonance with the 6-1 vibrational band of the $A - X$ system.

The 2-photon selection rules allow excitation of Rydberg states of Σ, Π and Δ symmetry. In the simulation we used the 3 Rydberg states of Σ^+ symmetry to simulate the band shape and achieved good agreement with experimental results; however, this assignment is tentative and higher precision data is needed to assign the electronic symmetry of the states involved in this second type of band.

The list of observed transitions is shown in Table 6.1 along with vibrational assignments and the energy difference, ΔE, between the ionization energy of SiO and the energy of SiO after 2-photon absorption.

We recorded the Ba photoionization spectrum to quantify the ionization potential depression due to the electric field of the trap (Fig. 6.8). The onset of the Ba^+ ion signal is observed at 41936 cm^{-1}, which is 99 cm^{-1} below the ionization energy of Ba. The weak Ba^+ signal observed below the onset is due to ionization of metastable excited states of Ba populated during ablation, probably belonging to the ^3D term. The difference between the observed and the actual ionization threshold is due to ionization of Rydberg states lying below the ionization threshold by the electric field of the trap (see section 6.2.5).

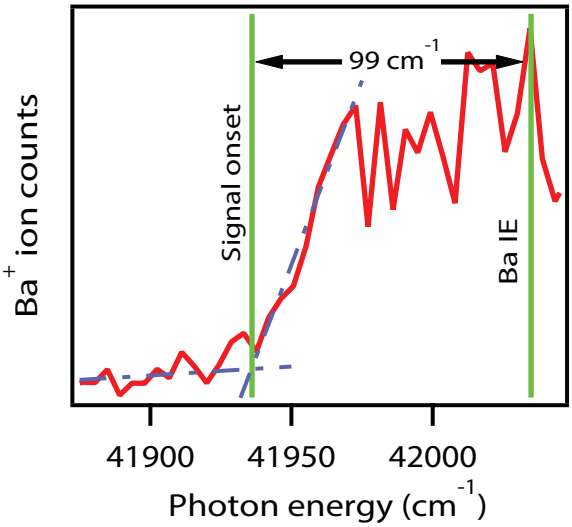

Figure 6.8. 1-photon photoionization spectrum of Ba in the ion trap (red trace). Dashed blue lines extrapolate the signal rise and the background to find the onset. Observed onset of ionization and field-free ionization energy of Ba are marked with vertical green lines.

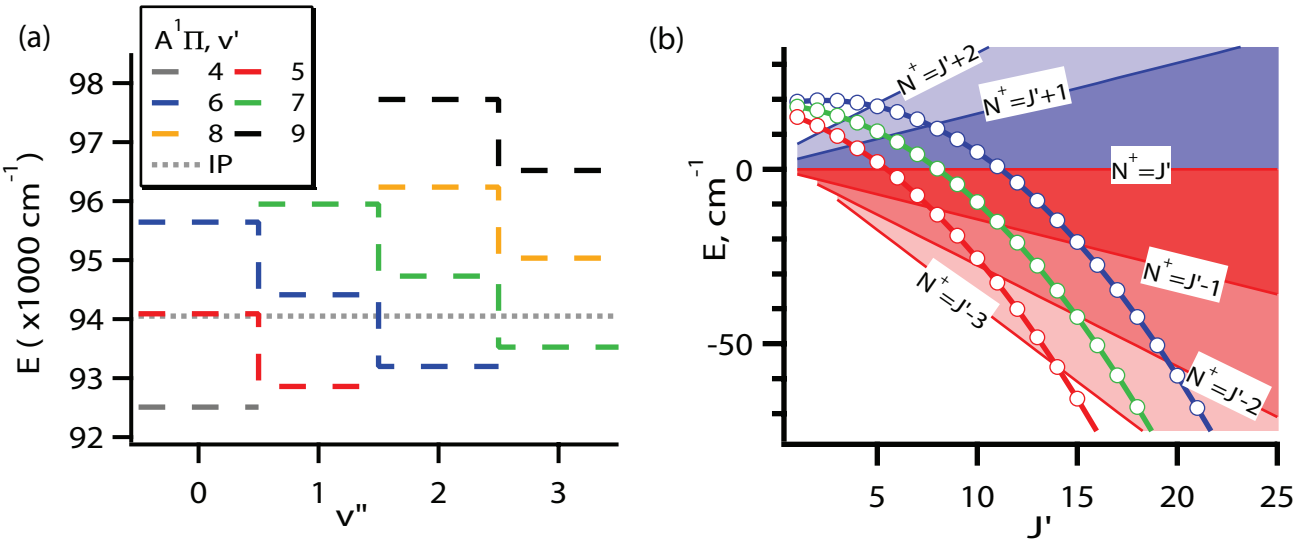

Figure 6.9. (a) The energy of SiO after a 2-photon transition via vibrational bands of $A - X$ transitions; (b) The energies of rotational levels of SiO after a 2-photon excitation of the (5,0) $A - X$ transition.

6.2.5. Discussion

The photon energy required for photoionization of SiO in a 1-color 2-photon transition can be defined as

$$h\nu \geq \frac{IE_{SiO} - E_i - \Delta E_F}{2} \tag{6.1}$$

where IE_{SiO} is the field-free ionization energy of SiO, E_i is the energy of the initial state of SiO, and ΔE_F is the depression of IE_{SiO} due to the electric field in the trap. Assuming that SiO is produced by ablation in the ground electronic state or quickly quenched to it by means of radiation and collisions, E_i is due to the vibrational and rotational population of the ground state. Fig 6.9a shows the energies of SiO after resonant 2-photon excitation on the $A - X$ transition with $v'' = 0 - 3$ relative to IE_{SiO}. The energies in this diagram are relative to the minimum of the $X^1\Sigma$ potential energy curve. The dashed grey line is the ionization energy of SiO in our trap for which we used the $IE_{SiO} - \Delta E_F$ value of 11.586 eV estimated from our data (see below). To ionize SiO in the trap, two photons must promote it above this level. For example, SiO molecules at $v'' = 0$ can be ionized via $A - X$ when $v' \geq 5$, ionization of $v'' = 1$ requires $v' \geq 6$ etc. Higher v'' levels require correspondingly higher v' levels of the A state of SiO. Bands with $\Delta v \leq 4$ cannot be observed in 1+1 REMPI spectrum, while all bands with $\Delta v = 5$ are located above the IE_{SiO} level. The $5 - 0$ band is only $\sim$23 cm^{-1} above the estimated value of IE_{SiO}. The rotational structure of this band is affected by proximity of the IE_{SiO}.

Figure 6.10 expands part of the SiO REMPI spectrum at 214 nm where the $5-0$ band is located. It has an abrupt drop of ion signal near 214.05 nm. The SiO $A - X$ spectrum

simulation suggests that the drop occurs near the $P(11)$, $Q(15)$ and $R(20)$ rotational lines. Figure 6.9b shows the energy levels of SiO excited with 2-photon absorption via rotational levels of the $5-0$ band. The red, green and blue curves with hollow circles denote excitation via P, Q and R rotational branches respectively. The energy scale is relative to the energy of the rotational levels of SiO^+, i.e. the horizontal line at $E = 0$ cm^{-1} corresponds to the SiO^+ molecules with $N^+ = J'$, the slanted straight lines below the horizontal line correspond to $N^+ = J' - 1$, $J' - 2$, and $J' - 3$, while those above it correspond to $N^+ = J' + 1$ and $J' + 2$. The Q line crosses $N^+ = J'$ line near $Q(8)$, $N^+ = J' - 1$ line near $Q(11)$ and $N^+ = J' - 2$ line near $Q(15)$. The crossings define the levels at which 2-photon ionization cannot produce SiO^+ molecules with N^+ equal or higher than the corresponding J'.

The abrupt drop of signal in the $5-0$ band is consistent with reduced photoionization efficiency for excitation that must occur via lines with $N^+ < J' - 2$ as shown in Fig. 6.9b. While ionization via these lines is energetically allowed if SiO^+ is produced at lower N^+ levels, angular momentum conservation requires the electron to detach as a high angular momentum partial wave. For example, ionization via the $Q(16)$ line can produce SiO^+ with $N^+ < 13$. If the photoionization of SiO obeys the Hund's case (b) selection rule [**170**], a transition with $|\Delta N| \leq l + 1$ for $N^+ = 13$ requires $l \geq 2$.

It was shown in [**166**] that the cross sections for photoionization of neutral particles tends to non-zero values near the threshold even for high angular momentum waves of the electron. In other words, partial waves of the electron near threshold are not limited to $l = 0$ or 1, higher l partial waves occur. Since total angular momentum is conserved, high values of l allow large $\Delta J = J'' - J^+$ change during photoionization. On the other

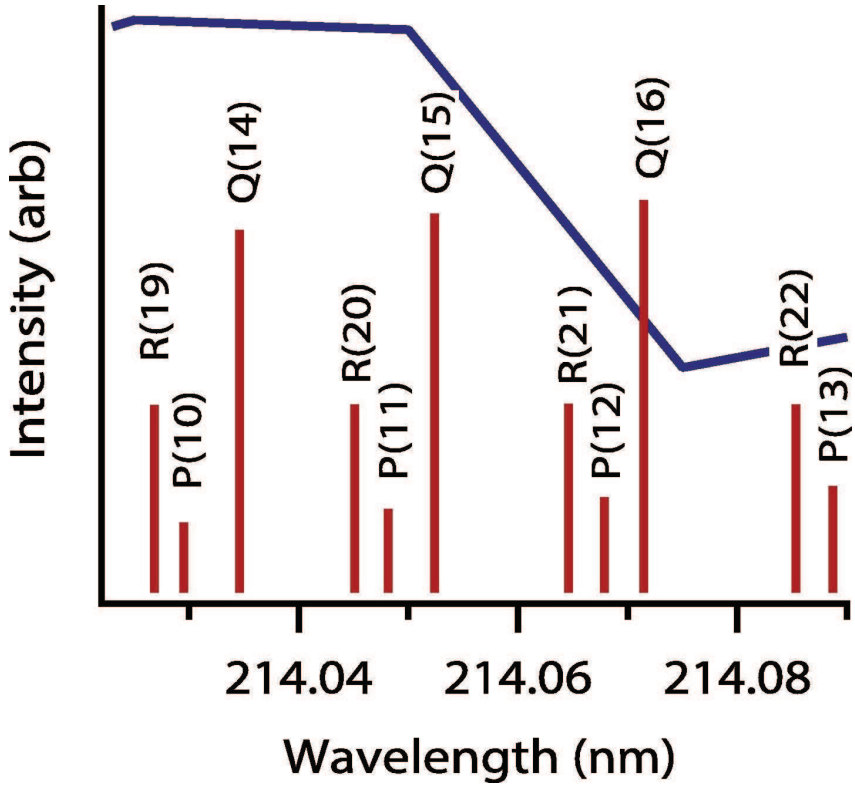

Figure 6.10. The $5-0$ band of $A-X$ of SiO near 214.05 nm (blue dotted line) overlaid with simulated rotational line positions (red vertical lines). The observed beginning of the cut-off corresponds to $Q(15)$, $P(11)$ and $R(20)$ rotational lines which is consistent with the prediction made above using Fig. 6.9 (b) with IP = 11.586 eV.

hand, several studies with PFI-ZEKE technique explored rotationally resolved spectra of different molecules near threshold. It was found that there are no strict selection rules but in many cases "propensities" for a small change of angular momentum upon ionization exist [**102, 165**], where lines with $\Delta J \leq 5/2$ are largest and intensity quickly falls off for higher ΔJ.

The abrupt drop of signal in the $5-0$ band near $Q(15)$ line is consistent with $l = 0$ or 1, i.e. propensity for small ΔJ change upon photoionization. If large ΔJ were allowed, one would expect a gradual reduction of intensity in the $5-0$ band as progressively larger

ΔJ values are reached at higher rotational lines (e.g. $\Delta J = 5/2$ at $Q(15)$, $\Delta J = 7/2$ at $Q(19)$ etc). Limiting l to 0 and 1 results in $|\Delta J| \leq 5/2$ or $|\Delta N| \leq 2$ propensity. The value of $IE_{SiO} - \Delta E_F$ of 11.586 eV satisfies this propensity simultaneously for $R(18)$, $Q(15)$ and $P(11)$ lines of the $5 - 0$ band (see Fig. 6.9b), in good agreement with the rotational levels near the cut-off in Fig. 6.10. It is possible to satisfy the requirement of $|\Delta J| \leq 3/2$ or $|\Delta N| \leq 1$ for $R(18)$, $Q(15)$, and $P(13)$ lines with a value of 11.583 eV, however it is in worse agreement with the observed cut-off. Propensities for $|\Delta J|$ values higher than $5/2$ are in even worse agreement with the observations. Therefore, we picked the value of 11.586±0.003 eV for $IE_{SiO} - \Delta E_F$ of SiO, where the uncertainty of 3 meV is due to a possibility of $\Delta J = 1$ error in the propensity for rotational levels change.

To obtain IE_{SiO} we have to account for depression of the ionization energy by the electric field in the quadrupole trap. The value of the IP depression, ΔE_F, is proportional to the square root of the electric field and may be estimated by the formula

$$\Delta E_F = c\sqrt{F} \tag{6.2}$$

where F is the field in units of V/cm, ΔE_F is in cm^{-1}, and $c = 4 - 6$ depending on the mechanism of ionization [**29**]. For diabatic ionization of Rydberg states $c = 4$ and for adiabatic ionization $c = 6$. The choice of mechanism depends on the slew rate of the electric field. When the slew rate is high, components of Stark manifolds diverge in energy without mixing and the diabatic mechanism is preferred. For a low slew rate or DC field the Stark states have enough time to mix and the ionization is adiabatic. We expect that the trap RF field acting on Rydberg states for many periods will mix the Stark states and result in adiabatic ionization.

The depression of 99 cm^{-1} corresponds to a field of 270 V/cm for Ba ions. The difference in molecular mass of Ba and SiO affects their relative stability in the trap, i.e. SiO^+ formed in a field of 270 V/cm may not be trapped as efficiently as Ba^+. We performed an ion trajectory simulation with SIMION 8.0 [**32**] where 1000 ions of $m/z =$ 138 and 44 were randomly generated inside the ion trap along the photoionization laser beam and their trajectories were simulated for 10 μs. Our simulations show that 61% of all trapped Ba^+ ions were created in a field $\leq$270 V/cm. In the SiO simulation the same fraction (61%) of the trapped ions were created in a field $\leq$130 V/cm. Depression of IE_{SiO} by such a field is $6\times\sqrt{130(V/cm)} = 68$ cm^{-1} or $\sim$8 meV. We estimate that the uncertainty of that figure is not more than 4 meV which equals the difference with the measured ΔE_F for Ba. Including these considerations yields an estimate of IE_{SiO} of 11.594$\pm$0.005 eV. This value is within error bounds of the most reliable previous measurements [**58, 8, 30, 83**]. Interestingly, the current measurement is almost halfway between the most accurate values obtained with PES [**30**] (11.61(1) eV) and a Rydberg formula fit [**8**] (11.584(11) eV) and is within the error bounds of both of them.

Our theoretical prediction for the IP = 11.6138(1) eV overestimates the experimental value by $\sim$20 meV. It is in good agreement for the CCSD(T)/CBS method which is known to achieve an accuracy of 10-20 meV in IP calculations [**85**]. The discrepancy between measured and calculated values may be due to unaccounted effects, such as relativistic motion or core correlation, and from high level dynamic correlation missing in CCSD(T). Previous calculations by Das et al [**25**] underestimated the IP by $\sim$0.7 eV, probably because the MRDCI method could not treat the dynamic correlation in SiO^+ and SiO at the same level.

The sharp bands near 216 nm were assigned to 2-photon Rydberg states transitions. To be prominent in the 1+1 REMPI spectrum, the 2-photon Rydberg state transition must have: 1) good FC overlap with the lower state, 2) high electronic transition probability, e.g. low principal quantum number and resonance enhancement for the 1-photon absorption, 3) high Boltzman population of the lower state, and 4) should be above the ion ground state to autoionize. Based on these assumptions, the Rydberg states involved in this transition is likely due to ($ns\sigma$, $np\sigma$, $nd\sigma$) $^1\Sigma^+$ [$X^2\Sigma^+, v^+ = 1$] and ($nd\delta$) $^1\Delta$ [$X^2\Sigma^+, v^+ = 1$] Rydberg states with $n = 12, 13$. These states are located ~900-1100 cm^{-1} below the $v^+ = 1$ level and above the IP of SiO. The lower state X, $v'' = 1$ has significant population at a temperature of 1000 K and the transition is resonantly enhanced due to the proximity to the A, $v' = 6$ level. Frank-Condon overlap favors transition from $v'' = 1$ to $v^+ = 1$ since SiO and SiO^+ have sufficiently similar bond length and vibrational frequency.

Using 1+1 REMPI on stronger bands of the $A - X$ transition resulted in several thousand SiO^+ ions loaded per single ablation event followed by REMPI ionization. The most convenient loading transition is (5,0) of $A - X$ at 213.977 nm as it is intense and SiO^+ can be loaded with only ~30-300 cm^{-1} of internal energy. Therefore, loading of vibrationally or electronically excited SiO^+ is avoided and the rotational temperature of loaded ions is significantly lower than that of the ablated SiO. Another advantage of the (5,0) transition is that it is not resonant with the $A - X$ and $B - X$ bands of the NO molecule, lying near 215 nm [**56**]. NO has a relatively low IP of ~9.26 eV [**124**] and can be 2-photon ionized below 267 nm. Even though ultrahigh vacuum is used in this work and the NO_x (NO + NO_2) concentration in the air is < 1 ppm, there is enough NO in the vacuum chamber to load a few NO^+ cations per laser pulse with 1+1 REMPI.

Depending on the RF amplitude used for the ion trap, depression of IE_{SiO} by the electric field may not be sufficient to ionize SiO via the (5,0) transition. In this case, an alternative is to use the transitions near 216-216.5 nm range which originate at $v'' = 1$ and produce SiO^+ up to 100-350 cm^{-1} above its ground state origin.

6.2.6. Conclusions

The 1+1 REMPI spectrum of SiO in the 210-220 nm range was recorded. Observed bands were assigned to the $A - X$ band system and 2-photon transitions were tentatively assigned to the $n = 12, 13$ ($ns\sigma$, $np\sigma$, $nd\sigma$) $^1\Sigma^+$ and ($nd\delta$) $^1\Delta$ [$X^2\Sigma^+, v^+ = 1$] Rydberg states. The characterized photoionization channels allow for loading SiO^+ ions into an ion trap where proper selection of the ionization channel allows for loading vibrationally and rotationally cold SiO^+. The observed spectrum enabled a more accurate estimation of the SiO IP than previous measurements found in literature with a value of 11.594(5) eV.

CHAPTER 7

Trapped SiO^+ Experiments

7.1. Characterization of the $C^2\Pi$ (i.e. $(2)^2\Pi$) State

In this section I discuss our work characterizing the previously unobserved $X^2\Sigma^+ \rightarrow (2)^2\Pi$ transition. The empirical convention for naming new states is to label the ground state X and the remaining states with the same spin quantum number are labeled alphabetically with increasing energy in uppercase letters. Excited states with different spin multiplicities are labeled alphabetically using lowercase letters. According to calculations, we expect two electronic states of the same spin to be between the $B^2\Sigma^+$ state and $(2)^2\Pi$. Unless electronic states are close in energy, the accuracy of calculations is typically beyond the level necessary for accurate energy ordering of electronic states. The electronic states below the $(2)^2\Pi$ state are not predicted to be particularly close so an argument can be made to label the newly discovered state as the $E^2\Pi$ state. Internally, however, we have referred to the $(2)^2\Pi$ state as the $C^2\Pi$ state and so I will typically refer to it as the C state in the remaining sections. At the time of writing this section a manuscript detailing our work is in preparation. The manuscript will discuss the unique role of quantum state control in characterizing the spectrum. The state label that we use in that manuscript will be the canonical one. For the purposes of this thesis, I will summarize the results we obtained in our characterization of the $C^2\Pi$ state and how its properties can be used

for state readout. Some of the discussion here may closely parallel the manuscript to be published.

A method for quantum state selective detection of SiO^+ is required to characterize control of the quantum state. Resonantly enhanced photodissociation is an efficient technique that has been used for efficient state detection of cations [**141, 110, 26**] and provides the inspiration for the approach used in this section. The work discussed in this section demonstrates that state detection for SiO^+ can be efficiently performed via a single photon predissociating process.

Before this study, none of the dissociating pathways of SiO^+ had been experimentally investigated, however predissociating quasi-bound states have been theoretically investigated [**22, 25, 61, 145**]. In 1999 Cai and François predicted avoided crossings of low-lying $^2\Pi$ states that result in quasi-bound states [**22**]. Calculations show an avoided crossing between the $(2)^2\Pi$ and $(3)^2\Pi$ states and another between the $(3)^2\Pi$ and $(4)^2\Pi$ states. They calculate the quasi-bound $(3)^2\Pi$ state to have an energy $T_e = 49760$ cm^{-1} and therefore inaccessible with our current lasers except with a two-photon transition. Poor vibrational wavefunction overlap is expected to also be an issue as the potential minimum is shifted outward by ~ 0.3 Å. On the other hand the $(2)^2\Pi$ state was calculated to be in a range of $T_e = 44000 - 45000$ cm^{-1} and therefore accessible with our available lasers.

7.1.1. Experimental Approach

Each experiment uses the setup described in chapter 5. Significant portions of the data collected in the experiments used to characterize control of the SiO^+ quantum state are used here for analysis in determining the molecular constants. Details of the experimental

methods for characterizing the control are available in section 7.4. As in all of the trapped SiO^+ experiments, SiO^+ was loaded into the ion trap using the $A^1\Pi - X^1\Sigma^+(5,0)$ 1+1 REMPI transition slightly blue-detuned from the IP cutoff described in section 6.2.5. The location of the cutoff suggests that the SiO^+ should be in the ground vibrational state with the rotational distribution expected to fall between the $N = 4$ and $N = 15$ rotational states. Blackbody radiation and collisions with the background gas will thermalize the population however this process will take minutes or even tens of minutes to completely thermalize in the low rotational states[1]. In contrast, the time for collecting a single data point is typically on the order of 30 s.

The $X^2\Sigma^+ \rightarrow C^2\Pi$ transition was first probed via a coarse scan using the 4 cm^{-1} broad Ekspla OPO (5.4.1) and the LCFMS frequency chirping method (5.6.2). The resulting spectrum, seen in the blue trace of Fig. 7.1, was recorded without any attempt to control the internal state of the SiO^+. The observed vibrational progression was the first confirmation of the existence of the dissociating state. The first attempt to characterize line assignments for rotational state readout was performed by recording the $C^2\Pi_{1/2}(v = 0) \rightarrow X^2\Sigma^+(v = 0)$ dissociation spectrum of the uncontrolled SiO^+ with the narrower linewidth Scanmate dye laser (5.4.1). We found the spectrum, shown in Fig. 7.2, to be too noisy to assign any spectral features without prior knowledge of the molecular constants.

The post-ionization distribution is expected to be clustered around $N = 4$, $N = 11$, and $N = 15$. The probing rate is expected to be comparable to the blackbody redistribution rates for the lowest of these rotational states and somewhat faster for the

[1]This time scale is empirically determined in section 7.3.3.

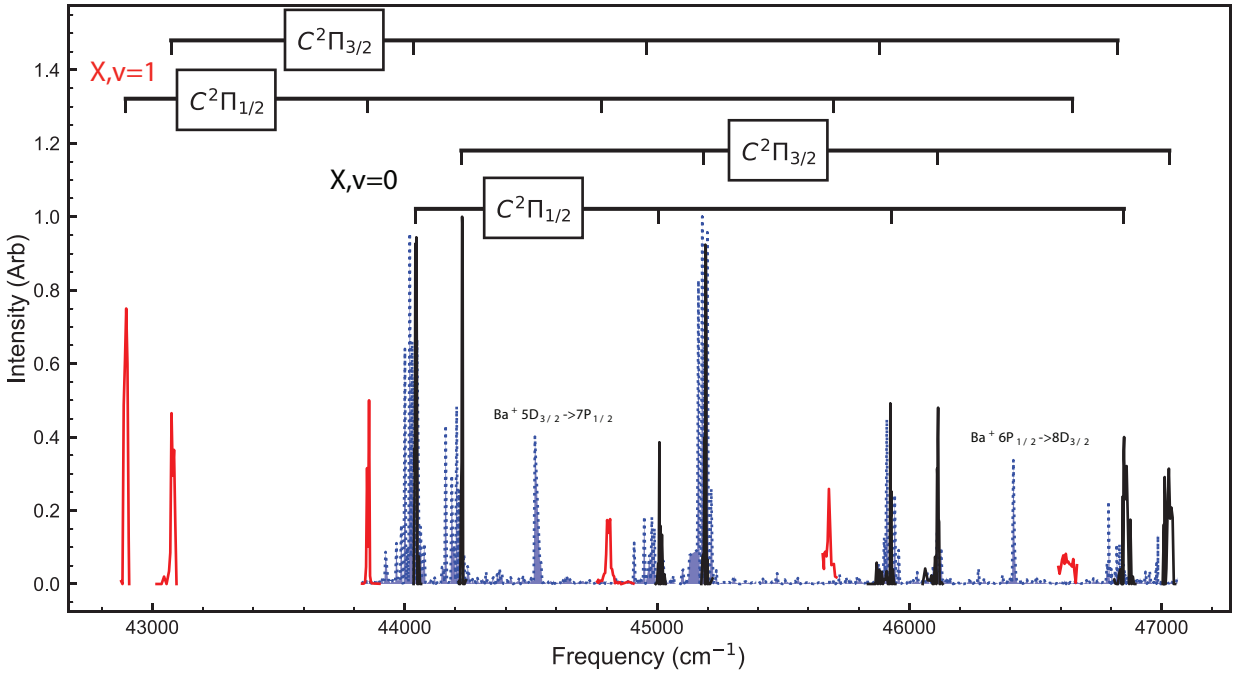

Figure 7.1. The vibrational progression of the $X^2\Sigma^+ \rightarrow C^2\Pi$ transition is plotted for the uncontrolled (blue), rotationally cooled (black), and the vibrationally excited (red) spectra. The uncontrolled SiO^+ population reflects the partially thermalized distribution due to loading via the 1+1 REMPI threshold transition described in section 6.2.5. Spectra recorded using the rotationally cooled samples (see section 7.3) were used to extract band origins for all transitions that weren't recorded using the more accurately and precisely determined dye laser spectrum. The red hotbands were generated after using control methods to populate low N of the $X, v = 1$ state as described in section 7.4.3. Upper spin orbit bands were obscured by the $X, v = 0$ lower spin orbit bands and are therefore not shown. The hotbands confirm the existence of a bound $v = 4$ level for at least the lower spin orbit state. Neglecting the $v = 0 \rightarrow v = 0, 1$ transitions which were measured with rotational resolution, the uncertainties for the band origins were ~ 8 cm^{-1} and were dominated by uncertainty in the calibration of the Ekspla. Included in the spectrum are two labeled Ba^+ transitions used for calibrating the frequency.

highest. This means that the probed distribution will non-thermal and the observed signal size for a given rotational state will be sensitive to the precise timing of the probe laser.

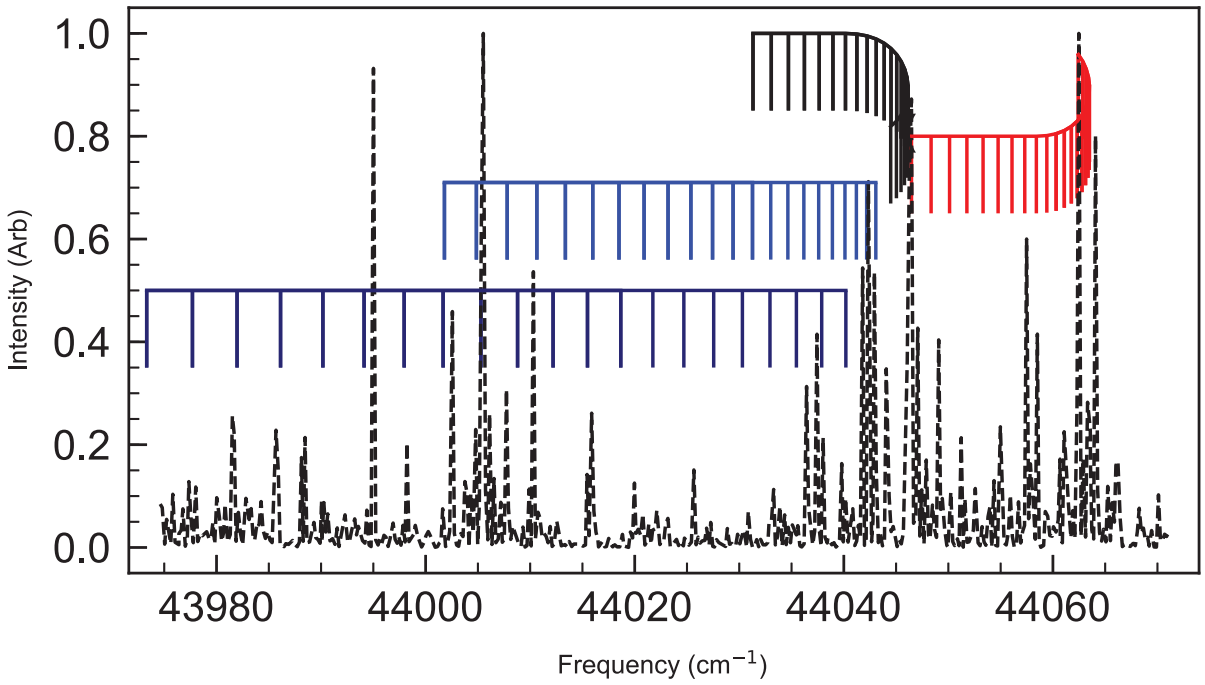

Figure 7.2. The uncontrolled dissociation spectrum of the SiO^+ $X^2\Sigma^+ \rightarrow (2)^2\Pi_{1/2}(0,0)$ transition. The spokes represent the O, P, Q, and R branches (left to right) for $N = 0$ to $N = 22$.

Furthermore, the optimal conditions for LCFMS require on order of 100 SiO^+ per sample implying that shot noise will contribute significantly[2]. These issues combined with heavy congestion of lines near the bandhead and origin explain the inability to interpret the spectrum.

Because of these challenges, control was used to assist in characterizing the $C^2\Pi$ state. In the process a useful interplay developed between characterizing the $X - C$ transition and improving the control technique. The quantum state control scheme is

[2]Low numbers are a consequence of fundamental limitations from Coulomb repulsion on the ion density. E.g. The SiO^+ number density in the laser cooled Coulomb crystal is 10^8 cm^{-3}. This is in contrast to 'low' density neutral beams which have densities exceeding 10^{12} cm^{-3} [**96**].

relatively straightforward and relies on the well-studied $B - X$ transition making precise characterization of the control unnecessary for achieving dramatic enhancement of the population in a select few rotational states. This allows us to overcome low statistics. Control and state detection were iteratively applied such that characterization of new $X - C$ transitions and the controlled distribution were performed simultaneously. As new lines were identified, molecular constants were refined and determined to increasingly higher order, enabling accurate extrapolation of higher energy rotational transitions. This iterative process was applied up through the production of rotational states well beyond thermal energies known as super-rotors [**90**].

The first use of control was rotational cooling into the ground state. A complete analysis of rotational cooling is discussed in section 7.3. Ground state preparation allowed for a two order of magnitude signal enhancement compared to thermal on measurement of transitions near the band origin and provided valuable information on the efficiency of dissociation and molecular constants describing the vibrational structure of the $C^2\Pi$ state. Later, full rotational control and some vibrational control was applied to more fully characterize the spectrum. For the most energetic states, control enhanced the signal by at least three or four orders of magnitude compared to thermal. Details on rovibrational control are described in section 7.4.

For study of the rotational structure, the SHG output of a dye laser (Lambda Physik Scanmate, see 5.4.1) was used to probe the spectrum. Light near 455 nm was generated by pumping a methanol solution of Coumarin 450 dye with the third harmonic of a pulsed YAG laser and subsequently passed through a home-built SHG stage to produce the light near 227 nm. An independent measurement of the laser linewidth shown in Fig. 7.3

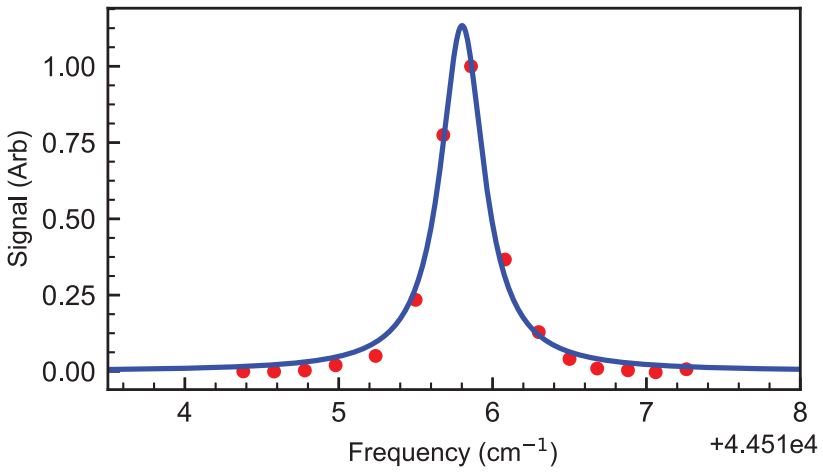

Figure 7.3. The $5d^2D_{3/2} \rightarrow 7p^2P_{1/2}$ transition of Ba^+ as recorded by the dye laser. The observed linewidth, averaged with other measurements, was found to be 0.239(7) cm^{-1} and is entirely dominated by the laser profile. See section 5.2 for more detail on methods used for this measurement.

was recorded to aid in characterization of the $X - C$ transition linewidths. Frequency calibrations for the OPO and dye laser are discussed in appendix B.1.

7.1.2. Molecular Constants

The vibrational energy levels and spin orbit splitting is modeled using a power series expansion described by

$$G(v, \Lambda, \Sigma) = T_e + \omega_e(v + \frac{1}{2}) - \omega_e x_e(v + \frac{1}{2})^2 + A_e \Lambda\Sigma \tag{7.1}$$

where $\Omega = \Lambda + \Sigma$ and the values are determined by the molecular term symbol $^{2s+1}\Lambda_\Omega^{+/-}$ and A_e is the spin orbit splitting.

Table 7.1. Molecular constants of $C^2\Pi$. Parameters and uncertainties obtained using fit with Eqn. (7.1).

Source	T_e (cm^{-1})	ω_e (cm^{-1})	$\omega_e x_e$ (cm^{-1})	A_e (cm^{-1})
This work	44222(2)†	989(3)	14.8(1.6)	181.0(2)‡
Theory [**22**]	44680	913.2	15.13	–
Theory [**61**]	44556	978	–	–
Theory [**25**]	44371	917	–	–
Theory [**145**]	44468.65	985.462	8.12351	153.63

† T_e is estimated using $\omega_e, \omega_e x_e$ of X from ref. [**24**].

‡ The splitting and structure of the C state is assumed to be the same in the fit.[3]

Band origins were determined using the broader linewidth OPO with the exception of the band origins measured by the dye laser of $X(v = 0) \rightarrow C(v = 0, 1)$ for both spin orbit states. In all, band origins for both spin orbit states were measured for $X(v = 0) \rightarrow C(v = 0 - 3)$ and $X(v = 1) \rightarrow C(v = 0)$. Band origins for the lowest spin orbit state only were measured for $X(v = 1) \rightarrow C(v = 1 - 4)$. The upper spin orbit states of the vibrational hot bands were obscured by overlap with transitions originating from $X(v = 0)$. Results of the fit to Eqn. (7.1) can be seen in Table 7.1 where the minimum of the X potential is used to define zero energy. Values are compared to previous theory calculations. The curvature (i.e. ω_e) of the potential is generally consistent with theory calculations, however calculations systematically overestimate the relative energy from the ground state.

Determination of the rotational structure for $C(v = 0, 1)$ was performed using line assignments obtained from the rotationally controlled spectra shown in Figs. 7.18 and 7.19 in section 7.4. Molecular constants are listed in Table 7.2 and are compared to previous theoretical calculations. A fit of the line assignments was performed in PGOPHER

10 [**164**] using fixed molecular constants for the $X^2\Sigma^+$ state experimentally determined by Cameron et al [**24**].

Constants in Table 7.2 are determined using the following relations defined in Herzberg [**56**]:

$$\begin{aligned} B_v &= B_e - \alpha_e(v + 1/2) \\ D_v &= D_e + \beta_e(v + 1/2) \end{aligned} \tag{7.2}$$

where

$$\begin{aligned} \beta_e &= D_e \left(8\frac{\omega_e x_e}{\omega_e} - 5\frac{\alpha_e}{B_e} - \frac{\alpha_e^2 \omega_e}{24 B_e^3} \right) \\ D_e &= 4\frac{B_e^3}{\omega_e^2} \\ \frac{\alpha_e}{B_e} &\approx \frac{\omega_e x_e}{\omega_e} = x_e \end{aligned} \tag{7.3}$$

are the analytically derived relationships for the rotational and vibrational coupling. The extracted constants for D_0, D_1, B_0, and B_1 from the separate rotational structure fits of each vibrational transition are found to be consistent with the analytical expressions for D_e, β_e, and α_e which increases confidence that the fitted parameters are determined accurately and demonstrates general consistency of vibrational and rotational parameters. Because the expression for α_e is a rough approximation, α_e was determined by taking the difference of B_0 and B_1 and then used to determine B_e. The value of the remaining terms (i.e. β_e and D_e) are derived using the expressions in Eqn. (7.3). These derived values are consistent with the expression in Eqn. (7.2). There is also good agreement of rovibrational structure with previous *ab initio* calculations by Shi et al [**145**].

Table 7.2. Molecular constants of $C^2\Pi$ state of SiO^+.

Source	B_e (cm^{-1})	r_e (Å)	$D_e \times 10^6$ (cm^{-1})	$\alpha_e \times 10^3$ (cm^{-1})	$\beta_e \times 10^6$ (cm^{-1})
This work	0.66921(15)	1.57564(18)	1.224(7)	7.15(15)	0.072(5)
Theory [**22**]	0.66698	1.5768	–	–	–
Theory [**61**]	0.6586	1.586	–	–	–
Theory [**25**]	0.6439	1.604	–	–	–
Theory [**145**]	0.66773	1.5750	1.2263	6.60150	–

v		$C^2\Pi$				
		origin (cm^{-1})	B_v (cm^{-1})	$D_v \times 10^6$ (cm^{-1})	$(q + p/2)$ (cm^{-1})	A (cm^{-1})
0	This work	44133.19(6)	0.66564(13)	1.26(5)	-0.0041(22)	180.11(11)
	Theory [**145**]		0.664405	1.23514		153.63
1	This work	45093.43(4)	0.65848(8)	1.293(18)	-0.034(11)	180.52(7)
	Theory [**145**]		0.657580	1.25843		153.63

7.1.3. Predissociation

The presence of rovibrational structure in the $C^2\Pi$ state with the presence of strong dissociation can be explained by the structure of the avoided crossing. The calculated $C^2\Pi$ potential energy curve forms a double-well potential with multiple quasi-bound vibrational modes. This structure can be seen in the potential energy curves (PECs) shown in Fig. 7.4 as calculated by Antonio G. S. de Oliveira-Filho and A. P. de Lima Batista [**116**]. Because the potential is quasi-bound, predissociation is possible via tunneling through the barrier. If this time scale is fast compared to the dissociating laser pulse duration and the radiative lifetime, it will contribute significantly to predissociation. The average lifetime for molecules in the quasi-bound state can be estimated by calculating the classical period of a harmonic oscillator and dividing by the the transmission probability at the classical turning point. That is we can imagine a semi-classical picture of the nuclei vibrating and each time the nuclei reach their maximum classical separation they have a probability of

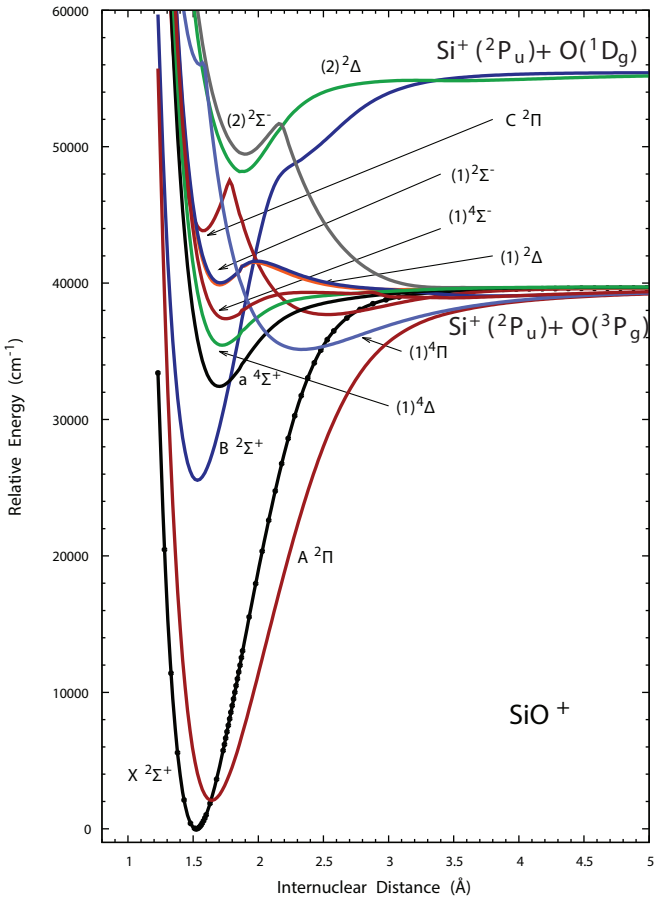

Figure 7.4. Unpublished *ab initio* potential energy curves provided through internal communication by Antonio G. S. de Oliveira-Filho and A. P. de Lima Batista [**116**].The predissociating C state can be seen to be quasi bound. Also present are $C^2\Pi$ state crossings with the $(1)^2\Delta$, $(1)^2\Sigma^-$, and the quartet $(1)^4\Pi$ state.

tunneling through the barrier and dissociating given by the transmission probability. The lifetime is therefore given by [**56**]

$$\tau = \frac{\tau_0}{2} e^{\frac{4\pi}{\hbar}\int dr\sqrt{2m(U(r)-E)}} \tag{7.4}$$

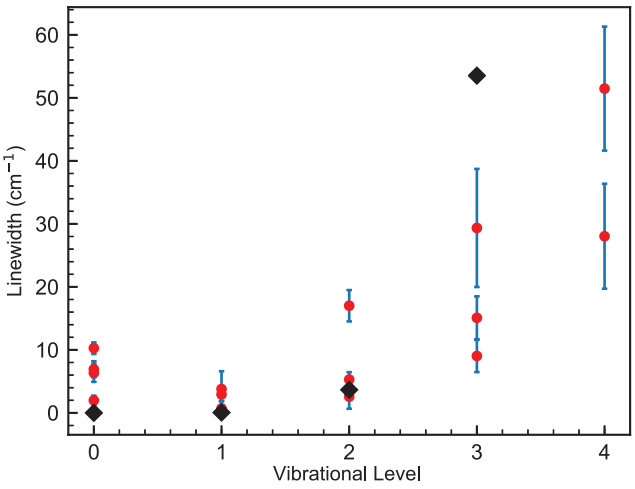

Figure 7.5. Observed linewidths of vibrational band origins of the C state as recorded by the Ekspla OPO shown in red with blue 1-σ error bars derived from Lorentzian fits. The black diamonds represent the calculated linewidths from Table 7.3. Observed linewidth is a convolution of the laser, the rotational distribution, and structure of each transition. Data includes both spin orbit states originating from $X, v = 0$ and the lower spin orbit of $X, v = 1$ hotbands. The $C, v = 4$ state is not able to be accessed from the $X, v = 0$ state and therefore only data from the $X, v = 1$ hotband is available.

where τ_0 is the period of the oscillator, m is the reduced mass, $U(r)$ is the potential, and the integral is calculated over the classically forbidden region. Calculated estimates of the lifetime performed by Antonio G. S. de Oliveira-Filho can be seen in Table 7.3. From Eqn. (7.4) we can see that we expect to see an exponential dependence on energy in the lifetime and therefore the observed linewidth. This is reflected in the calculated vibrational dependence of the lifetime which varies by more than 5 orders of magnitude.

The calculated lifetime limited linewidths from Antonio G. S. de Oliveira-Filho and A. P. de Lima Batista are also plotted alongside the linewidths of the band origins of the $X \rightarrow C$ transitions as measured using the OPO in Fig. 7.5. The recorded linewidths are subject to several factors that limit their accuracy and no corrections are attempted.

Rotational resolution is not possible because the linewidth of the OPO is $\sim$ 4 cm^{-1}. Furthermore, the number of lines present near the origin depends on which spin orbit state is probed and the distribution of the rotational population. These lines are not resolvable and therefore will contribute to artificial broadening of the spectrum. Most of the lines were recorded using the noisier frequency chirp method instead of the less noisy the single frequency method[4] and therefore the ability to fit the spectrum to an expected distribution and extract a linewidth is not feasible. The SNR of the higher vibrational levels was also reduced, likely due to a combination of weaker laser power at those wavelengths and smaller FCFs. The values in Fig. 7.5 are therefore not meant to provide an accurate quantitative description, rather they are meant to demonstrate the overarching qualitative behavior. Regardless, the accuracy of the highest observed vibrational levels is largely unaffected by the OPO linewidth and the rotational distribution bandwidth which are significantly smaller than the total observed linewidth. The values listed in Table 7.3 are the best attempt to estimate the actual lifetime limited linewidths.

Even without precise corrections to the observed linewidths, we are able to conclude some things about the data and the calculations. Assuming that levels above the top of the crossing are not also quasibound, the presence of $v = 4$ already indicates that the calculated quasi-well depth is too small. This could explain why the observed linewidth for $v = 3$ is smaller than the calculated linewidth as a larger barrier will result in an increased predissociation lifetime and therefore decreased linewidth.

This conclusion, however, is at odds with a comparison of the lifetime of $C(v = 0, N = 0)$ state which appears to be shorter than the calculated lifetime by more than an order

[4]See section 5.6.2.2.

of magnitude. A deeper well would suggest a long lifetime, however in section 7.3, I demonstrate that nearly all of the SiO^+ (94%) is dissociated in single pulse by an ~ 8 ns laser pulse implying that the $C(v = 0, N = 0)$ lifetime is < 3 ns (i.e. $\Gamma > 0.002$ cm^{-1}) and likely significantly shorter. The discrepancy suggests that the tunnel width may be significantly narrower than calculated or it may also imply the presence of an additional predissociating mechanism.

Several states are expected to overlap the $C^2\Pi$ state that may contribute to predissociation through a perturbative interaction. Cai and François calculate a crossing of the repulsive regions of the $(1)^2\Delta$ and $(1)^2\Sigma^-$ states with the bound region of C near the inner turning point around $v = 1$ [**22**]. They also predict an additional crossing of the repulsive region of the $(1)^4\Pi$ state at nearly the same energy on the outer classical turning point. Similarly, Chattopadhyaya et al reproduce the same crossings at similar energies [**25, 22**]. These crossings are also present in the unpublished PECs provided by de Oliveira-Filho and A. P. de Lima Batista [**116**] in Fig. 7.4. The role of perturbations from nearby states may also explain the large discrepancy in linewidth between the two $v = 3$ spin orbit states seen in Table 7.3.

Strict selection rules for perturbations dictate that the predissociative states must have $\Delta J = 0$ and both states must be positive or both must be negative [**56**]. This nominally rules out predissociation via the $(1)^2\Sigma^-$ state. The quartet state is capable of contributing via the spin-orbit interaction [**97**] and the $(1)^2\Delta$ also represents an allowed transition ($\Delta\Lambda = 0, \pm 1$) [**56**]. Unlike predissociation via tunneling, predissociation via coupling to a repulsive potential can exhibit vibrational predissociation preferences. Coupling depends on vibrational wavefunction overlap between the repulsive state and the (quasi-)bound

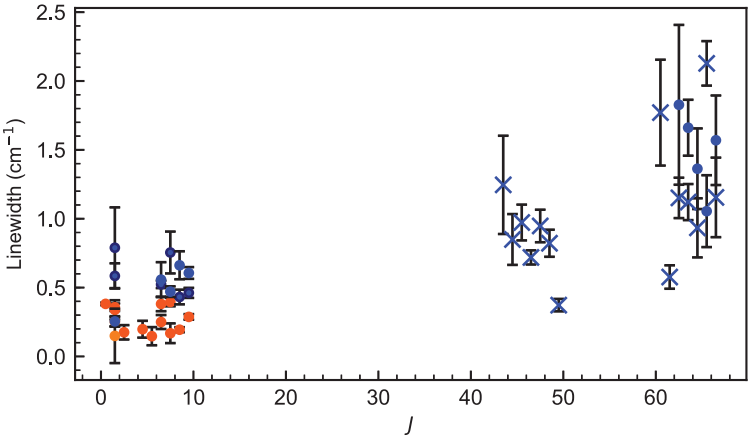

Figure 7.6. Observed linewidths of the $C^2\Pi$ state as a function of J for $v = 0$ (orange points) and for $v = 1$ (blue points). Linewidths are not corrected for contribution from the dye laser and no distinction is made for spin orbit state or rotationless parity. Data points marked with a cross indicate linewidths taken from transitions with unresolved spin-rotation splittings that may contribute to over estimation of the linewidth.

state which may not necessarily monotonically increase with vibrational energy as it does in the tunneling case. Similarly, the rotational state dependence may be non-trivial [**162**].

The rotational state dependence of the linewidths are shown in Fig. 7.6. The linewidths are determined by fitting the data from section 7.4 to a Lorentzian. Fitting to a Lorentzian proved to be significantly better than a Gaussian which exhibited poor agreement in the tails of the line profile. Only the data recorded using the single frequency method was used for linewidth extraction as the data recorded using the frequency chirp method was found to be inconsistent and unreliable[5]. Despite the anomalously large ground rovibrational linewidth[6], no obvious qualitative feature is present that would suggest the influence of a perturbing, predissociating repulsive potential well. Though data

[5]See again section 7.4 and generally section 5.6.2 for discussion of the techniques

[6] Equivalently, the anomalously short lifetime.

Table 7.3. Calculated vibrational energies and linewidths of $C^2\Pi$ provided by Antonio G. S. de Oliveira-Filho compared to the experimental values.

$C^2\Pi$		E (cm^{-1}) †		linewidth (cm^{-1})	
v	N	Thy	Expt.	Thy	Expt.
0		44327.49	44712.19(6)	0.00015	0.08(1)
1	0	45297.97	45672.70(4)	0.056	0.237(16)
2	0	46243.06	46591(6)	3.7	1.9(1.1)
3	0	47155.16	47509(8)	53.5	6(3)‡ 27(9)
4◇	0	–	48347(11)	–	38(6)

† Energies defined using minimum of X potential as 0.

‡ $v = 3$ showed different linewidths for the lower (top) and upper (bottom) spin orbit states.

◇ $v = 4$ was not quasi-bound in calculation. Measurement of the linewidth is for the lower spin orbit state only.

for the linewidths of large J are not shown for $v = 0$ due to the spectra being recorded with the frequency chirp method, there was no obvious indication of the linewidth changing between $J = 9.5$ and $J = 50.5$. The flatness of the linewidths in $v = 0$ at low J and the monotonic increase of linewidths in $v = 1$ with J is consistent with tunneling behavior. The linewidth is expected to increase in an exponential-like way with J. Such exponential behavior is seen, for example, in the dissociation of molecules with rotational energies above dissociation limit where dissociation is possible by tunneling through the centrifugal barrier [**168**].

The linewidths in Fig. 7.6 are plotted without correction for contribution from the laser and thus represent an overestimate of the natural linewidth. Independent measurement of the laser linewidth was found to be 0.239(7) cm^{-1} FWHM and described by a Lorentzian

(see Fig. 7.3). Some R branch transitions of $X^2\Sigma^+(v = 0) \rightarrow C^2\Pi_{3/2}(v = 1)$ are used in the figure for determining linewidths and are indicated by a cross. These transitions include contribution from both spin-rotation states of X to the same excited state of C which has the effect of systematically increasing the observed linewidth by approximately the spin-rotation splitting. The systematic shift was not observable for $J > 60$ though the splitting is between 0.62 and 0.67 cm^{-1} in this range. The splitting for $42.5 < J < 50.5$ ranges from 0.48 to 0.52 cm^{-1} and therefore should contribute significantly to the observed linewidth. Because both the measured profile of the transition and the laser are Lorentzian, a deconvolution of the measured profile to extract the natural linewidth is equivalent to subtracting the laser linewidth. An average over the linewidths for $J < 10.5$, which are observed to be constant within error for both $v = 0$ and $v = 1$, allows us to make an estimate and comparison of the calculated and observed linewidths for the ground rotational states of $v = 0, 1$. A comparison of calculated and observed linewidths are listed in Table 7.3. The $v = 0$ linewidth of 0.08(1) cm^{-1} is consistent with the lower bound 0.002 cm^{-1} determined by the minimum single pulse dissociation probability. Contribution to the linewidth from power broadening was avoided by using neutral density filters and observation of reduced dissociation rates.

7.1.4. Discussion

Firm conclusions on the influence of nearby perturbing states and tunneling lifetimes will require more accurate determination of C state rovibrational level lifetimes, including systematic analysis of e and f rotationless parity states and separate treatment of spin orbit states. The current analysis relies on a limited sampling of rotational state linewidths

in $v = 0, 1$ and poor resolution combined with noisy measurements recorded using the chirp method for the estimation of the linewidths of vibrational states greater than $v = 1$. Characterization of the broader OPO light source and the impact of the rotational distribution on the linewidths has not been carefully performed. This limits analysis and strength of conclusions that can be drawn from measurements of excited vibrational levels of C.

Application of molecular constants to reconstruct the potential energy curve would also help clarify the contribution of predissociation due to tunneling through the barrier and separate the contribution due to predissociation via interactions with other repulsive regions of electronic states. The analysis would also benefit from direct calculations of the effect of the perturbing interactions on the predissociation lifetime in a state-dependent way. The additional measurement of more extreme rotational states (i.e. super-rotor states) will help more carefully characterize the role of tunneling to carefully disentangle its affects from other perturbations. Though much of the linewidths left unmeasured will not likely be limited by the laser linewidth, measurement of the low v, J states with a narrowband CW laser can more precisely and accurately determine discrepancies between spin orbit states and rotationless parities. Careful comparison of line strengths can also be used to determine FCFs and transition dipole moments. Finally, the well-depth of the quasi-bound region has not been determined yet, nor has it been conclusively confirmed that $v = 4$ is the highest quasi-bound level. Determination of the highest quasi-bound level will significantly constrain uncertainty in the well depth and barrier width.

7.1.5. Conclusions

The $X^2\Sigma^+ \rightarrow C^2\Pi$ transition of SiO^+ has been recorded for the first time. We have observed the rotational structure of the $X^2\Sigma^+(v = 0) \rightarrow C^2\Pi_{1/2,3/2}(v = 0, 1)$ sub bands and identified the band origins of (0,$v < 4$) progression and (1,0) hotband for $\Omega = 1/2, 3/2$ as well as the (1,$v \leq 4$) hotband vibrational progression for $\Omega = 1/2$. Characterization and observation of the predissociating $C^2\Pi$ state was facilitated by laser control of the internal state of trapped SiO^+. This control overcame difficulties associated with low densities and quantities due to Coulomb repulsion.

The extracted molecular constants are generally in reasonable agreement with previous theoretical calculations. The presence of $v = 4$ is in conflict with the expected well-depth according to calculations which predict quasi-bound levels extending only to $v = 3$. Consequently the predicted tunneling lifetime is overestimated for $v = 3$. On the other hand, the predicted tunneling lifetimes of the lowest vibrational states appear to be significantly longer than observed even before correcting for the underestimated well-depth. This indicates that another predissociating mechanism is likely involved. More precise and accurate determination of rovibrational state dependence on linewidths is required to better understand the influence of all possible predissociating mechanisms before firmer conclusions can be drawn. Future experiments involving a tuneable narrowband CW laser are planned that will improve understanding of the $C^2\Pi$ state.

7.2. SiO^+ Reaction

The reaction of SiO^+ with H_2 has been suggested to play an important role in the production of interstellar SiO by Turner and Dalgarno, however it was unknown at the time whether this reaction was exothermic [**158**]. Later, Fahey et al observed that the reaction $SiO^+ + H_2 \rightarrow SiOH^+ + H$ was exothermic with a measured rate constant of $3.2(1.0)\times10^{-10}$ $cm^{-3}s^{-1}$ [**41**]. Because hydrogen gas is smaller than all other gases, it will diffuse through the vacuum chamber walls at the highest rate and therefore it is the most difficult gas to remove from the vacuum chamber after all other non-permanent outgassing sources have been depleted. Thus as the vacuum chamber reaches ultra high vacuum (UHV), hydrogen typically represents 95% of the background gas composition [**131**]. This presents an issue for experiments involving trapped SiO^+ as reactions with the background hydrogen will limit the lifetime of the trapped species and systematically bias results. It also presents opportunities to perform experiments on the reaction and its dependence on the internal state of SiO^+. In this section I discuss the measurements of the reaction rate of $SiO^+ + H_2 \rightarrow SiOH^+ + H$ and also estimate a rate constant of $8.5(3)\times10^{-11}$ $cm^{-3}s^{-1}$ which is in more than a 2σ tension with the only known previously recorded value found in the literature.

7.2.1. Experimental

For all experiments the setup described in detail in chapter 5 was used. In each instance a sample of order 100 SiO^+ was co-loaded into a laser-cooled Ba^+ Coulomb crystal (numbering of order 1000) using 1+1 REMPI on the (5,0) band of the $A-X$ transition of laser

ablated SiO. The reaction rate of SiO^+ with H_2 was measured using two qualitatively different methods.

The first method uses the LCFMS method described in section 5.6.2. The estimated mass resolving power is $\frac{m}{\Delta m} \approx 30$ which is not sufficient for resolving mass 44 (SiO^+) from mass 45 ($SiOH^+$). In terms of secular frequency, the linewidth of secular excitation corresponds to 11 kHz and the mass shift is 7 kHz. With enough averaging the contribution of the two resonances can be separated and the shift in frequency of the SiO^+ (reactants) relative to the $SiOH^+$ (products) can be discerned. An example of this shift in the secular frequency resonance can be seen in Fig. 7.7 where the peak of the signal asymptotically approaches a shift from the original peak by ≈ 7 kHz, consistent with an increase of 1 u.

Using this method, the background pressure was varied by applying various currents to a titanium sublimation pump (TSP). The pressure increased with the temperature of the TSP and was allowed to reach (quasi-)equilibrium. In all cases the background gas was assumed to be composed exclusively of hydrogen. This assumption is consistent with literature [**67, 131**] and in house measurements of other UHV systems using an RGA that show hydrogen composing $> 90\%$ of the background. Water, which can remain in vacuum systems for extended periods of time, was removed via baking and simultaneous application of a turbo molecular pump. It was also confirmed to not significantly contribute to the overall pressure with a noted lack of detectable Si^+ reaction via the exothermic reaction $Si^+ + H_2O \rightarrow SiOH^+ + H$ [**41**] over multiple hours of waiting. It is worth noting that no reactions resulting in a mass shift were observed with Si^+ nor with $SiOH^+$ and the only reaction with SiO^+ caused its mass to shift by 1 u (i.e. conversion to $SiOH^+$). This eliminates significant contribution from a number of gases found in the atmosphere

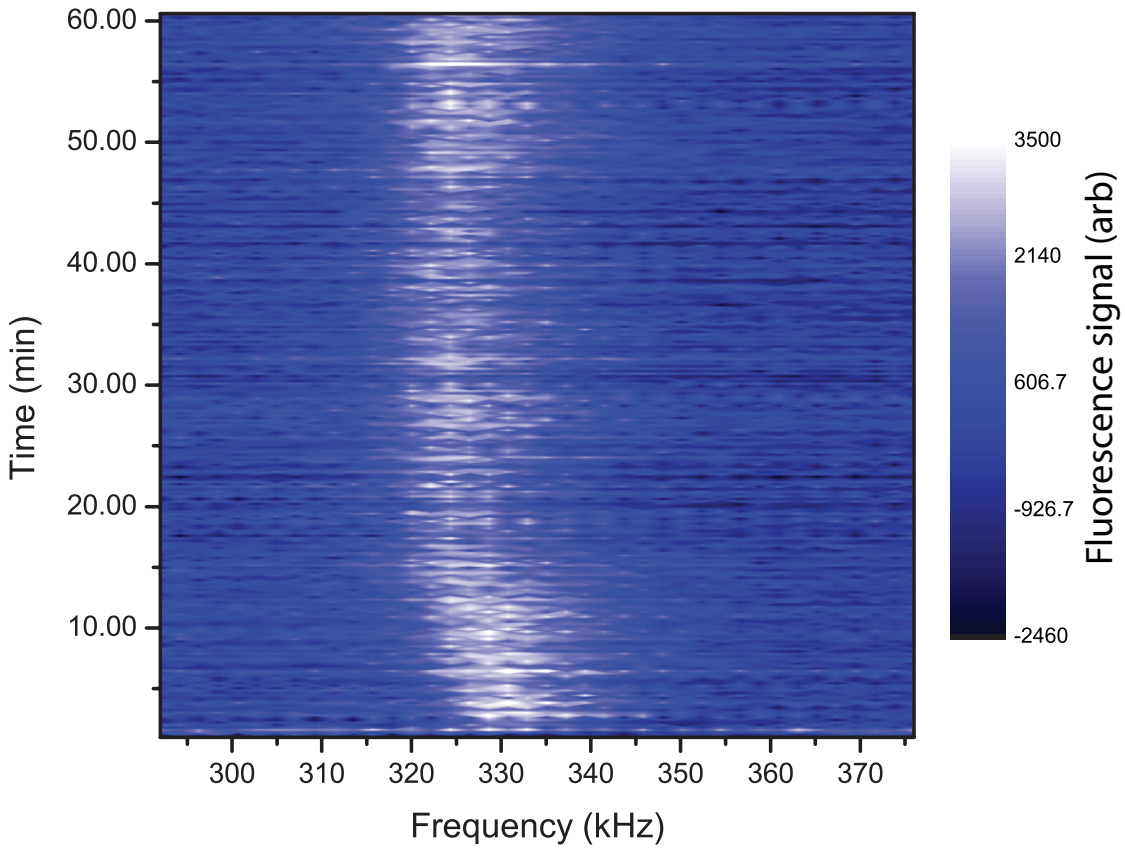

Figure 7.7. Ba^+ fluorescence as a function of secular excitation frequency using the frequency chirp method described in section 5.6.2. The shift in excitation frequency of the Ba^+ fluorescence dip indicates a shift in the mass over time due to H_2 reaction with SiO^+. Each horizontal time slice is modeled by the sum of two Gaussians, one at the mass of SiO^+ ($m = 44$ u) and one at $SiOH^+$ ($m = 45$ u) as shown in Fig. 7.8.

including N_2O, NO_2,and O_2 [**19**]. The presence of an ion pump also serves to remove noble gases which would otherwise be undetectable in reactions.

The second method for extracting the reaction rate relies on the complete dissociation of the unreacted SiO^+. After having trapped a sample of SiO^+ for a predetermined amount of time, the rotational cooling laser is turned on and the dissociation laser is pulsed until no further dissociation occurs. In this experiment the fraction of undissociated species

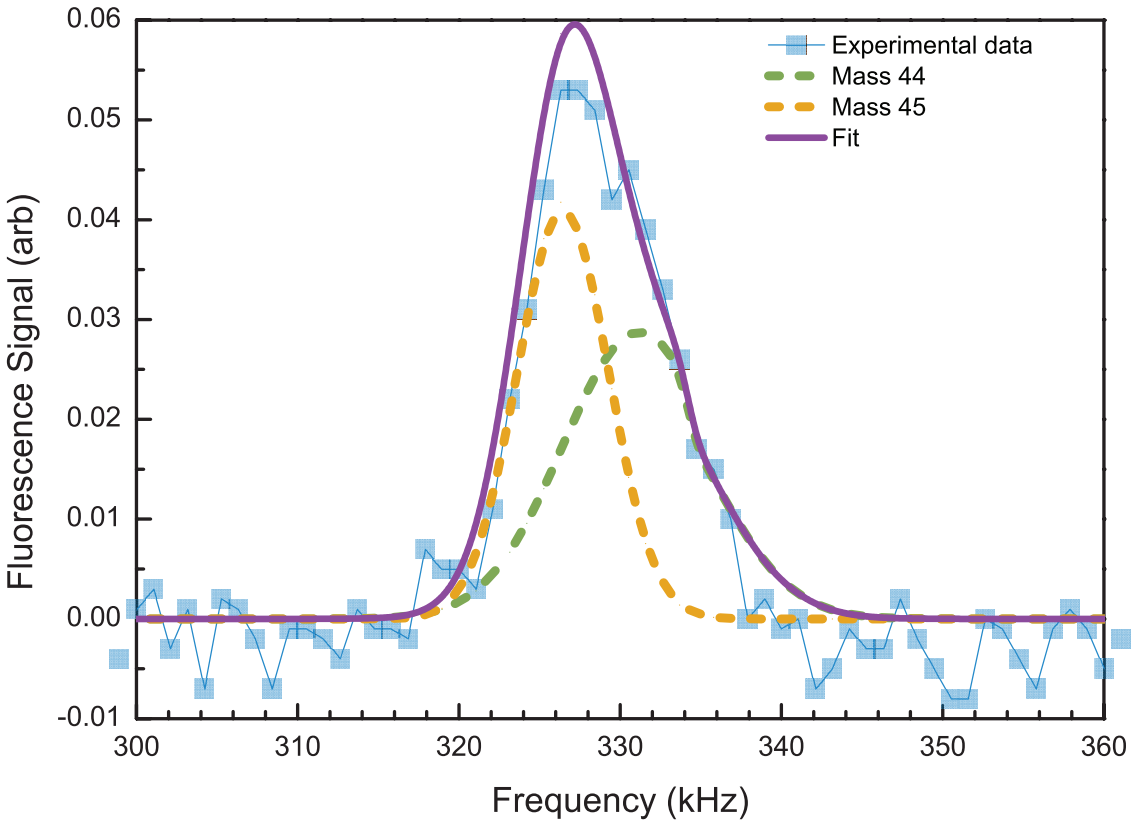

Figure 7.8. Each measurement of the secular frequency spectrum contains reacted and unreacted $SiOH^+$ that is modeled by the sum of two Gaussians. The reaction rate of the data in Fig. 7.7 is extracted using a global fit where the amplitude of the SiO^+ mass is modeled as an exponential decay and the amplitude of the $SiOH^+$ is modeled using an asymptotic rise with the same rate.

remaining in the trap corresponds to the fraction of SiO^+ converted into $SiOH^+$. This represents a more direct measurement of the reacted ratio at the expense of more time needed for collecting data.

7.2.2. Reaction Rate

The reaction rate recorded using the first method (i.e. monitoring the secular frequency resonance shift as a function of time) is extracted using a global double Gaussian fit of the mass spectrum as a function of time. An example of a single time slice of the spectrum is shown in Fig. 7.8. The model assumes a constant rate of conversion of SiO^+ into $SiOH^+$ or equivalently that the number density of hydrogen stays constant throughout the experiment. Thus a single reaction rate is used to model an exponential decay of the amplitude of the Gaussian centered at the frequency of the SiO^+ signal and a corresponding asymptotic increase of the amplitude of the Gaussian centered at the frequency of the $SiOH^+$ signal. Also known as a Stern-Volmer plot in the chemistry literature, Fig. 7.9 plots the fitted rates and their statistical uncertainties as a function of the estimated hydrogen number density. The (second-order) rate constant extracted from the slope of linear fit of the data is found to be $1.0(5) \times 10^{-10}$ cm^3s^{-1} which is a more than 2σ disagreement with the rate constant of $3.2(1.0) \times 10^{-10}$ cm^3s^{-1} measured by Fahey et al [**41**]. The large disagreement leaves open the possibility for unaccounted for systematic shifts. A number of systematic shifts are considered in appendix B.2 and ruled out as insignificant.

Close inspection of the fit in Fig. 7.9 shows large disagreement for several of the data points that is unlikely to be explained by statistical uncertainty in the extracted rate alone. This suggests that there exists another source of uncertainty. The source of this additional error(s) is not well understood, however changes in Doppler cooling lasers and patch potentials are known to occur on time scales shorter than experimental time scales ($\sim$ 50 min) and are capable of causing a shift in the secular frequency resonance.

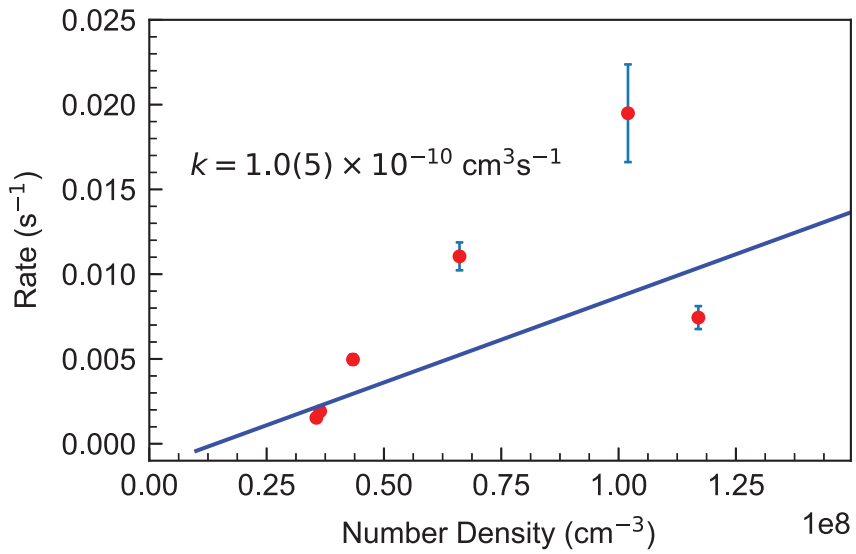

Figure 7.9. The measured reaction rate is plotted as a function of estimated number density according to the ion gauge reading in the vacuum chamber. Absolute calibration of the the ion gauge pressure is not known and thus the rate constant is extracted using a linear fit. Estimated number density is calculated using the gas correction factor of 0.46 assuming background gas is 100% hydrogen.

The size of the Coulomb crystal and the ratio of SiO^+ and Ba^+ can also change the coupling between $SiOH^+$ and SiO^+ as well as shift resonances. It is also possible that the composition of the gas released during heating of TSP changed from run to run as the sources for different gases released from the TSP were depleted over time. The scale of each of these effects has not been investigated in detail however they likely contribute significantly to the observed variation.

In an attempt to rule out potentially unknown systematic effects due to the method of extracting reaction rates from secular frequency measurements, the more direct approach of measuring the fraction of species near mass 44 able to be dissociated was performed as

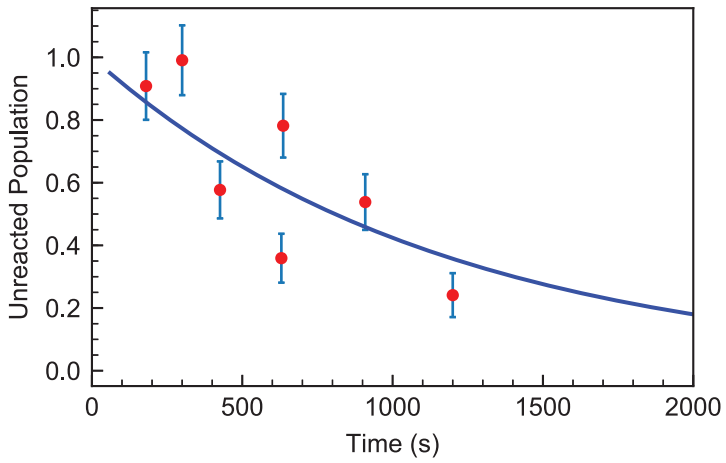

Figure 7.10. The measured reaction rate of $SiO^+ + H_2 \rightarrow SiOH^+ + H$ using dissociation of SiO^+. The data is fit to an exponential decay with the only free parameter being the fitted $1/e$ time constant of 17(3) min or (pseudo) first-order reaction rate of $0.98(17) \times 10^{-3}$ s^{-1}. The Hydrogen number density at the time of the measurement was 14×10^6 cm^{-3} according to the IG reading.

an independent check. The result of this measurement is shown in Fig. 7.10. This measurement was performed more than a year after the previously described measurements allowing the vacuum pressure to decrease by a factor of 2.5 from the lowest previous measurement. Extrapolation of the linear fit is found to be consistent with the dissociation measurement suggesting that no significant systematic effects due to the method of detecting the secular frequency are detectable.

A fit of all the data including the dissociation measurement was performed and the results are shown in Table 7.4. The refined rate constant is reduced from the previous linear fit but still consistent. The implied pressure reading offset from the fit is also consistent with the specified accuracy of the IG. In Table 7.4 I also list the calculated Langevin capture rate. Many ion-neutral reactions are barrierless and in the case of

Table 7.4. Rate constant extracted from linear fit of all data.

$SiO^+ + H_2 \rightarrow SiOH^+ + H$	
k (10^{-10} cm^3s^{-1})	0.85(33) 3.2(1.0) †
IG offset (10^{-10} Torr)‡	-2(4)
k_l (10^{-10} cm^3s^{-1})◇	11

† From ref. [**41**]

‡ IG offset calculated from linear fit and k

◇ The estimated Langevin capture rate constant for H_2.

an atomic ion and nonpolar neutral molecule, this means that the reaction rate is well approximated by the Langevin capture rate [**175**]. However, the observed reaction rate constant is more than an order of magnitude smaller than the Langevin rate. This suggests that the orientation of the SiO^+ with respect to the colliding H_2 is important for reactions and may imply internal state dependence of the rate constant.

7.2.3. Conclusions

The reaction rate and (in)elastic collision rate with the background gas have important implications for use of SiO^+ in ion trapping experiments. Understanding lifetimes, coherence times and the total time before needing a new sample of unreacted SiO^+ requires understanding these processes and the role of the UHV gas environment before their effects can be isolated from BBR, natural lifetimes, and laser coherences. A quantitative understanding of the reaction rate in the UHV environment is also necessary for progressing with more sophisticated chemistry measurements involving quantum state control. The ability to apply state control of SiO^+ (see section 7.4) opens up new ways to more

precisely test the dependence of the reaction rate on the internal state. Preliminary measurements are currently underway to test the dependence of the rotational energy of SiO^+ on its reaction rate with the background Hydrogen. In particular, we are investigating the regime where the rotational period approaches and becomes small compared to the collision time. This is also the regime where rotational energies are approaching dissociation. These regimes are not well studied in a controlled way and there is strong reason to suspect a nontrivial state dependence in these levels for inelastic collisional cross sections based on the calculated dependence of rotational energy separation and collision energy of molecular ions and neutral buffer gases [**120**]. The large discrepancy between the Langevin and reaction rates also suggest that the internal state may influence reaction dynamics in a way that a simple capture model can not describe.

The experiments described in this section provide important first steps to fully characterizing the behavior of SiO^+ with the background UHV environment. The measured rate constant of $0.85(33)\times10^{-10}$ cm^3s^{-1} is found to be in tension with a previous measurement of $3.2(1.0)\times10^{-10}$ cm^3s^{-1} by Fahey et al [**41**]. Systematic shifts large enough to explain the discrepancy between the two measurements have been determined to be unlikely. The experiment would benefit from an independent measurement of the pressure or the addition of a residual gas analyzer to increase confidence on these conclusions. However, based on the known information, an independent measure of the systematic effects is unlikely to resolve the tension.

7.3. SiO^+ Rotational Cooling

As discussed previously in chapter 2, the ability to prepare a well-defined quantum state is a prerequisite for many applications. Important to the process of gathering statistics is the time necessary for state preparation. In this section I discuss our experiment for determining the rate and fidelity of optical pumping for rotational cooling. Broadly speaking this was done by monitoring the fraction of dissociated SiO^+ recorded following excitation of the $|X^2\Sigma^+, v = 0, J = 1/2, + > \rightarrow |C^2\Pi_{1/2}, v = 0, J = 0.5, - >$ transition (see Fig. 7.11) as a function of the optical pumping time. Optical pumping was performed using the $N = 0$ target state spectral mask described in section 2.4 and shown in Fig. 2.4. Results indicate that after 25 ms nearly half of the population is in the ground rotational state. A second, longer time scale of ~ 100 ms determines when the remaining population initially in the odd parity rotational states is pumped into the (even parity) ground state. The measured time scale allows us to extract a radiative branching ratio estimate of 0.007(3) for $B \rightarrow A$ which was determined to be the dominant mechanism for parity exchange. After the 'parity barrier' is overcome, the ground state reaches a steady state population of 94(3)%, corresponding to a temperature of 0.53(6) K.

7.3.1. Experimental

The experimental setup is described in detail in chapter 5. Multiple experiments were conducted, but in every experiment each data point was recorded using a sample of order 100 SiO^+ that was co-loaded into a laser-cooled Ba^+ Coulomb crystal (of order 1000 Ba^+) using 1+1 REMPI on the (5,0) band of the $A - X$ transition of SiO. Post-ioinization, the population of SiO^+ is expected to be loaded into the trap between $N = 4$ and $N = 15$ in

the ground vibrational state by ionizing at energies just below the observed cutoff in the REMPI spectrum (see section 6.2.5). The process of loading and preparing for the next data point typically takes of order 30 seconds and thus the population is only partially thermalized[7]. Systematic effects due to reaction of SiO^+ with background H_2 gas (See section 7.2 for SiO^+ chemistry reaction experiments) were minimized by monitoring and limiting the amount of time each sample was loaded into the trap before a measurement was recorded.

To determine the cooling time and efficiency, the mass spectrum is recorded using the LCFMS frequency chirp method (see section 5.6.2.1) immediately after loading the SiO^+ sample in order to determine the relative quantity of SiO^+ in the trap. Following measurement of the mass spectrum, the spectrally pulse-shaped frequency doubled Mai-Tai laser (see pulse-shaping details in section 5.7) is switched on for a specified time-period using a single pass AOM. For this experiment, the $N = 0$ target state spectral mask described in section 2.4 and shown in Fig. 2.4 is applied. After passing through the pulse shaping setup, 50 mW of power remains in the beam which is then focused to a beam waist of ~ 300 μm onto the trapped SiO^+.

Following the specified time interval for optical pumping, a single pulse of the frequency doubled output of a dye-laser (section 5.4.1) tuned to the $Q(0)$ $|X^2\Sigma^+, v = 0, N = 0, J = 1/2, + > \rightarrow |C^2\Pi_{1/2}, v = 0, N = 0, J = 0.5, - >$ transition at 44044.5 cm^{-1} (see Fig. 7.11) is fired. After a single pulse of the dye laser, the mass spectrum was again recorded using the LCFMS frequency chirp method. The SiO^+ signal in the mass spectrum was

[7]Evidence for the initial distribution can be observed in the post-ionization, uncontrolled dissociation spectrum previously discussed (see Fig. 7.2). The time scale for thermalization out of $N = 0$ is also investigated in this work and corroborates the assertion that the distribution is not expected to completely thermalize.

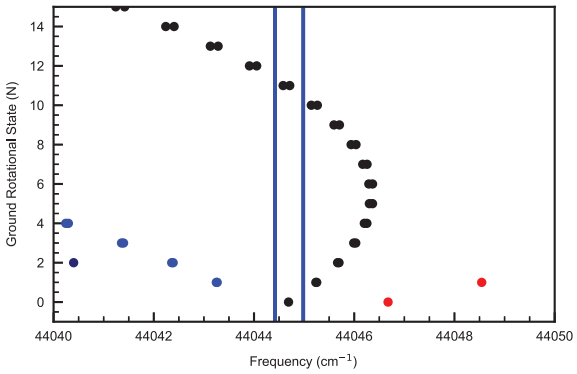

Figure 7.11. The $X^2\Sigma^+(v=0) \rightarrow C^2\Pi_{1/2}(v=0)$ Fortrat diagram. Each color corresponds to a different branch (red = R branch, black = Q branch, blue = P branch, dark blue = O branch). The $Q(0)$ transition is probed to estimate the optical pumping time. The blue vertical lines indicate the linewidth of the transition and show transitions that overlap the intended probe transition.

normalized to the signal taken before optical pumping to determine the fraction of SiO^+ that was dissociated.

The probe transition for monitoring the fraction of population is in a congested region of the spectrum. The intended transition and nearby transitions can be seen in the Fortrat diagram in Fig. 7.11. Because of the congestion it was necessary to measure how well each line could be resolved. To determine the line profile, the dye laser was scanned across the $R(0)$ transition at 44046.7 cm^{-1} using the less noisy single frequency method described in section 5.6.2.2. Briefly, for a single data point recorded using the single-frequency method, the dye-laser will fire onto the trapped ions at a 10 Hz rate as the signal is continuously monitored using the LCFMS method. The rate of SiO^+ depletion is then proportional to the probability of dissociation. The profile, recorded in Fig. 7.12, is best fit by a Lorentzian with a FWHM of 0.56 cm^{-1}. After recording the cooling time data, it was

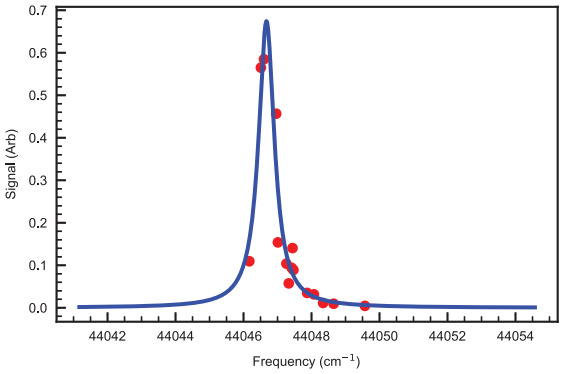

Figure 7.12. Single frequency measurement of the $X^2\Sigma^+(v = 0, N = 0, J = 1/2, +) \rightarrow C^2\Pi_{1/2}(v = 0, J = 3/2, -)$ transition. The profile is best fit by a Lorentzian (solid blue line) with a linewidth equal to 0.56 cm^{-2}. Observed profile is dominated by the laser linewidth. Later measurements confirm this assertion.

later determined that the linewidth is limited by the laser. In subsequent measurements the laser linewidth was able to be improved (see section 7.1).

In addition to determination of the cooling time-scales and efficiency, the time-scale for thermalization of the $N = 0$ state of the ground vibrational state was measured. This experiment was accomplished by optically pumping the trapped SiO^+ using the same $N = 0$ rotational cooling mask used in the cooling rate experiment. While the sample was being optically pumped, the mass spectrum was recorded using the LCFMS frequency chirp method such that the relative amount of SiO^+ in the trap before dissociation could be recorded. The process of loading and recording the mass-spectrum typically takes ~ 30 seconds, which is easily sufficient for reaching the steady state population distribution. After recording the mass spectrum, the optical pumping was switched off by the AOM. Next, after a specified delay time spanning 1 ms to 100 seconds, the pulsed dye laser tuned to the $Q(0)$ transition was fired for a single pulse. Following dissociation, the mass

spectrum was again recorded to determine the fraction of depleted SiO^+ in the trap. In this way the time scale for population leaving the ground rotational state was recorded.

7.3.2. Rotational Cooling Rate

The cooling time and efficiency data is plotted with the results of a rate equation simulation (see section 2.4) in Fig. 7.13. Nominally, the measurement is directly measuring the fraction of population in $N = 0$ after a specified pumping time. However, the congestion of nearby lines confounds the result somewhat. The initial decrease in the fraction dissociated seen in the data at early time scales is an artifact of coincident Q branch lines with the strongest overlapping transition involving $Q(11)$ (see Fig. 7.11). With the starting distribution expected to be distributed between $N = 4$ and $N = 15$ post ionization and time to partially thermalize, initial population is expected to be peaked around $N = 11$ and all of the population in odd parity rotational states larger than $N = 11$ are expected to quickly pass through it during optical pumping. This explains both the initial signal at short time scales and the subsequent rapid decrease toward zero before the expected increase in signal due to $N = 0$ population accumulation during rotational cooling.

In the simulation plotted in Fig. 7.13, the pumping rate of the pulse-shaped laser is calculated using measured power and focal spot size of the beam and the comb-tooth structure is assumed to be smoothed out. The spectral cutoff sharpness is assumed to have a 90-10 cutoff of 2.2 cm^{-1} which is comparable to the cutoff observed on the home-built spectrometer. The initial population distribution is assumed to be 293 K thermal where population is peaked between the $N = 11, 12$ rotational states, which is reasonably consistent with observations.

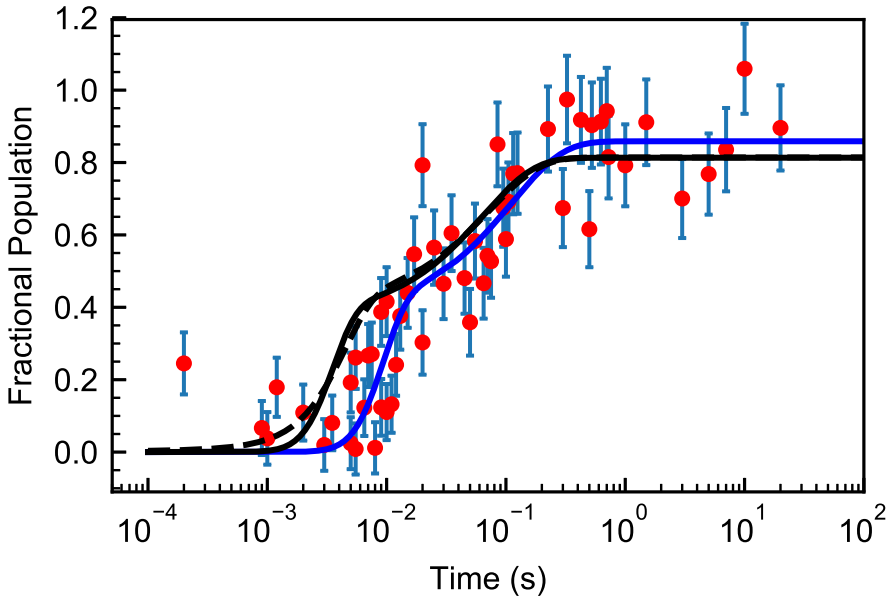

Figure 7.13. Plotted above are the data points and their estimated error bars representing the fraction of SiO^+ dissociated as a function of optical pumping time (red circles). Included in the plot are the rate equation simulation results for the fraction of population found in the ground state as a function of optical pumping time (black dashed line) with the corresponding fit of the data (solid blue line) and a fit of the simulation (solid black line). The fit functions were determined using a simplified cooling model described in the text. See Table 7.5 for details of the fit.

Ignoring the initial decline at short time scales in the data which can be explained by the coincidence of $Q(11)$ and $Q(0)$, two time scales are noticeably present in both the rate equation simulation and the data. The first is the rate for purely rotational cooling and determines the time scale for nearly half of the population to accumulate into the ground rotation state. The second is the time scale for the parity flipping mechanism and determines the rate for the remaining population to accumulate into the ground state. As discussed in section 2.4 this behavior is modeled by a series of first order differential

equations with a solution for the ground state given by

(7.5)

$$n_0(t) = A_{even}\left(1 - e^{-\lambda t}\sum_{i=0}^{M-1}\frac{(\lambda t)^i}{i!}\right) + A_{odd}\left(1 - e^{-\lambda t}\left(\sum_{i=0}^{M}\frac{(\lambda t)^i}{i!} - \frac{1}{(1-\lambda_A/\lambda)^M}\sum_{i=0}^{M-1}\frac{(\lambda-\lambda_A)^i t^i}{i!}\right) - \frac{e^{-\lambda_A t}}{(1-\lambda_A/\lambda)^M}\right)$$

where $A_{even,odd}$ represent the distribution of parity in the initial population, λ is the effective rate for transferring population to the next lowest rotational state of the same parity, and $\lambda_A \propto f_{B,A}\lambda$ is the rate of odd parity to even parity transfer via decay from B into A and subsequent decay into $X(v=0)$. Here, $f_{B,A}$ refers to the branching fraction of radiative decay from B to A. In the model, the value of M, not to be confused with the rotational state number, is equal to the number steps before reaching the ground state and is not a fitting parameter. That is for population beginning in the rotational state N_R there are $M = N_R/2$ steps for rotational states with even parity and $M = (N_R - 1)/2$ for rotational states with odd parity.

7.3.2.1. Estimated $B - A$ Branching Fraction. The results of the fit to the cooling data (see Fig. 7.13) are listed in Table 7.5. Notably, the extracted value for λ is consistent with the rate of the signal decrease at short time scales where we nominally measure the removal of population from $N = 11$. The initial distribution is assumed to peak around $N_R = 12$ and therefore $M = 6$ is used in the fitting function. By comparing the fitted parameters of the data to the parameters from the simulation a value of $f_{B,A} = 0.007(3)$ is extracted. This is consistent with previous experimental limits on $f_{B,A}$ which place it at a value of less than 0.01 [**151**]. Error bars are assigned to the data points by adding in quadrature the standard deviation (= 0.07) of the signal when no dissociation is attempted

Table 7.5. The fitted parameters to the cooling time data and simulation using Eqn. (7.5). The simulation, data and their fits can be seen in Fig. 7.13. Uncertainties are listed in parentheses.

Rotational Cooling Rate	Data	Simulation
λ (s^{-1})	650(90)	1400
λ_A (s^{-1})	9(4)	15.26
$f_{B,A}/\frac{\lambda}{\lambda_A}$	–	0.53
$f_{B,A}$	0.007(3)†	0.005801
Asymptotic limit	0.86(14)	0.813

† The data value is estimated using $f_{B,A}/\frac{\lambda}{\lambda_A}$ from the simulation fit.

and the estimated shot noise assuming 100 SiO^+ are loaded each attempt. The estimated number of SiO^+ loaded is corroborated using q-scan measurements and dark core volume and SiO^+ density estimates.

7.3.3. Cooling Efficiency and Thermalization Rate

The thermalization data seen in Fig. 7.14 is fit to an exponential decay and the results of the fit are provided in Table 7.7. These are compared to the rate equation simulation for the room temperature thermalization of the steady state distribution obtained in the simulation used in Fig. 7.13. These results can be used to provide an estimate for the steady state temperature and ground rotational state population, and the time scale for thermalization. An estimate of these parameters and their systematic shifts are listed in Table 7.6. The leading systematic shifts include reaction with the background hydrogen, impure isotope selection, and partial laser overlap of other dissociating transitions. The details of these systematics are discussed in appendix B.3. Accounting for all of the systematics, the steady state population becomes $n_0 = 0.94(3)$ which corresponds to a Maxwell-Boltzmann temperature of 0.54(6) K.

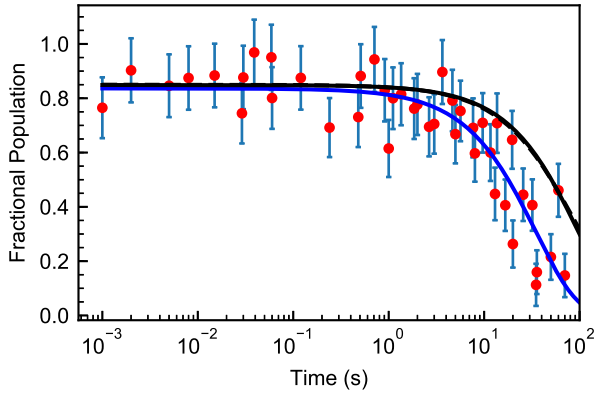

Figure 7.14. Fraction of SiO^+ dissociated as a function of time post optical pumping. In each instance, the sample was rotationally cooled into the ground state for several seconds before turning off optical pumping for a specified period of time and subsequently probing with the dissociation laser tuned on resonance with the $|X^2\Sigma^+, v = 0, J = 1/2, + > \rightarrow |C^2\Pi_{1/2}, v = 0, J = 0.5, - >$ transition (i.e. $Q(0)$). The amplitude of the fitted function was found to be 0.836(22), consistent with the asymptotic value for cooling of 0.86(14). See Tables 7.7 and 7.6 for details of the fit.

Table 7.6. **(Top)** The systematic effects and their estimated shift on the fitted parameter A (see Table 7.7) compared to the idealized case of $A = n_0$. See appendix B.3 for details of the systematic effects. **(Bottom)** The corrected estimate for n_0 is calculated by subtracting the shift from A. The corresponding Boltzmann temperature with an equivalent ground rotational state population is also listed.

	Shift of A	Uncertainty
Statistics	0	0.022
Isotope	-0.07	< 0.002
Reaction	-0.038	0.010
n_1	+0.006	< 0.006
Total	-0.102	0.024
Corrected Estimates		
n_0	0.94(3)	
T (K)	0.53(6)	

Table 7.7. The fitted parameters to the thermalization data and simulation. The simulation, data and their fits can be seen in Fig. 7.14. Estimated 1-σ uncertainties are listed in parentheses.

Thermalization time †	Data	Simulation
A	0.836(22)	0.849
τ (s)	35(4)	96

† Fits were done using $Ae^{-t/\tau}$

The thermalization time scale is 35(4) s as determined by the fit in Fig. 7.14. This time scale is sufficiently fast such that influence of the reaction with the background hydrogen is negligible. There are several mechanisms possibly involved in the observed thermalization time scale. The mechanisms can be separated into three major categories: inelastic collisions, blackbody radiation, and off resonant excitation by the Doppler cooling lasers. As ions in the trap are repelled by the Coulomb force, the source of collisions in vacuum will be due to the presence of background neutral gases. Ion-neutral collision rates are determined by the Langevin rate which provides an upper bound on the rate of inelastic collisions. Typically under UHV conditions the background gas is composed of primarily H_2. Assuming the background gas is composed completely of hydrogen, the gas corrected ion gauge reading during the experiment was 7(4)e-10 Torr which corresponds to an average Langevin collision time of 40(20) s. The precision of this estimate is limited by knowledge of the absolute calibration of the IG. Regardless, the estimated rates are comparable to the observed thermalization time scale and likely contribute significantly to the overall rate. Knowledge of the background pressure is more thoroughly discussed in section 7.2 where the experiments performed to measure reaction rates are covered.

The rate equation simulation does not include inelastic collisions and therefore represents the thermalization strictly due to BBR. Blackbody radiation can induce redistribution of the population via purely rotational, vibrational, or electronic transitions. Purely rotational transitions are expected to occur on a time scale of several to tens of minutes and therefore are unlikely to be a significant contributor to population redistribution. BBR-driven vibrational excitation is also expected to be negligible due to an anomalously small dipole transition moment. This is corroborated by an indirect measurement of the $v = 1$ lifetime found to be 1.0(5) s[8] which would imply a time scale of several minutes. The role of electronic transitions may be more significant than naively expected due to the presence of the low-lying A state, however the expected time scale is still several minutes. Qualitatively, BBR redistribution via vibrational and electronic transitions will behave differently than purely rotational BBR-driven redistribution. This is because a purely rotational transition will flip parity, however vibrational and electronic excitation will quickly undergo spontaneous relaxation into $X, v = 0$ meaning that population redistribution will be a parity preserving process. Because each rotational state alternates parity, redistribution via the parity preserving process will result in population flowing from $N = 0$ directly into $N = 2$. The simulation, in this case, is not expected to accurately reflect the BBR redistribution time because for historical reasons the A state energy used in the simulation is nearly 300 wavenumbers lower in energy than experimental observations indicate. Therefore the BBR intensity is expected to be significantly lower at the resonant energy in the real life case. Instead, the simulation results are meant to demonstrate the expected qualitative behavior of thermalization.

[8]See section 7.4

The third possibility for depopulating the ground rotational state is off resonant excitation via the Doppler cooling lasers. This has not been directly ruled out however it is not expected to be significant. The likelihood of such a process contributing significantly to the thermalization rate is discussed in appendix B.4.

7.3.4. Discussion

7.3.4.1. Cooling Rate Limitations. The cooling rate and the parity exchange rate are currently limited by the laser intensity. The extent to which the comb-teeth structure are limiting the rate is not well characterized, though it likely reduces the rate significantly as discussed in section 5.7.1. In principle, the use of polarized laser light to pump $X - B$ transitions could result in the formation of dark states. Because P branch transitions will always have a larger degeneracy in the ground state than in the excited state, linear combinations of magnetic sublevels will be dark to the laser [**15**]. This would also contribute to the slowing of cooling, however throughout the experiment a roughly 10 guass magnetic field is applied to prevent the existence of dark states in Ba^+. This same field is sufficient for achieving the same goal in SiO^+. See section 2.4.3 for more discussion. In the fully saturated regime the fundamental cooling rate is expected to be $\sim \Gamma/5.5$ or approximately a transfer time of ~ 0.4 μs per every two rotational states. The rate of parity transfer will likely be limited by the A state lifetime which is expected to be of order 1 ms.

7.3.4.2. Future Measurement Improvements. Analysis of the data is currently limited by poor SNR and confounding issues such as the proximity of dissociative transitions. Several things can be done and are currently being implemented to increase clarity and

accuracy of the observed data. To improve the thermalization and cooling time and efficiency data analysis, the dye laser linewidth has been reduced which will limit the effect of inclusion of $N = 1$ in the dissociated fraction. Thus repeating the experiment with a narrower linewidth in exactly the same way will improve systematics. Additionally, performing the dissociation analysis on the $R(0)$ transition will further isolate the intended probe state from nearby states. Eventually, the pulsed dye laser will be replaced with a narrow band tunable CW laser. This will allow us to probe states with precision only limited by the natural linewidth of the transitions and effectively eliminate any systematic issues related to congestion of lines and ultimately provide a more accurate and precise measurement of the $N = 0$ steady state population.

The extent of each thermalization mechanism is currently difficult to cleanly disentangle. Teasing out the various thermalization mechanisms can be done by applying the single-frequency method to the $R(1)$, $P(1)$, $R(2)$, and $O(2)$ transitions with a narrow band laser following ground state preparation. This will allow for much higher precision and accurate extraction of rates of population entering into each spin-rotation state of $N = 1$ and $N = 2$. The ratio and magnitude of these rates will be sensitive to which mechanism(s) are contributing to thermalization. Independent measurements of the A state lifetimes and improved measurements of the $v = 1$ state lifetime or alternatively, direct measurements of their BBR excitation rates would further serve to characterize these time scales. These measurements can be independently probed in several ways. As an example, the indirect $v = 1$ lifetime measure described in section 7.4 can be performed using the single frequency method by probing the $v = 1$ state with the CW laser tuned to the $X(v = 1) \rightarrow C(v = 0)$ Q branch. Alternatively, the lifetime can be measured directly

by preparing the $v = 1$ state and observing the time scale for population decay. Questions and answers regarding the collision rate can be further refined with the addition of a residual gas analyzer and systematic control of the gas composition and quantity of the vacuum chamber. Finally, the effect of the Doppler cooling lasers can be systematically ruled out by varying the intensity of each of the beams.

7.3.4.3. Comparison With Other Cooling Techniques. This work represents an extension of previous cooling by optical pumping techniques. Spectrally filtered broadband laser cooling of rotations was first performed on AlH^+ where ground state cooling from room temperature was achieved on a similar time scale (140 ms) and with comparable fidelity (95%, 3.8 K) [**91**] and is most suitable for other molecules with diagonal FCFs. The optical pumping technique in this work has achieved a rotational temperature (0.53 K) in a room temperature environment. In contrast, the more generally applicable buffer gas cooling, a rotational temperature of 7.5 K for MgH^+ was achieved in a $\sim$5 K cryogenic chamber using a He buffer gas on a similar time scale (10 s^{-1}) [**55**].

Other laser cooling techniques previously demonstrated on hydrides have relied on a blackbody assisted population redistribution process combined with pumping of narrowband vibrational overtones. This technique was able to cool on time scales of order 10 seconds to achieve 36.7% fidelity (20 K) in MgH^+ [**148**] and 78% fidelity (27 K) in HD^+ [**136**]. These other techniques have the advantage that they are generally applicable to any polar molecule whereas spectral filtering of a broadband source is most easily applied to specialized species with diagonal FCFs. However for species with higher reduced masses the BBR redistribution rate typically becomes prohibitively slow. Since application of the first narrowband vibrational resonance techniques, rotational cooling

via pumping of vibrational resonances has been applied to the polyatomic trapped neutral species CH_3F where the role of the blackbody assist was facilitated with the addition of microwave sources to drive purely rotational transitions [**51**]. Under this scheme the rate limiting step becomes the vibrational lifetime instead of the slower BBR time scales. Ultimately, the optical pumping technique used for SiO^+ and AlH^+ will be advantageous when faster cooling time scales are necessary as vibrational decays are typically many orders of magnitude slower than electronic decays.

7.3.5. Conclusions

Because cooling efficiency using spectral filtering is limited by spectral resolution, the fidelity of rotational cooling for heavier species will be limited due to their smaller rotational constants. This work demonstrates the extension of high ground state fidelity of the technique from the lighter hydrides to the heavier oxides. Limited by molecular beam transit time, optical pumping using a broadband laser diode combined with pulse shaping has also been applied to a molecular beam of the heavier species BaF with some success. Cournol et al has reported a rotational temperature of 6 K achieved in under 1 ms starting from a temperature of 52 K [**31**]. Extension of the optical broadband pulse shaping technique to the even heavier chlorides and beyond is possible using, for example, a virtual imaged phased array (VIPA) where sub GHz pulse shaping resolution has been achieved [**167**].

Though the exciting implication exists for the prospect of this technique or simple variations of this technique to work on other molecular species, it is important to also recognize that the value of a control technique does not rest exclusively on its generality.

With the demonstration of fast and efficient ground state preparation on SiO^+, further refinements to the technique may enable fluorescent imaging or even direct Doppler cooling. Such improvements would enable the realization of multi-ion molecular clocks which can be tuned to cancel Stark and second order Doppler shifts [**149, 3**]. More broadly it would enable rapid, non-destructive state detection which, like Ba^+, can be used as a general tool for many potential experiments.

7.4. Rovibrational Control

In the following experiments we apply the techniques described in chapter 2 to test the limits of arbitrary rovibrational control of SiO^+ and compare to expectations according to the simplified steady state model of appendix A.2.3. In these experiments we apply spectral masks chosen to demonstrate the range and consistency of state control from the extremes of complete removal of rotational energy to steady state preparation of so-called 'super-rotors', i.e. highly rotationally excited diatomic molecules [**90**]. Additional masks were applied to achieve preparation of low N in $v = 1$ of the X state to demonstrate proof of concept control over the vibrational degrees of freedom. In diagnosing issues with vibrational control, the lifetime of the $X, v = 1$ state was indirectly estimated to be 1.0(5) s. A manuscript describing these and updated results is in preparation.

7.4.1. Experimental

The rovibrational control experiments can be broadly separated into two categories: control and state detection. Control is performed using broadband spectral pulse shaping of a femtosecond laser. The pulse shaping setup is described in more detail in section 5.7 and a discussion of the function of the spectral mask shape for control is discussed in detail in chapter 2. As an example, the spectrum of the broadband laser with the mask used for populating rotational states near $N = 10$ is shown in Fig. 7.15. Pulse shaping masks of the broadband laser were chosen such that targeted rotational states from $N = 0$ to $N = 65$ of SiO^+ were deterministically prepared. Additionally, attempted demonstration of vibrational control by populating low N of $v = 1$ was achieved with partial success using masks designed for preparation of excited vibrational states. No attempts were made

to extend vibrational control to higher v due to the requirement of more complicated masks[9]. Similarly, the highest attempted target rotational state was also determined by technical constraints that limited it to near $N = 65$. Due to the location of the R branch bandhead ($N \approx 80$) higher energy rotational states require dynamic masks at the current spectral filtering resolution[10].

For state detection two primary methods were employed: the 'frequency chirp' method and the 'single frequency' method. Both are variants of the LCFMS method described in section 5.6.2. For faster, noisier scans of the spectrum the secular frequency chirping method was used (see section 5.6.2.1). In these scans the dissociating laser was pulsed several times at 10 Hz and the total fraction depleted was subsequently recorded. If a significant fraction of the original sample remained, the wavelength was changed and the process was repeated to record a new data point in the spectrum. This process was repeated until more than half of the original sample had been dissociated or if there was a high probability that the sample had significantly reacted with the background hydrogen gas to form $SiOH^+$ (i.e. if the sample had been exposed to background gases for 4 minutes). If either condition was met, then the sample was ejected from the trap and subsequently replaced. The chirp method is useful for rapid scanning of the spectrum where no signal is expected and was particularly useful in early experiments before the transition energies were known. In these early experiments control was used iteratively to characterize the $C^2\Pi$ state as described in section 7.1. However, because this method

[9]Efficient preparation of higher v and arbitrary N requires removal of multiple spectral regions. See 2.5.2 for more details.

[10]Preliminary tests performed since have indicated efficient preparation of rotational quanta $N > 170$ when applying a cutoff in the opposite direction near the band origin such that the entire R branch is optically pumped for $N < 170$.

sacrifices SNR in favor of quick scans, it provides less reliable information on relative distributions.

The single frequency method is described more fully in section 5.6.2.2. This method relies on continuous monitoring of the fluorescence modulation due to a 'single'[11] secular frequency excitation as the dissociation laser is pulsed at 10 Hz. This is in contrast to the frequency chirp used in the first method which collects a broad masss spectrum. In the single frequency method the dissociation laser is typically pulsed 300 times to collect a single data point in the spectrum. If steady state is achieved more rapidly than than the observed dissociation rate, then the observed rate will depend directly on the population. By pulsing the dissociating laser enough times to ensure complete dissociation of the sample, the single frequency method, unlike the chirping method, is able to maintain sufficient SNR for low population states. If dissociation depletes population in a target state more rapidly than steady state is achieved, then the observed rate reflects the rate of population flowing into the target state. We operate in this regime to measure the BBR excitation rate from $v = 0$ into $v = 1$.

7.4.2. Rotational Control

As experimental analysis of preparation of the rotational ground state was covered in detail in section 7.3, I begin discussion with preparation of excited rotational states. Unlike for $N = 0$, excited state preparation requires an extra filter in addition to the razor blade mask. An example of this additional filter is demonstrated in the $N = 10$ pulse-shaped femtosecond laser spectrum seen in Fig. 7.15. Briefly, the spectrum

[11] In practice it is multiple frequencies narrowly distributed around the resonance frequency so as to avoid issues with drifting or shifting secular frequencies.

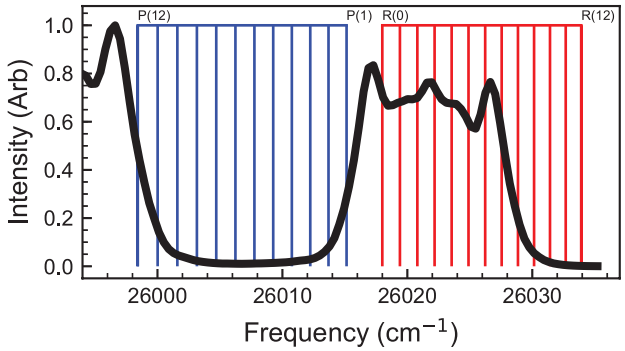

Figure 7.15. Plotted above is the broadband pulse shaped spectrum used to populate $N = 10$ and the SiO^+ $X^2\Sigma^+(v = 0) \rightarrow B^2\Sigma^+(v = 0)$ P (blue) and R (red) branch transitions up to $N = 12$. The overlap of the two demonstrate the relative intensity of the filtered broadband laser on resonance with each P and R branch transition. The relative intensities in the pulse shaped spectrum are used to calculate the expected steady state rotational distribution which is plotted in Fig. 7.16. The resulting experimental dissociation spectrum for this mask is plotted in Fig. 7.17.

is constructed such that the SiO^+ $X^2\Sigma^+(v = 0) \rightarrow B^2\Sigma^+(v = 0)$ P and R branch transitions are selectively pumped such that population is stochastically driven toward the target rotational state. In the case of the target $N = 10$ rotational state, this means that the frequency components of the broadband spectrum covering R branch transitions for $N > 9$ and P branch transitions for $N < 11$ are filtered out by the mask. Thus population beginning in $N < 10$ is stochastically driven towards higher rotational quanta and, similarly, population in $N > 10$ is pumped into lower rotational quanta. This general strategy is applied to preparation of arbitrary rotational quanta.

The details of the relative optical pumping transfer rates of the P and R branch transitions will determine how the population is distributed in the steady state. In Fig. 7.16 the relative optical pumping transfer rates are plotted as a function of rotational

number for both the R and P branches separately. These rates are determined using the unsaturated case described in appendix A.1. These rates assume the $X - B$ transition is described by ${}^1\Sigma \rightarrow {}^1\Sigma$ and therefore represents an average of the rates of the spin-rotation states for each rotational level in the actual ${}^2\Sigma \rightarrow {}^2\Sigma$ transition.

In Fig. 7.16 the R and P branch rates can be seen to decrease rapidly in a neighborhood around $N = 9, 10$. Qualitatively, we expect most of the population to be found in these states with transitions dark to the laser spectrum. The expected rotational distribution in the ground vibrational state is shown in black and estimated using the simplified steady state model described in appendix A.2.3. As anticipated, the population can be seen to be peaked where both the R and P branch transfer pumping rates are minimized.

The expected distribution according to the simplified steady state model can be qualitatively compared to the observed rotational dissociation spectrum distribution. Shown in Fig. 7.17 is the $X^2\Sigma^+(v = 0) \rightarrow (2)^2\Pi_{1/2}(v = 0)$ transition dissociation spectrum of SiO^+ that is optically controlled using the pulse shaped spectrum in Fig. 7.15. In this instance the dissociation spectrum was recorded using the single frequency method. Qualitatively it is immediately clear that for all four branches, only the presence of population in $N = 7 - 11$ is detectable. This is in exact agreement with the expected distribution of population.

Though the simplified model does not account for spin rotation splittings with e, f rotationless parity states, the different branches of the $X^2\Sigma^+ \rightarrow C^2\Pi_{1/2}$ transition allow us to look at the distribution of e, f states separately. In the ground state, where N specifies the total angular momentum excluding electron spin, the e rotationless parity states have total angular momentum $J = N + 1/2$ and f rotationless parity states have

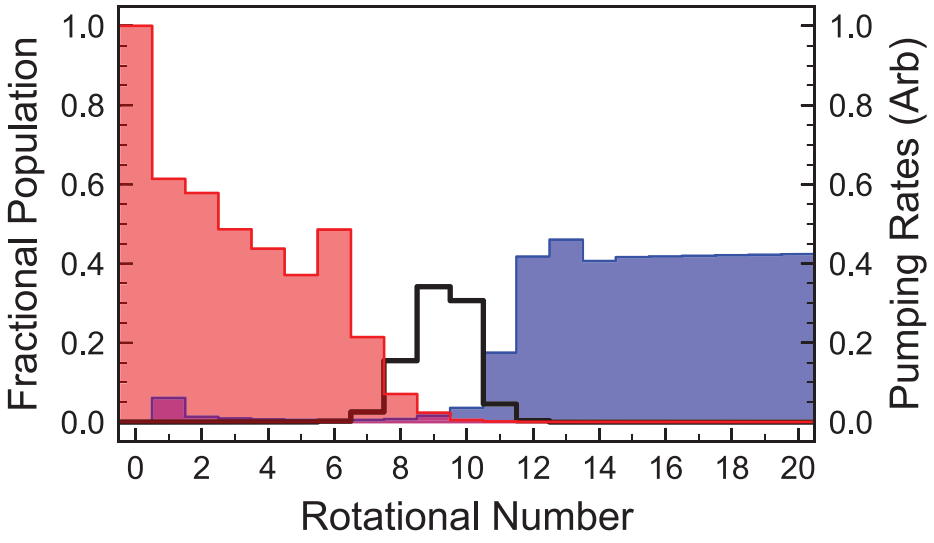

Figure 7.16. In red and blue are the relative pumping rates of the R (red) and P (blue) branch transitions normalized to the peak relative rate. The relative rates are calculated assuming intensity is below saturation using the relations derived from Eqn. (A.2) and using the spectrum in Fig. 7.15 to determine the relative intensities. The expected population distribution, plotted in black, is derived from these rates using Eqn. (A.14). The resulting experimental dissociation spectrum for this mask is plotted in Fig. 7.17.

total angular momentum $J = N - 1/2$. Due to parity and $\Delta J = -1, 0, +1$ selection rules, the $X^2\Sigma^+ \rightarrow C^2\Pi_{1/2}$ O branch transitions ($\Delta N = -2$) are exclusively dissociating population in f type states. Similarly, R branch ($\Delta N = +1$) transitions are exclusively dissociating e type transitions. This is a useful property for more precisely probing the population distribution at the spin-rotation level. On the other hand, though the P ($\Delta N = -1$) and Q ($\Delta N = 0$) branches contain transitions from both states at each N, the states are effectively degenerate. Therefore these branches are useful for extracting the more coarse, purely rotational distribution that the simplified steady state model

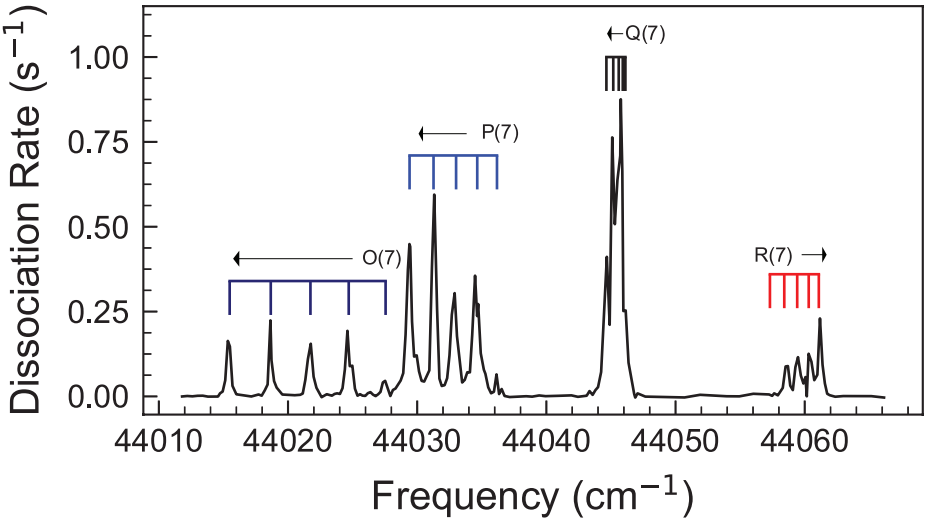

Figure 7.17. The $X^2\Sigma^+(v=0) \rightarrow (2)^2\Pi_{1/2}(v=0)$ dissociation spectrum of SiO^+ in the steady state during optical pumping via the pulse shaped broadband distribution seen in Fig. 7.15. The spectrum was recorded using the single frequency method. All four branches of the lowest spin orbit state are present with most of the population in $N = 8-11$ and some detectable in $N = 7$.

describes. From a qualitative picture only, there does not appear to be any significant discrepancy between the distribution in the e versus f rotationless parity states which suggests that the spin rotation splitting does not significantly alter the accuracy of the simplified model.

In Figs. 7.18 and 7.19 the dissociation spectra for various prepared masks are plotted. Besides the spectrum for $N = 10$, the spectra in Fig. 7.18 were acquired using the noisier frequency chirp method. In contrast, the spectra in Fig. 7.19 were recorded using exclusively the single frequency method and hence the quality of the spectra are significantly improved. In both figures the calculated simplified steady state model population distribution is plotted alongside the dissociation spectra for comparison. The model uses

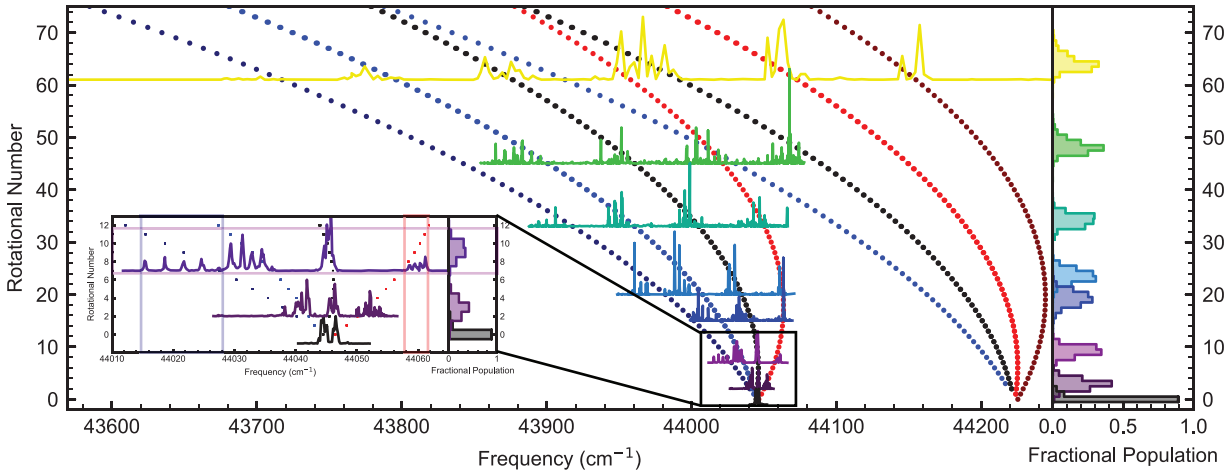

Figure 7.18. **(Left)** The $X^2\Sigma^+(v=0) \rightarrow C^2\Pi_{1/2,3/2}(v=0)$ Fortrat diagram and dissociation spectra of SiO^+ in the steady state during optical pumping via the pulse shaped broadband distributions with various target rotational states spanning $N = 0$ to $N = 65$. The spectra are distributed along the y-axis according to their expected rotational distribution. The line broadening observed in the spectrum near $N = 65$ is a consequence of using the less narrow OPO to record the dissociation spectrum. The observed rotational lines can be identified according to the underlying Fortrat diagram. The branches O (dark blue), P (blue), Q (black), R (red), and S (dark red) are labeled according to ΔN. All of the spectra plotted were recorded using the chirp method with the exception of the spectra at $N = 10$. **(Right)** The expected distribution for each corresponding spectral pulse shaping mask is plotted. **(Left-Inset)** The spectra for masks used to prepare $N = 0, 3, 10$ are zoomed in to show finer structure. The observed distribution can be compared to the expected distribution by extending horizontal lines from the expected range of N for the given mask. As an example this is done for the $N = 10$ mask spectrum. The O and R branch lines of the most extreme transitions present in this spectrum are partitioned with vertical lines. That all the Fortrat dots are contained within the boxed area indicates good agreement between the expected and observed distributions.

the raw the pulse shaping spectrum recorded by the home-built spectrometer. Here we again observe good qualitative agreement between the predicted population distribution

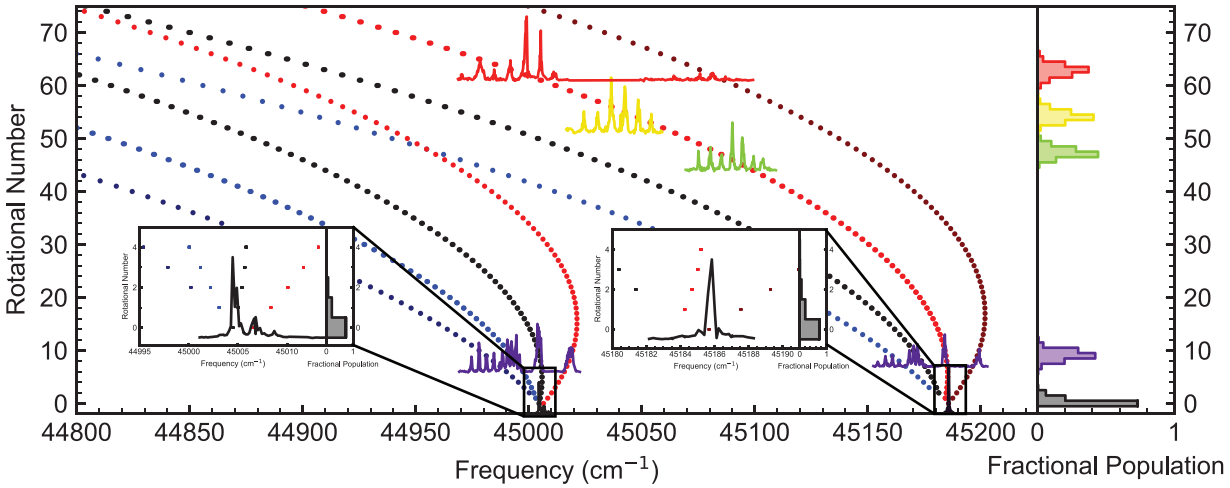

Figure 7.19. **(Left)** The $X^2\Sigma^+(v = 0) \rightarrow C^2\Pi_{1/2,3/2}(v = 1)$ Fortrat diagram and dissociation spectra of SiO^+ in the steady state during optical pumping via the pulse shaped broadband distributions with various target rotational states spanning $N = 0$ to $N = 65$. The spectra are distributed along the y-axis according to their expected rotational distribution. The observed rotational lines can be identified according to the underlying Fortrat diagram. The branches O (dark blue), P (blue), Q (black), R (red), and S (dark red) are labeled according to ΔN. Unlike the spectra in Fig. 7.18, all of the spectra in this plot were recorded using the single frequency method. **(Right)** The expected distribution for each corresponding spectral pulse shaping mask is plotted. **(Left-Inset)** The spectra for masks used to prepare $N = 0$ are zoomed in to show finer structure. The observed distribution can be compared to the expected distribution by extending horizontal lines from the expected range of N for the given mask.

and the observed spectrum. In both figures, the peak rotational line in the spectrum is typically within 2 rotational quanta of the predicted peak population.

As outlined in section 5.6.2.2, the single frequency method can provide us some information on the population distribution. Since we did not control for laser intensity nor did we confirm saturation of the dissociation probability per laser pulse we are limited in the conclusions that can be drawn about the absolute fractional populations in each

state. Nevertheless we are able to place a lower bound on the population in each state using the relation

$$n_i \approx 1 - e^{-R_i/10}. \tag{7.6}$$

where n_i is the fractional population in the i^{th} state and R_i is the dissociation rate of the corresponding probe transition in units of s^{-1} and divided by 10 Hz to get the per pulse rate[12]. If we use this relationship to compute the population we will be systematically overestimating the dissociation probability per pulse and therefore underestimate the population. Furthermore, we implicitly assume the time required for reaching a steady state after dissociation is much faster than the time between laser pulses. This too results in an underestimation of the population in the probe state as insufficient time between pulses prevents population from completely recovering the steady state distribution post dissociation.

The estimated lower bounds of the population for all of the spectra recorded of excited state N using the single frequency method are shown in Table 7.8. Additionally, the predicted distribution using the recorded spectrally filtered femtosecond laser spectrum is compared to the distribution estimated from the corresponding dissociation spectrum. Note that the special case of $N = 0$ is discussed in detail in section 7.3.

From the analysis it is clear that the distribution width and lower bound of the population do not vary significantly over the range of target rotational states for a given transition. For a given spin orbit state of a given vibrational state, the line strength of each branch will not vary significantly for high N. The dye laser efficiency also does

[12]For a more complete discussion of the relationship see section 5.6.2.2.

Table 7.8. The observed and predicted peak population and width of rotational state distribution for each of the masks investigated using the single frequency method. The observed total minimum population in $v = 0$ (i.e. $\sum_i n_i^{v=0}$) is also compared to the predicted total used by simulating the distribution using the simplified steady state model for $v = 0, 1, 2$ as described in appendix A.2.3.

Mask & dissociation spectrum		N_{peak}	ΔN †	$\sum_i n_i^{v=0}$ ‡
$X^2\Sigma^+(v=0) \rightarrow C^2\Pi_{1/2}(v=0)$				
$N = 10$	Expt.	10	3	> 0.18
	Calc.	9	2	0.85
$X^2\Sigma^+(v=0) \rightarrow C^2\Pi_{1/2}(v=1)$				
$N = 10$	Expt.	10	4	> 0.27
	Calc.	9	3	0.74
$X^2\Sigma^+(v=0) \rightarrow C^2\Pi_{3/2}(v=1)$				
$N = 10$	Expt.	10	2	> 0.12
	Calc.	9	2	0.94
$N = 46$	Expt.	46	2	> 0.08
	Calc.	47	2	0.65
$N = 56$	Expt..	56	3	> 0.14
	Calc.	54	2	0.80
$N = 62$	Expt.	62	2	> 0.15
	Calc.	63	2	0.93

† ΔN is estimated using the FWHM of the distribution rounded to the nearest integer

‡ Minimum populations for each N estimated using $1 - e^{-R}$ where R is the rate of dissociation per pulse.

not vary significantly over an equivalent range of use. This suggests that the probability for dissociation was not expected to vary significantly from transition to transition and spectrum to spectrum for the $X^2\Sigma^+(v = 0) \rightarrow C^2\Pi_{3/2}(v = 1)$ transitions. Thus we can tentatively conclude that the fidelity of state preparation is not strongly dependent on rotational state, even for those states with $X \rightarrow B$ transitions approaching the bandhead at $N \approx 80$.

Furthermore, the accuracy of the predicted peak rotational state population and distribution width is also not dependent on which rotational state is being targeted. There

is no clear systematic discrepancy between the predicted and observed peaks and they are consistently within 1 to 2 rotational quanta of each other. The distribution width also closely matches the predicted width, though the predicted width systematically (slightly) underestimates the observed width. The origin of this discrepancy is not yet fully understood.

One possibility for the discrepancy, and the explanation I find to be most likely, is a consequence of the model assuming that the rotational population is driven toward the same target rotational state in each diagonal transition of the excited vibrational states. This means that as the population vibrationally diffuses it is not expected to rotationally diffuse. However, in all of the masks used, only the ground vibrational state is driven towards a target state. Thus rotational diffusion is expected to coincide with vibrational diffusion. This would result in a systematic broadening of the rotational distribution for any target rotational state. Thus, masks appropriately constructed to address each diagonal vibrational transition may see narrower distributions with increased total populations in the target vibrational level.

An alternative possibility ignored by the simplified model includes contributions from BBR redistribution. The BBR redistribution will result in additional broadening of the rotational distribution beyond expectations of the model. If BBR were to explain the magnitude of the observed broadening, we would expect that the broadening, like the BBR rate, systematically increases with N. No dependence on N is observed, however.

7.4.3. Vibrational Control

Limited by the complexity of the pulse shaping mask we are currently able to produce, we were forced to modify the spectral mask from the ideal construction described in section 2.5.2. Two qualitatively different masks were used to prepare $v = 1$ population. The first mask used for preparing $X, v = 1$ shown in Fig. 7.20 a-i) is constructed by first placing a cutoff at $P_{1,1}(2)$ such that population in $v = 1$ is rotationally cooled on the (1,1) diagonal transition. Because the (0,0) transition overlaps with (1,1), the cutoff position corresponds to nearly the $P_{0,0}(18)$ transition. Thus to avoid dark states in $v = 0$, the R branch of (0,0) is included from $N = 0$ to $N = 20$. This mask therefore will cause population in $v = 0$ to be driven towards $N \approx 20$ where it will be rapidly cycled until off diagonal decays send population into $v = 1$. Once in $v = 1$ population is rotationally cooled and trapped in the low N dark states. The calculated population distribution for the two lowest vibrational levels are shown in Fig. 7.20 a-ii) which demonstrates the two distinct distributions expected for each vibrational level.

7.4.3.1. Non-Ideal Mask. The corresponding dissociation spectrum for the first mask is plotted in Fig. 7.21 and was recorded using the frequency chirping method. The presence of population in $v = 1$ is demonstrated with the appearance of vibrational hotbands. Despite the presence of the $v = 1$ hotbands, significant population is present in the ground vibrational state. As expected, the spectrum originating from $v = 0$ population is starkly different than the spectrum due to population originating in $v = 1$. The distribution according to the simulated population is expected to be between $N = 16$ and $N = 23$ for the ground vibrational state. In contrast, the spectrum due to population originating in

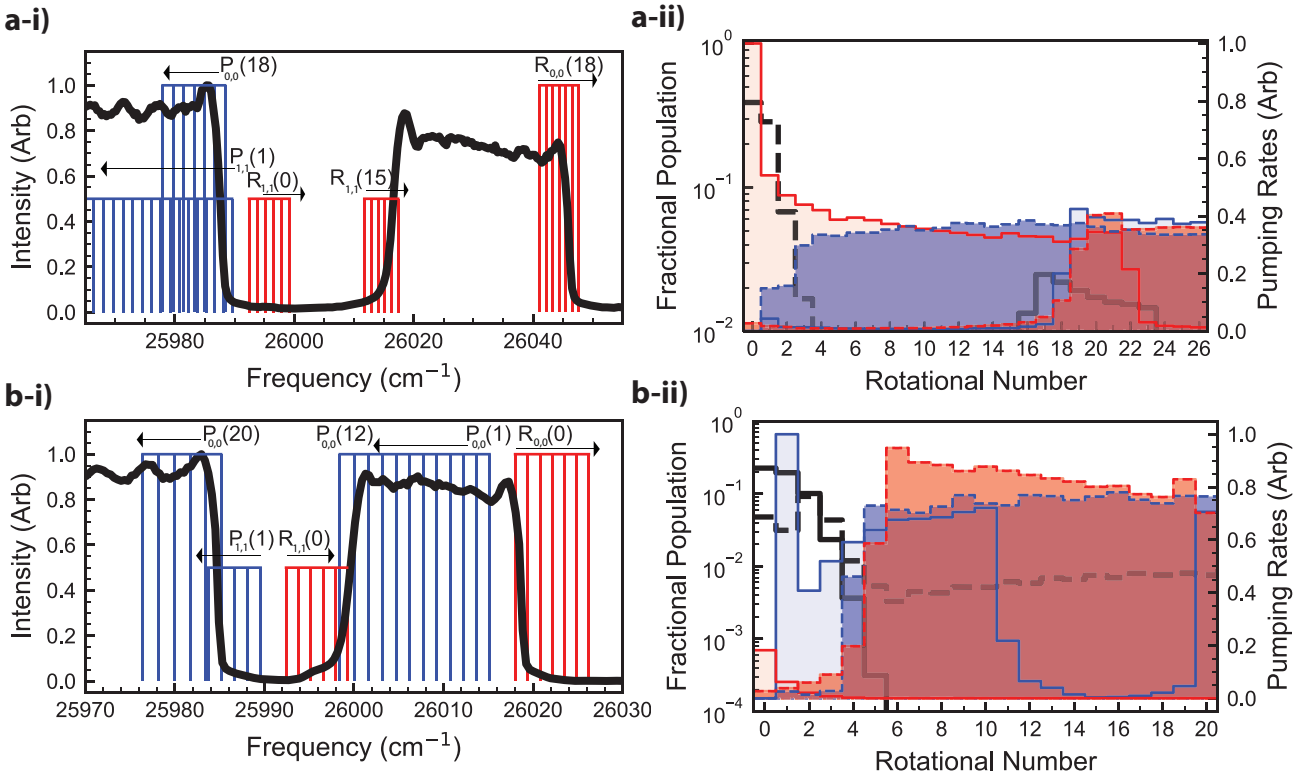

Figure 7.20. **i)** Shown are the two different masks used for preparing $v = 1$ population. Upper and lower red and blue spokes indicate the R and P branch transitions of the $X - B$ $v = 0$ and $v = 1$ diagonal transitions respectively. **ii)** The simulated population distributions for each mask are shown in black and the red and blue curves show the relative pumping rates of the R and P branches at each N. Solid (dashed) lines refer to population and pumping rates for $v = 0$ ($v = 1$) rotational states. **a)** The first mask relied on driving population to $v = 0, N \approx 20$ and rapidly cycling population before decaying into $v = 1$ where it would be driven down into the low N. **b)** The second mask relied on blackbody assistance to pump and cycle population to $v = 0, N = 0, 1$ before off diagonal decay into $v = 1$ where states are comparatively dark.

$v = 1$ is expected to be primarily in $N = 0, 1$. The observed spectra in Fig. 7.21 are compared to the simulated spectra which were constructed assuming a uniform distribution over the expected range of populated rotational states and a linewidth consistent with the

probe laser (Ekspla OPO, see 5.4.1) and no other inputs using PGOPHER 10 [**164**]. The actual observed distribution appears to largely agree with the simulated one for $v = 0$ and it appears to be somewhat broader than the simulated spectrum for $v = 1$. This discrepancy may be due to saturation of the signal or some broadening of the rotational distribution may occur due to the large separation on the rotational ladder between $v = 0$ and $v = 1$ target rotational states (≈ 20). Nevertheless, despite the lack of fitting parameters used in the simulation there is excellent qualitative agreement with the data for both vibrational populations. This suggests that the simplified steady state model is still able to accurately capture the relative rotational distribution in each vibrational level by treating them independently as I hypothesized in section 2.5.2.

Quantitatively the relative vibrational population distribution cannot be determined from the collected data. Even qualitatively, it is still unclear to what extent the model accurately captures the relative vibrational distribution. The model predicts the population in $v = 1$ to be approximately $5\times$ the population in $v = 0$[13]. Though no attempt was made to accurately probe the absolute or relative populations in each level, if the line strengths of the $X^2\Sigma^+(v = 1) \rightarrow C^2\Pi(v = 1)$ and the $X^2\Sigma^+(v = 0) \rightarrow C^2\Pi(v = 0)$ transitions are comparable, we would expect to see a narrow peak dominate the $X^2\Sigma^+(v = 0) \rightarrow (2)^2\Pi_{1/2}(v = 0)$ spectrum due to $X^2\Sigma^+(v = 1) \rightarrow C^2\Pi_{3/2}(v = 1)$ which shares a band origin less than 8 cm^{-1} to the red of $X^2\Sigma^+(v = 0) \rightarrow C^2\Pi_{1/2}(v = 0)$. That this is not observed does not necessarily indicate that most of the population is not in $v = 1$.

[13]It predicts $n_i^{v=0} = 0.15, n_i^{v=1} = 0.76$.

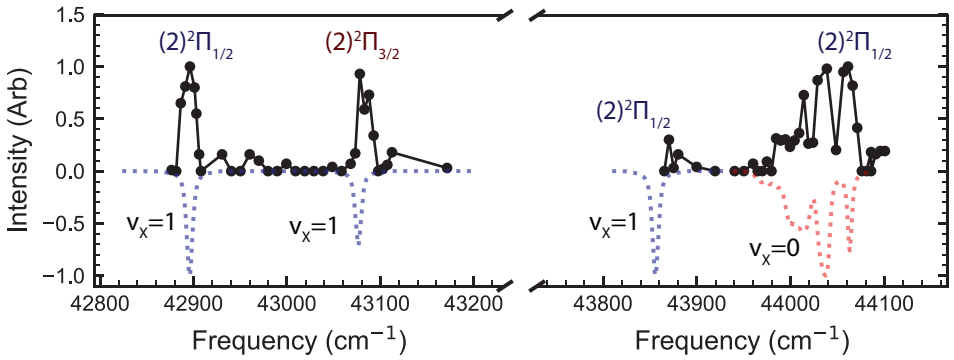

Figure 7.21. The observed (solid black lines) and simulated (dotted lines) dissociation spectrum using the control mask in Fig. 7.20 a-i). The simulated spectrum uses the populated rotational states in each vibrational level according to Fig. 7.20 a-ii) and assumes a linewidth of 5 cm^{-1} to account for the Ekspla linewidth. The observed spectrum was recorded using the *frequency chirp* method. The left hand side of the plot shows the $X^2\Sigma^+(v = 1) \rightarrow C^2\Pi(v = 0)$ hotband. The right hand side shows a portion of the $X^2\Sigma^+(v = 1) \rightarrow C^2\Pi_{1/2}(v = 1)$ hotband (simulated in blue) and the $X^2\Sigma^+(v = 0) \rightarrow C^2\Pi_{1/2}(v = 0)$ transition (simulated in red using evenly distributed rotational distribution of $N = 16 - 23$). The $X^2\Sigma^+(v = 1) \rightarrow C^2\Pi_{3/2}(v = 1)$ hotband would also be present however the signal is overwhelmed by signal due to $X(v = 0)$.

A simple Morse parameter calculation somewhat anomalously predicts a Franck-Condon factor to be more than 1000× smaller for (1,1) than for (0,0)[14].

Regardless, the relative population in $v = 1$ is expected to be degraded compared to the simplified model. A consequence of removing all dark states in $v = 0$ is that the rotational population in $v = 0$ is displaced approximately 20 rotational states away from the target state of $v = 1$. This increases the average rate of excitations for population in $v = 1$ and effectively reduces its lifetime. Additionally, the fidelity of the mask is

[14]Some evidence suggests that this is not actually the case as I will discuss in analysis of the second mask used. Regardless, it would be difficult to extract the peak without significant contrast as the band origin of $v = 1$ strongly overlaps with a strong peak in $v = 0$. Instead the upper spin orbit, where no overlap occurs, should be used to compare.

unnecessarily degraded due to the position of the R branch cutoff in $v = 0$ extending to $N = 22$ which was not understood until analysis of the measurement and the spectrally filtered laser spectrum had been performed. This adds to the degradation because the R branch for the cutoff in $v = 1$ is at $N = 19$ (see Fig. 7.20 a-ii)). A cutoff at $N = 19$ means that population entering $v = 1$ in rotational states at or beyond $N = 19$ will acquire an additional penalty (i.e. more average excitations and time) before reaching the ground rotational state. Therefore there are more opportunities for population leaving $v = 1$.

7.4.3.2. BBR Assist Mask. The second mask used to prepare $X, v = 1$ shown in Fig. 7.20 b-i) takes an alternative approach that more closely maps onto the ideal case described in section 2.5.2. This mask is constructed such that population accumulates in the low rotational states for both $v = 0$ and $v = 1$. This was done in an effort to avoid long rotational diffusion times in $v = 1$ which likely reduced the fidelity of the previous mask. That is, it is designed such that population is most likely to decay into $v = 1$ in the low rotational states where the mask is constructed such that these states are dark. This mask is in part a compromise to a technical challenge with the current version of the spectral shaping setup which doesn't allow for easy dynamic control of the mask.

The challenge comes from the following: In order to keep the low $N, v = 1$ states dark, the P branch of $v = 0$ for $N = 13$ to $N = 18$ must also not be optically pumped. Consequently we must rely on blackbody redistribution to diffuse population into $N < 13$ such that rotational energy can be removed via optical pumping. The time scale for this blackbody assisted mechanism was observed to be on the order of one minute. Evidence for the uncontrolled spectrum residing in this range is shown in Fig. 7.22 where

a simulated spectrum with uniform distribution between $N = 13$ and $N = 18$ is plotted for comparison.

During the recording of the spectrum the time spent waiting for the BBR assist mechanism was not controlled for and this likely explains the otherwise unexpected large variation sometimes present at similar energies in the spectrum. In future versions of the pulse shaping setup, the need for the BBR assisted mechanism can be nullified through the use of dynamic masks. This can be done by first pumping into $N = 0$ of the ground state and then reproducing a mask similar to the one used in this experiment.

In addition to issues with waiting for the BBR assist, the mask also suffers from issues that I only became aware of after analyzing the pulse shaping spectrum. As we were only interested in demonstrating the concept in these initial experiments, my strategy was to sacrifice a narrow rotational distribution for strong suppression of optical pumping rates near the band origin of $v = 1$. According to the simplified model, this has the unintended consequence of placing a slight upward 'pressure' on the rotational distribution that significantly reduces the effective lifetime of population in $v = 1$. In the band around the (1,1) origin, there is a slight preference for R branch transitions to be pumped. Thus a significant fraction of the population in $v = 1$ finds its way up the rotational ladder until it encounters transitions that undergo rapid excitation and cycling. According to the model this results in the majority of the population remaining in $v = 0$ ($\sim 1.7\times$ $v = 1$)[15].

[15]Specifically, the model predicts $n_i^{v=0} = 0.5, n_i^{v=1} = 0.3$.

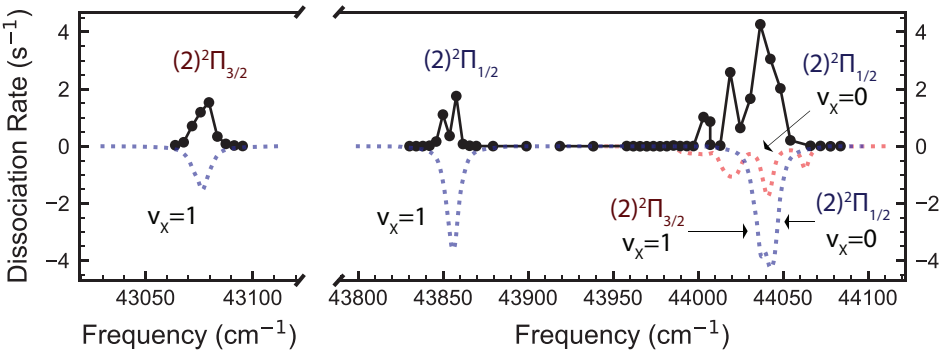

Figure 7.22. The observed (solid black lines) and simulated (dotted lines) dissociation spectrum using the control mask in Fig. 7.20 b-i). The simulated spectrum uses the populated rotational states in each vibrational level according to Fig. 7.20 a-ii) and assumes a linewidth of 5 cm^{-1} to account for the OPO linewidth. The observed spectrum was recorded using the *single frequency* method. The left hand side of the plot shows the $X^2\Sigma^+(v=1) \rightarrow C^2\Pi_{3/2}(v=0)$ hotband. The right hand side shows now, the full spectrum of the $X^2\Sigma^+(v=1) \rightarrow C^2\Pi_{1/2}(v=1)$ hotband (simulated in blue) and a combination of the $X^2\Sigma^+(v=0) \rightarrow C^2\Pi_{1/2}(v=0)$ and $X^2\Sigma^+(v=1) \rightarrow C^2\Pi_{3/2}(v=1)$ transitions. The red dotted lines simulate the uncontrolled population left in $v=0$ between $N=13$ and $N=18$. The blue dotted lines represent the simulated spectrum for population in $v=0,1$ between $N=0$ and $N=3$. As indicated by the arrows the origin of $X^2\Sigma^+(v=1) \rightarrow C^2\Pi_{3/2}(v=1)$ is nearly 7 cm^{-1} to the red of the $X^2\Sigma^+(v=0) \rightarrow C^2\Pi_{1/2}(v=0)$ origin.

For this BBR assisted mask we used the single frequency method to record the spectrum and thus are able to make some quantitative statements about the agreement between the expected population according to the simple model and the observed population. As in the previous section, we can use the observed maximum dissociation rate to place a lower bound on the population in $v=1$ which says that $n_i^{v=1} > 0.16$. Recalling the concern from analysis of the previous mask's dissociation spectrum that the FCF is potentially too small for observing significant contribution to the spectrum from

$X^2\Sigma^+(v=1) \rightarrow C^2\Pi_{3/2}(v=1)$ in its overlap with $X^2\Sigma^+(v=0) \rightarrow C^2\Pi_{1/2}(v=0)$ we can see that that the presence of a strong peak at 43855 cm^{-1} rules out this possibility. It, however, does not rule out the possibility of a spin-orbit dependent effect that reduces the possibility of dissociation. In the overlapped region for the dissociation spectrum recorded using the BBR assisted mask seen in the region between 44000 and 44060 cm^{-1} in Fig. 7.22, it is again difficult to extract the contribution due to $v = 1$ versus $v = 0$. Unfortunately, at the time of performing the experiment, the OPO was not sufficiently calibrated and the location of the $X^2\Sigma^+(v=1) \rightarrow C^2\Pi_{3/2}(v=1)$ band origin was not known to high accuracy. Thus we mistakenly assumed that the origins were well separated between the two vibrational bands. Nevertheless, in the overlapped region, it appears to be consistent with significant contribution from both vibrational levels. Assuming equivalent signal sizes for $X^2\Sigma^+(v=1) \rightarrow C^2\Pi_{1/2}(v=1)$ and $X^2\Sigma^+(v=1) \rightarrow C^2\Pi_{3/2}(v=1)$, then a lower bound on the population in $v = 0$ can be estimated as $n_i^{v=0} > 0.19$.

7.4.3.3. Lifetime and Fidelity Estimate for $v = 1$. Although the current data is unable to determine the population in $v = 1$ with anything better than crude bounds, there is qualitative consistency with expectations derived from the simplified steady state model. The bounds using the single frequency method for different masks are listed in Table 7.9. Because the current measurements only provide broad bounds and the simplified model assumes infinite lifetimes for excited vibrational levels, there is still an open question as to whether a mask similar to the one used can result in high fidelity state preparation in $v \geq 1$ with the optical pumping rates measured section 7.3.

Qualitatively, the bounds in Table 7.9 for different masks follow expectations. The maximal population in $v = 1$ for the purely rotational cooling mask (i.e. a cutoff at

$P(1)$) is found to be less than 1.8(5)%. This measurement was performed using the single frequency method to extract $p_{diss.} \times \sum_i n_i^{v=1}$. The value is then compared to the measured value for the BBR assisted mask. For this comparison I have assumed that the dissociation probability is constant between the two measurements. The maximum possible population for the BBR mask in $v = 1$ is then divided by the ratio to give us the bound. The same analysis is performed for the population with the rotational cooling mask with the cutoff position blue shifted to include $R(0)$ in the optical pumping. As expected the population in $v = 1$ is increased. This provides evidence that removing all the dark states in $v = 0$ causes population to vibrationally diffuse and provides the dominant mechanism for transferring population to $v = 1$. If the mask including $R(0)$ is modified by removing parts of the broadband spectrum that include the low N P and R branch transitions of $v = 1$ (i.e. the BBR assisted mask), the population in $v = 1$ is seen to increase by more than an order of magnitude. This behavior is exactly the qualitative behavior we'd expect using the simplified model.

With regards to the open question, the maximal population that can be accumulated in $v = 1$ will ultimately be limited by the finite lifetime of the excited vibrational states. The $v = 1$ lifetime, also listed in Table 7.9, is 1.0(5) s. Generally, the maximum population that can be accumulated will be determined by $\frac{R_{in}}{R_{out}+R_{in}}$ where $R_{in,out}$ describes the rate of population flow into and out of the state of interest. The rate of population flow into $v = 1$ can be estimated knowing the off diagonal branching ratio of $B(v = 0) \rightarrow X(v = 1)$, $f_{0,1} = 0.03$, and the average pumping rate $\lambda = 650\ \mathrm{s}^{-1}$. Using Eqn. (A.9), the population transfer rate to $v = 1$ is thus approximately $2f_{0,1}\lambda = 78\ \mathrm{s}^{-1}$. The Einstein $\mathcal{A}$ coefficient,

Table 7.9. The population bounds for different masks and the estimated lifetime for $v = 1$ are listed. The masks labeled $P(1)$ and $R(0)$ refer to modifications of the cutoff position for the $v = 0, N = 0$ masks used in section 7.3. The BBR assisted mask refers to that used in Fig. 7.20 b-i). Populations ranges were estimated using single frequency dissociation data with the ∼5 cm^{-1} broad pulsed OPO tuned to the $X^2\Sigma^+(v = 1) \rightarrow C^2\Pi_{3/2}(v = 0)$ transition at 43077 cm^{-1}. The lifetime estimate is derived in appendix B.5.

Mask	$p_{diss.} \times (\sum_i n_i^{v=1})$ †	$\sum_i n_i^{v=1}$
$P(1)$	0.0036(9)	$< 0.018(5)$ ‡
$R(0)$	0.011(6)	$< 0.054(28)$ ‡
BBR assisted	0.16	< 0.81
Estimated lifetime (s)		
$v = 1$	1.0(5)	

† These values also provide a lower bound on the population in $v = 1$ as $p_{diss} \leq 1$.

‡ Upper bound determined using contrast of signal and upper bound of the BBR assisted mask

i.e. the inverse lifetime, of $v = 1$ provides the minimum rate out of $v = 1$, $R_{out} = 1.0$ s^{-1}. Thus we get the estimate of a maximum possible population of ∼ 99%.

7.4.4. Conclusions

Exact quantitative results are currently limited by incomplete characterization and control of dissociation probabilities. The experimental setup has recently added a broadly tunable narrowband CW laser that will substantially improve the quality of characterization. Broadly speaking, even without exact quantitative knowledge, there is excellent qualitative agreement between experiment and theory suggesting that the rotational control techniques are performing well. The range of control was shown to populate narrow rotational distributions ($\Delta N \approx 3$) from the ground state to highly excited super rotor states up to rotational quanta of $N = 65$.

Extension of control to vibrational degrees of freedom has also been demonstrated as a proof of concept. Though quantitative analysis is again limited by knowledge of dissociation probabilities, qualitative behavior is functioning as expected. The crude estimation of the $v = 1$ lifetime equal to 1.0(5) s also suggests that even under the relatively low optical pumping laser intensities used, high fidelity state preparation is possible with more appropriately constructed spectral pulse shaping masks.

With the demonstration of the concept, the next logical step is to expand control to higher rovibrational states so that the extreme limits of control can be found. Plans are currently underway for implementing a digital micro-mirror array mask to construct more general masks capable of rapid dynamic control as proposed in [**62**]. These masks will be able to more closely reconstruct the idealized masks introduced in section 2.5.2.

The principle technique employed in this work, namely optically pumping transitions that stochastically flow population towards a targeted state left intentionally dark to the laser, has the possibility of becoming a very general technique. Theoretically, the only limiting factor on state preparation fidelity of an arbitrary target state in an arbitrary molecule is whether the target state has some transition that decays to it much more rapidly than population leaves the target state. Arbitrary molecules may lack the simplified structure that a diagonal FCF electronic transition affords and thus may require broad coverage of the spectrum to insure stochastic flow of population into the desired target state, however the development of supercontinuum lasers may ultimately limit the number of required lasers necessary for control to one.

Currently, spectral densities in supercontinuum lasers are too low to provide the repump rates that are practically necessary for molecules without diagonal FCFs. Thus

more general application of supercontinuum lasers will likely require much higher power specifications. Furthermore, to achieve high fidelity arbitrary state preparation, heavier diatomic molecules and more complicated polyatomic molecules will also contain a higher density of modes and congestion of lines that will require significantly improved pulse-shaping resolution beyond that achieved in this work. However, the recent demonstration of sub GHz pulse shaping resolution [**167**] suggests that there is significant room for immediate improvements.

In species or target states requiring resolutions better than what has been demonstrated, some of the requirements for pulse shaping may be relaxed with the inclusion of a small number of narrowband CW lasers that are frequency chirped over multiple transitions. Finally, the inclusion of polarization control over the pulse-shaped spectrum combined with magnetic field control also offer interesting possibilities for steady state preparation of aligned and oriented molecules or even coherent superpositions via coherent population trapping [**54**].

References

[1] Alekseyev, A. B., Liebermann, H.-P., Lingott, R. M., Bludskỳ, O., and Buenker, R. J. The spectrum of antimony hydride: An ab initio configuration interaction study employing a relativistic effective core potential. *The Journal of chemical physics 108*, 18 (1998), 7695–7706.

[2] Antypas, D., Budker, D., Flambaum, V. V., Kozlov, M. G., Perez, G., and Ye, J. Fast apparent oscillations of fundamental constants. *arXiv preprint arXiv:1912.01335* (2019).

[3] Arnold, K., Hajiyev, E., Paez, E., Lee, C. H., Barrett, M., and Bollinger, J. Prospects for atomic clocks based on large ion crystals. *Physical Review A 92*, 3 (2015), 032108.

[4] Arqueros, F., and Campos, J. Branching ratios for co+ electronic transitions. *Physica B+ C 112*, 1 (1982), 131–137.

[5] Auchter, C., Noel, T. W., Hoffman, M. R., Williams, S. R., and Blinov, B. B. Measurement of the branching fractions and lifetime of the 5 d 5/2 level of ba+. *Physical Review A 90*, 6 (2014), 060501.

[6] Baba, T., and Waki, I. Cooling and mass-analysis of molecules using laser-cooled atoms. *Japanese journal of applied physics 35*, 9A (1996), L1134.

[7] Baba, T., and Waki, I. Laser-cooled fluorescence mass spectrometry using laser-cooled barium ions in a tandem linear ion trap. *Journal of Applied Physics 89*, 8 (2001), 4592–4598.

[8] Baig, M., and Connerade, J. Rydberg series in the vacuum ultraviolet absorption spectrum of silicon monoxide. *Journal of Physics B: Atomic and Molecular Physics 12*, 14 (1979), 2309.

[9] Balakrishnan, N. Perspective: Ultracold molecules and the dawn of cold controlled chemistry. *The Journal of chemical physics 145*, 15 (2016), 150901.

[10] Barrow, R., and Stone, T. The identification of a new band system associated with gaseous silicon monoxide. *Journal of Physics B: Atomic and Molecular Physics 8*, 2 (1975), L13.

[11] Barry, J., McCarron, D., Norrgard, E., Steinecker, M., and DeMille, D. Magneto-optical trapping of a diatomic molecule. *Nature 512*, 7514 (2014), 286.

[12] Bell, M. T., and P. Softley, T. Ultracold molecules and ultracold chemistry. *Molecular Physics 107*, 2 (2009), 99–132.

[13] Berengut, J., and Flambaum, V. Comment on global positioning system test of the local position invariance of plancks constant. *Physical review letters 109*, 6 (2012), 068901.

[14] Berengut, J., Flambaum, V., King, J., Curran, S., and Webb, J. Is there further evidence for spatial variation of fundamental constants? *Physical Review D 83*, 12 (2011), 123506.

[15] Berkeland, D., and Boshier, M. Destabilization of dark states and optical spectroscopy in zeeman-degenerate atomic systems. *Physical Review A 65*, 3 (2002), 033413.

[16] Beutel, M., Setzer, K., Shestakov, O., and Fink, E. Thea1δ (a2) x3σ- (x21) transitions of sbh and sbd. *Journal of Molecular Spectroscopy 179*, 1 (1996), 79–84.

[17] Bishof, M., Zhang, X., Martin, M. J., and Ye, J. Optical spectrum analyzer with quantum-limited noise floor. *Physical review letters 111*, 9 (2013), 093604.

[18] Bitter, M., and Milner, V. Experimental observation of dynamical localization in laser-kicked molecular rotors. *Physical review letters 117*, 14 (2016), 144104.

[19] Bohme, D. K. Chemistry initiated by atomic silicon ions in the gas phase: formation of silicon-bearing ions and molecules. *International Journal of Mass Spectrometry and Ion Processes 100* (1990), 719–736.

[20] Bowe, P., Hornekær, L., Brodersen, C., Drewsen, M., Hangst, J., and Schiffer, J. Sympathetic crystallization of trapped ions. *Physical Review Letters 82*, 10 (1999), 2071.

[21] Cai, Z.-L., and François, J.-P. An internally contracted multireference configuration interaction analysis of the sio+ b2σ+–x2σ+ transition moment. *Chemical physics letters 282*, 1 (1998), 29–38.

[22] Cai, Z.-L., and François, J.-P. Ab initio study of the electronic spectrum of the sio+ cation. *Journal of molecular spectroscopy 197*, 1 (1999), 12–18.

[23] Calmet, X., and Fritzsch, H. The cosmological evolution of the nucleon mass and the electroweak coupling constants. *The European Physical Journal C-Particles and Fields 24*, 4 (2002), 639–642.

[24] Cameron, R., Scholl, T., Zhang, L., Holt, R., and Rosner, S. Fast-ion-beam laser spectroscopy of the b2σ+-x2σ+ and b2σ+-a2π systems of sio+: Deperturbation analysis. *Journal of Molecular Spectroscopy 169*, 2 (1995), 364–372.

[25] Chattopadhyaya, S., Chattopadhyay, A., and Das, K. K. Electronic spectrum of sio+: a theoretical study. *Journal of Molecular Structure: THEOCHEM 639*, 1-3 (2003), 177–185.

[26] Chen, K., Schowalter, S. J., Kotochigova, S., Petrov, A., Rellergert, W. G., Sullivan, S. T., and Hudson, E. R. Molecular-ion trap-depletion spectroscopy of bacl+. *Physical Review A 83*, 3 (2011), 030501.

[27] Chen, K., Sullivan, S. T., Rellergert, W. G., and Hudson, E. R. Measurement of the coulomb logarithm in a radio-frequency paul trap. *Physical review letters 110*, 17 (2013), 173003.

[28] Chou, C.-w., Kurz, C., Hume, D. B., Plessow, P. N., Leibrandt, D. R., and Leibfried, D. Preparation and coherent manipulation of pure quantum states of a single molecular ion. *Nature 545*, 7653 (2017), 203–207.

[29] Chupka, W. A. Factors affecting lifetimes and resolution of rydberg states observed in zero-electron-kinetic-energy spectroscopy. *The Journal of chemical physics 98*, 6 (1993), 4520–4530.

[30] Colbourn, E., Dyke, J., Lee, E., Morris, A., and Trickle, I. The vacuum ultra-violet photoelectron spectrum of the sio (x1σ+) molecule. *Molecular Physics 35*, 3 (1978), 873–882.

[31] Cournol, A., Pillet, P., Lignier, H., and Comparat, D. Rovibrational optical pumping of a molecular beam. *Physical Review A 97*, 3 (2018), 031401.

[32] D. Manura, D. D. *SIMION (R) 8.0 User Manual*. Scientific Instrument Services, Inc., Ringoes, NJ 08551, Jan. 2008.

[33] de Lima Batista, A. P., Sampaio de Oliveira-Filho, A. G., and Ornellas, F. R. Excited electronic states, transition probabilities, and radiative lifetimes of cas: A theoretical contribution and challenge to experimentalists. *The Journal of Physical Chemistry A 115*, 30 (2011), 8399–8405.

[34] DeMille, D., Cahn, S. B., Murphree, D., Rahmlow, D. A., and Kozlov, M. G. Using molecules to measure nuclear spin-dependent parity violation. *Physical Review Letters 100*, 2 (2008), 023003.

[35] DeMille, D., Sainis, S., Sage, J., Bergeman, T., Kotochigova, S., and Tiesinga, E. Enhanced sensitivity to variation of m e/m p in molecular spectra. *Physical review letters 100*, 4 (2008), 043202.

[36] Ding, S., and Matsukevich, D. Quantum logic for the control and manipulation of molecular ions using a frequency comb. *New Journal of Physics 14*, 2 (2012), 023028.

[37] Dirac, P. A. The cosmological constants. *Nature 139*, 3512 (1937), 323.

[38] Douglas, D. J., Frank, A. J., and Mao, D. Linear ion traps in mass spectrometry. *Mass spectrometry reviews 24*, 1 (2005), 1–29.

[39] Duff, M. How fundamental are fundamental constants? *Contemporary Physics 56*, 1 (2015), 35–47.

[40] Dunn, T., Rao, K., Nagaraj, S., and Verma, R. New spectrum of the sio+ moleculea correction. *Canadian Journal of Physics 47*, 19 (1969), 2128–2128.

[41] Fahey, D., Fehsenfeld, F., Ferguson, E., and Viehland, L. Reactions of si+ with h2o and o2 and sio+ with h2 and d2. *The Journal of Chemical Physics 75*, 2 (1981), 669–674.

[42] Fedchak, J. A., and Defibaugh, D. R. Long-term stability of metal-envelope enclosed bayard–alpert ionization gauges. *Journal of Vacuum Science & Technology A: Vacuum, Surfaces, and Films 30*, 6 (2012), 061601.

[43] Feller, D. Benchmarks of improved complete basis set extrapolation schemes designed for standard ccsd (t) atomization energies. *The Journal of chemical physics 138*, 7 (2013), 074103.

[44] Field, R., Lagerqvist, A., and Renhorn, I. The low lying electronic states of sio. *Physica Scripta 14*, 6 (1976), 298.

[45] Field, R., Lagerqvist, A., and Renhorn, I. A perturbation study of the low lying sio eletronic states. *The Journal of Chemical Physics 66*, 2 (1977), 868–869.

[46] Flambaum, V., and Kozlov, M. Enhanced sensitivity to the time variation of the fine-structure constant and m p/m e in diatomic molecules. *Physical review letters 99*, 15 (2007), 150801.

[47] Flambaum, V., and Kozlov, M. Limit on the cosmological variation of m p/m e from the inversion spectrum of ammonia. *Physical review letters 98*, 24 (2007), 240801.

[48] Flambaum, V., Leinweber, D., Thomas, A., and Young, R. Limits on variations of the quark masses, qcd scale, and fine structure constant. *Physical Review D 69*, 11 (2004), 115006.

[49] Gascooke, J. R., Alexander, U. N., and Lawrance, W. D. Two dimensional laser induced fluorescence spectroscopy: A powerful technique for elucidating rovibronic structure in electronic transitions of polyatomic molecules. *The Journal of chemical physics 134*, 18 (2011), 184301.

[50] Ghosh, P. K. *Ion traps*. 1995.

[51] Glöckner, R., Prehn, A., Englert, B. G., Rempe, G., and Zeppenfeld, M. Rotational cooling of trapped polyatomic molecules. *Physical review letters 115*, 23 (2015), 233001.

[52] Godun, R., Nisbet-Jones, P., Jones, J., King, S., Johnson, L., Margolis, H., Szymaniec, K., Lea, S., Bongs, K., and Gill, P. Frequency ratio of two optical clock transitions in yb+ 171 and constraints on the time variation of fundamental constants. *Physical review letters 113*, 21 (2014), 210801.

[53] Gonçalves dos Santos, L., de Oliveira-Filho, A. G. S., and Ornellas, F. R. The electronic states of teh+: A theoretical contribution. *The Journal of chemical physics 142*, 2 (2015), 024316.

[54] Gray, H., Whitley, R., and Stroud, C. Coherent trapping of atomic populations. *Optics letters 3*, 6 (1978), 218–220.

[55] Hansen, A. K., Versolato, O., Kristensen, S. B., Gingell, A., Schwarz, M., Windberger, A., Ullrich, J., López-Urrutia, J. C., Drewsen, M., et al. Efficient rotational cooling of coulomb-crystallized molecular ions by a helium buffer gas. *Nature 508*, 7494 (2014), 76.

[56] Herzberg, G. Molecular spectra and molecular structure. vol. 1: Spectra of diatomic molecules. *New York: Van Nostrand Reinhold, 1950, 2nd ed.* (1950).

[57] Hilborn, R. C. Einstein coefficients, cross sections, f values, dipole moments, and all that. *American Journal of Physics 50*, 11 (1982), 982–986.

[58] Hildenbrand, D. L., and Murad, E. Dissociation energy and ionization potential of silicon monoxide. *The Journal of Chemical Physics 51*, 2 (1969), 807–811.

[59] Hinkle, K., Barnes, T., Lambert, D., and Beer, R. Silicon monoxide in the 4 micron infrared spectrum of long-period variables. *The Astrophysical Journal 210* (1976), L141–L144.

[60] Hollberg, L., Oates, C. W., Curtis, E. A., Ivanov, E. N., Diddams, S. A., Udem, T., Robinson, H. G., Bergquist, J. C., Rafac, R. J., Itano, W. M., et al. Optical frequency standards and measurements. *IEEE Journal of Quantum Electronics 37*, 12 (2001), 1502–1513.

[61] Honjou, N. Ab initio configuration interaction study on the electronic structure of the 1–42π states of sio+ and the avoided crossings of the 2–42π potential energy curves. *Molecular Physics 101*, 20 (2003), 3063–3071.

[62] Horchani, R. Femtosecond laser shaping with digital light processing. *Optical and Quantum Electronics 47*, 8 (2015), 3023–3030.

[63] Hudson, E. R., and Campbell, W. C. Dipolar quantum logic for freely rotating trapped molecular ions. *Physical Review A 98*, 4 (2018), 040302.

[64] Hudson, J., Sauer, B., Tarbutt, M., and Hinds, E. Measurement of the electron electric dipole moment using ybf molecules. *Physical Review Letters 89*, 2 (2002), 023003.

[65] Huntemann, N., Lipphardt, B., Tamm, C., Gerginov, V., Weyers, S., and Peik, E. Improved limit on a temporal variation of m p/m e from comparisons of yb+ and cs atomic clocks. *Physical review letters 113*, 21 (2014), 210802.

[66] Hutson, J. M. Ultracold chemistry. *Science 327*, 5967 (2010), 788–789.

[67] Ishikawa, Y., and Nemanič, V. An overview of methods to suppress hydrogen outgassing rate from austenitic stainless steel with reference to uhv and exv. *Vacuum 69*, 4 (2003), 501–512.

[68] Jadraque, M., Santos, M., Díaz, L., Álvarez-Ruiz, J., and Martín, M. Silicon oxide cluster formation and stability in the laser ablation of sio targets. *The Journal of Physical Chemistry A 113*, 41 (2009), 10880–10885.

[69] Jansen, P., Bethlem, H. L., and Ubachs, W. Perspective: Tipping the scales: Search for drifting constants from molecular spectra. *The Journal of chemical physics 140*, 1 (2014), 010901.

[70] Jones, M., and Ceperley, D. M. Crystallization of the one-component plasma at finite temperature. *Physical review letters 76*, 24 (1996), 4572.

[71] Kajita, M. Evaluation of variation in \left (m_\mathrm {p}/m_\mathrm {e}\right) mp/me from the frequency difference between the {{}^{15}\hbox {N} _

{2}}ˆ{+} 15 n2+ and {}ˆ{87}\hbox {Sr} 87 sr transitions. *Applied Physics B 122*, 7 (2016), 203.

[72] Kajita, M. Accuracy estimation of the o 2 16+ transition frequencies targeting the search for the variation in the proton-electron mass ratio. *Physical Review A 95*, 2 (2017), 023418.

[73] Kajita, M., Gopakumar, G., Abe, M., Hada, M., and Keller, M. Test of m p/m e changes using vibrational transitions in n 2+. *Physical Review A 89*, 3 (2014), 032509.

[74] Kang, S.-Y., Kuang, F.-G., Jiang, G., Li, D.-B., Luo, Y., Feng-Hui, P., Li-Ping, W., Hu, W.-Q., and Shao, Y.-C. Ab initio study of laser cooling of alf+ and alcl+ molecular ions. *Journal of Physics B: Atomic, Molecular and Optical Physics 50*, 10 (2017), 105103.

[75] Karr, J.-P., Douillet, A., and Hilico, L. Photodissociation of trapped

\

mathrm {H} _ {2}ˆ{+} $ions for rem pd spectroscopy. Applied Physics B 107, 4 (2012), 1043 − −1052.$

[76] Ketterle, W., and Pritchard, D. E. Atom cooling by time-dependent potentials. *Physical Review A 46*, 7 (1992), 4051.

[77] Kobayashi, J., Ogino, A., and Inouye, S. Measurement of the variation of electron-to-proton mass ratio using ultracold molecules produced from laser-cooled atoms. *Nature communications 10*, 1 (2019), 1–5.

[78] Koelemeij, J., Roth, B., and Schiller, S. Blackbody thermometry with cold molecular ions and application to ion-based frequency standards. *Physical Review A 76*, 2 (2007), 023413.

[79] Kokish, M. G., Stollenwerk, P. R., Kajita, M., and Odom, B. C. Prospects for a polar-molecular-ion optical probe of varying proton-electron mass ratio. *Physical Review A 98*, 5 (2018), 052513.

[80] Kokkin, D. L., Ma, T., Steimle, T., and Sears, T. J. Detection and characterization of singly deuterated silylene, sihd, via optical spectroscopy. *The Journal of chemical physics 144*, 24 (2016), 244304.

[81] Kokkin, D. L., Steimle, T. C., and DeMille, D. Branching ratios and radiative lifetimes of the u, l, and i states of thorium oxide. *Physical Review A 90*, 6 (2014), 062503.

[82] Korobenko, A., Milner, A. A., and Milner, V. Direct observation, study, and control of molecular superrotors. *Physical review letters 112*, 11 (2014), 113004.

[83] Kostko, O., Ahmed, M., and Metz, R. B. Vacuum-ultraviolet photoionization measurement and ab initio calculation of the ionization energy of gas-phase sio2. *The Journal of Physical Chemistry A 113*, 7 (2009), 1225–1230.

[84] Kozlov, M. G., and Budker, D. Comment on sensitivity coefficients to variation of fundamental constants. *Annalen der Physik 531*, 5 (2019), 1800254.

[85] Lagerqvist, A., Renhorn, I., and Elander, N. The spectrum of sio in the vacuum ultraviolet region. *Journal of Molecular Spectroscopy 46*, 2 (1973), 285–315.

[86] Laher, R. R., and Gilmore, F. R. Improved fits for the vibrational and rotational constants of many states of nitrogen and oxygen. *Journal of Physical and Chemical Reference Data 20*, 4 (1991), 685–712.

[87] Le Roy, R. J. University of waterloo chemical physics research report, 2004.

[88] Le Roy, R. J. Level: A computer program for solving the radial schrödinger equation for bound and quasibound levels. *Journal of Quantitative Spectroscopy and Radiative Transfer 186* (2017), 167–178.

[89] Leibfried, D. Quantum state preparation and control of single molecular ions. *New Journal of Physics 14*, 2 (2012), 023029.

[90] Li, J., Bahns, J. T., and Stwalley, W. C. Scheme for state-selective formation of highly rotationally excited diatomic molecules. *The Journal of Chemical Physics 112*, 14 (2000), 6255–6261.

[91] Lien, C.-Y., Seck, C. M., Lin, Y.-W., Nguyen, J. H., Tabor, D. A., and Odom, B. C. Broadband optical cooling of molecular rotors from room temperature to the ground state. *Nature communications 5* (2014), 4783.

[92] Lien, C.-Y., Williams, S. R., and Odom, B. Optical pulse-shaping for internal cooling of molecules. *Physical Chemistry Chemical Physics 13*, 42 (2011), 18825–18829.

[93] Lin, Y.-W. *Towards the Precision Spectroscopy of a Single Molecular Ion*. PhD thesis, Northwestern University, 2016.

[94] Lin, Y.-W., and Odom, B. C. High extinction amplitude modulation in ultrashort pulse shaping. *arXiv preprint arXiv:1610.04324* (2016).

[95] Loh, H., Stutz, R. P., Yahn, T. S., Looser, H., Field, R. W., and Cornell, E. A. Rempi spectroscopy of hff. *Journal of Molecular Spectroscopy 276* (2012), 49–56.

[96] Lubman, D. M., Rettner, C. T., and Zare, R. N. How isolated are molecules in a molecular beam? *The Journal of Physical Chemistry 86*, 7 (1982), 1129–1135.

[97] Lundqvist, M., Edvardsson, D., Baltzer, P., Larsson, M., and Wannberg, B. Observation of predissociation and tunnelling processes in: a study using doppler free kinetic energy release spectroscopy and ab initio ci calculations. *Journal of Physics B: Atomic, Molecular and Optical Physics 29*, 3 (1996), 499.

[98] Luo, Y.-R. *Comprehensive handbook of chemical bond energies*. CRC press, 2007.

[99] Manai, I., Horchani, R., Lignier, H., Pillet, P., Comparat, D., Fioretti, A., and Allegrini, M. Rovibrational cooling of molecules by optical pumping. *Physical review letters 109*, 18 (2012), 183001.

[100] Martins, C. The status of varying constants: a review of the physics, searches and implications. *Reports on Progress in Physics 80*, 12 (2017), 126902.

[101] Matsuo, Y., Nakajima, T., Kobayashi, T., and Takami, M. Formation and laser-induced-fluorescence study of sio+ ions produced by laser ablation of si in oxygen gas. *Applied physics letters 71*, 8 (1997), 996–998.

[102] Müller-Dethlefs, K., and Schlag, E. W. Chemical applications of zero kinetic energy (zeke) photoelectron spectroscopy. *Angewandte Chemie International Edition 37*, 10 (1998), 1346–1374.

[103] Mulliken, R. S. The isotope effect in band spectra, iv: the spectrum of silicon nitride. *Physical Review 26*, 3 (1925), 319.

[104] Nagaraj, S., and Verma, R. New spectrum of the SiO^+ molecule. *Canadian Journal of Physics 46*, 14 (1968), 1597–1602.

[105] Nakamura, K. G., Kamioka, I., and Kitajima, M. Dynamics of sio desorption in reactive scattering of o2 with a silicon surface. *The Journal of chemical physics 104*, 9 (1996), 3403–3404.

[106] Nakamura, K. G., and Kitajima, M. Resonance enhanced multiphoton ionization detection of sio desorbing from a si (111) surface in reaction with o2. *Applied physics letters 65*, 19 (1994), 2445–2447.

[107] Nakamura, K. G., and Kitajima, M. Reactive scattering of o2 with the si (111) surface: Resonance enhanced multiphoton ionization of sio. *The Journal of chemical physics 102*, 21 (1995), 8569–8573.

[108] Nguyen, J., and Odom, B. Prospects for doppler cooling of three-electronic-level molecules. *Physical Review A 83*, 5 (2011), 053404.

[109] Nguyen, J. H., Viteri, C. R., Hohenstein, E. G., Sherrill, C. D., Brown, K. R., and Odom, B. Challenges of laser-cooling molecular ions. *New Journal of Physics 13*, 6 (2011), 063023.

[110] Ni, K.-K., Loh, H., Grau, M., Cossel, K. C., Ye, J., and Cornell, E. A. State-specific detection of trapped hff+ by photodissociation. *Journal of Molecular Spectroscopy 300* (2014), 12–15.

[111] Ni, K.-K., Ospelkaus, S., De Miranda, M., Pe'Er, A., Neyenhuis, B., Zirbel, J., Kotochigova, S., Julienne, P., Jin, D., and Ye, J. A high phase-space-density gas of polar molecules. *science 322*, 5899 (2008), 231–235.

[112] Nicholls, R. Franck-condon factors to high vibrational quantum numbers ii: Sio, mgo, sro, alo, vo, no. *J. Res. Natl. Bur. Stand. Sect. A 66* (1962), 227–231.

[113] Nicholls, R. Franck-condon factor formulae for astrophysical and other molecules. *The Astrophysical Journal Supplement Series 47* (1981), 279–290.

[114] Norrgard, E. B., Sitaraman, N., Barry, J. F., McCarron, D., Steinecker, M. H., and DeMille, D. In-vacuum scattered light reduction with black cupric oxide

surfaces for sensitive fluorescence detection. *Review of Scientific Instruments 87*, 5 (2016), 053119.

[115] Notarnicola, S., Iemini, F., Rossini, D., Fazio, R., Silva, A., and Russomanno, A. From localization to anomalous diffusion in the dynamics of coupled kicked rotors. *Physical Review E 97*, 2 (2018), 022202.

[116] Oliveira-Filho, A. G. S., and de Lima Batista, A. P. Sio+ potential energy curves. Unpublished, 2019.

[117] Ospelkaus, S., Ni, K.-K., Wang, D., De Miranda, M., Neyenhuis, B., Quéméner, G., Julienne, P., Bohn, J., Jin, D., and Ye, J. Quantum-state controlled chemical reactions of ultracold potassium-rubidium molecules. *Science 327*, 5967 (2010), 853–857.

[118] Ostendorf, A., Zhang, C. B., Wilson, M., Offenberg, D., Roth, B., and Schiller, S. Sympathetic cooling of complex molecular ions to millikelvin temperatures. *Physical review letters 97*, 24 (2006), 243005.

[119] Pankhurst, R. A complex band-spectrum associated with an oxide of silicon. *Proceedings of the Physical Society 52*, 5 (1940), 707.

[120] Pérez-Ríos, J., and Robicheaux, F. Rotational relaxation of molecular ions in a buffer gas. *Physical Review A 94*, 3 (2016), 032709.

[121] Ram, R., Engleman Jr, R., and Bernath, P. Fourier transform emission spectroscopy of thea2δ–x2π transition of sih and sid. *Journal of molecular spectroscopy 190*, 2 (1998), 341–352.

[122] Reddy, R., Ahammed, Y. N., Devi, B. S., Gopal, K. R., Azeem, P. A., and Rao, T. Spectroscopic studies on astrophysically interesting tao tas, zrs and sio+ molecules. *Astrophysics and space science 281*, 4 (2002), 729–741.

[123] Reilly, N. J., Schmidt, T. W., and Kable, S. H. Two-dimensional fluorescence (excitation/emission) spectroscopy as a probe of complex chemical environments. *The Journal of Physical Chemistry A 110*, 45 (2006), 12355–12359.

[124] Reiser, G., Habenicht, W., Müller-Dethlefs, K., and Schlag, E. W. The ionization energy of nitric oxide. *Chemical physics letters 152*, 2-3 (1988), 119–123.

[125] Riis, E., and Sinclair, A. G. Optimum measurement strategies for trapped ion optical frequency standards. *Journal of Physics B: Atomic, Molecular and Optical Physics 37*, 24 (2004), 4719.

[126] Rosner, S., Cameron, R., Scholl, T., and Holt, R. A study of thex2σ+ anda2π states of sio+ using fast-ion-beam laser spectroscopy. *Journal of molecular spectroscopy 189*, 1 (1998), 83–94.

[127] Roth, B., Blythe, P., and Schiller, S. Motional resonance coupling in cold multi-species coulomb crystals. *Physical Review A 75*, 2 (2007), 023402.

[128] Safronova, M., Budker, D., DeMille, D., Kimball, D. F. J., Derevianko, A., and Clark, C. W. Search for new physics with atoms and molecules. *Reviews of Modern Physics 90*, 2 (2018), 025008.

[129] Safronova, M. S. The search for variation of fundamental constants with clocks. *Annalen der Physik 531*, 5 (2019), 1800364.

[130] Salumbides, E., Niu, M., Bagdonaite, J., de Oliveira, N., Joyeux, D., Nahon, L., and Ubachs, W. Co a- x system for constraining cosmological drift of the proton-electron mass ratio. *Physical Review A 86*, 2 (2012), 022510.

[131] Scherschligt, J., Fedchak, J. A., Barker, D. S., Eckel, S., Klimov, N., Makrides, C., and Tiesinga, E. Development of a new uhv/xhv pressure standard (cold atom vacuum standard). *Metrologia 54*, 6 (2017), S125.

[132] Schmidt, P. O., Rosenband, T., Langer, C., Itano, W. M., Bergquist, J. C., and Wineland, D. J. Spectroscopy using quantum logic. *Science 309*, 5735 (2005), 749–752.

[133] Schmidt, R., and Lemeshko, M. Rotation of quantum impurities in the presence of a many-body environment. *Physical review letters 114*, 20 (2015), 203001.

[134] Schmidt, R., and Lemeshko, M. Deformation of a quantum many-particle system by a rotating impurity. *Physical Review X 6*, 1 (2016), 011012.

[135] Schnabel, R., Schultz-Johanning, M., and Kock, M. Fe ii lifetimes and transition probabilities. *Astronomy & Astrophysics 414*, 3 (2004), 1169–1176.

[136] Schneider, T., Roth, B., Duncker, H., Ernsting, I., and Schiller, S. All-optical preparation of molecular ions in the rovibrational ground state. *Nature Physics 6*, 4 (2010), 275–278.

[137] Scholl, T., Cameron, R., Rosner, S., and Holt, R. Beam-laser measurements of lifetimes in sio+ and n 2+. *Physical Review A 51*, 3 (1995), 2014.

[138] Schowalter, S. J., Chen, K., Rellergert, W. G., Sullivan, S. T., and Hudson, E. R. An integrated ion trap and time-of-flight mass spectrometer for chemical and photo-reaction dynamics studies. *Review of Scientific Instruments 83*, 4 (2012), 043103.

[139] Schulte, M., Lörch, N., Leroux, I. D., Schmidt, P. O., and Hammerer, K. Quantum algorithmic readout in multi-ion clocks. *Physical review letters 116*, 1 (2016), 013002.

[140] Schultz-Johanning, M., Schnabel, R., and Kock, M. A linear paul trap for radiative lifetime measurements on ions. *The European Physical Journal D-Atomic, Molecular, Optical and Plasma Physics 5*, 3 (1999), 341–344.

[141] Seck, C. M., Hohenstein, E. G., Lien, C.-Y., Stollenwerk, P. R., and Odom, B. C. Rotational state analysis of alh+ by two-photon dissociation. *Journal of Molecular Spectroscopy 300* (2014), 108–111.

[142] Shagam, Y., and Narevicius, E. Sub-kelvin collision temperatures in merged neutral beams by correlation in phase-space. *The Journal of Physical Chemistry C 117*, 43 (2013), 22454–22461.

[143] Shelkovnikov, A., Butcher, R. J., Chardonnet, C., and Amy-Klein, A. Stability of the proton-to-electron mass ratio. *Physical Review Letters 100*, 15 (2008), 150801.

[144] Shestakov, O., Gielen, R., Pravilov, A., Setzer, K., and Fink, E. Lif study of the b 1 σ+(b0+) x 3 σ-(x 1 0+, x 2 1) transitions of sbh and sbd. *Journal of molecular spectroscopy 191*, 1 (1998), 199–205.

[145] Shi, D., Li, W., Xing, W., Sun, J., Zhu, Z., and Liu, Y. Mrci study on electronic spectrum of several low-lying electronic states of the sio+ cation. *Computational and Theoretical Chemistry 980* (2012), 73–84.

[146] Sofikitis, D., Horchani, R., Li, X., Pichler, M., Allegrini, M., Fioretti, A., Comparat, D., and Pillet, P. Vibrational cooling of cesium molecules using noncoherent broadband light. *Physical Review A 80*, 5 (2009), 051401.

[147] Sofikitis, D., Weber, S., Fioretti, A., Horchani, R., Allegrini, M., Chatel, B., Comparat, D., and Pillet, P. Molecular vibrational cooling by optical pumping with shaped femtosecond pulses. *New Journal of Physics 11*, 5 (2009), 055037.

[148] Staanum, P. F., Højbjerre, K., Skyt, P. S., Hansen, A. K., and Drewsen, M. Rotational laser cooling of vibrationally and translationally cold molecular ions. *Nature Physics 6*, 4 (2010), 271–274.

[149] Stollenwerk, P., Kokish, M., de Oliveira-Filho, A., Ornellas, F., and Odom, B. Optical pumping of teh+: Implications for the search for varying mp/me. *Atoms 6*, 3 (2018), 53.

[150] Stollenwerk, P. R., Antonov, I. O., and Odom, B. C. Ip determination and 1+ 1 rempi spectrum of sio at 210–220 nm in an ion trap: Implications for sio+ ion trap loading. *Journal of Molecular Spectroscopy 355* (2019), 40–45.

[151] Stollenwerk, P. R., Odom, B. C., Kokkin, D. L., and Steimle, T. Electronic spectroscopy of a cold sio+ sample: Implications for optical pumping. *Journal of Molecular Spectroscopy 332* (2017), 26–32.

[152] Tabor, D. *Toward Rotational Cooling of Trapped SiO+ byOptical Pumping*. PhD thesis, Northwestern University, 2014.

[153] Thompson, R. C. Ion coulomb crystals. *Contemporary Physics 56*, 1 (2015), 63–79.

[154] Tong, X., Wild, D., and Willitsch, S. Collisional and radiative effects in the state-selective preparation of translationally cold molecular ions in ion traps. *Physical Review A 83*, 2 (2011), 023415.

[155] Tong, X., Winney, A. H., and Willitsch, S. Sympathetic cooling of molecular ions in selected rotational and vibrational states produced by threshold photoionization. *Physical review letters 105*, 14 (2010), 143001.

[156] Torres, R., Jadraque, M., and Martin, M. Silicon cluster formation in the laser ablation of sio at 308 nm. *Applied Physics A 80*, 8 (2005), 1671–1675.

[157] Torres, R., and Martin, M. Laser ablation and time-of-flight mass-spectrometric study of sio. *Applied surface science 193*, 1-4 (2002), 149–155.

[158] Turner, J., and Dalgarno, A. The chemistry of silicon in interstellar clouds. *The Astrophysical Journal 213* (1977), 386–389.

[159] Ubachs, W., Buning, R., Eikema, K., and Reinhold, E. On a possible variation of the proton-to-electron mass ratio: H2 spectra in the line of sight of high-redshift quasars and in the laboratory. *Journal of molecular spectroscopy 241*, 2 (2007), 155–179.

[160] Uzan, J.-P. Varying constants, gravitation and cosmology. *Living reviews in relativity 14*, 1 (2011), 2.

[161] Viteau, M., Chotia, A., Allegrini, M., Bouloufa, N., Dulieu, O., Comparat, D., and Pillet, P. Optical pumping and vibrational cooling of molecules. *Science 321*, 5886 (2008), 232–234.

[162] Wannous, G., Effantin, C., Martin, F., and d'Incan, J. Treatment of the predissociation of the a1σu+ state of as2 by the interaction with a repulsive state. *Journal of Molecular Spectroscopy 91*, 1 (1982), 1–8.

[163] Werner, H., Knowles, P., Knizia, G., Manby, F., Schütz, M., Celani, P., Györffy, W., Kats, D., Korona, T., Lindh, R., et al. Molpro, version 2015.1, a package of ab initio programs, 2015. *University of Cardiff Chemistry Consultants (UC3): Cardiff* (2017).

[164] Western, C. M. Pgopher: A program for simulating rotational, vibrational and electronic spectra. *Journal of Quantitative Spectroscopy and Radiative Transfer 186* (2017), 221–242.

[165] Wiedmann, R. T., White, M. G., Wang, K., and McKoy, V. Single-photon threshold photoionization of no. *The Journal of chemical physics 98*, 10 (1993), 7673–7679.

[166] Wigner, E. P. On the behavior of cross sections near thresholds. *Physical Review 73*, 9 (1948), 1002.

[167] Willits, J. T., Weiner, A. M., and Cundiff, S. T. Line-by-line pulse shaping with spectral resolution below 890 mhz. *Optics express 20*, 3 (2012), 3110–3117.

[168] Wolf, U., and Tiemann, E. Predissociation of tif by tunneling. *Chemical physics letters 133*, 2 (1987), 116–120.

[169] Woods, L. H. On the silicon oxide bands. *Physical Review 63*, 11-12 (1943), 426.

[170] Xie, J., and Zare, R. N. Selection rules for the photoionization of diatomic molecules. *The Journal of Chemical Physics 93*, 5 (1990), 3033–3038.

[171] Yamashiro, R., Matsumoto, Y., and Honma, K. Reaction dynamics of si (pj 3)+ o 2 si o (x σ+ 1)+ o studied by a crossed-beam laser-induced fluorescence technique. *The Journal of chemical physics 128*, 8 (2008), 084308.

[172] Yang, J., and Clouthier, D. J. Electronic spectroscopy of the previously unknown arsenic carbide (asc) free radical. *The Journal of chemical physics 135*, 5 (2011), 054309.

[173] Yu, S., Fu, D., Shayesteh, A., Gordon, I. E., Appadoo, D. R., and Bernath, P. Infrared and near infrared emission spectra of sbh and sbd. *Journal of Molecular Spectroscopy 229*, 2 (2005), 257–265.

[174] Zelevinsky, T., Kotochigova, S., and Ye, J. Precision test of mass-ratio variations with lattice-confined ultracold molecules. *Physical review letters 100*, 4 (2008), 043201.

[175] Zhang, D., and Willitsch, S. Cold ion chemistry. In *Cold Chemistry*. 2017, pp. 496–536.

[176] Zhang, Q.-Q., Yang, C.-L., Wang, M.-S., Ma, X.-G., and Liu, W.-W. Spectroscopic parameters of the low-lying electronic states and laser cooling feasibility of nh+ cation and nh- anion. *Spectrochimica Acta Part A: Molecular and Biomolecular Spectroscopy 185* (2017), 365–370.

[177] Zhang, Q.-Q., Yang, C.-L., Wang, M.-S., Ma, X.-G., and Liu, W.-W. The ground and low-lying excited states and feasibility of laser cooling for gah+ and inh+ cations. *Spectrochimica Acta Part A: Molecular and Biomolecular Spectroscopy 193* (2018), 78–86.

[178] Zheng, S. Conductance calculation-molecular flow, long tube of circular cross section. Tech. rep., 1993.

APPENDIX A

Optical Pumping

A.1. Pumping Rates

The analysis in section 2.4.1 for the Λ-type system can be completed for R branch transitions of $\Sigma-\Sigma$ too. The derivation is identical, however the degeneracies and branching fractions are different for each direction. In the saturated case such that $P_{N,N-1} >> \Gamma$ or $R_{N,N+1} >> \Gamma$ we have

$$\begin{aligned}
\lambda_N^P = \alpha_N^P \frac{g_{N-1}}{g_{N-1}+g_N}\Gamma &= \frac{N-1}{2N-1}\frac{2N-1}{2N-1+2N+1}\Gamma = \frac{1-1/N}{4}\Gamma \text{ for } N>1, \\
\lambda_N^R = \alpha_N^R \frac{g_{N+1}}{g_{N+1}+g_N}\Gamma &= \frac{N+1}{2N+3}\frac{2N+3}{2N+3+2N+1}\Gamma = \frac{1}{4}\Gamma \text{ for } N\geq 0
\end{aligned} \tag{A.1}$$

where $\alpha_N^P = \frac{N-1}{2N-1}$, $\alpha_N^R = \frac{N+1}{2N+3}$ is the branching ratio for decaying from $N\pm 1$ into $N\pm 2$ and $\frac{g_{N\pm 1}}{g_N}$ is the quasi-steady state fraction of population in the excited state, and Γ is the excited state inverse lifetime. Similarly, below saturation such that $P_{N,N-1} << \Gamma$ or $R_{N,N+1} << \Gamma$ we have

$$\begin{aligned}
\lambda_N^P = s_N^P \alpha_N^P (1-\alpha_N^P)\frac{g_{N-1}}{g_N}\Gamma &= s_N^P \frac{N-1}{2N-1}\left(\frac{2N-1-(N-1)}{2N-1}\right)\frac{2N-1}{2N+1}\Gamma \\
&= s_N^P \left(\frac{N(N-1)}{4N^2-1}\right)\Gamma \text{ for } N>1, \\
\lambda_N^R = s_N^R \alpha_N^R (1-\alpha_N^R)\frac{g_{N+1}}{g_N}\Gamma &= s_N^R \frac{N+1}{2N+3}\left(\frac{2N+3-(N+1)}{2N+3}\right)\frac{2N+3}{2N+1}\Gamma \\
&= s_N^R \left(\frac{N^2+3N+2}{4N^2+8N+3}\right)\Gamma \text{ for } N\geq 0.
\end{aligned} \tag{A.2}$$

If we are concerned with the rate of population diffusing to a separate decay path with branching ratio $f << \alpha$ as in an off-diagonal decay or a weak decay to an intermediate state, then this new population transfer rate can generally be described by:

$$\begin{aligned} \lambda_f^P(N) &= \frac{\lambda_N^P}{\alpha_N^P} f \text{ for } N > 1, \\ \lambda_f^R(N) &= \frac{\lambda_N^R}{\alpha_N^R} f \text{ for } N \geq 0. \end{aligned} \tag{A.3}$$

For the special case of the $P(1)$ transition the rate simply becomes $s_1^P f\Gamma/3$ for the below saturated case and $f\Gamma/3$ for the saturated case where the factor of $1/3$ is a consequence of degeneracy factors for $N'' = 1$ and $N' = 0$.

A.2. Steady State Approximations

We can write down a simplified rate equation that relies on the derived population transfer rates $\lambda_N^{P,R}$ and solve for the steady state condition to give us

$$\begin{aligned} \dot{n}_0 &= 0 = \lambda_2^P n_2 - \lambda_0^R n_0 \\ \dot{n}_1 &= 0 = \lambda_3^P n_3 - \lambda_1^R n_1 \\ \dot{n}_2 &= 0 = \lambda_4^P n_4 - (\lambda_2^P + \lambda_2^R) n_2 + \lambda_0^R n_0 \\ &\cdots \\ \dot{n}_i &= 0 = \lambda_{i+2}^P n_{i+2} - (\lambda_i^P + \lambda_i^R) n_i + \lambda_{i-2}^R n_{i-2} \\ &\cdots \end{aligned} \tag{A.4}$$

which allows us to relate the population in $N = t$ and $N = t \pm 2$ via

$$\begin{aligned} n_t &= n_{t+2}\frac{\lambda^P_{t+2}}{\lambda^R_t}, \\ n_t &= n_{t-2}\frac{\lambda^R_{t-2}}{\lambda^P_t}. \end{aligned} \tag{A.5}$$

Thus we can relate the relative population of any one rotational state to any other rotational state of the same parity (and vibrational level). More generally we can derive the total population in a given parity rotational ladder, $\left(\sum n\right)_\pm$, relative to the population in a single state of the same parity:

$$\begin{aligned} \left(\sum n\right)_\pm &= n_t\left(\sum_{i=0}^{j-1}\prod_{k=0}^{i}\frac{\lambda^P_{t-2k}}{\lambda^R_{t-2k-2}} + 1 + \sum_{i=0}^{i}\prod_{k=0}^{i}\frac{\lambda^R_{t+2k}}{\lambda^P_{t+2k+2}}\right), \text{ for } j > 0 \\ &\equiv n_t Z_t \end{aligned} \tag{A.6}$$

where $t = 2j$ for positive parity or $t = 2j + 1$ for negative parity, and Z_t^{-1} can be interpreted as the probability of being in the t^{th} rotational state among population in the same rotational parity ladder.

A.2.1. Parity Distribution

The relative population distribution between each separate parity rotational ladder will be mediated by whatever the dominant parity exchange mechanism is. Here I will derive the relative distribution assuming the dominant mechanism is via a cascading decay into the ground state due to weak branching f to an intermediate state. This is the case for SiO^+ which is expected to have the dominant mechanism be a cascading decay through the A state.

In the steady state, the total flow of population leaving a particular parity of the intermediate state must equal the flow of population into that parity. The pumping rate into an intermediate state is described in Eqn. (A.9) and because the process for populating the state is a single excitation followed by a single decay, the parity is preserved. Conversely, the decay out of the intermediate state is a parity changing process which, in the steady state, means that the population flow out of one parity of the intermediate state must equal the flow into the opposite parity of the ground state. We can define this total flow out of each set of states of the same parity in the ground vibrational state to be proportional to

$$\begin{aligned}\zeta^{+}_{v=0} &= \sum_{i=0}\left(\frac{\lambda^{P}_{2i}}{\alpha^{P}_{2i}}+\frac{\lambda^{R}_{2i}}{\alpha^{R}_{2i}}\right)n^{v=0}_{2i}\\ \zeta^{-}_{v=0} &= \sum_{i=0}\left(\frac{\lambda^{P}_{2i+1}}{\alpha^{P}_{2i+1}}+\frac{\lambda^{R}_{2i+1}}{\alpha^{R}_{2i+1}}\right)n^{v=0}_{2i+1}.\end{aligned} \tag{A.7}$$

It is convenient to then define $\mathcal{Z}^{v}_{t}\equiv\zeta^{\pm}_{v}/n^{v}_{t}$ which allows us to consider flow rates explicitly in terms of the pulse shaped spectrum by noting that

$$\begin{aligned}\mathcal{Z}^{v}_{t} = &\sum_{i=0}^{j-1}\left(\frac{\lambda^{P}_{t-2i-2}}{\alpha^{P}_{t-2i-2}}+\frac{\lambda^{R}_{t-2i-2}}{\alpha^{R}_{t-2i-2}}\right)\prod_{k=0}^{i}\frac{\lambda^{P}_{t-2k}}{\lambda^{R}_{t-2k-2}}\\ &+\left(\frac{\lambda^{P}_{t}}{\alpha^{P}_{t}}+\frac{\lambda^{R}_{t}}{\alpha^{R}_{t}}\right)+\sum_{i=0}\left(\frac{\lambda^{P}_{t+2i+2}}{\alpha^{P}_{t+2i+2}}+\frac{\lambda^{R}_{t+2i+2}}{\alpha^{R}_{t+2i+2}}\right)\prod_{k=0}^{i}\frac{\lambda^{R}_{t+2k}}{\lambda^{P}_{t+2k+2}},\ \text{for } j>0.\end{aligned} \tag{A.8}$$

If we assume decay of the intermediate state is a uniform rate, Γ_I, then we have the following relationship between parities:

$$f_I \zeta_0^+ = \Gamma_I I_+ = f_I \zeta_0^- = \Gamma_I I_-$$

$$\zeta_0^+ = \zeta_0^-, \quad I_- = I_+ \tag{A.9}$$

$$\frac{n_{t+1}^0}{n_t^0} = \frac{\mathcal{Z}_t^0}{\mathcal{Z}_{t+1}^0}$$

where $I_\pm$ is the total population in either parity of the intermediate state, and f_I is the branching ratio into the intermediate state.

A.2.2. Vibrational Distribution of SiO^+

If we assume the vibrational states are long lived compared to the vibrational diffusion time due to off-diagonal decay, then we can compare the relative populations in the vibrational levels independently from the vibrational lifetimes. In SiO^+, population in the A state preferentially decays to the ground vibrational level of X. This limits the effective distance the population can vibrationally diffuse in the X state via off diagonal decay. Because $B \rightarrow X$ has nearly diagonal FCFs, decay from B will strongly prefer decays of $\Delta v = \pm 1$ over decays of $|\Delta v| > 1$. Assuming a random walk we might expect the maximum vibrational diffusion from the ground state would be approximately $\Delta v \approx \sqrt{n_s f_{\Delta v=1}}$ where $n_s = 1/f_{B,A}$ is the average number of scatters before a decay to the A state and subsequent return to the ground vibrational state of X. For SiO^+ we have that $f_{\Delta v=1} = 1/33$ and $f_{B,A} \approx 1/140$, and thus we expect the vibrational diffusion to extend to $v \approx 2$ from the ground state.

Let us label the branching ratio of $B(v') \rightarrow X(v'')$ to be $f_{v',v''}$. Then according to calculation, and consistent with experimental data, we have $f_{v,v\pm1} >> f_{B,A}, f_{v,v\pm2}$. If we also assume that optical pumping is significantly faster than the spontaneous decay rate of excited vibrational levels, then we can expect that each parity will have its own, independent vibrational distribution determined by the following relations

$$\begin{aligned} f_{0,1}\zeta_0^{\pm} &= f_{1,0}\zeta_1^{\pm} \\ (f_{1,0}+f_{1,2})\zeta_1^{\pm} &= f_{0,1}\zeta_0^{\pm} + f_{2,1}\zeta_2^{\pm} \\ f_{1,2}\zeta_1^{\pm} &= f_{2,1}\zeta_2^{\pm} \\ &\cdots \\ f_{v,v+1}\zeta_v^{\pm} &= f_{v+1,v}\zeta_{v+1}^{\pm}. \end{aligned} \tag{A.10}$$

In a nearly diagonal molecule, the FCFs will also be approximately symmetric meaning that $q_{v,v+1} \approx q_{v+1,v}$. Thus the ratio of branching fractions will be proportional to the ratio of their transition energies cubed. So it is convenient to define

$$\beta \equiv \left(\frac{T_e - \omega_X}{T_e + \omega_B}\right)^3 \approx \frac{f_{v,v+1}}{f_{v+1,v}} \approx \frac{4}{5} \tag{A.11}$$

such that

$$\begin{aligned} \zeta_v^{\pm} &= \frac{f_{v+1,v}}{f_{v,v+1}}\zeta_{v+1}^{\pm} = \frac{\zeta_{v+1}^{\pm}}{\beta}, \\ \frac{n_t^{v+1}}{n_t^v} &= \beta\frac{\mathcal{Z}_t^v}{\mathcal{Z}_t^{v+1}}, \quad \frac{n_t^{v+k}}{n_t^v} = \beta^k\frac{\mathcal{Z}_t^v}{\mathcal{Z}_t^{v+k}} \end{aligned} \tag{A.12}$$

A.2.3. Simplified Steady State Model for SiO^+

The net population in the target states can be estimated using the following relations:

$$\begin{aligned}
\sum_k \left(\sum n^k\right)_\pm &= n_t^v \sum_k \frac{n_t^k}{n_t^v} Z_t^k = n_t^v \sum_k \beta^{k-v} \frac{\mathcal{Z}_t^v}{\mathcal{Z}_t^k} Z_t^k, \\
\frac{n_{t+1}^v}{n_t^v} &= \frac{\mathcal{Z}_t^v}{\mathcal{Z}_{t+1}^v}, \\
I_+ + I_- &= 2n_t^v \frac{f_I}{\Gamma_I} \left(\sum_k \frac{n_t^k}{n_t^v} \mathcal{Z}_t^k\right) = n_t^v \mathcal{Z}_t^v \frac{2f_I}{\Gamma_I} \left(\sum_k \beta^{k-v}\right)
\end{aligned} \tag{A.13}$$

where $\left(\sum n^k\right)_\pm$ is the sum over the (fractional) population in one parity in the low lying vibrational states of X and $I_p m$ represents the total population in the intermediate state A. Thus we can express the sum of all fractional populations in terms of the population in the target state $N = t$ in the vibrational state v as

$$\begin{aligned}
1 &= \sum_k \left(\left(\sum n^k\right)_+ + \left(\sum n^k\right)_-\right) + I_+ + I_- \\
&= n_t^v \sum_k \beta^{k-v} \left(\frac{\mathcal{Z}_t^v}{\mathcal{Z}_t^k} Z_t^k + \frac{n_{t+1}^v}{n_t^v} \frac{\mathcal{Z}_{t+1}^v}{\mathcal{Z}_{t+1}^k} Z_{t+1}^k + \mathcal{Z}_t^v \frac{2f_I}{\Gamma_I}\right) \\
&= n_t^v \mathcal{Z}_t^v \sum_k \beta^{k-v} \left(\frac{Z_t^k}{\mathcal{Z}_t^k} + \frac{Z_{t+1}^k}{\mathcal{Z}_{t+1}^k} + \frac{2f_I}{\Gamma_I}\right).
\end{aligned} \tag{A.14}$$

From this expression the population for any state can be estimated.

A.2.4. $N = 0$ Steady State of SiO^+

Experimentally we are in the unsaturated case for optical pumping. If we model the pulse-shaped spectrum as constant before the cutoff and then having a cutoff with a sharpness σ_c at near the band origin then we can parametrize the spectral intensity in Eqn. (A.2)

in terms of rotational number by setting

$$\begin{aligned}\lambda_N^P &= s_0\left(\frac{N(N-1)}{4N^2-1}\right)\Gamma \text{ for } N>1,\\ \lambda_N^R &= s_0 e^{-\frac{2B_0(\Delta+2+N)}{\sigma_c}}\left(\frac{N^2+3N+2}{4N^2+8N+3}\right)\Gamma \text{ for } N\geq 0\end{aligned} \tag{A.15}$$

where Δ is a term that depends on precisely where the cutoff is located such that special case of $P(1)$ is $\lambda_f^P(0) = s_0 f e^{-\frac{2B_0\Delta}{\sigma_c}}\Gamma/3$. For the excited vibrational states we can assume that the cutoff begins after $R(2)$.

If we parametrize the cutoff sharpness according to the rotational constant by defining $\epsilon \equiv e^{-\frac{2B_0}{\sigma_c}}$[1] as the suppression of the spectral intensity over the spacing between consecutive rotational transitions, then we can determine the necessary cutoff for significant population accumulation in the ground rotational state. By calculating Eqn. (A.14) to $\mathcal{O}(\epsilon^4)$ we find

$$n_0^0 \approx 1 - \overbrace{12\epsilon^2}^{n_1^0} - \overbrace{5\epsilon^{2+\Delta}}^{n_2^0} - \overbrace{(\beta+\beta^2)9\epsilon^{2+\Delta}}^{n^{v>0}} - \overbrace{(1+\beta+\beta^2)\frac{8f_I s_0\Gamma}{\Gamma_I}\epsilon^{2+\Delta}}^{I_+ + I_-} + \mathrm{O}(\epsilon^4) \tag{A.16}$$

which provides us information on the leading order behavior of the population distribution. From this we note that the population in $N=1$ is suppressed independently from the cutoff position by ϵ^2. That is, it is insensitive to the location of the cutoff between $P(2)$ and $P(1)$. Everywhere else, the population is suppressed by $\epsilon^{2+\Delta}$ and thus to maximize the $N=0$ population, $\Delta=1$ should be used, i.e. the cutoff should begin at $P(2)$[2].

[1] The actual cutoff suppression is better described by a Gauss error function.

[2] If population in $N=1$ is pumped too slowly, however, then BBR redistribution may become significant and the observed distribution may be degraded. In this case, a cutoff closer to $P(1)$ may maximize the $N=0$ population.

Compared to population in $N = 1$, population in the intermediate state (i.e. the A state of SiO^+) is suppressed by a factor of $\epsilon^{\Delta \frac{8 f_{B,A} s_0 \Gamma_B}{\Gamma_A}}$. Under experimental conditions $f_A s_0 \Gamma$ was observed to be $\sim 100^{-1}$ ms^{-1} (see section 7.3) which is significantly smaller than Γ_A which is expected to be ~ 1 ms^{-1}. Thus it is not expected to contribute significantly. If the overall intensity is increased then significant population accumulation may begin to occur in the A state as $f_{B,A}\Gamma_B/\Gamma_A \approx 10^2$.

Outside of the high intensity regime, to leading order, the loss of population in $N = 0$ is accumulation of population in the $N = 1$ state of $v = 0$. Thus the requirement for significant population accumulation in $N = 0$ is that $12\epsilon^2 << 1$. To achieve a state preparation fidelity of >90% this requirement suggests that the cutoff suppression needs to be better than a decade per $2B_0$.

APPENDIX B

SiO^+ Experiments

B.1. Dissociating Laser Frequency Calibration

Calibration of the fundamental wavelength output of the dye laser was performed using a wavemeter (Bristol 871 Laser Wavelength Meter) with accuracy limited only by the laser linewidth. During the dye laser frequency measurements with the wavemeter, the wavemeter reading was observed to hop between two modes that were consistently offset by 63.77 cm^{-1}. The preferred mode detected by the wavemeter was highly sensitive to alignment and would sometimes shift as the dye laser wavelength was scanned. The correct mode was determined by calibrating to the Ba^+ $5d^2D_{3/2} \rightarrow 7p^2P_{1/2}$ transition at 224.639 nm (see Fig. 7.3).

Calibration of the OPO using the wavemeter was not found to be possible through direct measurement. Instead a linear fit using multiple Ba^+ transitions and $X \rightarrow C$ transitions accurately identified by the dye laser over the range of 42870 cm^{-1} to 47415 cm^{-1} using the spectrum in Fig. 7.1 was used and an overall calibration uncertainty of 8 cm^{-1} is estimated from the fit.

B.2. Reaction Systematics

We can evaluate the range of possible systematic shifts by introducing a simple equation and determine how different unknowns can effect the measured value for the rate

constant, $k_m^{\mathrm{H_2}}$, versus the true rate constant, $k_t^{\mathrm{H_2}}$ by modeling the effects of possible inaccuracies on the measured (pseudo) first order rate, R_m, and the measured H_2 gas density, n_m with the following relations:

$$\begin{aligned} R_m &= k_t^{\mathrm{H_2}} n_{\mathrm{H_2}} + k^i n_i \\ n_m &= \frac{s_c/s_t}{C_{\mathrm{H_2}}}(C_{\mathrm{H_2}} n_{\mathrm{H_2}} + C_i n_i + c_0) \\ k_m^{\mathrm{H_2}} &= \frac{R_m}{n_m - \frac{c_0 s_c}{s_t C_{\mathrm{H_2}}}} = k_t^{\mathrm{H_2}} \frac{s_t}{s_c} \frac{1 + \frac{k^i n_i}{k_t^{\mathrm{H_2}} n_{\mathrm{H_2}}}}{1 + \frac{C_i n_i}{C_{\mathrm{H_2}} n_{\mathrm{H_2}}}} \end{aligned} \tag{B.1}$$

where s_t, s_c are the true and calibrated sensitivity factors for the IG, n is the number density, c_0 is some constant offset of the IG pressure reading that will cancel when determining the linear slope, C is a gas correction factor for the IG, and parameters indexed with i are the average values for non-hydrogen components of the background.

From Eq. (B.1), we find that the background gas composition will lead to a negative shift in $k_m^{\mathrm{H_2}}$ if $k_i/k_t^{\mathrm{H_2}} < C_i/C_{\mathrm{H_2}}$ and to a positive shift otherwise. The fractional magnitude of the shift will be proportional to $n_i/n_{\mathrm{H_2}}$ and therefore it will be small compared to the statistical uncertainty and is unlikely to explain the discrepancy between our measured value and the one measured by Fahey et al.

Another potential systematic shift is a consequence of the ion gauge (IG) location in the vacuum chamber. The chamber housing the ion trap is connected to these elements by a 2-3/4 inch conflat and is separated by less than 20 cm from the IG[1]. The relative positioning will result in a differential pressure between the IG and the trap such that the pressure reading on the IG is expected to underestimate the pressure at the trap. This

[1]See Fig. 5.1 of chapter 5 for schematic of the vacuum chamber.

is equivalent to decreasing the true sensitivity, s_t in Eq. (**??**), and therefore results in a positive shift in the estimated rate constant. The precise difference in the pressure near the IG and the pressure near the trap is difficult to estimate, however the fractional change in pressure will be less than the ion pump speed divided by the conductance between the two locations. For our vacuum chamber this suggests that the shift will be smaller than the statistical uncertainty of the fit[2].

Besides a differential pressure effectively reducing the sensitivity of the IG, the sensitivity of the IG itself may change over time. The IG (Granville-Phillips 370 Stabil-Ion) has not been recalibrated since it was purchased and has been in constant use under UHV conditions for over 6 years. A study of the stability of the Stabil-Ion IG over a 15 year period by Fedchak and Defibaugh at NIST, however, reports that the long term stability is 2 to 3% [**42**]. Thus it is unlikely that a change in the sensitivity of the IG has contributed significantly to the measured rate constant.

An additional systematic could exist if the relative gas composition changes significantly as the TSP is heated to raise the pressure. This would have the effect of adding a curve to the plot in Fig. 7.9. Whether the curve is positive or negative will depend on how C_i/C_{H_2}, $k_i/k_t^{\mathrm{H}_2}$, and n_i/n_{H_2} change with gas composition. If the curve is negative it will result in an negative shift of the slope accompanied by a positive shift in the offset of the linear fit. Conversely, a positive curve will result in a positive shift of the slope and a negative offset of the linear fit. In the linear fit, the offset was found to be

[2]An estimate on the conductance under free molecular flow between the IG and the trap is 130 l/s for hydrogen which is approximately 3× the ion pump speed (20 l/s nominal speed, 2×20 l/s for H_2). The conductance of a cylindrical tube is estimated using the relation $C = 3.81(T/M)^{1/2}(D^3/L)$ where the conductance is $[C] = l/s$, the tube diameter is $[D]$ =cm, the tube length is $[L]$ =cm, the temperature is $[T]$ =K, and the mass of the gas is $[M]$ =u [**178**]

-14(20)$\times 10^6$ cm^{-3} ($-4(6) \times 10^{-10}$ Torr) or otherwise consistent with zero and therefore consistent within the specified accuracy of the ion gauge (4% at 10^{-8} Torr).

B.3. $N = 0$ Cooling Efficiency Systematics

The quantitative details of the systematic effects are listed in Table 7.6. Here, I discuss how each shift is estimated.

B.3.1. Reactions

Reaction of SiO^+ with background H_2 gas contributes a systematic decrease in the measured steady state fraction dissociated. A minimum of 10 s after loading is required to perform the baseline measurement. Loading and triggering of the dissociation pulse are performed manually and typically add an additional 10-20 s to the sample's background gas exposure time. Attempts to characterize the reaction rate which are discussed in section 7.2 suggest a $1/e$ time of 11(2) minutes. Thus the expected fraction of the SiO^+ that is expected to be reacted before the dissociation experiment begins is 3.8(1.0)%. Therefore the maximum possible dissociation fraction expected is the unreacted fraction of the sample $f = 0.962(1)$.

B.3.2. Isotope Shifts

Isotope shifts are calculated using the moment of inertia dependence of the new molecular constants obtained in section 7.1 for the C state and the constants for X from [**24**]. The most abundant isotope is $^{28}Si^{16}O$ with a natural abundance of 92%. ^{16}O has a 99.8% natural abundance therefore the remaining natural isotopes of SiO are primarily other isotopes of silicon which has natural abundances of ^{29}Si (4.7%) and ^{30}Si (3.1%). For

the $X - B$ transition the isotope shift for $P(1)$ and $R(0)$ in each case is less than 0.2 cm^{-1} and therefore the effectiveness of the rotational cooling mask is not significantly affected though it will be (progressively) degraded for the heavier isotopes. The isotope shift is much more pronounced in the $X^2\Sigma^+ \rightarrow C^2\Pi$ transition and significantly shifts the dissociating transitions relative to the pulsed laser linewidth. For the $Q(0)$ transition, the isotope shift for $^{29}Si^{16}O$ and $^{30}Si^{16}O$ is expected to be 0.51 and 0.99 cm^{-1} respectively. Therefore, the probability for dissociating population in the ground state of the lower abundance isotopes is reduced according to their detuning and the Lorentzian profile of the laser (i.e. reduced by $\frac{1}{1+4(\Delta/\Gamma)^2}$, where $\Gamma = 0.56$ cm^{-1}).

B.3.3. Nearby Transition Overlap

A positive systematic shift due to the nearby $Q(1)$ transition will also contribute to the total. The $Q(0)$ transition is approximately 0.98 laser linewidths detuned from the $Q(1)$ transitions (see Fig. 7.11). Similarly, $Q(1)$ is expected to shift another 0.50 and 0.98 cm^{-1} away from the probe wavelength for $^{29}Si^{16}O$ and $^{30}Si^{16}O$ isotopes respectively. Thus, in the steady state we are probing a linear combination of the unreacted fraction of the sample, f, in $N = 0, 1$ with different weights according to isotopes and detuning from the laser. A reasonable approximation using Eqn. (A.16) of appendix A.2.4 is to assume that the population in $N = 1$ accounts for ~ 0.4 of the population not in $N = 0$[3]. If we let n_i represent the fraction of population in the i^{th} rotational state then we can write $n_1 \approx 0.4(1 - n_0)$.

[3]Here I assume that the spectral intensity at $P(1)$ is $\sim 0.9\times$ that at $P(2)$.

B.4. $N = 0$ Thermalization via Off Resonant CW Excitation

Here I consider a possible source of thermalization due to off resonant excitation of the Ba^+ CW Doppler cooling lasers. To reproduce an excitation rate consistent with observations, the detuning of the Doppler cooling lasers must be be of order $\Delta \sim \frac{\Gamma}{2}\sqrt{\Gamma_{i,j}\tau}$ where τ is the observed time scale. Even in the case of a fully allowed transition with perfect vibrational overlap and an upper state lifetime comparable to the $6P_{1/2}$ state of Ba^+, the detuning from resonance would need to be less than 10 wavenumbers to significantly contribute to the observed thermalization time scale. Vibrational spacing is of order 900 cm^{-1}, therefore the detuning of the lasers from any transition will likely be greater than 10 wavenumbers. Additionally, the FCFs will generally increase the lifetime (and therefore decrease the linewidth) of the nearest states because they reduce their transition dipole moment with the ground state. A more realistic estimate would suggest that the detuning must be $<< 1$ wavenumber before it can significantly contribute to the measured rate.

B.5. The $v = 1$ Lifetime Estimate

The $v = 1$ lifetime is estimated indirectly using the single frequency method in the fast dissociation regime. For this measurement the rotational cooling mask is applied to accumulate population in the ground rotational state of $v = 0$. Then, after turning off the optical pumping, the $X^2\Sigma^+(v = 1) \rightarrow C^2\Pi_{3/2}(v = 0)$ transition at 43077 cm^{-1} is pumped by the broadband OPO such that the first several rotational states of $v = 1$ are covered. Under these conditions the only mechanisms for transferring population to $v = 1$ are either collisions or black body. Collisions exciting vibrations will be suppressed due to the large

separation in energy between vibrational levels compared to the thermal energy of the collisions and therefore the dominant mechanism will be due to BBR. If the time scale for dissociating is faster than the Einstein $\mathcal{A}$ coefficient we measure, then the observed dissociation rate can be considered to be a measure of the BBR rate. The BBR rate can then be related to the Einstein coefficient using the relation $R = A(exp(\frac{\Delta E}{kT}) - 1)^{-1}$. If the time scale for dissociating is slower than the Einstein $\mathcal{A}$ coefficient, then the probability of dissociation multiplied by the population will be related to the observed rate via the relation $p_{diss.}n^{v=1} \approx 1 - e^{-R/10}$. Under these conditions we can estimate the population in $v = 1$ using the Boltzmann distribution which is 0.4% at room temperature. The observed dissociation rate is 0.0037(18) s^{-1}. If this were to be a measurement performed in the slow dissociation regime, then $p_{diss.} \approx 0.09$. However, from the data taken using the BBR assisted mask, we know that $1 > p_{diss.} > 0.2$. Because the laser is pulsed at 10 Hz, this implies that the dissociation rate is bounded by $2\ s^{-1} < R_{diss.} < 10\ s^{-1}$ which exceeds the estimate for the $\mathcal{A}$ coefficient ($A = 1.0(5)\ s^{-1}$) and (crudely) justifies the approximation.